UC Davis

UC Davis Electronic Theses and Dissertations

Title

Scalable Quantum Nanophotonics with Integrated Color Centers in Silicon Carbide

Permalink

https://escholarship.org/uc/item/40g0q9cx

ISBN

9798193262077

Author

Saha, Pranta

Publication Date

2026-09-08

Peer reviewed|Thesis/dissertation

eScholarship.org Powered by the California Digital Library
University of California

Scalable Quantum Nanophotonics with Integrated Color Centers in Silicon Carbide

By

Pranta Saha

Dissertation

Submitted in partial satisfaction of the requirements for the degree of

Doctor of Philosophy

in

Electrical and Computer Engineering

in the

Office of Graduate Studies

of the

University of California

Davis

Approved:

Marina Radulaski, Chair

Saif Islam

Jeremy Munday

Committee in Charge

2026

Copyright © 2026 by
Pranta Saha
All rights reserved.

To my dear friend

Lord Shri Krishn

Abstract

Scalable quantum networks for distributed quantum computing and global quantum communication require high-fidelity spin-photon interfaces integrated with foundry-compatible photonic hardware. Color centers in silicon carbide (SiC) have emerged as a promising solid-state platform due to their isolated deep-level encapsulation, long-lived spin coherence, near telecom emission, and the host material's commercial 200 mm wafer availability. Enhancing the performance of these quantum emitters requires nanophotonic integration to overcome low extraction efficiency owing to total internal reflection, explore light-matter interactions, and perform on-chip quantum information processing. However, photonic integration of quantum-grade SiC has been fraught with challenges in thin-film material quality and scalability limits in conventional bulk fabrication techniques.

To overcome these manufacturing limitations, this dissertation establishes a comprehensive theoretical, fabrication, and experimental framework for wafer-scale angle-etched bulk 4H-SiC quantum nanophotonics using an Ion Beam Etching (IBE) process. First, a complete computational pipeline employing Finite-Difference Time-Domain (FDTD), Finite-Difference Eigensolver (FDE), and Plane Wave Expansion (PWE) methods is developed to design and optimize triangular cross-section passive and active devices, including single-mode waveguides, directional beam splitters, fishbone grating couplers, photonic crystal mirrors, and nanobeam cavities. Next, a wafer-scale IBE process is engineered to fabricate nanophotonic patterns directly on bulk 4H-SiC substrates, while systematically optimizing the key process parameters to achieve minimal sidewall angular mismatch

and high processing uniformity across large areas. Finally, using room-temperature and cryogenic confocal photoluminescence spectroscopy alongside optical transmission setups, freestanding 4H-SiC nanophotonic structures with integrated nitrogen-vacancy (NV^-) centers are experimentally characterized. By uniting advanced numerical modeling with foundry-compatible IBE process development, this work builds the foundational manufacturing infrastructure needed to transition SiC quantum photonics from isolated laboratory prototypes to scalable high-volume quantum repeater hardware.

Acknowledgments

They say *it takes a village to raise a child*, but it certainly takes an entire ecosystem of mentors, collaborators, and friends to raise a PhD. Completing this doctoral journey was made possible through the collective guidance, wisdom, and generous support of many exceptional individuals that shaped me into a researcher.

At the heart of this journey, I want to first express my deepest gratitude to my advisor, Prof. Marina Radulaski. Under her expert guidance, I gained a rigorous foundation in quantum physics, expanding my understanding of key theoretical principles and mastering advanced research methodologies. Her unwavering support, guidance, patience, and trust through all the highs and lows were instrumental in bringing the projects to fruition. I am also immensely thankful to Marina for providing access to cutting-edge facilities and equipment, fostering valuable domestic and international collaborations, and offering me opportunities to present at premier conferences, experiences that profoundly shaped my scientific trajectory. Beyond her research mentorship, Marina nurtured my broader growth as a professional, patiently providing guidance to sharpen my presentation and scientific communication skills. I am equally grateful for the opportunity to serve as the lead TA under her instruction in EEC 189L Quantum Computing course, which introduced me to modern research-based pedagogical methodologies. Above all, I want to thank Marina for giving me the intellectual freedom to take risks and learn from failures. Her enduring belief and encouragement made this journey truly rewarding and enjoyable.

I am grateful to my committee members Prof. Saif Islam and Prof. Jeremy Munday for their valuable feedback in completing this dissertation. I feel truly overwhelmed with the kindness and support Prof. Islam has shown me throughout the journey. Prof. Islam provided me with the fundamentals of nanofabrication in his graduate course, always welcoming my naive questions with patience during office hours, which laid an essential technical foundation for my research. In addition, the opportunity Prof. Islam provided to participate in CITRIS workforce development workshops significantly refined my ability to communicate complex scientific ideas to broader audiences. I am equally grateful to Prof. Munday, whose instruction marked my first dedicated quantum engineering course.

His amiable nature and engaging teaching style made the learning enjoyable and ignited my lasting curiosity for quantum technologies. I would like to thank the ECE department and also extend my sincere gratitude to Prof. Juan Sebastian Gomez-Diaz, Prof. William Putnam, Prof. Erkin Seker, and Prof. Josh Hihath for their instruction and mentorship during coursework, which deepened my foundational knowledge in electromagnetics, photonics, nonlinear optics, device fabrication, and molecular engineering. The rigorous problem sets and term final projects served as a continuous source of inspiration, helping me brainstorm and develop new ideas directly applicable to my doctoral research. I would also want to acknowledge the guidance and support I received from the Physics department during my PhD coursework on quantum technology.

I extend my sincere gratitude to the staff and user community at the Molecular Foundry in Lawrence Berkeley National Laboratory. In particular, I am grateful to Scott Dhuey and Selven Virasawmy at the Nanofabrication Facility, as well as Tevye Kuykendall at the Inorganic Nanostructures Facility, for generously sharing their technical expertise and providing crucial support throughout my nanofabrication efforts. At UC Davis, my experimental work relied heavily on the resources and support from the Center for Nano-MicroManufacturing (CNM2) facility. I would like to thank Ryan Anderson, Vishal Narang, Chan Kim, and the entire CNM2 staff for their constant assistance and dedication to maintaining a world-class cleanroom facility. I am specially indebted to Vishal, whose technical guidance and hands-on troubleshooting were indispensable in developing and optimizing the etching recipes.

My heartfelt thanks also go to our international collaborators for their exceptional collaborative spirit, technical expertise, and shared scientific vision. I am grateful to Prof. Jörg Wrachtrup, Prof. Florian Kaiser, and their group members Charles Babin, Marcel Krumrein, and Jonathan Körber at the University of Stuttgart for the collaborative project on color center integrated 4H-SiC triangular cross-section waveguides. I am also grateful to Prof. Kai Müller, Prof. Jonathan Finlay, and their students Stefan Strohauer, Fabian Wietschorke, Rasmus Flaschmann, Lucio Zugliani, and Christian Schmid at the Technical University of Munich for collaboration on integrating superconducting nanowire

single photon detectors on 4H-SiC. Specially, I want to thank Kai for hosting me in Munich, where I got to visit the advanced optical laboratories and nanofabrication facilities. I am also very grateful to Kai for sharing his deep technical expertise and guidance on my projects during his visits to UC Davis.

I owe immense gratitude to all the Radulaski Lab group members for creating such an amazing environment for learning and growing together. First and foremost, I want to thank Sridhar Majety (was also the first student of the group) for being such a wonderful mentor and a great friend who helped me from navigating graduate school dynamics to providing hands-on training in nanofabrication. I am proud of what our collaborative efforts achieved throughout the period and even more grateful that our friendship continues to thrive beyond academia. I am also thankful to Victoria Norman for patiently mentoring me on building optical setups and helping me acclimate to the new environment. I extend my gratitude to Alex Rubin who not only boosted our experimental efforts but also enriched our understanding of the color center physics. The amount of effort Alex invested in expanding our experimental capability and automation served as a constant driving force for me to work even harder to fabricate new devices. Working with junior PhD students Elnaz Hamdarsi, Nathan Gonzalez, and Rubek Poudel was an absolute joy. Their curiosity and dedication not only offered me the opportunity to grow as a mentor but also continually elevated my design and process workflows. Lastly, I want to thank my graduate mentees Dinesh and Madhu, as well as undergraduate mentees Akhil, Eliana, Zbynka, Jack, and Madeleine for their significant contribution to our simulation, layout, and experimental efforts. Witnessing their growth and celebrating their successes has been one of the most rewarding parts of this journey.

Life beyond the cubicle, cleanroom, and optical benches was kept grounded, joyful, and sane thanks to an extraordinary circle of friends and family in Davis and the Bay Area. I am specially grateful to Sudipta, Chris, Abir, Ayesha, Nusha, Yael, Anindya, Rishad, Ahasan, Mohiuddin, and Rifat for always being there through every stage of this adventure. I owe a special debt of gratitude to my aunt Deepa, uncle Mithilesh, Ruby dida, Deepu dadu, and uncle Pronoy for generously making California feel like a second

home. I am also thankful to my cherished friends Swastika, Rocky, Lincon, Shiblee, Akib, Rushrukh, Shahad, and Etika for their encouragement and support from different parts of the world.

I am forever indebted to my parents who first inspired me to pursue a PhD and remained an enduring source of strength and encouragement throughout. Their passion for science and education provided both the essential foundation and the fuel to embark on this journey. My heartfelt gratitude goes to my lovely wife Toma for generously supporting me through every thick and thin, and for filling my life with warmth and color beyond the realm of the grayscale SEM images. Lastly, I offer my profound gratitude and surrender to my eternal friend Lord Shri Krishn, to whom this dissertation is dedicated, for imparting the timeless philosophy of *action without attachment*, a guiding compass that made completing this journey possible!

Author List

Portions of Chapters 2 and 3 appeared in the following publications:

S. Majety, **P. Saha**, V. A. Norman, M. Radulaski, "Quantum information processing with integrated silicon carbide photonics", *Journal of Applied Physics*, 131(13), 130901 (2022).

V. A. Norman, S. Majety, A. H. Rubin, **P. Saha**, ... M. Radulaski, "Sub-2 Kelvin Characterization of Nitrogen-Vacancy Centers in Silicon Carbide Nanopillar", *ACS Photonics* 12, 5, 2604–2611 (2025).

A. H. Rubin, V. Žalandauskas, **P. Saha**, R. Poudel, A Teien, L. Hofmann, N. R. Gonzalez, S. Dhuey, M. E. Bathen, M. Radulaski, "Seeing the forbidden: overcoming optical selection rules through nanophotonic integration", *arXiv*:2605.04277 (2026).

Portions of Chapter 4 appeared in the following publications:

S. Majety, V. A. Norman, L. Li, M. Bell, **P. Saha**, M. Radulaski, "Quantum photonics in triangular-cross-section nanodevices in silicon carbide", *Journal of Physics: Photonics*, 3(3), 034008 (2021).

C. Babin, ... S. Majety, **P. Saha**, M. Radulaski, N. T. Son, J. Ul-Hassan, F. Kaiser, J. Wrachtrup, "Fabrication and nanophotonic waveguide integration of silicon carbide colour centres with preserved spin-optical coherence", *Nature Materials*, 21, 67–73 (2022).

Chapter 5 appeared in the following publication:

P. Saha, S. Majety, M. Radulaski, "Utilizing photonic band gap in triangular silicon carbide structures for efficient quantum nanophotonic hardware", *Scientific Reports*, 13, 4112 (2023).

Chapter 6 appeared in the following publication:

S. Majety*, **P. Saha***, Z. Kekula, S. Dhuey, M. Radulaski, "Triangular Cross-Section Beam Splitters in Silicon Carbide for Quantum Information Processing", *MRS Communications*, 1-7 (2024).

Chapter 7 appeared in the following publication:

S. Majety, V. A. Norman, **P. Saha**, A. H. Rubin, S. Dhuey, M. Radulaski, "Wafer-Scale Integration of Freestanding Photonic Devices with Color Centers in Silicon Carbide", *npj Nanophotonics* 2, 3 (2025).

Chapter 8 appeared in the following publication:

P. Saha, A. H. Rubin, S. Majety, S. Dhuey, M. Radulaski, "Triangular cross-section grating couplers for integrated quantum nanophotonic hardware in silicon carbide", Special Collection *'Emerging Leaders in Materials Science'*, *APL Materials* 13, 071102 (2025).

Portions of Chapter 11 appeared in the following publication:

S. Majety, S. Strohauer, **P. Saha**, ... K. Müller, M. Radulaski, "Triangular Quantum Photonic Devices with Integrated Detectors in Silicon Carbide", *Materials for Quantum Technology*, 3, 015004 (2023).

Contents

Abstract . . . iii

Acknowledgments . . . v

Author List . . . ix

List of Figures . . . xv

List of Tables . . . xxix

1 Introduction **1**

1.1 Motivation . . . 2

1.2 Contribution . . . 4

1.3 Thesis Outline . . . 6

2 Quantum Nanophotonics in SiC **7**

2.1 Color Center Systems . . . 7

2.2 SiC: A Promising Quantum Optical Material . . . 11

2.3 Nanophotonic Integration . . . 15

2.4 Progress Towards Scalability: A New Angle . . . 18

3 Nanofabrication & Experimental Methods **21**

3.1 Nanofabrication . . . 21

3.1.1 Color Center Generation and Activation . . . 22

3.1.2 Process Flow . . . 23

3.1.3 Inductively Coupled Plasma-Reactive Ion Etching . . . 25

3.1.4 Ion Beam Etching . . . 27

3.1.5 Post-Etching Process . . . 29

3.2 Optical Characterization . . . 30

3.2.1 Cryogenic 4f-Confocal Microscopy Setup . . . 31

3.2.2 Room-Temperature 2f-Confocal Microscopy Setup . . . 34

4 Color Center Photonics with Triangular Geometry in SiC **35**

4.1 Optimal Position for Color Center Integration in Triangular Geometry . . 35

4.2 Design Optimization of Triangular Cross-Section Waveguides for V2 Centers in 4H-SiC 37

5 Photonic Bandgap Engineering with 1D Triangular Cross-Section Photonic Crystal in 4H-SiC **42**

5.1 Triangular Cross-Section Photonic Crystal 43

5.2 Dispersion Relations in Triangular Geometry 45

5.3 Effects of Parameters on PBG Formation 46

5.4 Results and Discussion 48

5.5 Conclusion 51

6 Triangular Cross-Section Beam Splitters for On-Chip Interferometry **52**

6.1 Evanescent Coupling via Single-Mode Waveguides 53

6.2 Integrated 4H-SiC Beam Splitter in Triangular Geometry 57

6.3 Fabrication of Closely Spaced Triangular Waveguides in 4H-SiC 59

6.4 Discussion 60

7 Wafer-Scale Integration of Color Centers with 4H-SiC Nanophotonic Devices **62**

7.1 Wafer-Scale Etching of 4H-SiC 62

7.2 Nanofabrication Methods 67

7.3 Results and Discussion 68

8 Wafer-Level Testing with Triangular Cross-Section Fishbone Grating Couplers **71**

8.1 Triangular Cross-Section Fishbone Grating Coupler 72

8.1.1 Single-Mode Waveguide 72

8.1.2 Adiabatic Taper 74

8.1.3 Fishbone Grating 74

8.2 Design Optimization 76
8.3 Experimental Results 80
8.3.1 Nanofabrication Process 81
8.3.2 Transmission Measurements 82
8.3.3 Cryogenic Photoluminescence Spectroscopy Measurements 87
8.3.4 Collection Efficiency Calculation 89
8.4 Outlook 90

9 Systematic Analysis of Nanofabrication Processes and Parameter Optimization 92
9.1 Comparative Analysis of ICP-RIE Processes 93
9.2 Beam Extraction Physics and Etch Angle Optimization in RIBE 97
9.2.1 Discharge Chamber and Screen Grid: Sheath Formation and Meniscus Physics 98
9.2.2 Acceleration Grid: R Parameter and Perveance Mechanics 100
9.2.3 Deceleration Grid and Space-Charge Neutralization 103
9.2.4 Experimental Results: Angle-Etch Fidelity and Benchmark Comparison 104
9.2.5 Practical Tool Non-Idealities: Nanoquest II Analysis 106

10 Nanophotonic Manipulation of Color Center Emission 109
10.1 Photonic Crystal Mirror 109
10.2 Photonic Crystal Cavity 112

11 Outlook 119
11.1 Monolithic Heterogeneous Integration 119
11.2 The Broader Quantum Landscape in SiC 121

List of Figures

2.1 (a) Schematic representation of simplified energy level diagram showing excitation and relaxation pathways isolated within the electronic bandgap of the host material. (b) Corresponding emission spectrum of a color center, consisting of a sharp zero-phonon line (ZPL) and a broad phonon sideband (PSB). 9

2.2 Entanglement scheme for (a) Λ-system and (b) II-system. 10

2.3 Color centers in 4H-SiC and their emission spectrum. 13

2.4 (a) The crystal structure of 4H-SiC showing the stacking of the atomic bilayers in the ABCB sequence, the inequivalent h and k lattice sites, and the four possible (hh, kk, hk, kh) configurations of the nitrogen-vacancy (NV^-) center. (b) The transition dipole moment planes (yellow disks) for axial (hh, kk) and basal (hk, kh) defects. (c) Photoluminescence spectrum of NV^- center below 2 K with distinct ZPLs corresponding to different configurations. 14

2.5 The SEM images of photonic devices in 4H-SiC. **Passive devices** (clockwise from top left): Triangular cross-section waveguide in 4H-SiC with integrated silicon vacancies [21], nanopillars in 4H-SiC with silicon vacancies [85], vertical coupler fabricated in 4H-SiCOI to convert free-space Gaussian beam into fundamental waveguide mode [86]; **Active Devices:** Suspended nanobeam array fabricated in 4H-SiCOI and (below) magnified image of individual nanobeam PCC with integrated silicon vacancies [20], nanobeam PCC in 4H-SiC with integrated neutral divacancies [19], and triangular cross-section nanobeam PCC fabricated in 4H-SiC [87]. 16

2.6 Schematic representation of fabrication pathways for integrated SiC quantum nanophotonic hardware. 19

3.1 Stopping and Range of Ions in Matter (SRIM) calculated depth distribution profiles of implanted $^{14}N^{+}$ ions and corresponding lattice vacancies (damage events and target recoils) in 4H-SiC for (a) 375 keV ion energy at a fluence of 1×10^{14} cm^{-2} and (b) 65 keV ion energy at a fluence of 1×10^{12} cm^{-2}. 23
3.2 Nanofabrication process flow for SiC photonic hardware. 24
3.3 Illustration of an ICP-RIE system. 25
3.4 Schematic representations of (a) Ion beam etching (IBE) system, (b) Reactive ion beam etching (RIBE) process, and (c) Chemically assisted ion beam etching (CAIBE) process. 27
3.5 SEM images of fabricated 4H-SiC triangular cross-section suspended devices (a) without and (b) with (52° tilt) critical point drying in the post-etching process workflow. 29
3.6 Schematic representation of 2D scanning cryogenic 4f-confocal microscopy setup where green lines show the excitation path and red lines show the collection path. 31
3.7 (a) Photoluminescence (PL) spectra comparing VV^0 and NV center emission from fabricated 1100 nm diameter nanopillars and reference unetched bulk regions. (b) 2D PL map of an array of 600 nm diameter nanopillars. (c) Low temperature NV ensemble optical lifetime measurements from the 600 nm diameter nanopillars. 33
3.8 (a) Schematic representation of room-temperature 2f-confocal microscopy setup. (b) Spectral profile of transmission efficiency through a 10 μm waveguide. 34

4.1 Normalized electric field intensity ($|E|^2$) profiles of TE and TM polarized modes supported by triangular-cross-section SiC waveguides with $0.5 \leq \lambda/d \leq 2$ and $30° \leq \alpha \leq 40°$. 36

4.2 Normalized depth h/a of the electric field intensity maximum $|E|^2_{\max}$ and the effective index of refraction of TE and TM modes supported in a triangular-cross-section SiC waveguide, as a function of the geometry parameters. 37

4.3 TE mode profiles of triangular waveguides with variable etch angle α and width d. Device configurations with highest waveguide coupling efficiency for each α are highlighted by the red boxes. 38

4.4 (a) Coupling efficiencies of a V2 center (horizontal electric dipole) to triangular waveguides with variable etch angle α and width d. (b) Coupling efficiencies as a function of emitter depth; the color legend in (a) applies to this plot. (c) Coupling efficiency variations with lateral displacement of emitters. 39

4.5 Coupling efficiencies of a horizontal electric dipole (emitter) to the six lowest-energy TE modes of the triangular cross-section waveguides with (a) $\alpha = 45°$ and (b) $\alpha = 75°$. The coupling efficiencies are evaluated after 10 μm propagation. 40

5.1 (a) Schematic of the 1D photonic crystal unit cell. (b) Electric field lines (arrow) associated with corresponding TE-like (red) and TM-like (blue) modes. (c) n_{eff} and VFF calculation as a function of r/a for $\alpha = 45°$. . . 44

5.2 Dispersion relations for TE (red) and TM (blue) modes in the triangular cross-section 1D photonic crystal. The red (blue) shaded regions show the photonic band gaps for the TE (TM) modes. Parameters of the photonic crystal are: (a) $\alpha = 35°, w = 1.2a, r = 0.35a$. (b) $\alpha = 45°, w = 1.2a, r = 0.4a$. (c) $\alpha = 60°, w = 1.35a, r = 0.43a$. 45

5.3 (a)-(d) TE/TM photonic band gap in frequency (c/a) and gap size (%) w.r.t. normalized hole radii (r/a) for the 45° triangular cross-section waveguide with w values of $1.2a, 1.35a, 1.5a$, and $1.75a$, respectively. In the frequency plots, the center points are midgap (f_{m}) frequencies and the error bars indicate band widths (Δf) for the corresponding TE/TM modes. The dashed circle shows the TE-TM gap overlap for the dispersion relations demonstrated in Figure 5.2b. 47

5.4 TE/TM gap size (%) in $w = 1.2a$ with varying normalized hole radii (r/a) for three α values. 49

5.5 (a) TE-pass filter in 35° waveguide with $(a, w, r) = (390, 682, 156)$ nm. (b) Polarization-independent mirror in 45° waveguide with $(a, w, r) = (475, 570, 190)$ nm. (c) TM-pass filter in 60° waveguide with $(a, w, r) = (337, 590, 135)$ nm. The dashed (black) arrow shows the direction of light propagation. 50

6.1 The coupling of a TE-oriented dipole emission at the centroid of the triangular profile into the f-TE mode (C_{fTE}) as a function of the waveguide width for three etch angles (α). Insets show electric field intensity profiles of the f-TE mode, TE supermode 1, and TE supermode 2 (top to bottom), at optimal waveguide widths supporting single-mode propagation, for $\alpha = 30°, 45°, 60°$. The electric field intensity of the TE supermodes were plotted for adjacent identical waveguides with a 200 nm gap between them. 54

6.2 (a) Top view of the S-bend BS in 4H-SiC and the inset shows the triangular cross-section geometry. (b) The fraction of the f-TE input mode coupling to f-TM (C_{fTM}) mode along the bend with variations in bend y-span (b_{y}) for $\alpha = 30°$, $w = 550$ nm, and $L_{\mathrm{C}} = 30$ μm. (c)-(d) Propagation of E_{z} field in the xy plane of the structure described in (b) for b_{y} values of 20 μm and 35 μm, respectively. 55

6.3 (a) L_C values for 50:50 splitting with an increasing gap g in $\alpha = 30°$, 45°, 60° BS. (b) Top view of the E-field intensity profile for the integrated 50:50 BS SiC structure with $\{\alpha, w, b_x, b_y, g, L_C\} = \{30°, 550$ nm, 20 μm, 35 μm, 300 nm, 44 μm$\}$ indicated by dashed circle in Figure 6.3a. 58

6.4 The SEM images of ion beam etched waveguides in 4H-SiC. (a)-(c) 800 nm wide waveguides with gaps of 100 nm, 200 nm and 300 nm respectively. (d) 1000 nm wide waveguides with a gap of 500 nm. Inset shows a FIB-SEM of the fabricated 1000 nm waveguide with a triangular cross-section. The scale bar is 2 μm. 60

7.1 a) The process flow for the nanofabrication of triangular cross-section photonics in 4H-SiC. b) Schematic of the Reactive Ion Beam Etching (RIBE) with a tilting substrate holder, used to nanofabricate suspended structures with triangular cross-section in bulk 4H-SiC. c) Variation of the etch-angle of triangular structures (α) as a function of the tilt angle of the substrate holder (φ). d-f) SEM images of the triangular cross-section profile of a 1 μm wide waveguide, showing etch angles for tilt angles d) 30°, e) 45°, and f) 60°. 63

7.2 a) Illustration showing the placement of 4H-SiC samples on a 6-inch substrate holder. The positioning of the 4H-SiC samples represent circumferences of wafers up to 5 inches in diameter. (Insets) 4H-SiC samples on the substrate holder and the cross-sectional profiles of the nanofabricated 1 μm waveguides from some of the illustrated chips. b-c) The achieved b) etch rate and c) etch angle (α) uniformity as a function of distance from the center of the substrate holder, showing 5.4% and 2.9% variability, respectively. 64

7.3 SEM images of the nanofabricated SiC photonic devices using the wafer-scale angle-etch RIBE process: a) 0.8 μm waveguides with notch couplers, b) microring resonator with radius 20 μm, c) photonic crystal cavity of width 0.9 μm, with 0.495 μm spacing between adjacent elliptical holes, d) racetrack resonator with a width of 0.8 μm and radius of curvature 24.6 μm, e) fish-bone grating coupler with teeth of width 2 μm and spacing of 0.8 μm, and f) microdisk resonators with radii 1.25 μm, 2.5 μm and 5 μm. SEM images in a-d) are obtained with the nickel metal hard mask on top of the devices, while e-f) have the nickel mask removed. 66

7.4 a) Photoluminescence spectrum of an angle-etched 4H-SiC ring resonator with integrated color centers at $T = 7$ K, showing ZPLs from divacancy (VV^0) centers (1070 - 1130 nm) and NV centers (1170 - 1245 nm), marked with purple and green arrows respectively. (Inset) SEM image of the triangular cross-section ring resonator fabricated using the optimized wafer-scale RIBE process, the blue dot indicates the spot where photoluminescence spectra were obtained from. b) High resolution comparison of NV center ZPL photoluminescence from 4H-SiC bulk (marked by an orange dot in the SEM image) and waveguide (green dot) measured at $T = 1.56$ K with peak and linewidth fits to a Lorentzian curve shown in the table. 69

8.1 (a) A perspective figure of the triangular cross-section grating couplers (GCs) used for the characterization of color center coupling with integrated nanophotonic hardware. The red sphere at the center of the waveguide represents the color center. (b) Top view of triangular cross-section fishbone GC with three regions: (i) waveguide, (ii) adiabatic taper, and (iii) fish-bone grating. (c) Grating period a and duty cycle DC which satisfy the 1st order vertical grating phase matching condition for $w_{\text{bone}} = 0.258\lambda_0$, $0.323\lambda_0$, $0.387\lambda_0$. 73

8.2 (a) Coupling efficiency (C_{EFF}) of horizontal and vertical dipoles into the fundamental transverse electric (f-TE) and the fundamental transverse magnetic (f-TM) modes, respectively, of triangular waveguides with etch angle, $\alpha = 45°$.(b) Taper width w_2 w.r.t taper length L_{taper} for taper angles $\theta_{\mathrm{taper}} = 1°, 2°, 3°$. The dashed (black) line shows the fabrication constraint imposed on w_2. (c) Effective refractive indices n_{eff} of the f-TE and the f-TM modes along L_{taper} for $\theta_{\mathrm{taper}} = 1°, 2°, 3°$. (d) Top view cross-section of the electric field (E-field) intensity ($|\mathrm{E}|^2$) profile for the adiabatic taper design with $\theta_{\mathrm{taper}} = 2°$, $L_{\mathrm{taper}} = 3.225\lambda_0$, and $w_2 = 0.774\lambda_0$ where the f-TE mode of the waveguide with $w_1 = 0.548\lambda_0$ is injected into the taper region. The cross-section is taken at the centroid plane of the maximum taper width $w_{\mathbf{2}}$. 75

8.3 (a) Side view of the FDTD simulation setup for calculating collection efficiency. (b) Collection efficiency (C_{fTE}) for the f-TE mode injection from the waveguide with variation in DC and a. The dashed (blue) circle indicates the most optimized design for the maximum C_{fTE}. (c)-(d) The far field radiation pattern and the side view cross-section $|\mathrm{E}|^2$ distribution, respectively, of the triangular GC with $DC = 0.2$ and $a = 0.742\lambda_0$, marked with blue dashed circle in (b). 77

8.4 (a) Collection efficiency of the optimized design with periodic grating for the f-TE and f-TM modes as a function of normalized wavelength λ/λ_0. (b) Side view of the FDTD simulation setup for calculating the incoupling efficiency. (c) Incoupling efficiency for the s-polarized and p-polarized Gaussian beams as a function of normalized wavelength λ/λ_0. (d) The side view cross-section $|\mathrm{E}|^2$ distribution of the triangular GC for an s-polarized Gaussian beam focused from above at λ_0. 78

8.5 (a) C_{fTE} with variation in aperiodic factor f for linear increase and decrease of a. The dashed (black) circle shows the most efficient aperiodic design for the maximum C_{fTE}. (b) Collection efficiency of the optimized design with aperiodic grating, marked with a black circle in (a), as a function of normalized wavelength λ/λ_0. (c)-(d) The side view cross-section $|\mathrm{E}|^2$ distribution and the far field radiation pattern, respectively, of the triangular aperiodic GC with $f = 0.07$ at λ_0. (e) Incoupling efficiency for the s-polarized and p-polarized Gaussian beams as a function of normalized wavelength λ/λ_0 for the optimized aperiodic GC. (f) The side view cross-section $|\mathrm{E}|^2$ distribution of the triangularly shaped aperiodic GC for an s-polarized Gaussian beam focused from above at λ_0. 80

8.6 (a) Nanofabrication process flow of triangular cross-section fishbone GC in SiC. (b)-(c) Side view and (d)-(e) Perspective view SEM images of the triangular cross-section periodic and aperiodic GCs, respectively, with a 52° tilt. (f)-(g) Top view SEM images of triangular cross-section periodic and aperiodic GCs, respectively. Inset (d) shows the side view (52° tilt) of a periodic GC after vertical etch, scale bar indicates 5 μm. Inset (e) shows the FIB cross-section SEM image (52° tilt) of a triangular waveguide with $\alpha \simeq 42°$, scale bar indicates 1 μm. All the SEM images, except inset (e), are obtained with the nickel hard mask on top of the devices. 82

8.7 (a) A sketch of the experimental setup used to characterize fabricated devices; TL: tunable laser, PMF: polarization-maintaining fiber, FC: fiber coupler, M: mirror, BS: 10:90 (R:T) beamsplitter, L: achromatic doublet lens, SMF: single-mode fiber, MS: manual switch, PD: photo detector, PDA: photodiode amplifier, DUT: device under test, SWIR: short-wave infrared. (b) The spectral profile of transmission efficiency of two identically fabricated devices (periodic GCs connected by a 20 μm waveguide) showing uniform performance. (c) Transmission efficiency as a function of the polarization of the incoupled light, where 0° corresponds to the polarization orthogonal to the waveguide propagation direction. (d) The spectral profile of transmission efficiency of devices with periodic and aperiodic GCs (waveguide length 10 μm). 83

8.8 (a) The spectral profile of transmission efficiency through a pair of periodic GCs connected by a waveguide with varying length. (b) Transmission efficiency as a function of the waveguide length for a set of wavelengths indicating waveguide loss in the range [0.3, 0.4] dB/μm. Error bars indicate the uncertainty in dB. 85

8.9 (a) Depth profile of implanted $^{14}N^{+}$ ion and induced vacancy concentrations in 4H-SiC, as simulated by stopping and range of ions in matter (SRIM). The top right inset illustrates the spatial overlap between the f-TE mode and regions containing vacancy-type defects and NV ensemble in the triangular waveguide. The bottom right inset shows the 2D Photoluminescence scan of the NV centers, scale bar indicates 10 μm. (b) Simulated coupling fraction into the f-TE mode in one direction (C_{fTE}) and collection efficiency through an objective with 0.85 NA from the top of a triangular waveguide ($C_{\mathrm{wvg,top}}$) as a function of emitter positions spanning the spatial range of NV ensemble marked in (a). 86

8.10 (a) The 2D and 1D scans of normalized photoluminescence (PL) from SiC triangular waveguides terminated by periodic and aperiodic GCs, respectively, with the excitation beam fixed at the center of a 10 μm waveguide exciting an ensemble of NV centers. The dashed boxes in the 1D PL plots highlight the regions corresponding to the results presented in (b) and (c). (b) PL counts from periodic and aperiodic GCs collected through an analyzer, 0° corresponding to the polarization orthogonal to the waveguide propagation direction. The inset shows PL counts from the NV centers in bulk 4H-SiC, the elliptical shape originating from the non-uniform polarization mixing in the SMF coil of the excitation beam. (c) Normalized PL spectra collected from the center of the waveguide (where NV centers are excited), periodic GC, and aperiodic GC, respectively. 88

9.1 SEM images (52° tilt) of fabricated nanostructures (Ni mask on top) after vertical etching with ICP power = 1000 W, RF bias power = 260 W, pressure = 5 mTorr, temperature = 20°C, SF_6:O_2 = 40:10 sccm using (a) Oxford PlasmaLab 150 and (b) PlasmaTherm Apex SLR ICP/RIE tools, respectively. Inset scale bar indicates 5 μm 93

9.2 SEM images (45° tilt) of fabricated test structures (Ni mask on top) after vertical etching with (a) ICP power = 300 W, RF bias power = 280 W; (b) ICP power = 280 W, RF bias power = 300 W; and (c) ICP power = 200 W, RF bias power = 300 W. The orange dashed circles indicate the pinholes and microcracks on the Ni mask. (d) SEM image (52° tilt) of the test structures from (c) after subsequent angle-etching. 95

9.3 (a) 4H-SiC etch depth as a function of time; the saturation point indicates the time when the 94 nm Ni mask layer is completely consumed. SEM images (52° tilt) of fabricated (b)-(c) test structures and (d) photonic crystal pattern after vertical etching with the optimized SF_6/Ar recipe. All the images are taken with the Ni hard mask on top. 96

9.4 (a) Schematic representation of ion trajectories from a plasma sheath in a beamlet (through aperture) inside a three-grid accelerator. (b) Corresponding potential variation through the grids and apertures, where V_{B} is beam voltage and V_{Acc} is acceleration voltage. 97
9.5 Effect of R on ion beam divergence for dual-grid Ar ion thrusters with a large grid separation ratio, $l_g/d_s = 1.00$. The characteristic plots are adapted from *Aston et al.* (1978) [212]. 101
9.6 Representative ion trajectories in a half-beamlet for three perveance conditions: (a) over-perveance with direct acceleration grid interception, (b) under-perveance producing crossover interception, and (c) optimal perveance. The schematic diagrams are adapted from 2D charge-exchange (CEX) mechanism calculations in an ion thruster textbook [216]. 102
9.7 Etch angle offset as a function of system perveance $P = I_{\mathrm{B}}/{V_{\mathrm{T}}}^{3/2}$, tuned by adjusting the ion beam current I_{B} at a fixed total voltage V_{T}. Experimental data points represent mean values with standard deviation error bars from FIB cross-section measurements of 3 μm, 3.5 μm, and 4 μm wide stripes. Top SEM images (52° tilt) show the FIB cross-sections of 3.5 μm wide stripes with inner sidewall angle for each data point, and the scale bars indicate 4 μm. Literature data from *Zubrzycki et al.* (1999) [218], *Chia et al.* (2022) [209], and *Majety et al.* (2025) [182] for comparison across different material systems. 105
9.8 (a) Images of the accelerator grid back plane after 2 weeks and 4 months of usage. (b) SEM images (52° tilt) of nanophotonic patterns after grid coating degradation, exhibiting severe micromasking. Fraction of I_{Acc} as a function of (c) ion beam current I_{B}, where the fraction overshoots beyond the 10% optimal threshold due to direct ion impingement caused by grid degradation, and (d) total gas flow rates, where the fraction deviates from a linear increase, following the onset of micromasking presented in (b). . 107

10.1 Band structure analyses from PWE simulations and corresponding FDTD reflectivity simulation results for (a) Design (i): $\{w, a_1, r_1\} = \{720, 530, 185\}$ nm with $\alpha = 45°$ and (b) Design (ii): $\{w, a_2, r_2\}$=$\{720, 511, 178.4\}$ nm with $\alpha = 45°$. 110

10.2 (a) Broadband power fraction results from fundamental TE mode injection in Design (ii). (b) Side view normalized E-field intensity ($|E|^2$) profiles of Design (ii) at $\lambda = 1131$ nm, 1282 nm, and 1368 nm, respectively. 111

10.3 (a) Reflectivity variation of Design (ii) with inner wall angle $0° \leq \theta \leq 22°$. SEM (52° tilt) images of fabricated photonic crystal mirror (b) after vertical etching (with Ni mask on top) and (c) after angle-etching and subsequent post-etching processes. 112

10.4 (a) Schematic diagram of zero-cavity length photonic crystal cavity design with quadratic tapering of the major axis radii over 30 elliptical holes on each end, where w is the waveguide width and a is the lattice constant. (b) E_y-field intensity profile (at the centroid plane) of the fundamental cavity mode at a resonant wavelength of 1219.5 nm. (c)-(d) Fundamental cavity resonances and corresponding Q-factors with the variation in inner sidewall angle θ for Design (i) and (ii), respectively, as mentioned in Table 10.1. 113

10.5 (a) Side view SEM image of the photonic crystal cavity (PCC) pattern after vertical etching. The inset scale bar indicates 4 μm. (b) Perspective view SEM image of the PCC after angle-etching. (c) Side view SEM image of the PCC after post-etching processes. (d) SEM image of the PCC sidewall profile taken from a broken device. All the SEM images are obtained at a 52° tilt angle, where (a) and (b) are taken with the Ni mask on top. . . . 114

10.6 (a) Schematic diagram of the inversely tapered photonic crystal cavity design with terminal Bragg mirrors, where w is the waveguide width, a_{mirror} is the lattice constant of the Bragg mirror, a_{center} is the lattice constant at the center, and r_{x} and r_{y} are the minor and major axis radii of the elliptical holes, respectively. 115

10.7 (a)-(b) PWE simulation results of the TE photonic bandgap size $\Delta f/f_{\mathrm{m}}$ (Δf: bandgap, f_{m}: gap center) as a function of the normalized minor axis radius r_{x}/a and major axis radius r_{y}/a of the elliptical holes, where the triangular waveguide width $w = 1.98a$ and etch angle $\alpha = 45°$. (c) Gap size as a function of the normalized waveguide width w/a for three $\{r_{\mathrm{x}}, r_{\mathrm{y}}\}$ combinations of $\{0.37, 0.575\}a$, $\{0.38, 0.55\}a$, and $\{0.4, 0.65\}a$. (d) Band structure of the optimized configuration $\{w, r_{\mathrm{x}}, r_{\mathrm{y}}\} = \{1.7, 0.37, 0.575\}a$. (e) Broadband reflectivity variation with no. of holes for the Bragg mirror configuration of $\{a_{\mathrm{mirror}}, w, r_{\mathrm{x,mirror}}, r_{\mathrm{y,mirror}}\} = \{471, 800, 174, 271\}$ nm. . 116

10.8 (a) Geometric parameter profile of the quadratically tapered photonic crystal nanobeam cavity showing the symmetric variation of the lattice constant a, major axis radius r_{y}, and minor axis radius r_{x} from the cavity center through the taper and into the terminal Bragg mirror. (b) Corresponding E_y-field intensity profile (at the centroid plane) of the f-TE cavity mode at $\lambda = 1256$ nm with a Q-factor of 1.2×10^6. 117

10.9 (a) Geometric parameter profile of the hybrid-tapered photonic crystal nanobeam cavity where the lattice constant a is modulated following a sinusoidal profile, while the major axis radius r_{y} and minor axis radius r_{x} are modulated quadratically from the cavity center to the terminal Bragg mirror. (b) Corresponding E_y-field intensity profile (at the centroid plane) of the f-TE cavity mode at $\lambda = 1240$ nm with a Q-factor of 8.26×10^6. . 118

11.1 (a)-(b) SEM images (52° tilt) of NbTiN thin film overlaid onto 4H-SiC triangular waveguides after angle etching and post-etching processes, respectively. SEM images of AlScN integrated 4H-SiC triangular waveguides (c) after lift-off (top view) and (d) after angle etching (52° tilted image). The inset in (c) shows a successful device after lift-off, and the scale bar indicates 20 μm. 120

List of Tables

8.1 Efficiency of individual components for the four nominal wavelengths . . 85
8.2 Grating coupler efficiency 90

9.1 Comparison of angular offsets between this work and reported values in literature 105

10.1 Zero-cavity length photonic crystal cavity design parameters and respective results 113

Chapter 1

Introduction

Quantum information processing (QIP) stands at a critical threshold as the field transitions from monolithic quantum processors to distributed architectures. Individual quantum processing units have demonstrated remarkable milestones across the most mature platforms such as superconducting [1], photonic [2], neutral atom [3], and trapped-ion [4]. However, scaling these individual systems to the millions of physical qubits required for fault-tolerant computation encounters several physical and technical bottlenecks, including spatial constraints, signal crosstalk, and thermal dissipation limits [5]. Distributed quantum computing resolves these scaling barriers by interconnecting multiple modular quantum processing units of similar or different quantum modalities. Linking quantum nodes over short-range, metropolitan, and cross-continent distances forms the foundation of the quantum internet, which unlocks unprecedented applications including unhackable quantum key distribution [6], remote quantum sensing [7], and blind quantum cloud computing [8]. Achieving this interconnected future requires robust quantum networks capable of transferring quantum states reliably over arbitrary distances, which will consequently define and establish the hardware infrastructure for next-generation quantum technology.

1.1 Motivation

The realization of a global quantum internet relies on distributed quantum networks capable of transmitting quantum information across metropolitan and continental scales. As direct optical transmission over optical fiber suffers from exponential photon loss, long-distance quantum communication fundamentally requires quantum repeater architectures [9]. At the core of every quantum repeater node lies a high-fidelity spin-photon interface comprising a stationary quantum memory, either electron or nuclear spin, deterministically coupled to a flying photonic qubit, a near telecom band photon. While individual laboratory demonstrations have successfully verified the underlying physics of remote entanglement, transitioning these proof-of-concept nodes into practical multi-node quantum networks presents a primary engineering challenge: scalability. A functional quantum repeater network demands thousands to millions of high-performance identical quantum photonic nodes, which requires bridging the gap between chip-scale laboratory prototypes and industry-standard wafer-scale manufacturing.

Building a scalable quantum repeater architecture imposes stringent material and physical constraints on the quantum hardware: (i) atomic-scale structural homogeneity to minimize emission inhomogeneous broadening across a wafer, (ii) long-lived spin coherence (T_2, T_2^*) for extended quantum information storage, (iii) bright and coherent photon emission in the optical fiber telecom windows, and (iv) compatibility with high-yield wafer-scale semiconductor manufacturing protocols. While platforms such as semiconductor quantum dots [10], 2D material defects [11], and color centers in diamond [12] and silicon [13] possess unique optical, spin, or manufacturing advantages, they are collectively constrained by fundamental trade-offs between spin coherence, telecom emission, structural uniformity, and large-area wafer availability.

Silicon carbide (SiC) overcomes this hardware paradox by combining industrially mature wafer-scale manufacturing with deep-level color centers that feature long spin coherence [14] and near telecom optical transitions [15]. However, transforming these quantum emitters into efficient quantum repeater nodes requires nanophotonic integration to overcome low photon extraction and enhance light-matter interactions. Preserving the host

material's pristine bulk crystal during nanofabrication is critical, where standard thin-film approaches introduce crystalline mismatch [16], surface roughness [17], and residual strain [18] that degrade quantum coherence, or niche approaches like photoelectrochemical etching [19] and fusion bonding [20] still lack wafer-scale uniformity. Consequently, angle-etching emerged as a key strategy to create freestanding nanostructures directly from high-purity bulk SiC substrates without compromising crystal quality.

Angle-etching method produces a unique triangular cross-section profile within nanofabricated photonic structures. While initial demonstrations of bulk triangular photonics (both in diamond and SiC) used Faraday-cage assisted angular etching [21] within conventional reactive ion etching (RIE) tools, this method is fundamentally limited by the cage geometry with mm-scale processing capacity. To realize scalable high-yield QIP hardware, the diamond quantum optics community first made the transition from Faraday cage etching to a wafer-scale ion beam etching (IBE) process [22], which offers a promising, highly uniform, and most importantly, wafer-scale angular milling alternative. Moreover, the IBE process has been well studied for surface-relief slanted- or blazed-grating structures in fused silica [23] and quartz [24] platforms to implement AR/VR waveguide display combiners and diffractive optical elements [25]. Conversely, the IBE process for SiC has not been well explored.

To bridge this technological gap, this dissertation systematically investigates triangular cross-section nanophotonics alongside the experimental realization of the IBE methodology specifically for bulk 4H-SiC. As triangular photonics in 4H-SiC has not been well studied in the literature, this work first establishes a comprehensive numerical modeling framework for both passive and active photonic devices using Finite-Difference Time-Domain (FDTD) [26], Finite-Difference Eigensolver (FDE) [27], and Plane Wave Expansion (PWE) [28] methods. Combining this theoretical foundation with the developed wafer-scale IBE process, color center integrated highly uniform 4H-SiC quantum photonic devices are fabricated and subsequently characterized. Consequently, this integrated modeling, fabrication, and characterization toolkit builds the foundational hardware infrastructure necessary for wafer-scale high-volume manufacturing, paving the way for scalable

quantum repeater networks.

1.2 Contribution

While the nature of my projects has been highly collaborative, I have led and demonstrated the primary theoretical, fabrication, and experimental efforts presented in this dissertation. In the numerical modeling framework, I led the analysis methodology for studying the supported modes in triangular structures using the FDE (Lumerical MODE) method, which later paved the way for designing single-mode waveguides using the FDTD (Lumerical FDTD) method. I also performed the primary simulations for on-chip triangular beam splitters based on the directional evanescent coupling between single-mode waveguides. In addition, I developed the computational domain for triangular cross-section fishbone grating coupler simulations, which later has been utilized by our group for asymmetric grating coupler simulations in the silicon-on-insulator (SOI) platform. Moreover, I optimized high-transmission zero cavity length photonic crystal cavity designs for targeting particular wavelengths from color center photoluminescence and introduced a new design specifically for isolating single color centers within a very small optical mode volume. On the other hand, I led the development of PWE simulations for understanding triangular cross-section photonic crystal band structure and band gaps, based on the symmetry analysis of modes using the open-source MIT Photonic Bands (MPB) package. Although PWE simulation results historically showed mismatch with FDTD results, I refined the PWE approach to obtain converging results with FDTD simulations. Lastly, I performed nanopillar simulations for analyzing both excitation and collection efficiencies, which revealed the dual-utility nature of this nanophotonic integration.

My most pivotal contributions during the PhD program have been in the nanofabrication infrastructure development for 4H-SiC. At the UC Davis Center for Nano-Micro Manufacturing (CNM2), I developed the first working recipe for high-aspect ratio anisotropic vertical etching of 4H-SiC using the PlasmaTherm Apex SLR ICP/RIE tool. In addition, I also fine-tuned the inductively coupled plasma-reactive ion etching (ICP-RIE) recipe for 4H-SiC in the Molecular Foundry at Lawrence Berkeley National Laboratory (LBNL)

as the Oxford PlasmaLab 150 tool went through several upgrades over the past couple of years. On the other hand, the previous wafer-scale angle-etching recipe developed by our group consistently exhibited angular mismatch between substrate tilt and device sidewall angle. A similar trend has been observed in different material platforms with no in-depth investigation, often attributing it to mask erosion. I systematically investigated the IBE process to identify the process parameters responsible for this angular mismatch, developed new recipes, and obtained the smallest angular mismatch in comparison with contemporary literature. Additionally, with the new studies, I helped build new IBE recipes for a variety of material processing, currently utilized at CNM2. Moreover, I have upgraded our process flow, from sample mounting to post-etching processes, for making stable and efficient quantum nanophotonic hardware.

From the characterization perspective, I initially started with building and aligning the cryogenic 4f-confocal microscopy setup in collaboration with my colleagues. Later, I moved on to independently constructing the room-temperature confocal microscopy setup from scratch and collected the first photoluminescence data of the group from silicon vacancy and nitrogen vacancy centers in 4H-SiC. I refashioned the same setup for obtaining grating-to-grating transmission measurements and developed the characterization workflow.

All of these efforts were made possible by the continuous support through funding agencies, awards, and fellowships. Therefore, I'd like to acknowledge support from NSF CAREER (Award 2047564), AFOSR Young Investigator Program (Award FA9550-23-1-0266), Costas John Spanos Semiconductor Manufacturing Award, Dissertation Fellowship, and Advancement-to-Candidacy Fellowship. Work at the Molecular Foundry was supported by the Office of Science, Office of Basic Energy Sciences, of the U.S. Department of Energy under Contract No. DE-AC02-05CH11231.

1.3 Thesis Outline

The dissertation is organized into 11 chapters that systematically progress from fundamental concepts and numerical modeling to wafer-scale nanofabrication and experimental characterization. Chapter 1 establishes the motivation, core research objectives, and key contributions of this work. Chapter 2 expands the context described in Chapter 1 with a focus on scalable quantum optics in SiC, detailing color center physics, material advantages, and progress toward scalable hardware. Chapter 3 outlines the core nanofabrication methodologies and experimental characterization setups utilized throughout this research. Chapters 4 through 6 present the numerical design and optimization framework for 4H-SiC triangular cross-section waveguides, photonic crystals, and beam splitters, respectively. Chapter 7 demonstrates the first wafer-scale fabrication of bulk freestanding devices integrated with nitrogen vacancy centers in 4H-SiC using the IBE process. Chapter 8 covers the modeling, optimization, nanofabrication, and quantitative characterization of triangular cross-section fishbone grating couplers for wafer-level testing. Chapter 9 provides a systematic study on the process optimization and recipe development of vertical and angle-etching routines, with an in-depth investigation on the IBE process. Chapter 10 delineates the design and fabrication of triangular cross-section photonic crystal mirrors and cavities. Chapter 11 summarizes the key milestones achieved in this dissertation and provides an outlook on future directions for scalable SiC quantum photonic architectures.

Chapter 2

Quantum Nanophotonics in SiC

Building scalable quantum photonic systems based on solid-state emitters requires careful consideration of the quantum defect itself as well as the host material in which it is embedded. The optical, spin, and electronic properties of the emitter are intrinsically related to the surrounding crystal environment [29], while the achievable light-matter interaction is governed by the nanophotonic structures used to interface with the emitter [30]. As a result, the choice of material platform and integration strategy plays a central role in determining device performance, scalability, and reproducibility. This chapter provides an overview of quantum nanophotonics in SiC with an emphasis on color center systems, material properties relevant to quantum optics, and nanophotonic integration approaches. Progress toward scalable implementations is also discussed to highlight the transition from chip-scale prototypes to industry-standard, wafer-scale manufacturing, which forms the core of the subsequent chapters.

2.1 Color Center Systems

An optical fiber based quantum internet requires hardware nodes that can act as a high-fidelity spin-photon interface which maps long-lived spin coherence onto efficient photon emission near telecom bands. To realize these individual nodes, their building blocks must be integrated at the chip level into quantum photonic integrated circuits. Such on-chip integration demands reliable quantum emitters compatible with industry-scale manufacturing, where scalability depends heavily on the structural homogeneity of the

emitter itself along with the fabrication uniformity of the solid-state host platform [31].

Historically, epitaxially grown semiconductor Quantum Dots (QDs) have set the benchmark for high-performance quantum optical metrics such as near-unity quantum efficiency in coherent photon generation [32], fast radiative lifetimes [10], near-unity indistinguishability [33] and single-photon purity [34], and telecom band emission [35]. However, scalability with QDs is fundamentally limited by severe inhomogeneous broadening due to their strain-driven, self-assembled growth mechanisms [36]. The structural inhomogeneity of QDs, stemming from size and shape variations, alters emission wavelengths at the wafer scale. Moreover, QDs have relatively limited spin coherence (T_2^*) due to the dense bath of nuclear spins in their compound III-V host lattice, which restricts their feasibility in large quantum repeater graph state generation [37].

Alternatively, quantum emitters in 2D materials such as point defects in hexagonal boron nitride and transition metal dichalcogenides offer high fidelity single-photon emission [11] and excellent light extraction due to their atomically thin profiles that don't suffer from total internal reflection (TIR) [38]. Although their native defect emission typically spans from visible to near-infrared (NIR) spectrum, deterministic strain engineering by integrating 2D monolayers on specialized nanostructures can deform local bandgap and tune emission into telecom wavelengths [39]. Yet, 2D platforms face severe scaling bottlenecks due to the following reasons: (i) the microscopic origins of single-photon emission in most materials are not well understood as it occurs from random, unverified crystallographic defects or uncontrolled local strain [11], (ii) spectral instability from environmental contaminants and fluctuating charge noise as the surface-bound emitters are directly exposed [40], (iii) introduction of local defects, wrinkles, and cracks even with advanced wafer-scale transfer techniques [41], and (iv) absence of a highly coherent, microwave-controllable, and reliable spin interface [42]. While rigorous engineering efforts are underway within both platforms to address respective limitations, these persistent challenges highlight the need for an alternative solid-state architecture that possesses well-defined structural homogeneity, long-lived spin coherence, and long-term scalability required for practical industrial deployment.

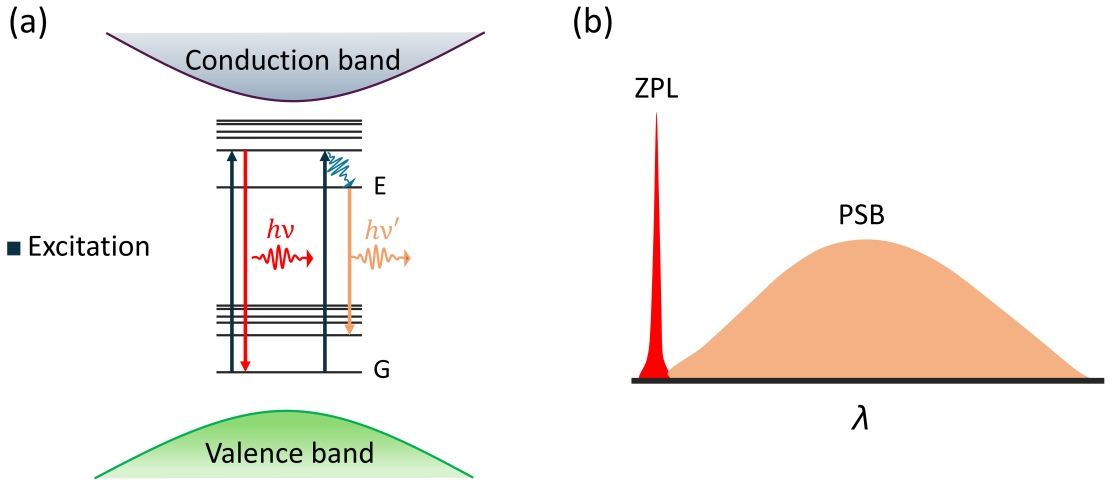

Figure 2.1. (a) Schematic representation of simplified energy level diagram showing excitation and relaxation pathways isolated within the electronic bandgap of the host material. (b) Corresponding emission spectrum of a color center, consisting of a sharp zero-phonon line (ZPL) and a broad phonon sideband (PSB).

Luminescent point defects in bulk wide bandgap semiconductors, collectively known as color centers, have positioned themselves as prominent candidates because their deep bulk encapsulation naturally combines atomic-scale structural homogeneity with robust, long-lived spin coherence [43]. Color centers can be formed by vacancies, misplaced atoms, foreign species atoms, and atom-vacancy complexes. By localizing nearby electronic orbitals, they behave as quasi-atoms with a set of ground and excited states within the bandgap of the host material as shown in Figure 2.1a. Hence, the defect's internal electronic states are isolated from the valence and conduction bands of the host material. Optical excitation drives transitions between the discrete, atom-like energy levels to emit highly pure single photons. In the absence of electron-phonon coupling, this emission would occur entirely via the zero-phonon line (ZPL), where a purely radiative decay generates a coherent photon without any simultaneous dissipation of energy into lattice vibrations. However, local dynamic interactions with the surrounding crystal cause a portion of the excited population to decay via phonon emission. Consequently, this vibrational coupling splits the emission spectrum of color centers into the coherent ZPL and a broad, incoherent phonon sideband (PSB), shown in Figure 2.1b. The ratio of ZPL to

total emission is quantified by the Debye-Waller Factor (DWF), a critical figure of merit for quantum emitters where a high DWF ensures an increased generation rate of optically indistinguishable photons necessary for QIP protocols [44].

The operational backbone of quantum networking architectures is the spin-photon interface, which utilizes optically addressable intrinsic angular momentum, i.e., spin sublevels formed by the electronic configuration of the color center. Through spin-dependent optical selection rules under resonant excitation, a localized stationary spin qubit can map its quantum state onto a traveling photon via subsequent radiative relaxation, translating local memory coherence into a flying quantum state. Although remote entanglement can employ various photonic degrees of freedom, polarization-based encoding serves as a representative framework to delineate the fundamental mechanics of spin-photon entanglement. Depending on the local crystal strain and field configurations of the defect, the spin-photon entanglement typically operates under one of the two distinct regimes: (i) three-level Λ-system for high strain and (ii) parallelized II-system for low strain [45]. Figure 2.2 illustrates the energy level diagrams of a color center with spin $S = 1$ for both cases.

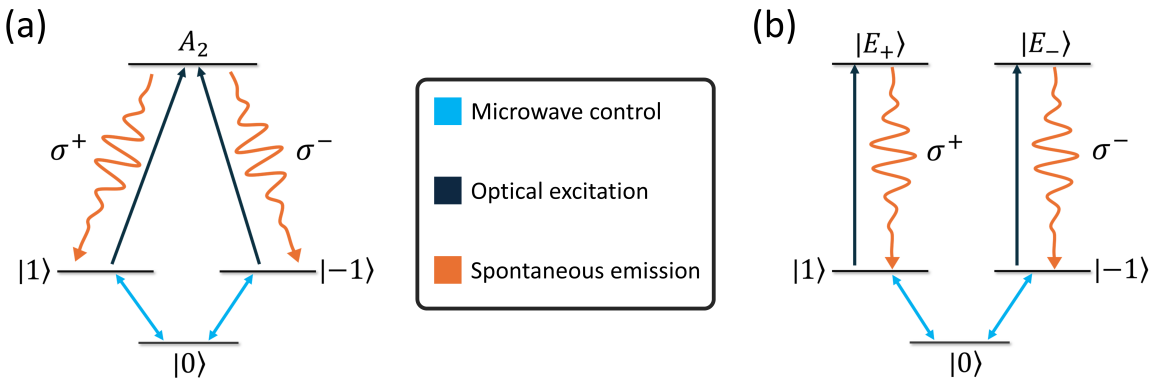

Figure 2.2. Entanglement scheme for (a) Λ-system and (b) II-system.

For an $S = 1$ system, there are three spin sublevels in both ground and excited states, corresponding to the magnetic spin quantum numbers $m_S = -1, 0, +1$, which are intrinsically degenerate in the vacuum. Although external magnetic fields can be applied to lift the degeneracy, in the absence of an external field, spin-orbit and spin-spin interactions

typically split the three sublevels based on zero-field splitting (ZFS), where the $|m_S = 0\rangle$ state forms the lowest energy sublevel and the $|m_S = \pm 1\rangle$ states form the higher energy degenerate sublevels. The primary difference between the Λ and II systems is the excited-state manifold comprising $|E_+\rangle$ and $|E_-\rangle$. While the degenerate $|E_+\rangle$ and $|E_-\rangle$ states strongly mix in a Λ-system (high strain regime), they do not mix in a II-system (low strain regime). Therefore, the optical cross-transitions are strictly forbidden by selection rules for the II-system, making the decay path deterministic. Conversely, for the Λ-system, the single shared excited state is symmetrically coupled to both ground states where the system decays probabilistically according to its branching ratio. The underlying spin-photon entanglement protocol can be illustrated using the II-system as an instructive framework: (i) Initialization: with off-resonant optical pumping, the system is spin polarized to $|m_S = 0\rangle$ ground state, (ii) Superposition: a microwave π pulse transfers the state from $|0\rangle$ to $|+\rangle \equiv |1\rangle + |-1\rangle$, (iii) Entanglement: a linearly polarized resonant optical pulse coherently transfers the population according to selection rules $|1\rangle \leftrightarrow |E_+\rangle$ and $|-1\rangle \leftrightarrow |E_-\rangle$, and subsequent emission of a photon results in the entangled state $|1\rangle|\sigma^+\rangle + |-1\rangle|\sigma^-\rangle$, where σ^+ and σ^- denote the right- and left-circularly polarized light, respectively. When these flying photon qubits are relayed from two spatially distant nodes to an intermediate location, a joint Bell-state measurement executes entanglement swapping and projectively establishes high-fidelity remote entanglement between the stationary color center systems without requiring local physical interaction.

2.2 SiC: A Promising Quantum Optical Material

Foundational breakthroughs across distinct material platforms have systematically guided the evolution of color centers as a reliable quantum optical interface. Diamond has been the most extensively studied platform, with its native negatively charged nitrogen-vacancy (NV^-) center pioneering benchmarks such as loophole-free Bell inequality violation [46], multi-second spin coherence times [47], room temperature operation [48], deterministic control of multi-qubit nuclear registers [49], all-photonic quantum repeater graph state generation [50, 51], multi-node quantum network [52, 53], and metropolitan-scale her-

alded entanglement [54]. Due to its excellent sensitivity to local magnetic and thermal variations along with long spin coherence at ambient temperatures, NV^- center in diamond is currently one of the leading modalities for quantum sensing [55], already being deployed in space missions [56]. Yet, for optical networking, a lack of inversion symmetry in NV^- center configuration makes the defect vulnerable to spectral diffusion from local field fluctuations [57], while a low DWF limits its ZPL efficiency [30]. To resolve these optical limitations, research has expanded into inversion-symmetric group-IV defects in diamond, notably the negative silicon-vacancy (SiV^-) and tin-vacancy (SnV^-) complexes. These systems exhibit inherent lifetime-limited optical linewidths [58, 59], coherent spin control [60, 61], single-shot readout [62, 63], and their nanophotonic integration with optical cavities has demonstrated quantum registers [12], multi-qubit quantum network [64], and distributed blind quantum computing [8]. Despite these milestones, diamond remains constrained by its color center emission wavelengths and scalability. The ZPLs of most investigated color centers sit near or within the visible spectrum, incompatible with telecom fiber networks. While heteroepitaxial growth is maturing, it has yet to achieve industrial scale, limiting most demonstrations to thin-film diamond where high crystal quality cannot be scalably maintained.

Seeking to natively match the telecom infrastructure, alternative research tracks have prioritized color centers in silicon (Si) and rare-earth ions in exotic crystal hosts like yttrium aluminum garnate (YAG) and yttrium orthovanadate (YVO_4). Although Si is the most industrially mature platform for co-packaged optics and hosts color centers like G, T, and C_i centers with telecom band emissions, their optical transitions typically rely on shallow bound excitons rather than deeply isolated defect states [31] due to a smaller electronic bandgap of 1.12 eV. This bound exciton nature limits their radiative efficiency [65], lowers their brightness [13], and makes them highly susceptible to photoionization [66]. On the other hand, rare-earth platforms are heavily bottlenecked by manufacturing and scalability limitations as the exotic crystal hosts lack mature semiconductor processing while high-yield wafer-scale device fabrication is exceptionally difficult due to the requirement of localized physical milling [67].

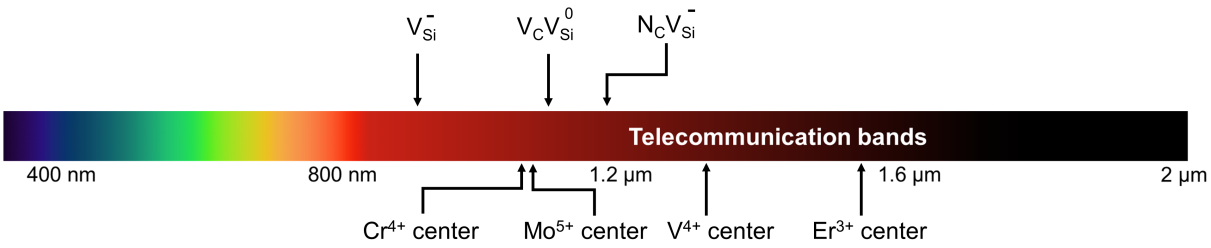

Figure 2.3. Color centers in 4H-SiC and their emission spectrum.

SiC addresses these compounding constraints by offering a commercially established semiconductor platform with a wide bandgap of ~ 3.26 eV, capable of hosting deep-level point defects. Though SiC is available in 250 distinct polytypes, three of them have been prominent in industry and research: cubic 3C-SiC, and hexagonal 4H- and 6H-SiC. Among these, 4H-SiC has emerged as the most promising platform for quantum networking architecture. It hosts a variety of optically addressable color centers, including the silicon vacancy (V_{Si}^-) [68], divacancy (VV^0) [69], NV^- center [70], and transition metal defects like chromium (Cr^{4+}) [71], molybdenum (Mo^{5+}) [72], vanadium (V^{4+}) [73], and erbium (Er^{3+}) [74], with emission wavelengths in the NIR to telecom bands, shown in Figure 2.3. Research with 4H-SiC color centers has rapidly progressed from fundamental physics to advanced hardware control, demonstrating room-temperature coherent spin manipulation [75], single-shot nuclear spin readout fidelities exceeding 99% [76], single-shot electron spin readout [14], seconds-long spin coherence times [14], and multi-qubit nuclear spin registers [77]. Moreover, the translation of these benchmarks into scalable hardware is boosted by the decades-long presence of 4H-SiC in power electronics industry, ensuring high-purity substrates are routinely available at wafer scales up to 200 mm in diameter. This commercial maturity paired with high thermal conductivity, high electrical breakdown voltage, and strong second-order ($\chi^{(2)}$) and third-order ($\chi^{(3)}$) optical nonlinearities enabling efficient active modulation, makes 4H-SiC uniquely suitable for high-density co-packaged optics architectures.

Beyond high-quality wafer availability, enhanced quantum optical performance in 4H-SiC is augmented by targeted material synthesis through isotopic purification [78]. The nuclear spin bath within the surrounding crystal matrix exhibits a dual functionality: a

primary source of magnetic dephasing and a localized resource for long-lived quantum memory registers. In naturally available SiC, 4.7% ^{29}Si and 1.1% ^{13}C atoms possess a nuclear spin of $I = 1/2$. Isotopic purification systematically depletes the host matrix of magnetic isotopes to enrich the lattice with spin-0 isotopes (^{28}Si, ^{12}C), which eliminates the dense nuclear spin bath responsible for magnetic noise and extends spin coherence times by orders of magnitude. By optimizing the isotopic fraction [79], the number of usable nuclear memories can be maximized leading to electron spin control with fidelity >99%, millisecond electron spin coherence times, coupling to nuclear spin with 1 kHz resolution [80], and ultra-narrow inhomogeneous broadening [81].

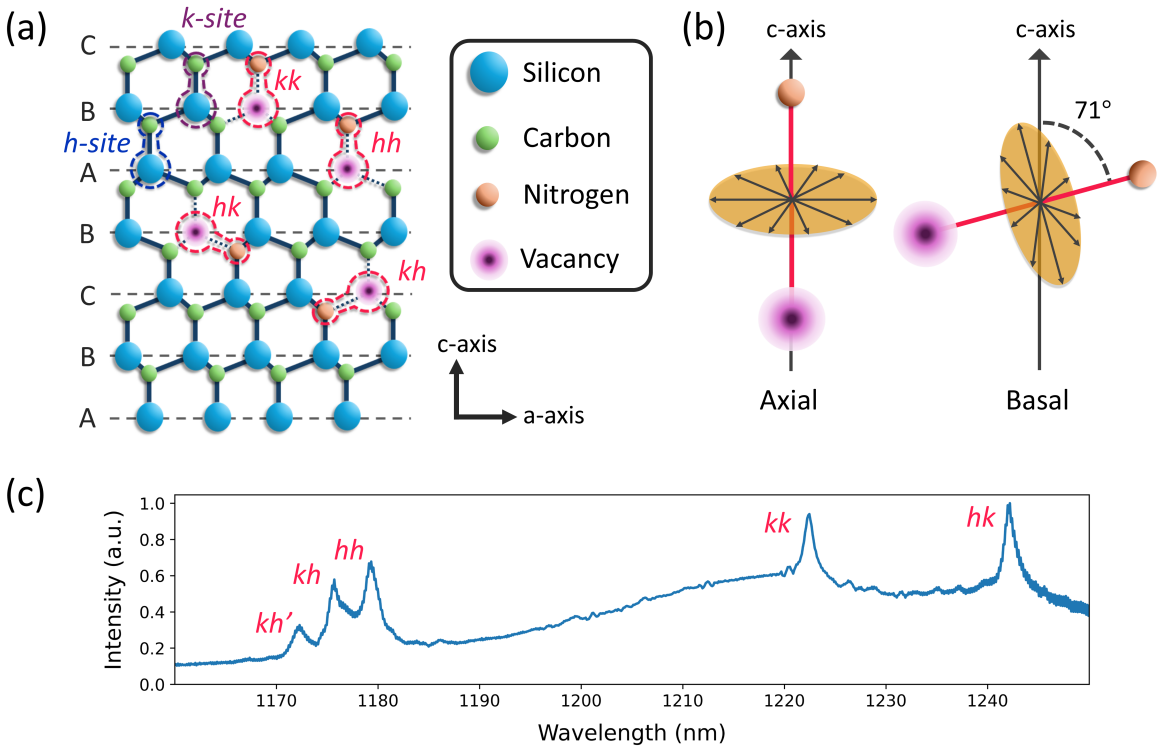

Figure 2.4. (a) The crystal structure of 4H-SiC showing the stacking of the atomic bilayers in the ABCB sequence, the inequivalent h and k lattice sites, and the four possible (hh, kk, hk, kh) configurations of the nitrogen-vacancy (NV^-) center. (b) The transition dipole moment planes (yellow disks) for axial (hh, kk) and basal (hk, kh) defects. (c) Photoluminescence spectrum of NV^- center below 2 K with distinct ZPLs corresponding to different configurations.

A compelling defect in 4H-SiC is the NV^- center, which replicates the electronic structure ($S = 1$) of the well-studied diamond NV^- center inside a foundry-compatible

substrate. Because of this identical configuration, the extensive suite of quantum control methodologies, entanglement protocols, and multi-qubit manipulation techniques developed for the diamond archetype applies directly to the 4H-SiC system. This defect complex is formed when a nitrogen atom substitutes for a carbon atom adjacent to a vacant silicon site. The structural distribution of the defect, illustrated in Figure 2.4a, is governed by the underlying bilayer stacking sequence of 4H-SiC, which repeats in an ABCB pattern along the crystal c-axis. This specific periodicity creates inequivalent quasi-hexagonal (h) and quasi-cubic (k) lattice sites for both the nitrogen substitution (N_{C}) and the silicon vacancy (V_{Si}). Consequently, the NV[1] center can settle into four distinct orientations: *hh*, *kk*, *hk*, and *kh*. The axial defects *hh* and *kk* have their dipoles oriented along the c-axis and show C_{3v} point-group symmetry, while the basal defects *hk* and *kh* have their dipoles oriented at an angle of 71° w.r.t. the c-axis and exhibit C_{1h} point-group symmetry. Figure 2.4b shows the spatial orientations of the optical dipole transition moment planes originating from the axial or basal configuration, which align either perpendicular or oblique to the c-axis [82]. Each configuration emits at a distinct ZPL close to the telecom O-band: *kh* at 1176 nm, *hh* at 1179 nm, *kk* at 1223 nm, and *hk* at 1242 nm, presented in Figure 2.4c. Although there has been much debate on the origin of the 1173 nm peak, often attributing it to tungsten impurity [70], symmetry analysis of the *kh* defect confirms the presence of a second excited state, resulting in the 1173 nm ZPL [83]. Isolating these specific geometric alignments allows for the precise optimization of directional dipole coupling to nanophotonic modes to maximize photon extraction efficiency and minimize spectral diffusion. Owing to this readily available experimental toolset and near telecom emission, the NV center in 4H-SiC is prioritized for further investigation to realize the fundamental building blocks of scalable photonic integrated architectures.

2.3 Nanophotonic Integration

Nanophotonic integration provides the definitive architectural blueprint required to overcome the photon collection and interaction bottlenecks inherent to bulk high refractive index ($n \simeq 2.6$) 4H-SiC substrate. In unpatterned bulk substrates, the narrow critical

[1]The negative charge is ignored in the rest of the dissertation.

angle ($\theta_c \simeq 22.6°$) restricts the free-space collection efficiency of color center photoluminescence (PL) to a few perecent and traps the vast majority of generated photons within the high-index substrate. Passive devices address this geometric constraint by sub-wavelength dielectric engineering to route and extract photons. In contrast, active devices modify the local density of optical states to enhance light-matter interactions. This is strictly necessary for NV centers in 4H-SiC due to their low DWF [84]. Coupling this defect complex to localized resonant cavities provides the Purcell enhancement required to channel emission preferentially into the ZPLs. Figure 2.5 illustrates a few exemplary demonstrations of nanophotonic integration in 4H-SiC.

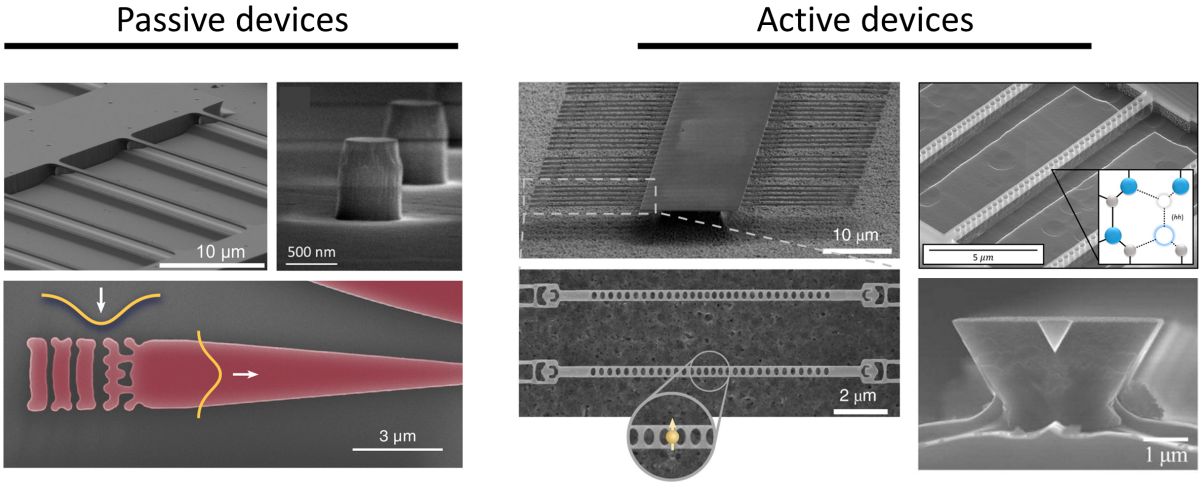

Figure 2.5. The SEM images of photonic devices in 4H-SiC. **Passive devices** (clockwise from top left): Triangular cross-section waveguide in 4H-SiC with integrated silicon vacancies [21], nanopillars in 4H-SiC with silicon vacancies [85], vertical coupler fabricated in 4H-SiCOI to convert free-space Gaussian beam into fundamental waveguide mode [86]; **Active Devices:** Suspended nanobeam array fabricated in 4H-SiCOI and (below) magnified image of individual nanobeam PCC with integrated silicon vacancies [20], nanobeam PCC in 4H-SiC with integrated neutral divacancies [19], and triangular cross-section nanobeam PCC fabricated in 4H-SiC [87].

Passive photonic devices range from localized out-of-plane extraction geometries to interconnected routing networks. Early efforts focused on solid immersion lenses [88, 89] and nanopillars [85, 20] to redirect emission into external collection optics. While these structures significantly improve vertical free-space collection efficiency, they are inherently isolated and cannot facilitate on-chip routing. On-chip information processing requires planar components, beginning with optimized waveguides that ensure high optical con-

finement and minimal propagation losses. Planar routing can be further enhanced by photonic crystal mirrors, which form photonic bandgaps via periodic dielectric modulations. Within these routing networks, directional couplers utilize the evanescent field overlap between parallel waveguides to achieve deterministic power splitting and quantum interference. Finally, for efficient external connectivity, grating couplers provide the necessary phase-matching conditions to convert tightly confined on-chip guided modes into free-space or optical fiber modes.

Active nanophotonics extends beyond passive routing to fundamentally modify light-matter interaction through cavity quantum electrodynamics. Color centers are integrated with photonic crystal cavities (PCCs) to achieve simultaneous spatial and temporal confinement of light. This light-matter interface is characterized by two distinct metrics: Purcell factor and cooperativity. Purcell factor (F_P) characterizes the enhancement of the emitter's radiative decay rate into a localized cavity mode at a resonant wavelength (λ), and is governed by the ratio of the quality factor (Q) to the mode volume (V):

$$F_P = \left[\frac{3}{4\pi^2}\left(\frac{\lambda}{n}\right)^3\left(\frac{Q}{V}\right)\right]\left[\left|\frac{E}{E_{\max}}\right|\cos(\phi)\right]\xi$$

F_P can be maximized by optimally positioning the color center within the cavity, corresponding to the spatial overlap term $|E/E_{\max}|\cos(\phi)$, where ϕ represents the angle between the emitter's transition dipole moment and the polarization direction of the cavity's electric field. To obtain a similar F_P value for different color centers, the requirement on the Q/V value changes with the DWF (ξ) of the color center. Scaling F_P is critical for channeling spontaneous emission preferentially into a single optical mode, maximizing single-photon source brightness, and outpacing spectral diffusion to preserve photon indistinguishability.

However, the Purcell factor considers only cavity-resonant radiative transitions and neglects competing decay and decoherence pathways, such as non-radiative relaxation, phonon sideband emission, and pure dephasing. In contrast, the cooperativity (C) quantifies the overall coherence of the system by evaluating the light-matter coupling strength against the constituent dissipation pathways. It is the ratio of the radiative emission rate

through the cavity to the total decay rate of the emitter in the absence of the cavity:

$$C = \frac{4g^2}{\kappa\gamma}$$

where g is the emitter-cavity coupling strength, κ is the cavity field decay rate, and γ is the emitter's total homogeneous dephasing rate. As a result, within the weak coupling regime ($C < 1$), the emission through the cavity remains smaller compared to the overall emission. Achieving deterministic atom-photon interactions requires entering the strong coupling regime ($C > 1$), where the coherent coupling rate exceeds all systematic decay and dephasing mechanisms [90, 91]. This distinct operational threshold transforms the system from a localized directional emitter into a coherent quantum interface, enabling deterministic spin-photon entanglement, quantum state transfer, and high-fidelity quantum logic operations, required for a scalable quantum repeater memory.

2.4 Progress Towards Scalability: A New Angle

Although classical nanophotonic architectures can be scaled through a wide variety of material processing, solid-state quantum applications impose a strict requirement for maintaining the pristine optical and spin coherence of integrated color centers. Early exploratory efforts in SiC photonics focused on the cubic polytype (3C-SiC), leading to the demonstration of coupling optically addressable color centers with nanophotonic cavities [92]. From a nanofabrication perspective, heteroepitaxial 3C-SiC thin films on sacrificial silicon substrates offer a highly viable route, as it provides a high refractive index contrast relative to air and enables direct wet chemical undercutting to isolate suspended waveguides and resonators. However, the quantum optical performance of color centers within these heteroepitaxial films was severely compromised due to the substantial lattice mismatch ($\sim 20\%$) and the difference in thermal expansion coefficients ($\sim 8\%$) between the silicon substrate and the grown 3C-SiC layer [16]. These disparities introduce a high density of threading dislocations, stacking faults, and anti-phase boundaries [93] which consequently generate fluctuating local strain fields as well as charge traps, resulting in severe spectral diffusion, optical linewidth broadening, and rapid spin decoherence. On the other hand, the so-called "Smart Cut" wafer bonding technique can produce high

quality single-crystal layers on insulating substrates. But the high-dose ion implantation required to induce mechanical exfoliation causes significant lattice damage and residual strain. This localized crystalline disruption exhibits charge and magnetic noise that persist even after high-temperature annealing, eventually degrading the optical and spin coherence required for high-fidelity quantum nodes.

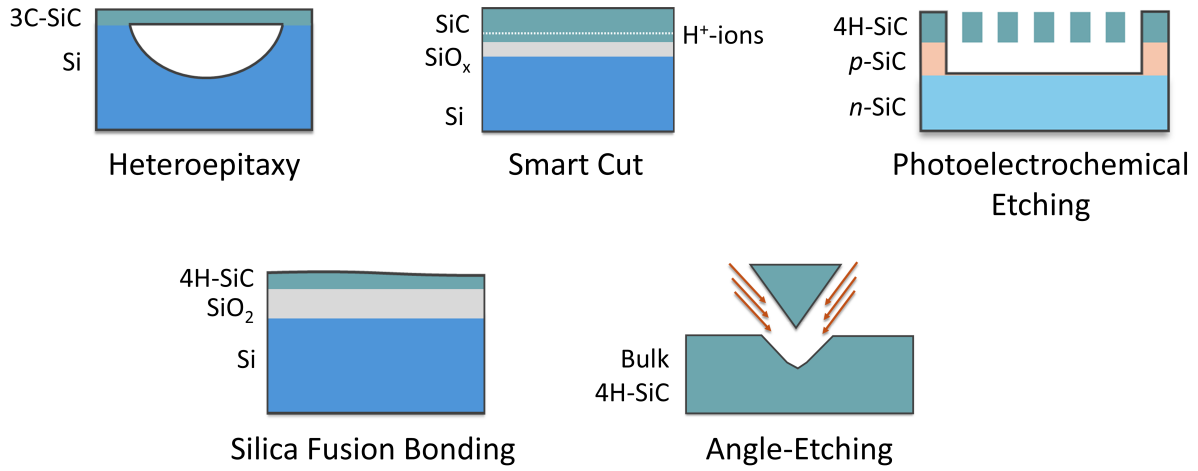

Figure 2.6. Schematic representation of fabrication pathways for integrated SiC quantum nanophotonic hardware.

To address these limitations, alternative thin-film fabrication pathways such as photoelectrochemical (PEC) etching [19] and wafer-bonded SiCOI [20] platforms utilized the 4H polytype. However, these techniques have their own scaling bottlenecks. PEC etching is fundamentally constrained by strict doping-dependent etch selectivity while suffering from surface roughness and chemical contamination. Conversely, silica fusion bonding and chemical mechanical planarization routines required for 4H-SiCOI generally result in poor film uniformity, 2-5 μm total thickness variation across a 100 mm wafer, whereas $<$ 10 nm of variation is required for wafer-scale production [94]. As the color centers exhibit their pristine narrow optical linewidths and longest optical coherence in high-purity bulk crystal, the angle-etching method emerged as a promising undercutting nanofabrication technique that mills directly into a bulk substrate at oblique angles to achieve suspended devices, naturally yielding a characteristic triangular cross-section profile as shown in Figure 2.6. Early chip-scale implementations of this technique relied on Faraday cage

assisted angular etching within a conventional reactive ion etching (RIE) tool. By enclosing the bulk sample within a specialized metallic mesh cage, accelerated reactive ions are redirected at a non-orthogonal trajectory to fabricate freestanding nanostructures. This approach achieved remarkable pioneering successes in both diamond and SiC QIP hardware, enabling the fabrication of high-Q optical resonators [87, 95], nanocavities with cooperativities exceeding 100 [96], cavity-coupled multi-qubit quantum network [64], and $> 90\%$ coupling efficiencies from emitter-cavity systems to fiber [97].

Despite these successful demonstrations, Faraday cage assisted angular etching remains suitable for prototyping individual components, having intrinsic limitations in scaling due to the following reasons: (i) processable sample sizes that fit the cage, (ii) fixed etching angle defined by the cage geometry, and (iii) the geometric lack of universality, requiring conical cages for circular components and prism-type cages for rectangular structures. On the other hand, ion beam etching (IBE) has been identified as a highly scalable technological alternative, which utilizes a collimated beam of high-energy ions to etch bulk substrates tilted at an angle and provide uniform processing across entire wafers. While IBE has demonstrated excellent results in bulk diamond quantum nanophotonics [22], the diamond platform remains bottlenecked by the absence of large-area wafer scalability. Therefore, this dissertation undertakes a comprehensive investigation into establishing a scalable material architecture for QIP hardware by engineering IBE methodology specifically optimized for bulk 4H-SiC wafers.

Chapter 3

Nanofabrication & Experimental Methods

Operational quantum hardware based on SiC triangular cross-section photonic designs requires nanoscale control over both defect creation and geometric patterning. In this chapter, we provide an overview of the nanofabrication process workflow including color center generation and activation, followed by advanced dry etching techniques to sculpt the SiC substrate with sub-micron precision. Subsequent light-matter interactions are evaluated using specialized cryogenic and room-temperature confocal microscopy setups designed to characterize individual quantum systems. These nanofabrication and experimental methodologies provide the foundational toolkit to translate abstract designs into high-performance quantum nanophotonic hardware.

3.1 Nanofabrication

Scaling solid-state quantum hardware demands manufacturing frameworks compatible with commercial semiconductor foundries. Due to the decades-long presence in power electronics industry, 4H-SiC is commercially available in standardized wafer formats. In this work, we either use a 4-inch diameter, 500 μm thick, on-axis (c-axis oriented normal to the wafer surface), high-purity semi-insulating (HPSI) or a 4-inch, 350 μm thick, 4° off-axis (c-axis tilted 4° w.r.t. the wafer normal), high-purity 7 μm n-type epilayer bulk 4H-SiC wafer from Wolfspeed. Although all downstream lithographic and etching protocols

are engineered for full wafer-scale compatibility, laboratory processing is executed on discrete 5 mm × 5 mm dies singulated by Disco DAD 321 precision dicing system. Prior to lithographic patterning, NV centers are introduced within the bulk substrate via ion implantation, occasionally with an implantation mask, and structurally activated through high-temperature annealing.

3.1.1 Color Center Generation and Activation

Color centers are predominantly generated via implantation, a process wherein energetic projectiles such as electrons, protons, neutrons, or ions are accelerated to penetrate the host material surface. This ballistic introduction of defects is conventionally followed by thermal annealing under high-vacuum or inert atmospheres to activate the dopants and structurally repair the associated crystal lattice degradation. However, this lattice reconfiguration is typically incomplete for 4H-SiC even at temperatures beyond 1600°C [98, 99], which may completely annihilate the defect centers. The remaining residual damage introduces localized strain and charge traps, creating primary decoherence pathways for the electron spin that compromise the operational fidelity of QIP hardware. The decoherence can be partly minimized by using lighter projectiles such as electron and proton, intermediate-mass ion species like helium, argon and nitrogen, or *in situ* doping during epitaxial growth. Furthermore, spatial distribution and emitter positioning can be optimized using advanced localization techniques such as focused ion beam (FIB) milling [100], direct laser writing [101, 102], proton beam writing [103], or targeted implantation through lithographic masks [104]. Despite the setbacks, ion implantation remains the standard technique for color center generation due to its excellent depth control, predictable spatial positioning, and availability of industrial resources.

In this work, NV centers are engineered within the 4H-SiC crystal matrix through commercial ion implantation (CuttingEdge Ions, LLC) using $^{14}N^{+}$ ions. Implantation fluences are calibrated to 1×10^{14} cm^{-2} for generating ensembles [105], and a few lower doses have been investigated for isolating single NV centers, where 1×10^{12} cm^{-2} showed the most promising results [106]. Acceleration energies are calculated using Stopping and Range of Ions in Matter (SRIM), a Monte Carlo simulation tool, to precisely align

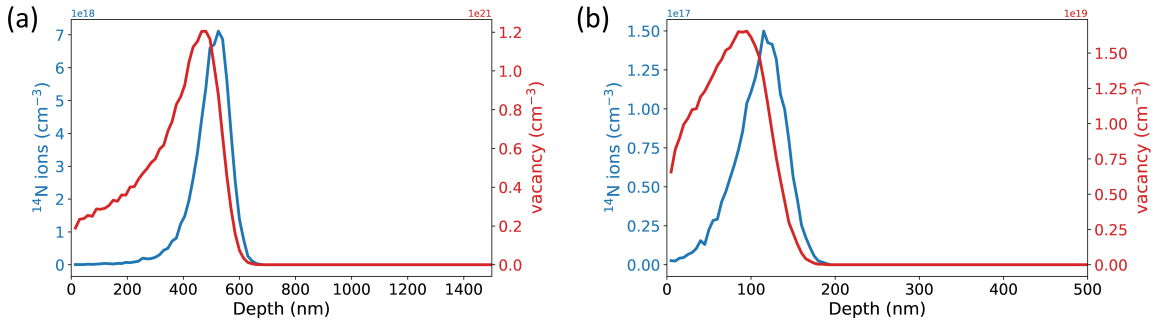

Figure 3.1. Stopping and Range of Ions in Matter (SRIM) calculated depth distribution profiles of implanted $^{14}N^{+}$ ions and corresponding lattice vacancies (damage events and target recoils) in 4H-SiC for (a) 375 keV ion energy at a fluence of 1×10^{14} cm^{-2} and (b) 65 keV ion energy at a fluence of 1×10^{12} cm^{-2}.

the defect distribution with the vertical field maxima of the respective nanophotonic structures. For 1 μm nanopillar arrays, an energy of 375 keV is used to target $\sim$ 500 nm depth at the longitudinal midpoint for maximizing mode overlap. For triangular cross-section devices, we use 65-70 keV energy for implanting nitrogen ions at a shallower depth of $\sim$ 110 - 130 nm to optimize positioning within the fundamental optical mode. The depth profiles of nitrogen ions and associated vacancies for both configurations are shown in Figure 3.1. Post-implantation thermal activation is subsequently conducted in a 1-inch Lindberg Blue tube furnace at 1050°C under a nitrogen atmosphere (500 sccm supply) for 60 minutes to form the NV center complex and stabilize the host lattice. It should be noted that the associated vacancies typically diffuse toward to the top surface with the increase in annealing temperature [107].

3.1.2 Process Flow

Following ion implantation and annealing, the subsequent process steps are illustrated in Figure 3.2. First, the chips are cleaned in a 4:1 (96% H_2SO_4 : 30% H_2O_2) piranha solution for 30 minutes. To mitigate electron accumulation and associated beam-charging distortions during electron beam lithography (EBL) on the semi-insulating substrates, a thin 7 nm titanium (Ti) layer is blanket-deposited via a CHA electron beam evaporator. This conductive film undergoes rapid volatilization during the initial seconds of the downstream fluorine-based dry etching processes, having negligible impact on the overall

etch kinetics. Then, the dies are spin-coated with e-beam resist (PMMA C4) at 2000 rpm for 45 seconds to yield a nominal thickness of 350 nm and baked in an oven at 180°C for 5 minutes. Following this, an anti-static agent, aquaSAVE, is spin-coated over the resist stack at 2000 rpm and stabilized via hotplate baking at 100°C for 1 minute. Later, high-resolution pattern definition is executed within either a Raith EBPG5200 or Vistec VB300 EBL system, and the exposed resist is subsequently developed in a 3:1 IPA:MIBK solution for 1 minute.

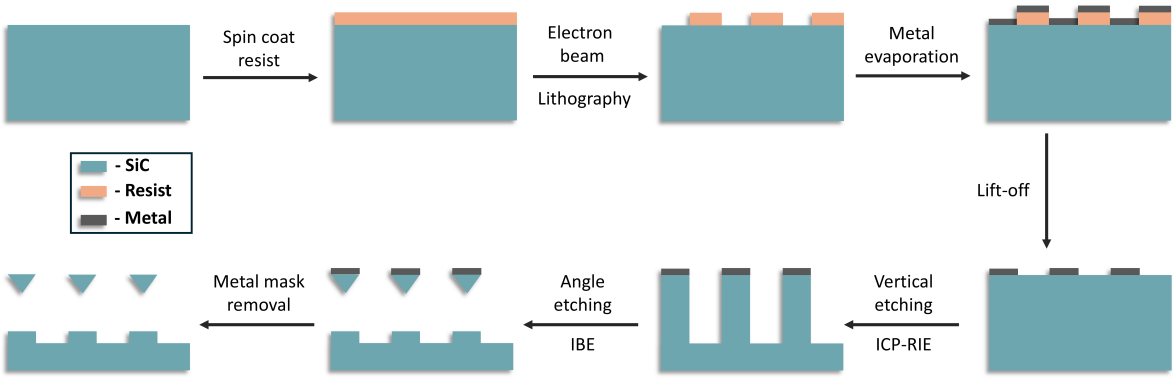

Figure 3.2. Nanofabrication process flow for SiC photonic hardware.

We use a metal hard mask for dry etching processes, where the developed samples are first coated with a 5 nm thin titanium (Ti) adhesion layer followed by a thick nickel (Ni) layer using the CHA electron beam evaporator. The thickness of the Ni layer is chosen based on the device geometry and the etching mechanisms. For nominal triangular cross-section structures, we use a 120 nm thick Ni layer as the hard mask. The underlying mask pattern is physically transferred to the metal layer using a standard lift-off technique, which involves ultrasonic agitation in dichloromethane (DCM) followed by acetone and a final rinse in isopropanol (IPA) to cleanly dissolve the resist profile. Finally, the patterned chips undergo anisotropic dry etching, utilizing either standalone inductively coupled plasma-reactive ion etching (ICP-RIE) or a sequential combination of ICP-RIE and IBE to define the designed nanophotonic structures.

3.1.3 Inductively Coupled Plasma-Reactive Ion Etching

SiC is chemically inert and a hard material to etch because of its high silicon-carbon bond energy of 4.6 eV. To achieve precise anisotropic top-down processing, we employ dry etching via an inductively coupled plasma-reactive ion etching (ICP-RIE) process. An ICP-RIE process begins with supplying a gas mixture into a vacuum chamber containing the target substrate. A high-frequency (2 MHz) electric current passing through coils positioned above the chamber generates an oscillating magnetic field, which ionizes the gas molecules into a reactive plasma with positive ions, negative electrons, and neutral radicals via electron-impact ionization and dissociation.

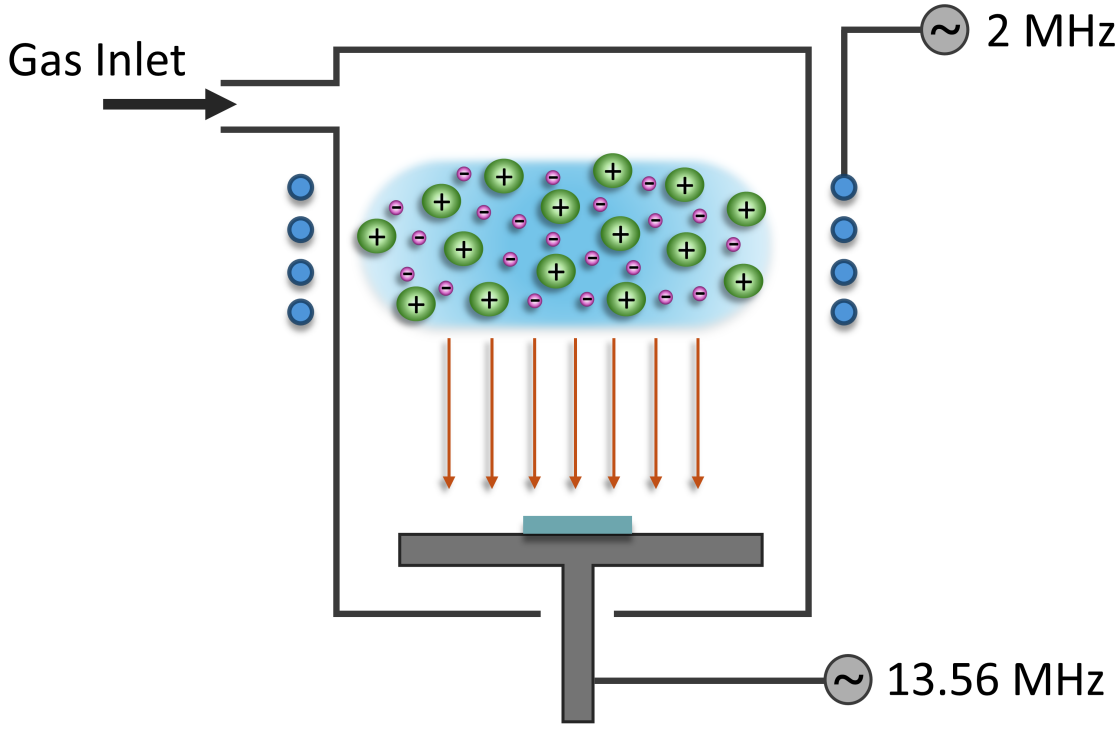

Figure 3.3. Illustration of an ICP-RIE system.

To control ion acceleration independently, a separate RF bias (13.56 MHz) is applied to the substrate platen. As lightweight electrons possess higher mobility than heavy ions, they rapidly accumulate on the platen surface during positive half-cycles, establishing a negative DC self-bias. Consequently, this negative potential repels background electrons and the depletion of electrons from the plasma creates an ion-rich plasma sheath directly

above the substrate. The strong electric field developed within this sheath accelerates the positive ions vertically toward the substrate. Material removal occurs through a simultaneous combination of chemical reactions and directional physical sputtering. The final profile is controlled by balancing these two mechanisms via three primary parameters: ICP power, self-bias voltage, and chamber pressure. Tuning the ICP power modulates the plasma density to scale chemical radical generation, while increasing the bias voltage (via RF bias power) increases the kinetic ion energy that enhances substrate activation, physical sputtering, and vertical directionality. Finally, adjusting the chamber pressure alters the ion mean free path, which limits isotropic neutral diffusion and enforces strict vertical anisotropy. This process is utilized for fabricating vertical nanopillars as well as for obtaining a deeper undercut in triangular cross-section devices. We use sulfur hexafluoride (SF_6) and oxygen (O_2) gases to drive the following chemical reactions that etches SiC by producing volatile gases:

$$SF_6 \; + \; e^- \longrightarrow \; SF_x + \; F^\bullet + \; e^-$$

$$O_2 \; + \; e^- \longrightarrow \; 2O^\bullet + \; e^-$$

$$SiC \; + \; xF^\bullet + \; yO^\bullet \longrightarrow \; SiF_4 \uparrow \; + (CO, CO_2, COF_2) \uparrow$$

The addition of oxygen prevents carbon accumulation by forming volatile species such as CO, CO_2, and COF_2, which also increases the availability of fluorine radicals to react with silicon. However, an excess of oxygen supply can lead to the formation of non-volatile silicon oxides (SiO_x) on the substrate surface and brittle nickel oxides (NiO_x) on the mask surface. While SiO_x redeposits on the surface and lowers the etch rates, NiO_x tends to form pits in the mask layer due to random grain orientations and defects. In the absence of oxygen, carbon residues remain on the substrate surface and form CF_x polymers that redeposit on the substrate. In this work, we develop recipes for anisotropic vertical etching of 4H-SiC across two distinct tools, Oxford PlasmaLab 150 at Lawrence Berkeley National Laboratory (LBNL) and PlasmaTherm Apex SLR RIE/ICP at UC

Davis CNM2. Based on the tool geometry and reactive radical generation efficiency, we optimize the reactive gas supply and the control parameters for high-aspect ratio anisotropic vertical etch. In a subsequent chapter, we describe the detailed recipes and cross-tool performance comparisons. Overall, we use a 4:1 ratio of SF_6 to O_2 for achieving optimal results in both vertical and angle-etching processes [108, 109].

3.1.4 Ion Beam Etching

For SiC triangular cross-section device fabrication, we employ angle-etching by utilizing an ion beam etching (IBE) process, which offers wafer-level scalability. In the IBE method, a collimated beam of high-energy inert or reactive gas ions are directed toward a patterned substrate to remove material. Unlike typical ICP-RIE systems, an IBE system decouples plasma generation from the substrate processing environment by isolating the plasma within a distinct discharge chamber. The primary gas species are ignited inside this discharge chamber using an independent RF ICP source to establish a dense plasma. The positive ions are then extracted and accelerated as a highly collimated beam using a

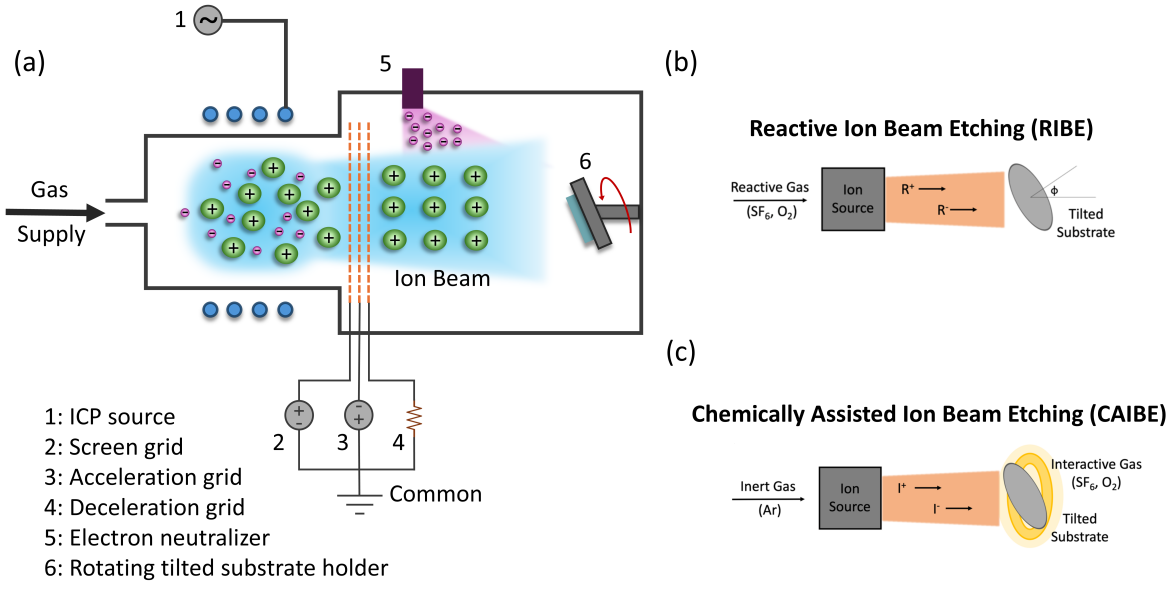

Figure 3.4. Schematic representations of (a) Ion beam etching (IBE) system, (b) Reactive ion beam etching (RIBE) process, and (c) Chemically assisted ion beam etching (CAIBE) process.

multi-grid assembly composed of a positive screen grid, a negative acceleration grid, and a neutral deceleration grid. To neutralize the space-charge accumulation of this positive ion stream, an integrated low-frequency neutralizer ion source injects a continuous flux of low-energy electrons into the positive ion beam before it reaches the target substrate. Finally, the collimated beam strikes the chips on a specialized multi-axis substrate holder, capable of precise tilting for directional etching and continuous rotation for structural uniformity.

This system can be operated via two chemically enhanced derivatives depending on how we introduce the reactive species: reactive ion beam etching (RIBE) and chemically assisted ion beam etching (CAIBE). In a RIBE framework, reactive gases are directly fed into the discharge chamber, generating an ion beam that is itself reactive, as shown in Figure 3.4b. In a CAIBE process, only inert gases are fed into the source chamber to form a purely physical ion beam, while reactive gases are supplied through an independent gas ring near the substrate, as illustrated in Figure 3.4c. The high-energy inert ion beam physically impacts the neutral molecules in the gas ring and subsequently generates reactive species that etch the target substrate. Both methods can achieve desired etch angles with some trade-offs. While CAIBE extends grid longevity by isolating the source components from corrosive environments [110], RIBE provides superior etch mask selectivity and large-scale wafer processing [111].

In this work, we utilize the Intlvac Nanoquest II system at UC Davis CNM2 for implementing the RIBE process with SF_6 and O_2 chemistry to fabricate triangular cross-section 4H-SiC photonic nanodevices. This setup enables us to exploit simultaneous physical sputtering and directional chemical etching while preserving excellent mask integrity over extended processing runs. Implementing the RIBE process with reactive gases comes with a lot of challenges in controlling the ion beam optics and beam divergence angle, specifically when the reactive species themselves react with the grid material. To maintain a concise architectural overview within this chapter, we investigate the components, ion beam control parameters, grid degradation, and process optimization in a subsequent chapter.

3.1.5 Post-Etching Process

Upon completing the dry etching sequences, we chemically remove the residual metallic hard mask layers from the SiC substrates. The chips are immersed in Transene's nickel etchant TFB at 40°C and titanium etchant TFTN at ∼ 80°C for 2-3 minutes to strip away the nickel and titanium films. Under standard operating procedures for these acid-based wet chemistries, the traditional cleaning routine concludes with a deionized (DI) water rinse and a subsequent nitrogen gas blow-dry. However, this standard blow-dry process presents a severe physical stability challenge for the undercut devices. The high

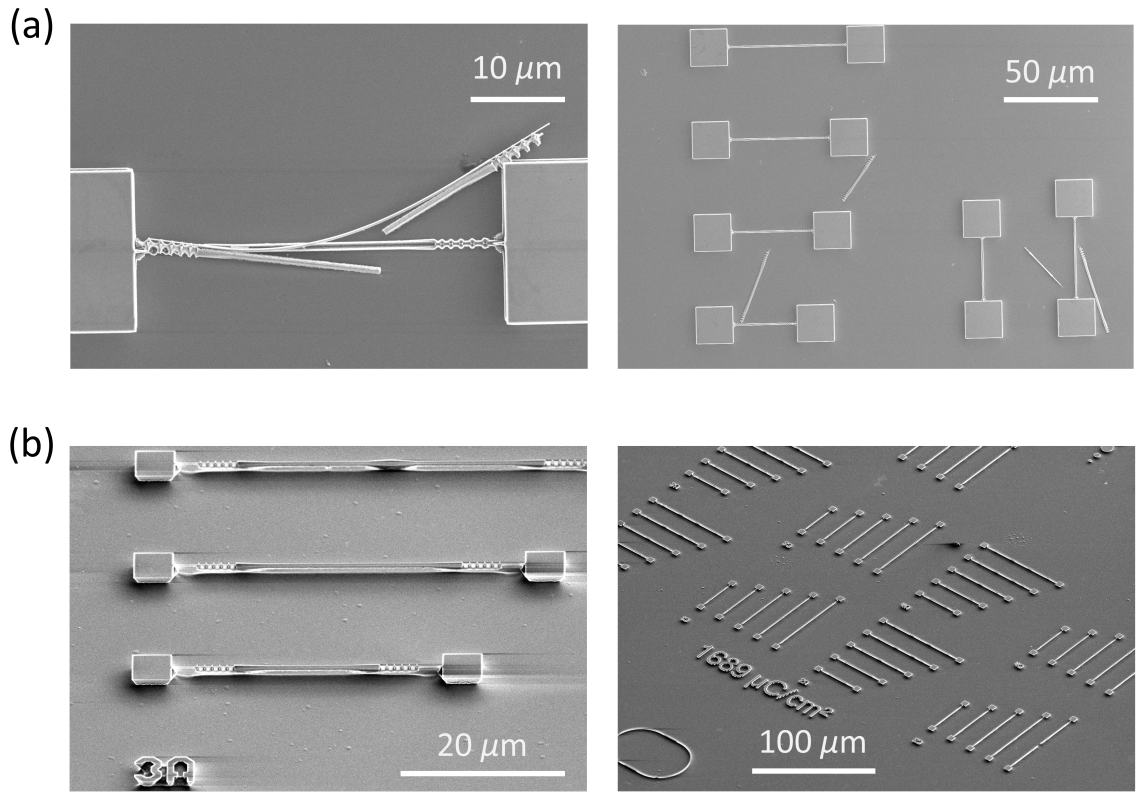

Figure 3.5. SEM images of fabricated 4H-SiC triangular cross-section suspended devices (a) without and (b) with (52° tilt) critical point drying in the post-etching process workflow.

viscosity and surface tension of water generate intense capillary forces at the liquid-gas interface as the liquid recedes from the substrate surface. These interfacial forces pull on the suspended nanophotonic structures, causing them to fracture and eventually break,

as shown in Figure 3.5a. Consequently, this structural collapse drastically reduces our device fabrication yield to $\sim 60\%$.

To overcome this mechanism, we integrate a critical point drying (CPD) sequence into our post-etching workflow. In this process, liquid CO_2 serves as the final drying medium, but it is completely immiscible with water. Therefore, we execute a series of controlled fluid exchanges to condition the samples. We dip the chips in DI water immediately after each chemical etchant step, and subsequently submerge them in IPA to act as a mutual intermediate solvent. This intermediate bath allows the IPA to completely displace any water molecules trapped within the sub-micron gaps of our freestanding structures. The IPA-soaked chips are then loaded into the Tousimis AutoSamdri 815 Critical Point Dryer system at UC Davis CNM2. The tool replaces the surrounding IPA with liquid CO_2 under high pressure using a flushing process, brings the system past the thermodynamic supercritical point, and vents the fluid purely as vapor. This methodology eliminates the formation of a liquid-gas phase boundary on the suspended features, and increases our final device fabrication yield to $\sim 99\%$, as shown in Figure 3.5b.

3.2 Optical Characterization

To evaluate our fabricated 4H-SiC quantum hardware, we perform photoluminescence (PL) and time-resolved photoluminescence (TRPL) spectroscopy measurements. In PL spectroscopy, the solid-state color centers are optically excited with an above bandgap or a resonant laser source to collect and analyze their subsequent photon emission. This technique provides a direct method to assess the optical quality, spectral signatures, and emission efficiency of the engineered defects. On the other hand, TRPL monitors the temporal decay of the emission following a pulsed laser excitation. We employ TRPL to extract excited-state lifetimes, which serve as a critical metric for QIP as this parameter directly governs the rate and efficiency of resource generation. We utilize two optical characterization setups to validate our devices under varying environmental conditions: a cryogenic 4f-confocal microscopy setup for low-temperature PL, TRPL, and photon correlation measurements, and a room-temperature 2f-confocal microscopy setup for photonic

device characterization through grating-to-grating transmission.

3.2.1 Cryogenic 4f-Confocal Microscopy Setup

NV center in 4H-SiC does not exhibit distinct ZPLs above 80 K as strong electron-phonon coupling broadens the emission spectrum at elevated temperatures. Therefore, operating within a cryogenic system is necessary to suppress these thermal lattice vibrations. This allows us to resolve the sharp ZPL features and accurately evaluate the emission characteristics of the defect complex. Figure 3.6 delineates the cryogenic 4f-confocal microscopy setup utilized in this work.

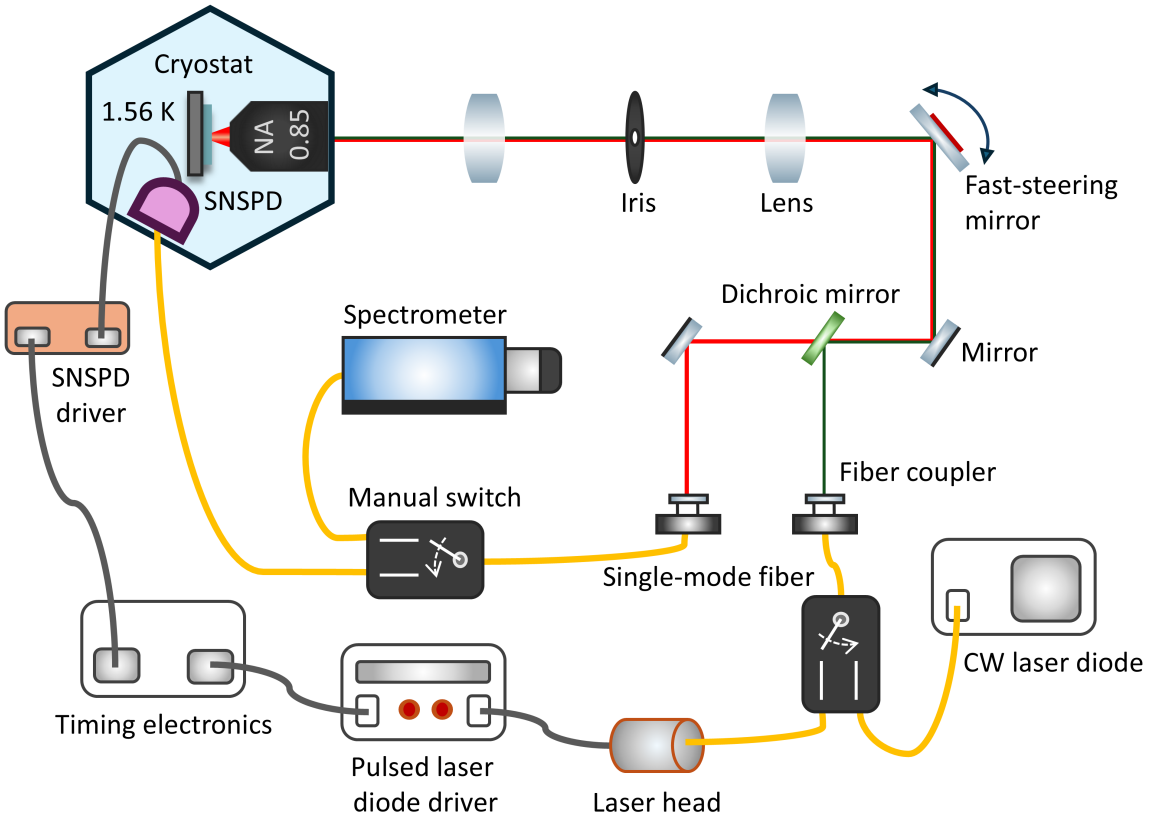

Figure 3.6. Schematic representation of 2D scanning cryogenic 4f-confocal microscopy setup where green lines show the excitation path and red lines show the collection path.

For PL spectroscopy, we use a 785 nm continuous-wave (CW) pump laser (Thorlabs)

to achieve above-band[1] excitation. The pump laser is first incident on a dichroic mirror with a cut-on wavelength of 1100 nm, meaning it reflects below and transmits light above 1100 nm. Then, the pump laser is directed onto an XY rotating fast-steering mirror (Newport FSM-300). Subsequently, the excitation beam goes through a 4f-confocal configuration, which comprises a mirror, two lenses with focal length f, and a microscope objective. This configuration is used to precisely translate the rotation by the fast-steering mirror onto the sample, which enables 2D scanning of randomly positioned color centers as well as color center integrated nanophotonic device performance. Figure 3.7b shows the raster scan of an array of NV center integrated nanopillars. The excitation laser then passes through a high numerical aperture NA = 0.85 microscope objective and is focused on the sample placed inside a closed-cycle cryostat, Montana Instruments XP-100. The cryostat features a 2-inch diameter sample space and a base temperature of 1.56 K. The incident light excites the color centers, resulting in PL emission. The emitted light is collected by the same microscope objective and traces the same path as the excitation beam. Finally, the PL emission transmits through the dichroic mirror and is collected via a fiber coupler. Through a single-mode fiber, the fiber coupler is connected to a spectrometer (Andor SR-750) for spectral analysis, or a superconducting nanowire single photon detector (SNSPD) for 2D scanning. The SNSPD and corresponding control electronics are sourced from Quantum Opus. The SNSPD has an operational temperature below 2.5 K and exhibit peak quantum efficiency at 1310 nm. As our cryostat can cool down to 1.56 K, the SNSPD is directly housed within the cryostat, which establishes an integrated cryogenic system for emission, collection, and photon-detection (ICECAP) [112]. With this configuration, we eliminate the need for a secondary cryostat and achieve a significantly smaller physical footprint than traditional multi-cryostat systems. Utilizing this setup, we not only can validate the optical integrity of well-characterized color centers after nanophotonic integration, but also unravel the structural properties of new or poorly understood color centers [83].

[1] Above-band refers to excitation energy higher than the NV defect's optical transition and lower than the bandgap of 4H-SiC.

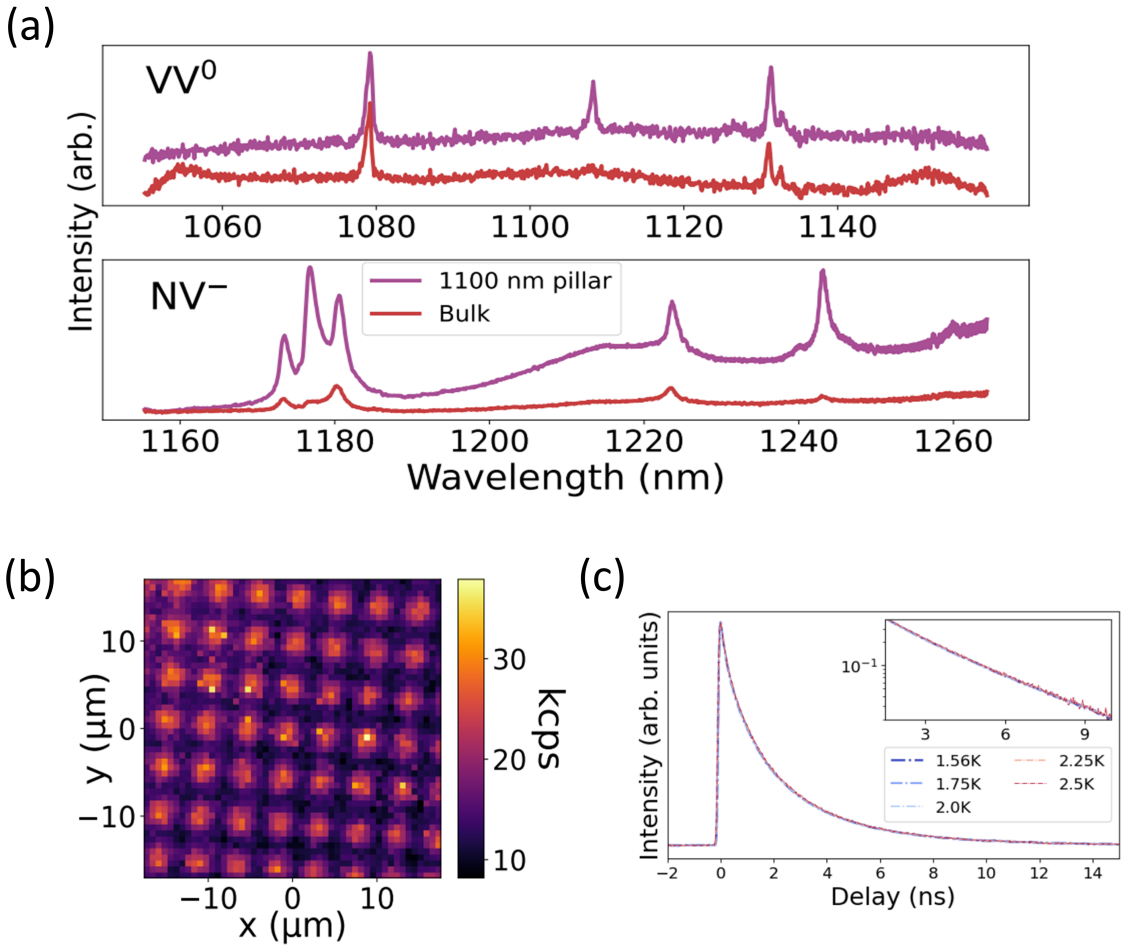

Figure 3.7. (a) Photoluminescence (PL) spectra comparing VV^0 and NV center emission from fabricated 1100 nm diameter nanopillars and reference unetched bulk regions. (b) 2D PL map of an array of 600 nm diameter nanopillars. (c) Low temperature NV ensemble optical lifetime measurements from the 600 nm diameter nanopillars.

For TRPL, we modify the ICECAP system by including a pulsed excitation laser alongside time-correlated photon counting electronics. We use a 1080 nm picosecond pulsed laser (PicoQuant PDL 800D) with selectable repetition rates from 31.25 kHz to 80 MHz. For time-correlated single-photon counting, we use PicoHarp 300, which is connected to both the laser (driver) and the Quantum Opus SNSPD driver. Whenever a laser pulse is triggered, the sync out pin of the laser driver sends an electrical pulse to the timing electronics. Following each detection of emitted photons, the SNSPD driver sends another pulse to the timing electronics. The timing electronics is a highly linear ramp

generator that starts at the laser driver output pulse and is stopped by the SNSPD driver output pulse. The result is a voltage proportional to the time difference between the two signals. By repeating the process for many cycles, we obtain time-correlated emission lifetime distribution, presented in Figure 3.7c.

3.2.2 Room-Temperature 2f-Confocal Microscopy Setup

The schematic layout for our room-temperature confocal microscopy setup is illustrated in Figure 3.8a. While we occasionally use this setup for a quick room-temperature PL verification, we mostly utilize it to characterize fabricated photonic devices through transmission measurements (Figure 3.8b). For these experiments, a Santec TSL 570A tunable

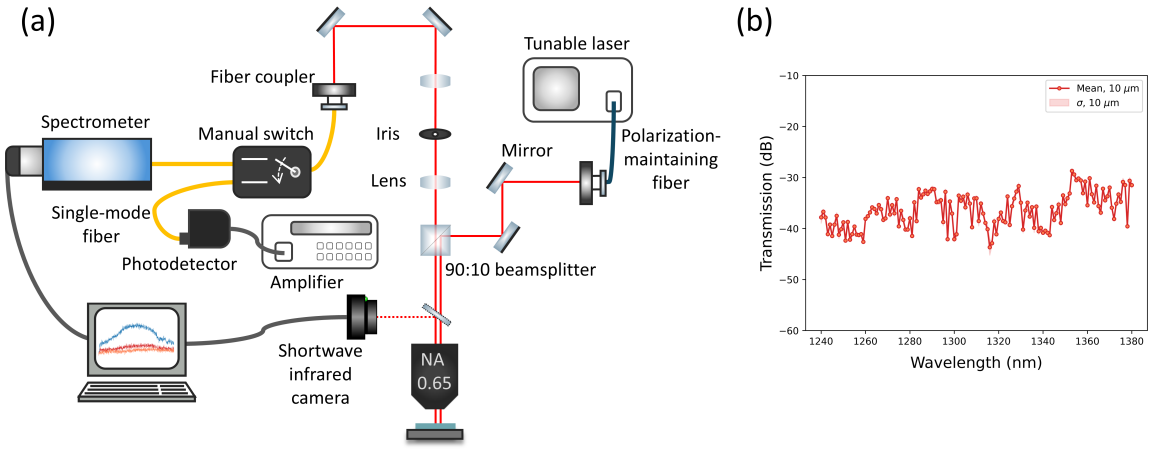

Figure 3.8. (a) Schematic representation of room-temperature 2f-confocal microscopy setup. (b) Spectral profile of transmission efficiency through a 10 μm waveguide.

laser provides an excitation beam spanning a wavelength range from 1240 nm to 1380 nm. We focus this beam directly onto an input vertical grating coupler on the fabricated chip. The transmitted light then emerges from a separate output vertical grating coupler, which serves as the collection spot. We align the setup to ensure this collection spot is positioned exactly at the center of the collection path. To obtain pristine transmitted signal, we employ a 2f-confocal configuration, comprising two lenses with focal length f and an iris, which eliminates the background noise from the scattered input beam by discarding the high-frequency components at the Fourier plane. Subsequently, a fiber coupler collects the spatially filtered transmission signal and routes it to a photodetector.

Chapter 4

Color Center Photonics with Triangular Geometry in SiC

While the physical properties of SiC color centers are well understood, the optical behavior and modal characteristics of triangular cross-section devices remain relatively understudied, specifically for color center integration. In this chapter, we address this gap by investigating the light confinement capabilities of monolithic triangular SiC waveguides. We first perform a modal analysis of the fundamental modes to map their spatial electric field profiles and identify the optimum position for color center integration. Then, we present a design framework to integrate V2 centers within 4H-SiC triangular waveguides for establishing highly efficient quantum photonic interfaces.

4.1 Optimal Position for Color Center Integration in Triangular Geometry

A waveguide uses total internal reflection to confine propagating light in the high refractive index material. The triangular cross-section waveguide modeled in this study using Finite-Difference Eigensolver (FDE, Lumerical MODE) was parametrized by the wavelength to the top-width ratio λ/d and the half-angle α. The fundamental transverse-electric (TE) and transverse-magnetic (TM) modes are studied for $0.5 \leq \lambda/d \leq 2$ and $30^\circ \leq \alpha \leq 40^\circ$, with obtained mode profiles shown in Figure 4.1.

To find the optimal positioning of the color center in the waveguide, we analyze the

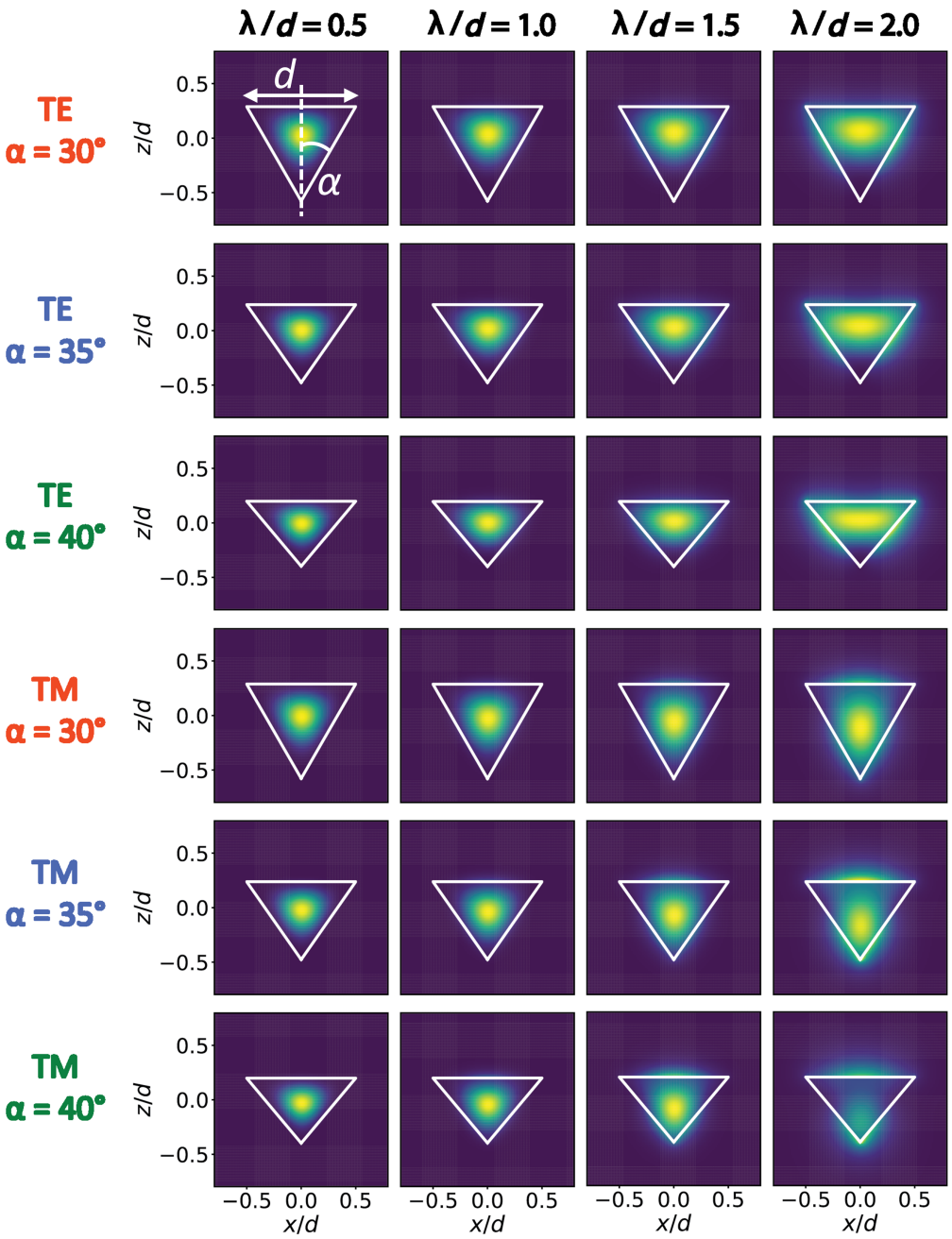

Figure 4.1. Normalized electric field intensity ($|E|^2$) profiles of TE and TM polarized modes supported by triangular-cross-section SiC waveguides with $0.5 \leq \lambda/d \leq 2$ and $30° \leq \alpha \leq 40°$. .

depth h at which the electric field intensity maximum ($|E|^2_{\max}$) of a mode is positioned relative to the waveguide's top plane. As λ/d increases, $|E|^2_{\max}$ for TE (TM) polarized mode shifts towards (away from) the top waveguide surface, i.e., the depth h decreases (increases). This behavior is consistent for all studied half-angle values α, as shown in Figure 4.2a. For higher values of λ/d, the mode becomes less confined and the evanescent losses into the surrounding medium dominate, as can be observed in mode profiles in Figure 4.1. These observations are consistent with the trend in the effective refractive index (n_{eff}) values shown in Figure 4.2b. When $n_{\text{eff}} \sim 1.5$, significantly below the SiC refractive index $n = 2.6$, $|E|^2_{\max}$ for the TM mode lies outside the waveguide and results in lossy propagation.

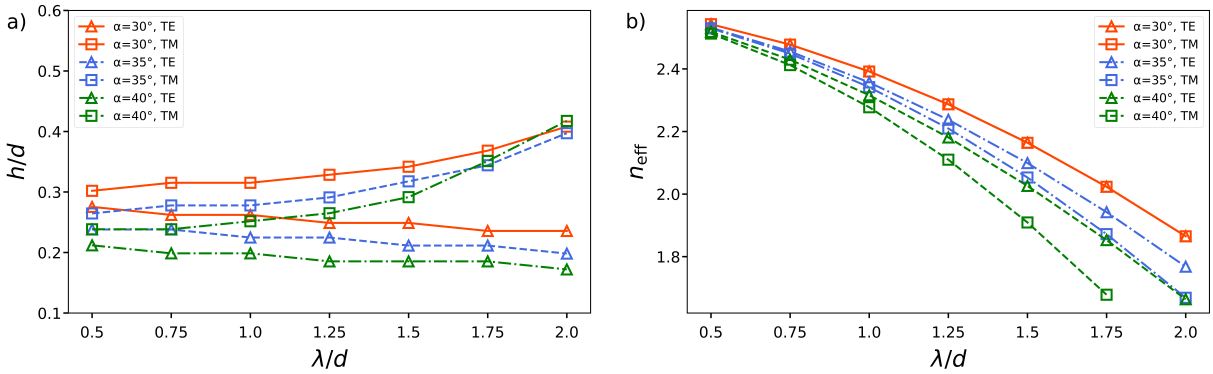

Figure 4.2. Normalized depth h/a of the electric field intensity maximum $|E|^2_{\max}$ and the effective index of refraction of TE and TM modes supported in a triangular-cross-section SiC waveguide, as a function of the geometry parameters.

4.2 Design Optimization of Triangular Cross-Section Waveguides for V2 Centers in 4H-SiC

Through a collaborative effort, we establish a systematic design optimization workflow to evaluate the integration of V_{Si} with 4H-SiC triangular waveguides in terms of both optical stability and spin coherence. V_{Si} in 4H-SiC has two inequivalent lattice sites (h, k), corresponding to two distinct ZPLs, V1 (861.6 nm) and V2 (916.5 nm). We model the V2 center by placing a 917 nm wavelength horizontal electric dipole at the centroid of the triangular cross-section for efficient excitation of the fundamental TE mode. As single-mode propagation is crucial for QIP, we optimize the parameters not only for higher

coupling efficiency but also for the least supported modes. We first perform a geometric sweep of the triangular waveguide parameters, shown in Figure 4.3, where we identify a preferential width d for each studied etch angle α. Finite-Difference Time-Domain (FDTD) and FDE reveal that the optimized mode shape is highly localized within the waveguide core and exhibit a profile that is more rectangular than circular. For a baseline geometry of etch angle $\alpha = 45°$ and width $d = 1000$ nm, the coupling efficiency into the fundamental TE (f-TE) mode is $\sim 30\%$, corresponding to 15% in each direction. However, scaling down the waveguide width to 500 nm boosts this coupling efficiency to 82%. Broadening the parameter space across a wide range of configurations (Figure 4.4a), $30° \leq \alpha \leq 75°$ and 400 nm $\leq d \leq 1000$ nm, indicates that steeper etching angles are advantageous for high coupling efficiencies over a broader range of waveguide widths.

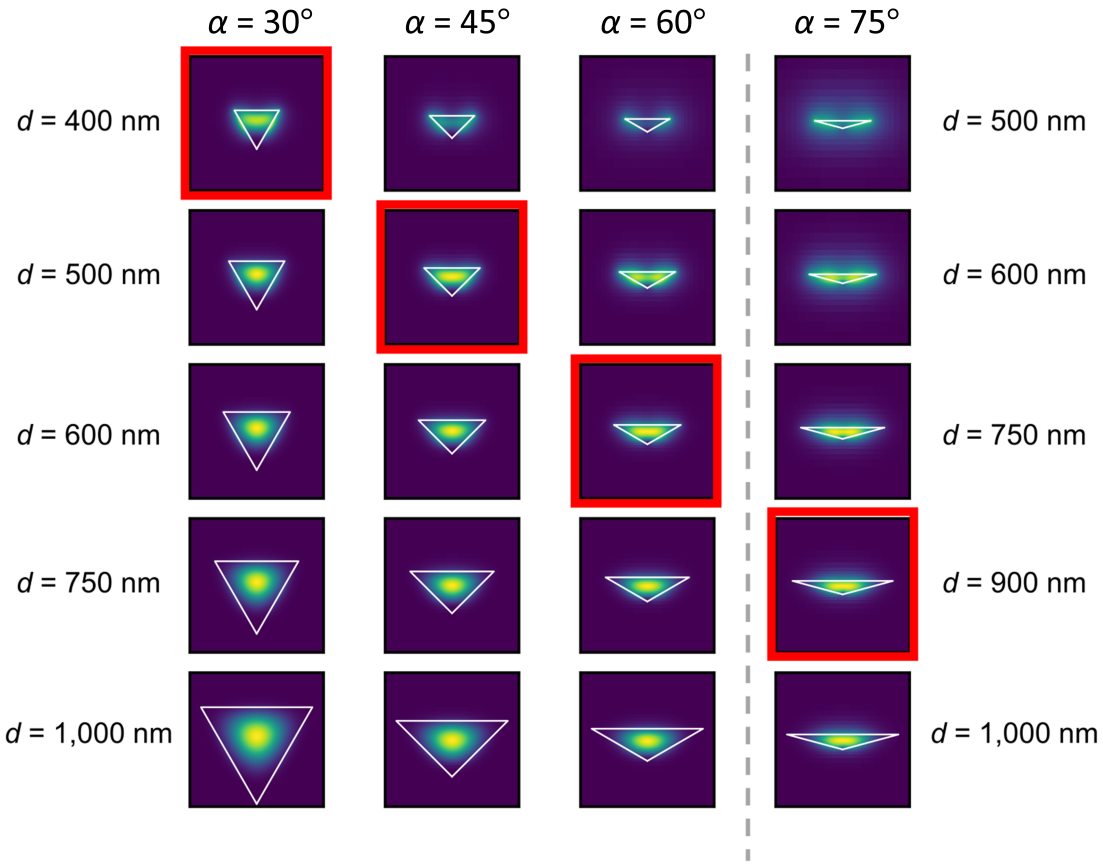

Figure 4.3. TE mode profiles of triangular waveguides with variable etch angle α and width d. Device configurations with highest waveguide coupling efficiency for each α are highlighted by the red boxes.

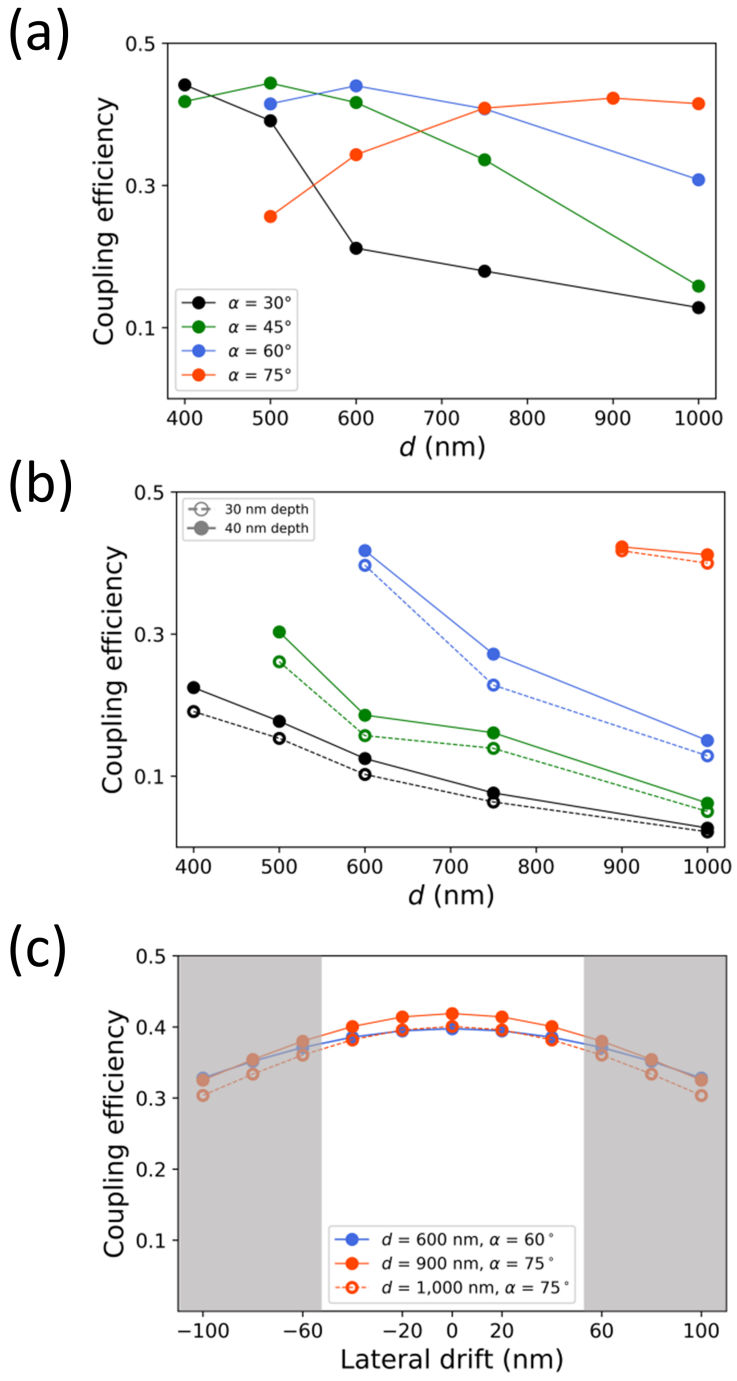

Figure 4.4. (a) Coupling efficiencies of a V2 center (horizontal electric dipole) to triangular waveguides with variable etch angle α and width d. (b) Coupling efficiencies as a function of emitter depth; the color legend in (a) applies to this plot. (c) Coupling efficiency variations with lateral displacement of emitters.

As He^+ ion implantation has been utilized to create the V2 centers in 4H-SiC, we adapt our optimization workflow to accommodate the spatial tolerances associated with ion implantation depth of 30-40 nm. Figure 4.4b shows that f-TE coupling efficiency remains remarkably stable within this shallow depth range, with steeper sidewall angles consistently yielding superior coupling. Moreover, we evaluate the impact of lateral emitter displacement, which is experimentally bounded to ± 54 nm due to the 100 nm aperture diameter of the implantation mask. Figure 4.4c shows that such lateral offsets do not significantly degrade performance, as the f-TE mode coupling efficiencies remain within $\sim 10\%$ of their peak values. To ensure single-mode propagation, we additionally simulate the first six lowest-energy TE modes for devices with etch angles of 45° and 75° for a 30 nm deep emitter. Figure 4.5 shows that $(\alpha, d = 45°, 500 \text{ nm})$ and $(\alpha, d = 75°, 900 \text{ nm})$ configurations provide $\sim 80\%$ coupling efficiency into the f-TE mode without noticeable excitation of higher-order modes.

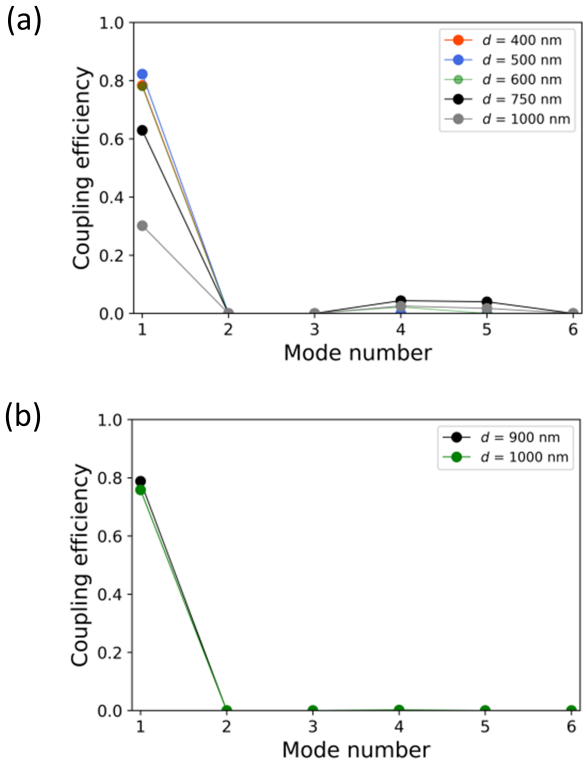

Figure 4.5. Coupling efficiencies of a horizontal electric dipole (emitter) to the six lowest-energy TE modes of the triangular cross-section waveguides with (a) $\alpha = 45°$ and (b) $\alpha = 75°$. The coupling efficiencies are evaluated after 10 μm propagation.

Our modeling results demonstrate that the triangular geometry is robust to moderate fabrication errors such as vertical and lateral displacement of integrated color centers, fabrication dimension and surface roughness imperfections. These design guidelines are directly implemented by our collaborators for fabricating V_{Si} integrated 4H-SiC triangular cross-section waveguides using Faraday cage assisted angle-etching technique. Experimental characterization of the final devices confirms that the intrinsic spin optical properties of V_{Si} suffer no degradation upon integration with the triangular nanostructures [21]. This successful preservation of spin coherence and optical stability of color centers integrated with triangular devices validates our design methodology and proves that triangular SiC architectures represent a highly robust and scalable route for QIP hardware.

Chapter 5

Photonic Bandgap Engineering with 1D Triangular Cross-Section Photonic Crystal in 4H-SiC

The formation of photonic band gaps (PBGs) in photonic crystals (PhCs) has been explored in the past three decades after the discovery made by Yablonovitch and John [113, 114]. Although wave propagation in periodic structures has almost been a century-long study [115], PhCs have gained attention due to their robust light confinement capability, scalability, and small footprint [116, 117]. Combination of different scatterers with unique lattice geometries [118, 119, 120, 121, 122, 123, 124, 125, 126, 127, 128] has led to wider PBGs by reducing the structure symmetry and found applications in polarization beam splitters [129, 130], optical logic gates [131, 132], mirrors [133, 134], sensors [135, 136], lasers [137, 138], solar cells [139, 140], and more. Nevertheless, most of these studies have been conducted on either slab, rectangular, or cylindrical geometry. On the other hand, triangular cross-section PhCs have mostly been studied for constructing active photonic devices [95, 87, 141] whereas the dispersion relations and PBG formations are yet to be discussed in detail. We explore these properties to advance the photonic integration in SiC color center based quantum devices.

In this chapter, we begin by defining the relevant parameters for analyzing PBG formation in SiC triangular cross-section PhCs. Using the plane wave expansion (PWE)

method, we calculate the band structures and discuss the dispersion relations related to individual geometries. We then observe the effects of parameter variation on PBGs and examine the designs in terms of nanofabrication. We conclude by proposing three photonic devices along with their structural configurations and operational wavelength ranges which have the potential to be essential components of integrated photonic circuits.

5.1 Triangular Cross-Section Photonic Crystal

In this section, we define the parameters of the triangular cross-section photonic crystal. Traditionally, the periodic dielectric waveguides have periodicity along the direction of light propagation [142]. The triangular cross-section PhC in this study is realized in a similar fashion. Our 1D PhC structure is designed by inserting cylindrical air holes along y axis in the SiC triangular cross-section waveguide as shown in Figure 5.1a. The most significant parameters of the PhC are its lattice constant a, waveguide width w, hole radius r, and etch angle α. We examine three α values 35°, 45°, and 60°, which fall under realistic fabrication parameters of the state-of-the-art processes [21, 87, 143]. We vary the width w from $1.2a$ to $2.25a$, and the radius r from $0.25a$ to $0.45a$. We consider the refractive index of SiC to be $n_{\text{SiC}} = 2.6$.

Based on the existence of a mirror symmetry plane ($z = 0$) perpendicular to the direction of periodicity, the photonic modes can be decoupled into TE-like and TM-like polarizations as illustrated in Figure 5.1b. Modes with electric field lines having odd symmetry about $z = 0$ are TE-like as the electric field lies in the plane of propagation. On the other hand, TM-like modes have even symmetry at $z = 0$ and the electric field lies in a direction perpendicular to propagation.

We use the effective refractive index (n_{eff}) as a useful parameter for understanding the modal profiles in a photonic device [144, 128, 141]. It is defined as the ratio of propagation constant (β) of a mode to the vacuum wavenumber ($2\pi/\lambda$). In triangular geometry, the TE/TM polarized modes supported by the structure propagate according to their corresponding n_{eff} values. Modes with lower n_{eff} are not well contained within the structure and become evanescent [141]. As guided modes depend on n_{eff}, which is a strong

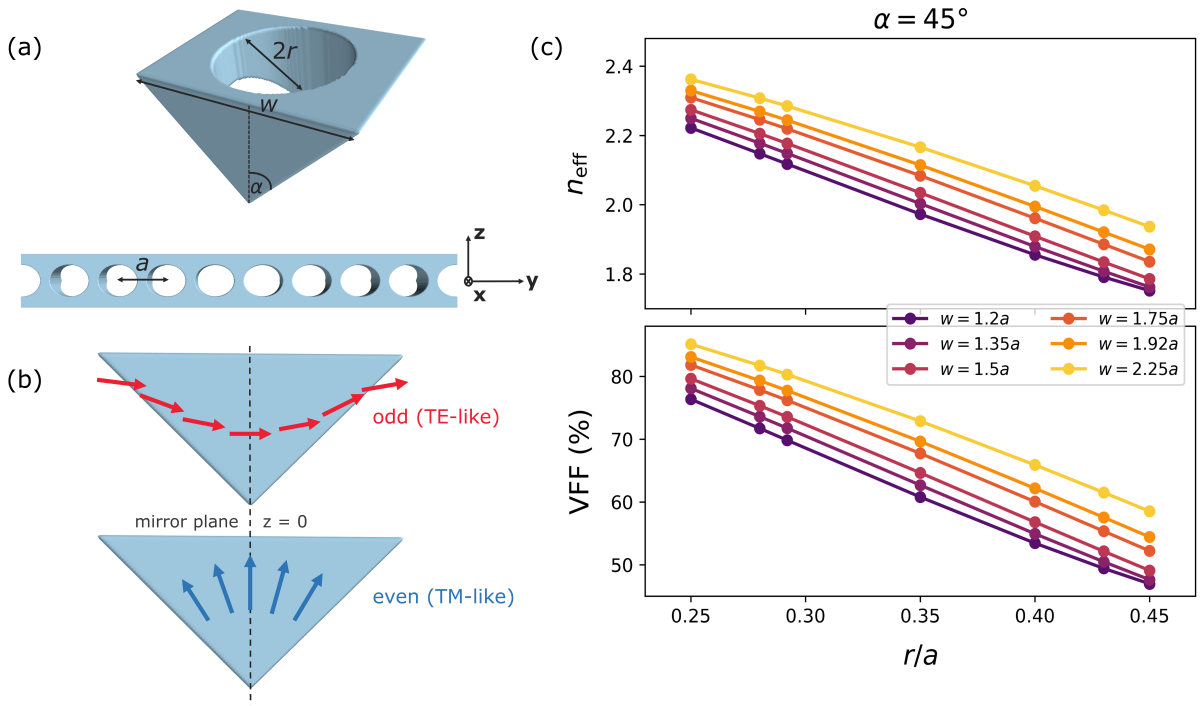

Figure 5.1. (a) Schematic of the 1D photonic crystal unit cell. (b) Electric field lines (arrow) associated with corresponding TE-like (red) and TM-like (blue) modes. (c) n_{eff} and VFF calculation as a function of r/a for $\alpha = 45°$.

function of the effective dielectric present in the photonic device, its value can help us interpret the dispersion relations and changes in PBGs due to parameter variation in the proposed 1D PhC. Hence, in the following, we come up with an analytical expression for estimated n_{eff} derived from the volumetric fill factor (VFF) of SiC in the PhC structure:

$$n_{\text{eff}} = \text{VFF} \times n_{\text{SiC}} + (1 - \text{VFF}) \times n_{\text{air}}$$

Figure 5.1c demonstrates the changes in VFF and n_{eff} as a function of the normalized hole radii (r/a) in the 45° angle-etched waveguide with various w values. The plots show that n_{eff} reduces for higher r/a and increases for higher w. The latter happens due to the enlargement of the triangular cross-section with incremental w which leads to greater n_{eff} and more supported modes. We observe similar trends and values for 35° and 60°.

5.2 Dispersion Relations in Triangular Geometry

While extensively studied in rectangular cross-section photonic crystals, the dispersion relations and PBG formations are not well understood in triangular geometry. Plane wave expansion (PWE) method has been widely used for analyzing PhCs due to its efficiency and accuracy in computing PBGs [145, 125, 146]. It is a direct frequency eigensolver method, derived from Maxwell's equations for a sourceless medium, where the eigenvalues are mode frequencies, and the eigenstates (plane wave solutions) are characterized by wavevector $\mathbf{k}$ and a band number. The irreducible Brillouin zone, which contains allowed wavevectors with non-redundant mode frequencies, lies in the range of $(0, 0, 0)$ to $(0, \pi/a, 0)$ in the $\mathbf{k}$-space for 1D PhC according to our definition of periodicity [147]. We have used MIT Photonic Bands (MPB) [148] to employ the PWE method for investigating band structure and PBG formation in the above-mentioned irreducible Brillouin zone of the triangular cross-section PhC.

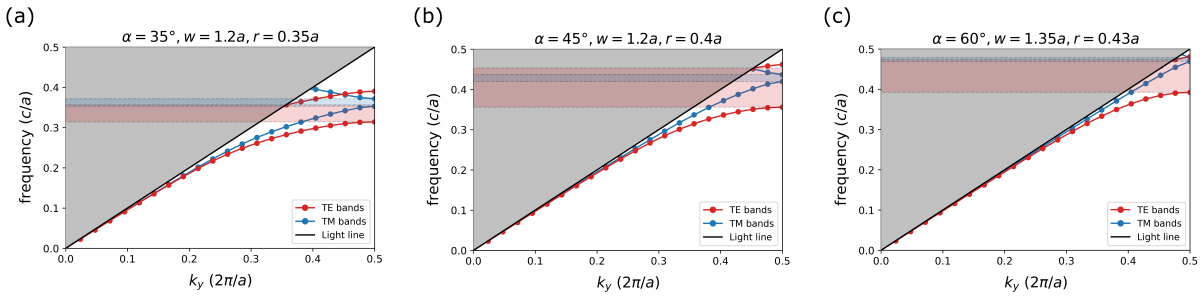

Figure 5.2. Dispersion relations for TE (red) and TM (blue) modes in the triangular cross-section 1D photonic crystal. The red (blue) shaded regions show the photonic band gaps for the TE (TM) modes. Parameters of the photonic crystal are: (a) $\alpha = 35°, w = 1.2a, r = 0.35a$. (b) $\alpha = 45°, w = 1.2a, r = 0.4a$. (c) $\alpha = 60°, w = 1.35a, r = 0.43a$.

The dispersion relations for three different PhC parameter sets (α, w, r) are presented in Figure 5.2. In the band structure, the first TE/TM band (dielectric band) is the fundamental mode with the fewest nodes and the lowest frequency. The fundamental mode is well guided by the structure in all three PhCs. However, the higher-order mode (air band) for TE/TM is not entirely guided due to the light line effect, and becomes more radiative with α getting larger, as depicted in Figure 5.2. The TE (TM) PBG is

formed by the range of frequencies present between the minima of the air band and the maxima of the dielectric band for the corresponding TE (TM) mode below the light line ($\omega < ck$). All three angle-etched 1D PhCs show both TE and TM band gaps. TE band gaps are larger than TM gaps due to the connected dielectric lattice structure which is in accordance with the general intuition [149]. Figure 5.2 also shows that 45° and 60° PhCs exhibit comparable TE gaps, while the 35° band gap is reduced. On the other hand, the TM gaps are comparable in 35° and 45° cases, and reduced for 60°.

Complete PBG refers to the region of forbidden propagation frequencies in the band structure regardless of polarization and is formed in the overlap of the TE and TM band gaps. Though conventional multilayered 1D PhCs lack a complete PBG [150], the triangular cross-section geometry offers complete PBG for all three studied angles α. As PBG is the principal characteristic of a PhC, it is desired to obtain a design with as wide complete PBG as possible. Figure 5.2 demonstrates that the largest complete PBG can be achieved with the 45° structure as the TM gap is completely buried within the TE gap. Complete PBG in the other two cross-sections occurs from a small overlapping region between the TE and TM band gaps. Even though in two (w, r) sets, the 60° geometry shows buried complete PBGs, these gaps are about four times narrower compared to the 45° case. Therefore, 45° angle-etched triangular cross-section 1D PhC is more favorable for polarization-independent light confinement.

5.3 Effects of Parameters on PBG Formation

In this section, we further analyze the effects of parameters to achieve the best-performing design in the 45° angle-etched waveguide. Scale-invariant nature of Maxwell's equations actuates the idea of presenting parameters and results in terms of lattice constant a. Consequently, the gap width Δf, where f is frequency expressed in units of c/a, is not a useful measure to understand the extent of a PBG. The gap-to-midgap ratio ($\Delta f/f_{\mathrm{m}}$), popularly known as the gap size, is a more telling characterization of the gap width as it is independent of the scaling. Figure 5.3 manifests TE-TM gap (c/a) and gap size (%) variation with r/a in $\alpha = 45°$ waveguides having several widths w. With incremental

r/a, the n_{eff} decreases, leading to an increase in f_{m} for both the TE and TM band gaps, consistent with the literature [151]. The opposite happens when w increases, due to the increased n_{eff}, for a corresponding r/a value.

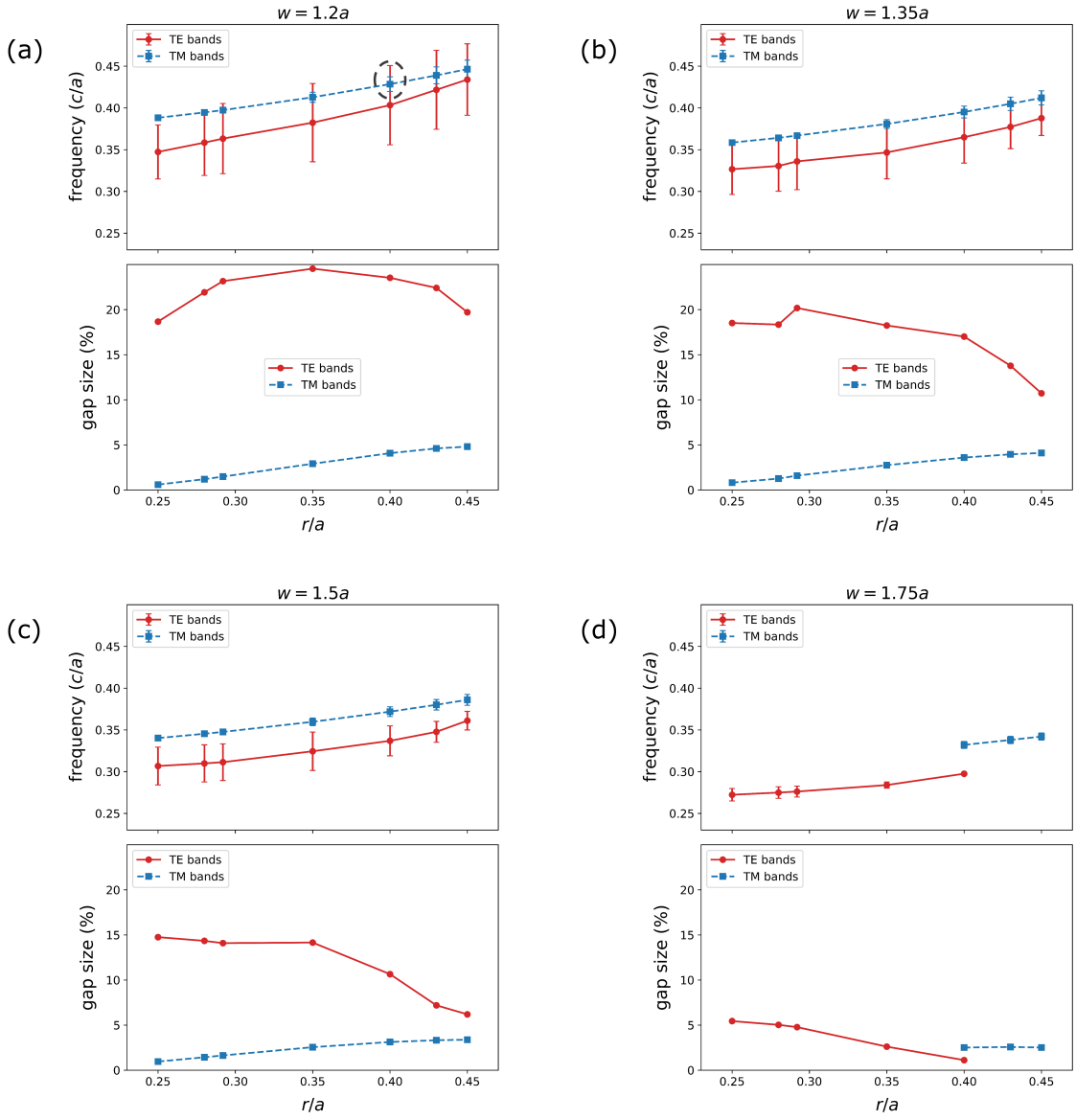

Figure 5.3. (a)-(d) TE/TM photonic band gap in frequency (c/a) and gap size (%) w.r.t. normalized hole radii (r/a) for the 45° triangular cross-section waveguide with w values of $1.2a, 1.35a, 1.5a$, and $1.75a$, respectively. In the frequency plots, the center points are midgap (f_{m}) frequencies and the error bars indicate band widths (Δf) for the corresponding TE/TM modes. The dashed circle shows the TE-TM gap overlap for the dispersion relations demonstrated in Figure 5.2b.

In smaller w such as $1.2a$ and $1.35a$, the TE gap size initially increases with r/a owing

to fewer supported modes as a result of lower VFF and n_{eff}, but shrinks after reaching the resonant condition at which the gap size is maximum. This happens on account of the reduction in effective dielectric contrast with higher r/a values. Apparently, TE gap size in PhCs with larger widths w is smaller due to greater n_{eff}, and TE band gap vanishes above $w = 1.75a$. On the contrary, the TM gap size monotonically grows with r/a, however, the band gap disappears for larger widths, identical to the TE case. From Figure 5.3 and the above discussion, it is evident that complete PBG (either buried or overlap) mostly occurs for smaller widths and TE/TM band gap totally vanishes for waveguides with larger widths ($w > 1.75a$).

5.4 Results and Discussion

The demonstrated work provides insights into the dispersion relations in the non-standard, triangular geometry of photonic crystals. Figure 5.4 delineates a general comparison of TE/TM gap sizes among three etch angles for a constant width ($w = 1.2a$). We observe that a unique trend emerges from unique geometry. For the 35° triangular cross-section, the TE gap size appears stable with changes in hole radii, whereas the TM gap size variation is identical to the 45° case. On the other hand, the TE and TM gap sizes in the 60° geometry follow the same trend as the 45° TE case. In general, TE gaps in 35° and TM gaps in 60° cease to exist for PhCs with $w > 1.5a$.

In addition to discussing the formation of photonic band gaps in photonic crystals with variation in parameters, it is imperative to evaluate the practicality and robustness of the designs in terms of fabrication. For instance, it is challenging to fabricate larger holes ($r \geq 0.43a$) in smaller widths ($w \leq 1.35a$) because of the following two issues: i) there is $\leq 18\%$ (of waveguide width w) space between the edge of the waveguide and the holes, and ii) only $\leq 14\%$ (of unit cell a) room available between two adjacent holes. Therefore, a trade-off may need to be made deliberately, depending on the application, between the PBG size and the complexity of fabricating the device. Our recent work illustrates the design of a 60° angle-etched triangular cross-section 1D PhC mirror for enhancing the quantum efficiency of *in situ* superconducting nanowire single photon detectors (SNSPDs)

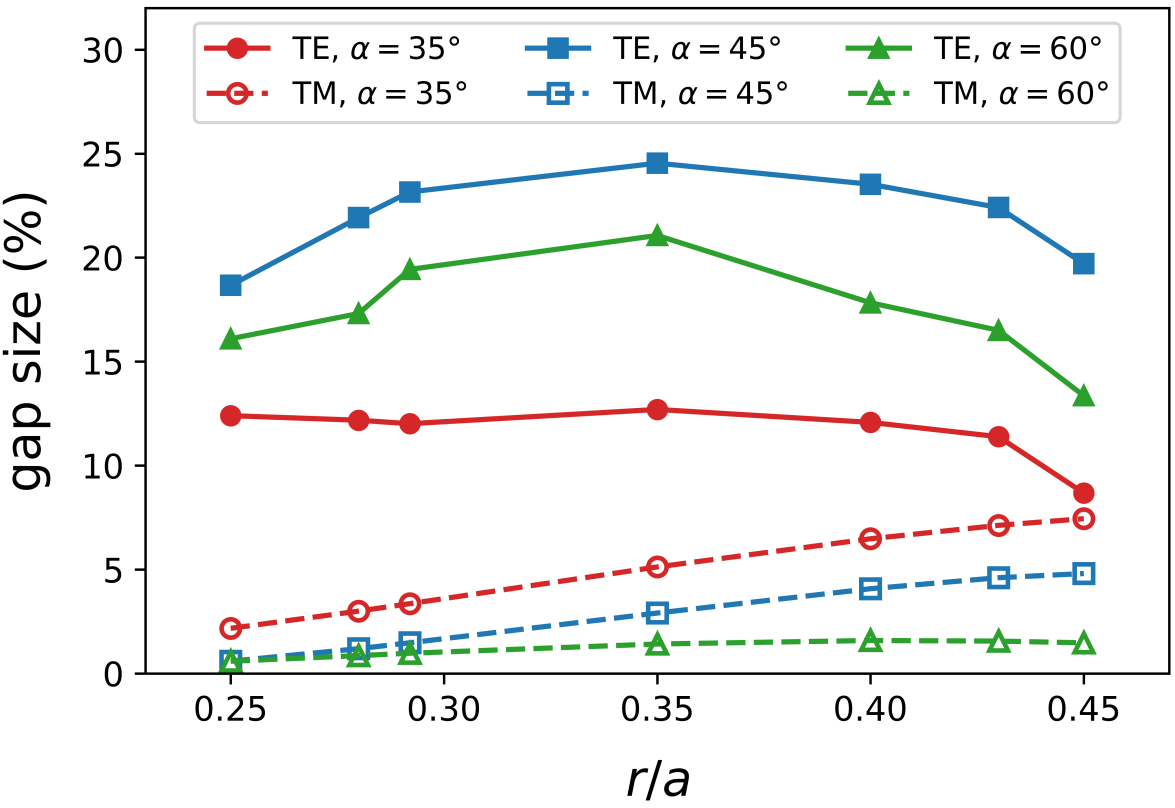

Figure 5.4. TE/TM gap size (%) in $w = 1.2a$ with varying normalized hole radii (r/a) for three α values.

[152]. Even though 60° geometry does not provide the largest complete PBG, waveguide in this geometry supports single mode propagation for NV center emission in 4H-SiC which is essential for single photon detection as well as quantum communication [153, 154].

Individual geometry offers distinct applications based on the PBG formation. We foresee three such applications from which integrated photonics with triangular geometry can benefit greatly. Operational ranges, discussed in the following, are scaled to fit wavelengths of different 4H-SiC color center emissions by updating the lattice constant a, which depends on the choice of the center wavelength of the band gap.

Quantum communication through optical fiber network requires emission around the telecommunication bands for minimal loss of information. Vanadium (V^{4+}) defects in 4H-SiC covers the entire O-band spectrum with 25-50% Debye-Waller factor [73]. The photoluminescence features show that V^{4+} in 4H-SiC mostly emits TE-polarized light

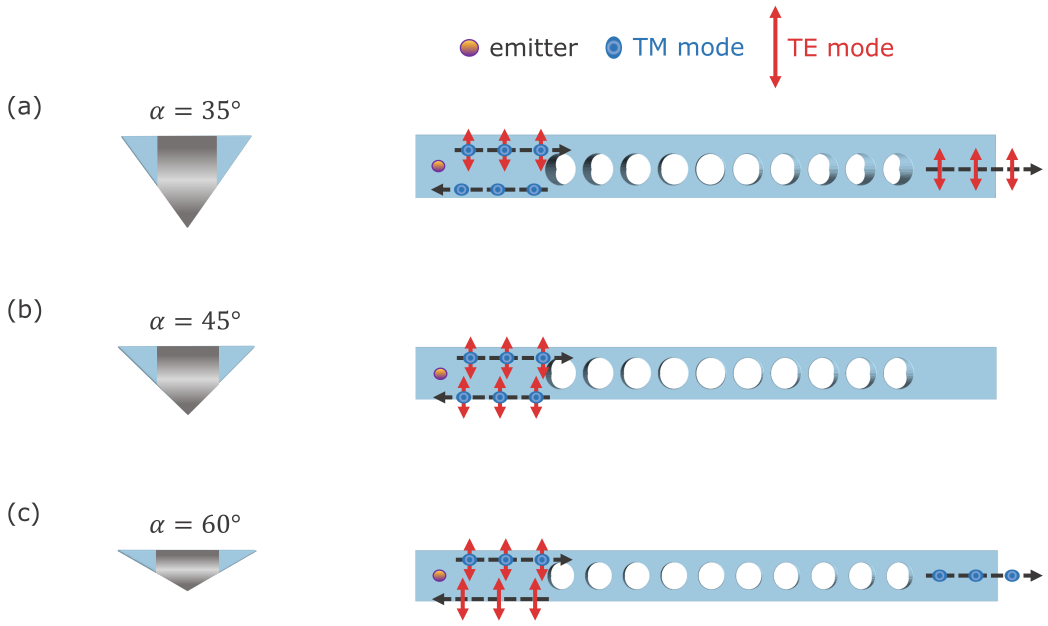

Figure 5.5. (a) TE-pass filter in 35° waveguide with $(a, w, r) = (390, 682, 156)$ nm. (b) Polarization-independent mirror in 45° waveguide with $(a, w, r) = (475, 570, 190)$ nm. (c) TM-pass filter in 60° waveguide with $(a, w, r) = (337, 590, 135)$ nm. The dashed (black) arrow shows the direction of light propagation.

[155]. One can make a TE-pass filter (Figure 5.5a) for vanadium color center emission in the 1285 - 1344 nm range, where the TM band gap forms in the 35° waveguide with $(a, w, r) = (390, 682, 156)$ nm photonic crystal parameters.

Silicon (V_{Si}) vacancy in 4H-SiC exhibits excellent optical stability and coherent spin control even in triangular waveguide structures with emissions from 861 nm to 918 nm [88, 80, 21]. The dipole polarization of single silicon vacancy center in 4H-SiC is mostly TM [85] and 60° waveguide with $(a, w, r) = (337, 590, 135)$ nm operates as a TM-pass filter (Figure 5.5c) for V_{Si} emission from 840 nm to 1015 nm where the TE band gap is formed.

Longer spin coherence time is necessary for photonic-cluster based quantum computation and communication. With the combination of isotopic purification and dynamic decoupling, spin coherence time of 5s has been reported in neutral divacancy (VV^0) in SiC [14] which is the highest among the defect spin qubits in SiC. Due to the nature of electronic structure, selection rules, and symmetry [45, 156], divacancy emission has both

TE and TM polarizations with ZPL ranging from 1078 nm to 1132 nm. A polarization-independent mirror (Figure 5.5b) for divacancy emission can be constructed using the 45° waveguide with the parameters $(a, w, r) = (475, 570, 190)$ nm that provides complete PBG from 1087 nm to 1132 nm. This happens because of the large overlapping TE-TM band gap region formed in the $\alpha = 45°$ triangular cross-section waveguide PhC.

5.5 Conclusion

Photonic integration of SiC color centers is known to enhance the efficiency of quantum hardware [157]. Here, the triangular geometry of devices can provide a combination of the pristine optical properties of the implanted color centers and the sample-agnostic nanofabrication. We have presented how photonic band gaps can be formed and applied in this geometry. As color centers have optical dipole-like emissions, the exploration of the dispersion relations and PBG formations in triangular cross-section 1D PhCs can play a significant role for robust light confinement in quantum photonic hardware. Our simulated results show that the nature of PBG configurations primarily depends on the etch-angle and varies intuitively with other PhC parameters. The three proposed devices can control quantum light propagation with mode selectivity and the parameter features are suitable for nanofabrication as well. These designs have the potential to improve the performance of integrated photonic devices with applications in quantum communication and quantum computing.

Chapter 6

Triangular Cross-Section Beam Splitters for On-Chip Interferometry

The existing QIP algorithms require error correction and heralded measurements to process information reliably and efficiently. Hence, one of the near-term goals is to build on-chip programmable photonic mesh networks to perform fault-tolerant QIP [158, 159, 160]. Successful implementation of such quantum mesh photonic hardware requires efficient single-photon generation, manipulation, entanglement, and detection [161, 162, 152]. Beamsplitters (BS) play a crucial role in on-chip photonic QIP circuits for generating multiphoton correlation [163, 159] and can be used to realize several important operations like entanglement generation and single-photon interferometry (Hong-Ou-Mandel and Hanbury Brown-Twiss). Moreover, a universal quantum computer with linear optical quantum computing protocols has been proposed using BS, phase shifters, single-photon sources, and photo-detectors [164]. Among the most studied forms of BS, such as Y-branch, directional coupler (DC), and multi-mode interferometer (MMI), DC is the most suited for on-chip QIP as it can function with single-mode waveguides [165].

In this chapter, we explore triangular cross-section 50:50 BS in 4H-SiC necessary for performing on-chip quantum interferometry. We construct such a device that splits an input beam into two output beams of equal intensity using two concurrent waveguides. In the front and back regions, the waveguides are far apart (no electromagnetic interaction) at either end (input, output) of the device, while in the middle overlap region, the waveguides

propagate in close proximity to create an electromagnetic interaction between their fields. When two indistinguishable photons, each entangled to the spin of a quantum emitter, arrive at the inputs of a 50:50 BS at the same time, they undergo bunching to exit together through the same output, creating remote entanglement between the two spins. Here we specifically study 50:50 BS designs for nitrogen vacancy (NV) color centers in 4H-SiC, with single-photon emissions in the telecommunication wavelength range (1176 - 1243 nm) [166, 167].

Using the FDTD method, we first optimize the width of triangular cross-section waveguides to achieve single-mode propagation (fundamental TE mode) and high coupling efficiency of the color center (NV in 4H-SiC) emission into that single mode, for different etch angles. Next, we investigate the formation of supermodes when two identical single-mode waveguides are placed adjacent to each other. We then study the waveguide mode conversion in bent waveguides and find suitable waveguide bend geometries to maintain the same waveguide mode in the straight and bent regions of the waveguide. We use this understanding to design triangular cross-section 50:50 BS in 4H-SiC. Finally, we explore the fabrication of the simulated triangular cross-section waveguide configurations required for a 50:50 BS.

6.1 Evanescent Coupling via Single-Mode Waveguides

Color center emission is dipole-like, and such emission can couple to fundamental TE (f-TE), fundamental TM (f-TM), and other higher-order modes that are supported in triangular cross-section waveguides [141]. It has been shown that for each etch angle there exists an optimal width for single-mode (f-TE) propagation in triangular cross-section waveguides [21], which is a necessity for QIP applications [168]. So, to achieve high coupling efficiencies for color center emission, the color center should be positioned in a single-mode waveguide at the maximum electric field (E-field) intensity point of the f-TE mode [21, 152], which is at the centroid of the triangle.

We use FDTD package in Lumerical software to estimate the coupling efficiency of color center emission into the f-TE mode (C_{fTE}) for different widths (w) and etch angles

(α) of a triangular cross-section waveguide (the angle at the apex of the triangle is 2α). We position the dipole emitter at the centroid of the triangle with an emission wavelength of 1230 nm. We find that for each α there exists a width with the highest coupling ($> 80\%$) to the f-TE mode, as shown in Figure 6.1. For our 50:50 BS simulations, we choose the optimal width values (w = 550 nm, 650 nm, 800 nm for $\alpha = 30°, 45°, 60°$ respectively) slightly lower than the widths with the highest C_{fTE}. The reason being that the waveguides with lower width have slightly higher evanescent fields (top panels of inset in Figure 6.1), necessary to create meaningful coupling between the adjacent waveguides in the BS, while only slightly reducing C_{fTE} ($< 1\%$).

The mode profile of the waveguide f-TE (f-TM) mode has an E-field intensity maximum closer to the top surface (apex) [141]. As the waveguide width decreases, the E-field intensity maximum of the f-TM mode moves closer to the apex and becomes evanascent

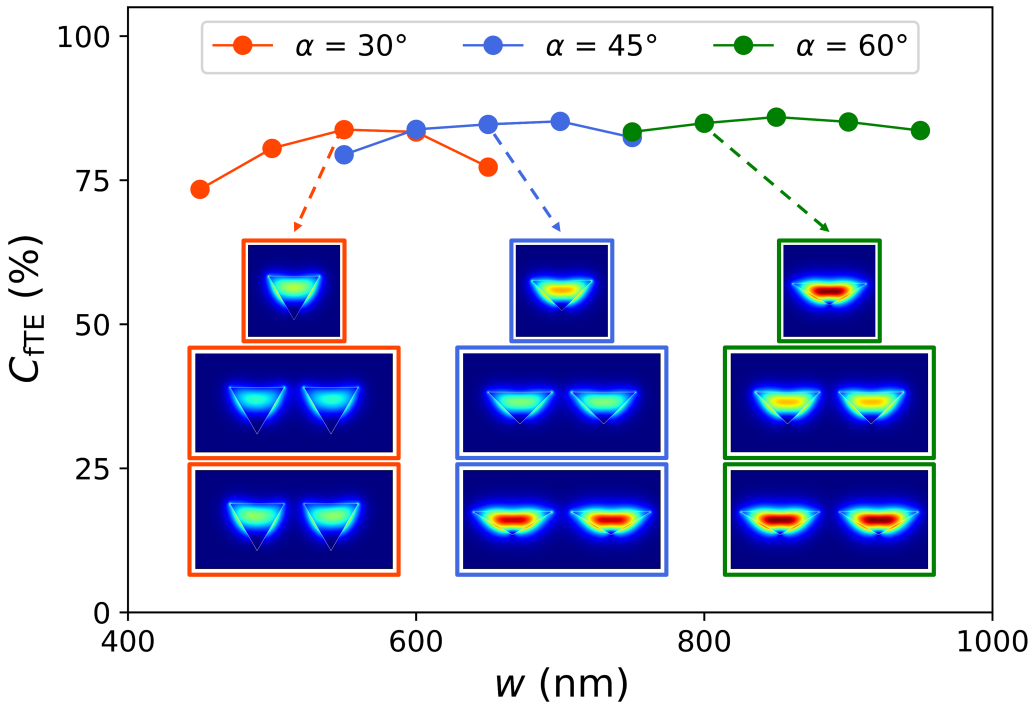

Figure 6.1. The coupling of a TE-oriented dipole emission at the centroid of the triangular profile into the f-TE mode (C_{fTE}) as a function of the waveguide width for three etch angles (α). Insets show electric field intensity profiles of the f-TE mode, TE supermode 1, and TE supermode 2 (top to bottom), at optimal waveguide widths supporting single-mode propagation, for $\alpha = 30°, 45°, 60°$. The electric field intensity of the TE supermodes were plotted for adjacent identical waveguides with a 200 nm gap between them.

(not supported in the waveguide). Using the MODE package in Lumerical software, we find that at these optimal widths for $\alpha = 45°$ and $60°$, the waveguide supports only the f-TE mode. However, for $\alpha = 30°$, both f-TE and f-TM modes are supported in the waveguide at the optimal and smaller widths. The height of the triangle varies inversely with α, and hence the widths needed for the f-TM to become evanescent are much smaller than the optimal width for $\alpha = 30°$.

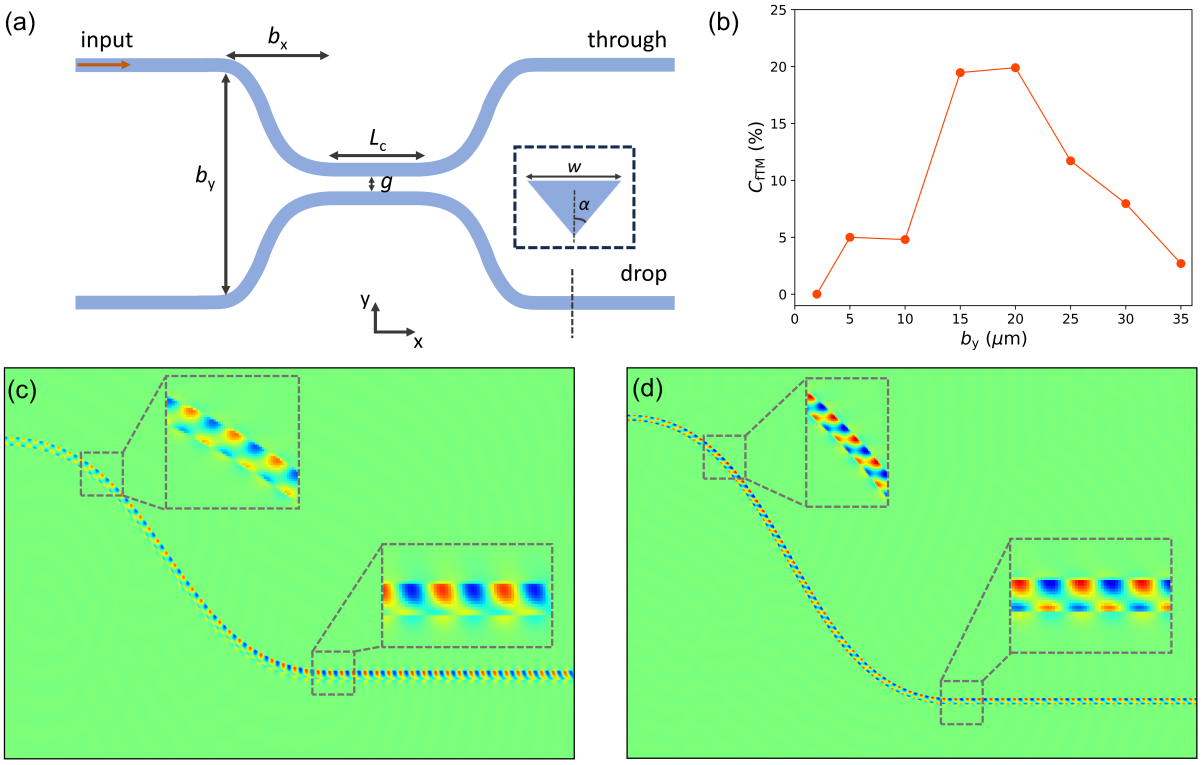

Figure 6.2. (a) Top view of the S-bend BS in 4H-SiC and the inset shows the triangular cross-section geometry. (b) The fraction of the f-TE input mode coupling to f-TM (C_{fTM}) mode along the bend with variations in bend y-span (b_{y}) for $\alpha = 30°$, $w = 550$ nm, and $L_{\mathrm{C}} = 30$ μm. (c)-(d) Propagation of E_{z} field in the xy plane of the structure described in (b) for b_{y} values of 20 μm and 35 μm, respectively.

In this work, we design a 50:50 BS using two identical triangular cross-section waveguides with three regions: 1) input and output - where the waveguides are far apart with zero electromagnetic interaction, on either ends of the BS, 2) bent waveguide region, and 3) coupling region - where the waveguides are close enough to electromagnetically interact, as shown in Figure 6.2a. When light is injected into the f-TE mode of one of the waveguides on the input side (top left), it propagates through the straight and bent re-

gions of that waveguide. When it reaches the coupling region, some of the light in the top waveguide is coupled into the bottom waveguide as it propagates along. Then the light in both waveguides pass through the bent and straight regions to reach the output ports (through and drop ports). The proportion of light coupled into the bottom waveguide is determined by the coupling strength between the individual waveguide modes and the length of the waveguides in the coupling region.

When two identical waveguides are close to each other, the individual modes (f-TE) in each of the waveguides superimpose to form a supermode. The coupling between the two waveguides can be analyzed in terms of a pair of TE supermodes, as shown in the inset of Figure 6.1. For a BS with power P_0 in one of the waveguides at the beginning of the coupling region, the coupling length (L_C) required for a power P_2 to couple into the other waveguide is given by:

$$L_C = \frac{\lambda_0}{\pi \Delta n_{\text{eff}}} \sin^{-1} \sqrt{\frac{P_2}{P_0}}$$

where λ_0 is the free space wavelength, Δn_{eff} is the difference in effective refractive indices of the two TE supermodes [169]. The coupling length is inversely proportional to the coupling strength between the waveguides given by Δn_{eff}, which in turn depends on the confinement of the individual waveguide modes and gap between the individual waveguides in the coupling region. For a 50:50 BS, where there is 50% light in both the waveguides after the coupling region, the ratio P_2/P_0 equals 0.5. We use MODE package in Lumerical software to estimate the effective index of the two TE supermodes, for calculating the theoretical values of L_C for various BS geometries studied in the following section.

6.2 Integrated 4H-SiC Beam Splitter in Triangular Geometry

Recent advances in on-chip splitting mostly include rectangular or slab waveguides [165]. For performing QIP with integrated color centers in 4H-SiC, we construct the BS structure with symmetric triangular cross-section single-mode S-bend waveguides with an overlap region to enable DC. Figure 6.2a shows the top view schematic of the BS with coupling length L_{C}, gap between the waveguides in the coupling region g, S-bend x-span b_{x}, S-bend y-span b_{y}, and the inset shows the triangular waveguide cross-section with w and α. In this work, we investigate 50:50 BS in triangular cross-section waveguides with $\alpha = 30°$, 45°, 60°, which can be fabricated with the state-of-the-art processes, by varying the gap g between waveguides and consequently L_{C}.

In Lumerical FDTD simulations (mesh size = 30 nm), we choose 20 μm for b_{x} and 10 μm for b_{y}, where b_{x} corresponds to the terminal points and b_{y} corresponds to the curvature control points of the S-bend (Bézier curve), for $\alpha = 45°$, 60°. For $\alpha = 30°$, we need to account for potential higher-order mode conversion due to the bending curvature as the n_{eff}, one of the most important parameters for understanding mode propagation, of the f-TE and the f-TM modes are virtually the same in the waveguides with $\alpha = 30°$. Hence, the f-TE mode can transform into the f-TM due to identical n_{eff} and inter-mode coupling via bends [170]. Keeping $b_{\mathrm{x}} = 20$ μm constant, we vary b_{y} for modulating the bend curvature of the $\{\alpha, w, L_{\mathrm{C}}\} = \{30°, 550$ nm, 30 μm$\}$ BS structure.

To test the inter-mode coupling (cross-talk), we inject via the f-TE mode at the input port and collect via the f-TM mode at the through port of the BS. It is observed in Figure 6.2b that coupling to the f-TM mode (C_{fTM}) initially increases with the increase in b_{y} and after reaching a maximum value of $\sim$ 20% for $b_{\mathrm{y}} = 20$ μm, C_{fTM} gradually decreases dropping down to 2.7% with $b_{\mathrm{y}} = 35$ μm. This trend occurs due to the expansion of the curved path with increasing b_{y}, however, after the inversion point, the bending becomes so gradual that the S-bend mimics a straight path. For a better understanding of the f-TE and f-TM mode coupling, we also study the E_{z} fields of the minimum and maximum C_{fTM} as E_{z} field is a good indicator of the existence of the TE and TM modes [171]. Figure

6.2c shows that at the starting point of the bending region with $b_y = 20$ μm, E_z has a nodal plane in the triangular waveguide which corresponds to the f-TE mode and at the ending point, E_z field starts to develop in the waveguide, confirming the coupling to the f-TM mode. On the other hand, for b_y value of 35 μm, there is a constant E_z nodal plane indicating the f-TE mode throughout the S-bend, depicted in Figure 6.2d, which makes this bend structure suitable for maintaining the single-mode propagation in the BS.

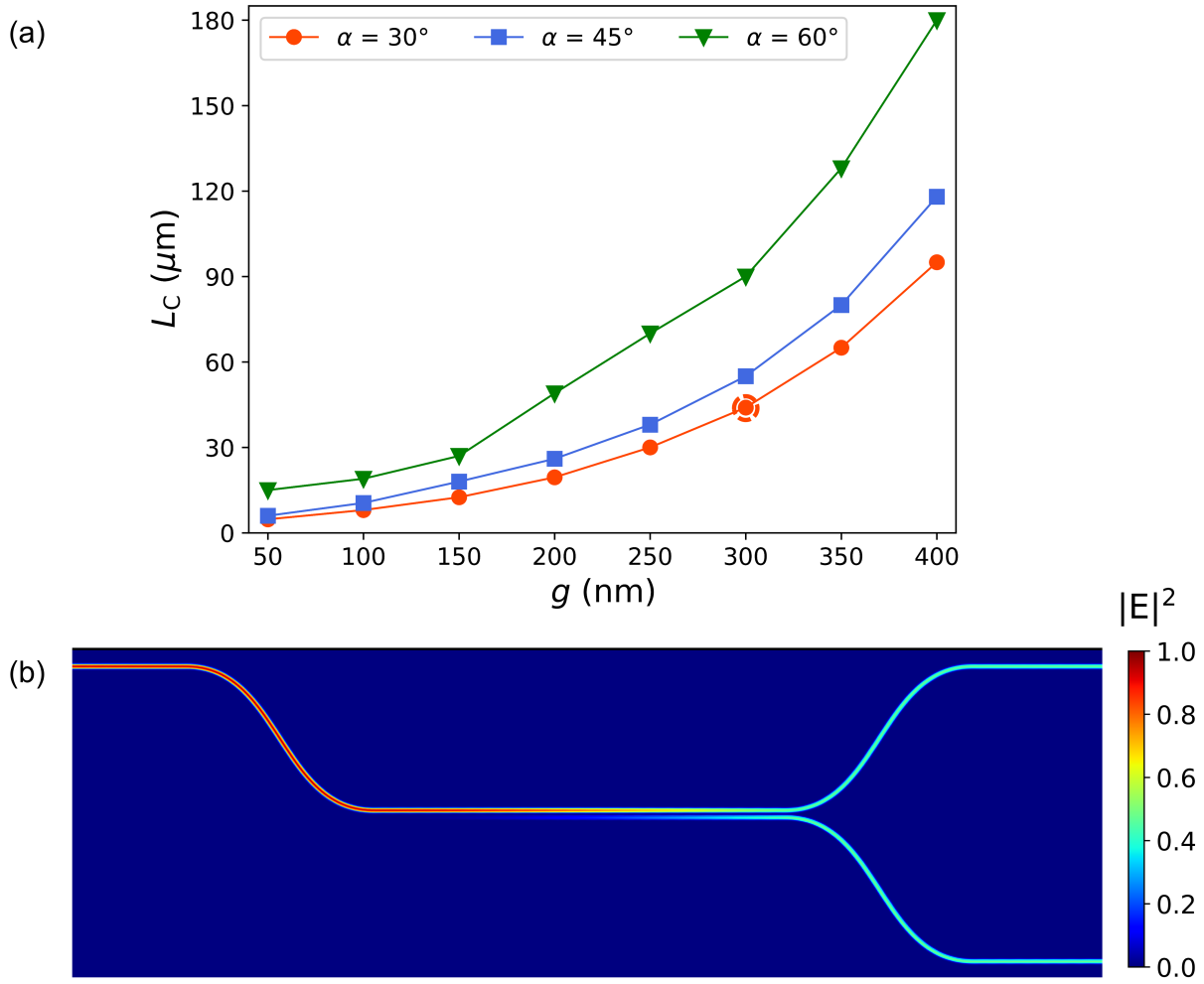

Figure 6.3. (a) L_C values for 50:50 splitting with an increasing gap g in $\alpha = 30°$, 45°, 60° BS. (b) Top view of the E-field intensity profile for the integrated 50:50 BS SiC structure with $\{\alpha, w, b_x, b_y, g, L_C\} = \{30°, 550$ nm, 20 μm, 35 μm, 300 nm, 44 μm$\}$ indicated by dashed circle in Figure 6.3a.

The above discussions lead us to the optimal selection of w and b_y of the 50:50 BS for each α. We choose 650 nm and 800 nm as w for $\alpha = 45°$, 60°, respectively, with b_y

= 10 μm in order to maximize the coupling and maintain single-mode propagation for establishing a suitable environment for QIP with the triangular cross-section BS. For α = 30° waveguides, we pick w = 550 nm and b_y = 35 μm to achieve similar outcomes. We vary the gap g from 50 nm to 400 nm to explore a range of designs. Figure 6.3a shows that with increasing g, L_C shoots up rapidly for all three etch angles, experiencing minor losses (< 1.5%) upon propagation through the entire BS. We observe another interesting phenomenon that L_C for the 50:50 BS with α = 60° is dramatically longer than the α = 30° and α = 45° BS for a particular g when $g \geq$ 200 nm. As a result, owing to smaller footprints, α = 30° and α = 45° BS appear as better candidates than the α = 60° BS for integrated quantum mesh photonic circuitry.

6.3 Fabrication of Closely Spaced Triangular Waveguides in 4H-SiC

Triangular cross-section photonics has previously been fabricated in SiC through Faraday cage assisted etching method [172, 87, 21] suitable for chip-scale integration of color centers with no degradation in color-center properties compared to the bulk substrate[21]. This approach could be brought to wafer-scale using IBE [22]. Therefore, we test a new IBE process to fabricate triangular cross-section waveguides in 4H-SiC, with varying gaps between waveguides (100 nm, 200 nm, 300 nm, 500 nm). This provides insight into what spacings between the waveguides in the coupling region of the simulated 50:50 BS are fabrication friendly, using the IBE process.

We use electron beam lithography to define the patterns on 4H-SiC substrates and then the pattern is transferred to a 120 nm thick nickel hard mask deposited using an electron beam evaporation, through a lift-off process. Triangular cross-section waveguides are then fabricated by IBE with SF_6 and O_2 chemistry. We use focused ion beam (FIB) - scanning electron microscope (SEM) to confirm the triangular cross-section of the fabricated waveguides, as shown in the inset of Figure 6.4d. We measure the etch angle (α) of these waveguides to be 30°. For adjacent waveguides with gaps of 100 nm and 200 nm, we observe no substantial etch in the region between the waveguides, as shown in Figure

6.4a-b. For waveguide gaps $\geq$ 300 nm (300 nm, 500 nm), the fabricated waveguides have triangular cross-sections, as shown in Figure 6.4c-d. The lack of etching in the region between the waveguides for smaller waveguide gaps may be due to the inability of the ions which are incident at an angle on the substrate, to reach well below the surface level of the substrate, and also reduced etching caused by mass-transport issues in those closely spaced regions.

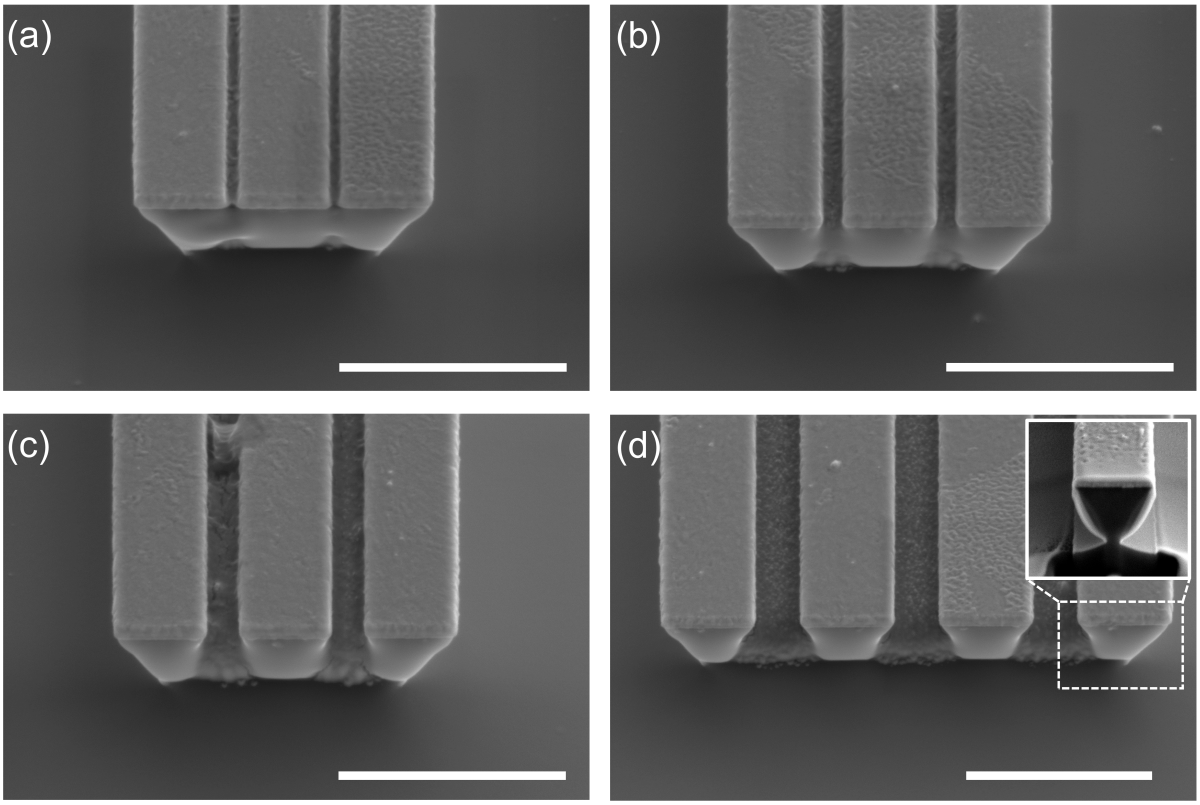

Figure 6.4. The SEM images of ion beam etched waveguides in 4H-SiC. (a)-(c) 800 nm wide waveguides with gaps of 100 nm, 200 nm and 300 nm respectively. (d) 1000 nm wide waveguides with a gap of 500 nm. Inset shows a FIB-SEM of the fabricated 1000 nm waveguide with a triangular cross-section. The scale bar is 2 μm.

6.4 Discussion

The modeling results presented in this work offer an approach to build low-loss triangular cross-section 50:50 BS in 4H-SiC necessary to perform key quantum interferometry operations for QIP applications. Here, triangular cross-section photonics provide a scalable route to integrate color centers into quantum photonic devices and circuits. More-

over, high-performance triangular cross-section photonic structures in 4H-SiC like waveguides, waveguides with integrated SNSPDs, photonic crystal mirrors, and photonic crystal cavities, that facilitate efficient generation, collection and detection of single-photon emission from color centers, necessary for applications in QIP have been demonstrated [21, 141, 152, 171]. Thereby, NV center in 4H-SiC with emission wavelengths near the telecommunications range is most suited for building large-scale quantum communication networks.

Our initial fabrication tests show that triangular cross-section waveguides with gaps greater than 300 nm can be fabricated using the wafer-scale IBE process. From the simulations, we note that for a waveguide gap $g \geq 300$ nm in the coupling region, $\alpha = 30°$ and 45° offer 50:50 BS with fabricatable footprints (e.g. coupling region $L_C \leq 50$ μm), for applications in QIP. Here, supporting structures for waveguide suspension would need to be designed. The IBE process conditions could be further optimized to achieve triangular cross-section waveguides with waveguide gap ≤ 300 nm, by choosing process conditions that result in a predominantly chemical etch. Under such etch conditions, the byproducts of the etch are volatile gases (SiF_4, CO, CO_2), preventing re-deposition, allowing the etch to continue. When there is a reasonable physical etch component, the sputtered material has a higher chance of re-deposition, especially when the gap between the waveguides is small, resulting in a slower etch or sometimes no etch. Another alternative could be choosing a steeper etch angle, because such waveguides would not require a deep etch to release the structure.

Triangular cross-section photonics in 4H-SiC provides an avenue to achieve efficient chip- and wafer-scale integration of color centers, with very little degradation of color center properties compared to bulk, essential for applications in QIP. Our simulation results demonstrate that 50:50 BS necessary for applications in QIP can be implemented using triangular geometry and our initial etch tests show that IBE is suitable for achieving this.

Chapter 7

Wafer-Scale Integration of Color Centers with 4H-SiC Nanophotonic Devices

As high purity 4H-SiC wafers are commercially available and with several key QIP demonstrations missing, developing a scalable angle-etch process in 4H-SiC using IBE is imperative. In this chapter, we examine a novel method for the fabrication of suspended photonic devices with triangular cross-sections on a wafer-scale in bulk 4H-SiC using reactive ion beam etching (RIBE), a variation of IBE. We develop a RIBE process to etch a variety of suspended photonic structures for a range of angles. Next, we demonstrate the wafer-scale nature of the etch process for a 5-inch diameter wafer, which is the first such wafer-scale process demonstrated for etching suspended structures in any bulk material. Finally, we use PL measurements to confirm that the optical properties of the color centers integrated into the fabricated photonic structures were preserved, which is key to building QIP hardware with color centers as quantum emitters.

7.1 Wafer-Scale Etching of 4H-SiC

Ion beam etching is a physical milling process in which inert gases such as Argon are ionized in an RF ion source, and these ions are extracted as a collimated beam through a series of grids and accelerated towards the substrate to etch the target substrate. Variations of this process, reactive ion beam etching (RIBE) and chemically assisted ion beam

etching (CAIBE) have a chemical etch component and are particularly useful for selective etching or etching materials that are tolerant to milling.

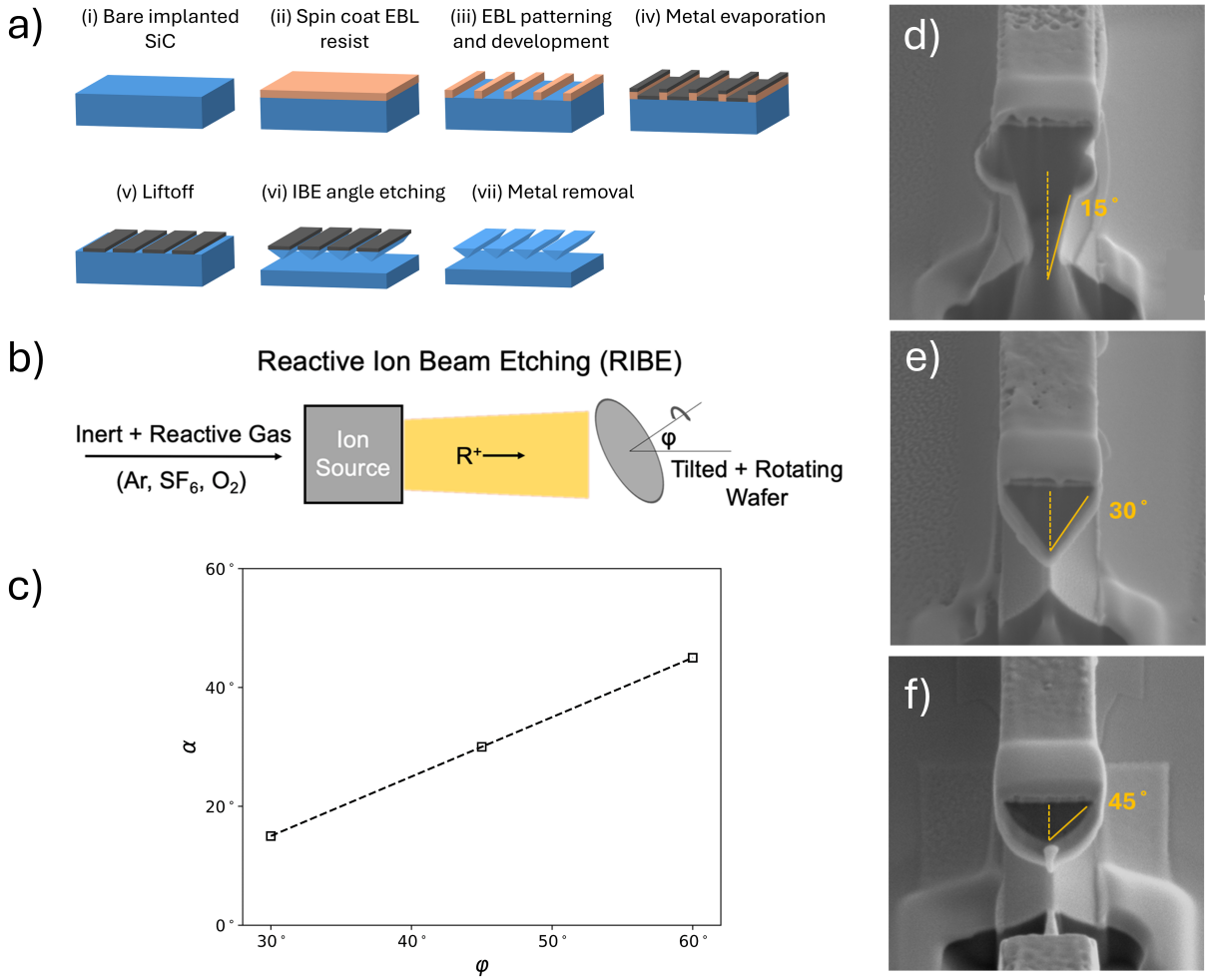

Figure 7.1. a) The process flow for the nanofabrication of triangular cross-section photonics in 4H-SiC. b) Schematic of the Reactive Ion Beam Etching (RIBE) with a tilting substrate holder, used to nanofabricate suspended structures with triangular cross-section in bulk 4H-SiC. c) Variation of the etch-angle of triangular structures (α) as a function of the tilt angle of the substrate holder (φ). d-f) SEM images of the triangular cross-section profile of a 1 μm wide waveguide, showing etch angles for tilt angles d) 30°, e) 45°, and f) 60°.

The triangular cross-section photonic devices were nanofabricated using the process flow as shown in Figure 7.1a (details in 7.2). We developed a RIBE process involving SF_6 and O_2 gas chemistry, while maintaining the SF_6 to O_2 flow rates at a ratio 4:1 (etch process parameters in 7.2). The undercut in these photonic structures was achieved by tilting the substrate holder (Figure 7.1b), to direct the ions underneath the nickel

hard mask layer and rotation of substrate holder was used to ensure uniform etch in all directions. The etch angle (α), defined as the half angle at the apex of the triangular cross-section, varies linearly with the tilt angle of the substrate holder (φ), as shown in Figure 7.1c. The realized etch angle of the fabricated devices deviates from the expected etch angle, determined by the tilt angle, by 15°. The underlying reasons for this angle mismatch are further investigated in a subsequent chapter. Figure 7.1d-f shows the SEM images of the cross-section of a 1 μm waveguides etched at tilt angles 30°, 45°, and 60° respectively. The devices etched at a tilt angle of 60° (Figure 7.1f) is the highest etch angle (45°) reported for triangular cross-section devices fabricated in 4H-SiC, with an undercut of $> 1\mu$m.

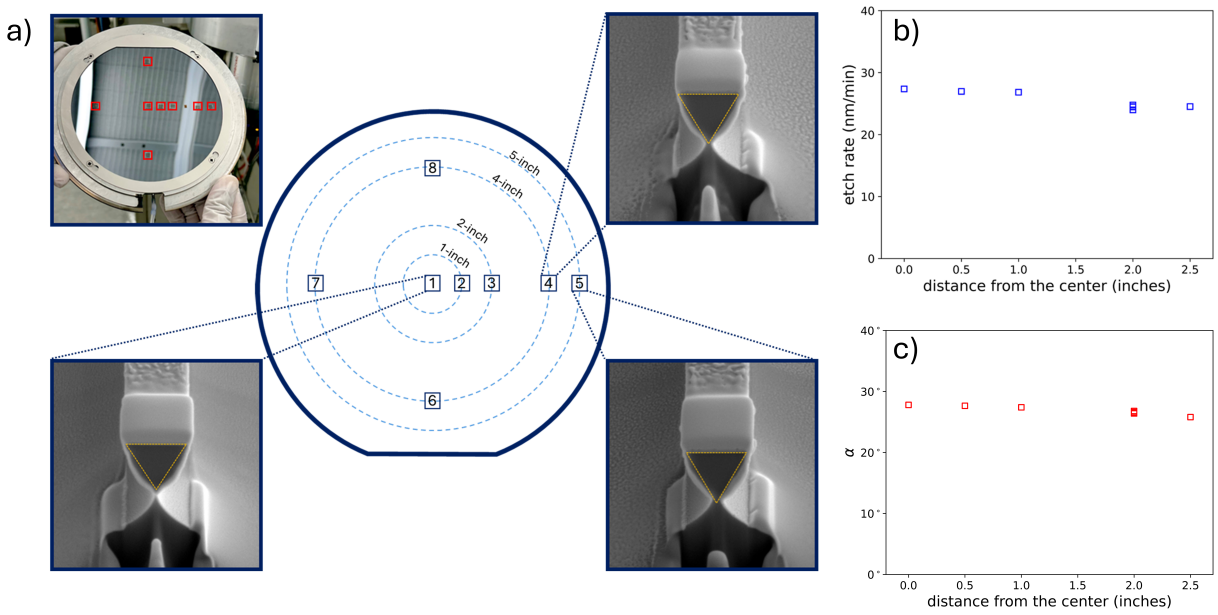

Figure 7.2. a) Illustration showing the placement of 4H-SiC samples on a 6-inch substrate holder. The positioning of the 4H-SiC samples represent circumferences of wafers up to 5 inches in diameter. (Insets) 4H-SiC samples on the substrate holder and the cross-sectional profiles of the nanofabricated 1 μm waveguides from some of the illustrated chips. b-c) The achieved b) etch rate and c) etch angle (α) uniformity as a function of distance from the center of the substrate holder, showing 5.4% and 2.9% variability, respectively.

We tested the wafer-scale nature of the RIBE process by placing a total of eight patterned 4H-SiC samples on a 6-inch silicon substrate holder at locations as follows: one sample each at the center, on the circumferences of 1-, 2- and 5-inch wafers, and four

samples on the circumferences of a 4-inch wafer, as shown in Figure 7.2a. All the eight samples were etched simultaneously using the RIBE process developed at a tilt angle of 45° for a total of 70 minutes. The SEM images of the cross-section profiles of a 1 μm waveguide on samples placed at the center and on the circumferences of 4- and 5-inch wafers are shown in the insets of Figure 7.2a. We find that both the etch rate and the etch angle decrease linearly along the radius of the wafer, as shown in Figure 7.2b-c. The variation of etch angle along the radius could be attributed to the non-uniformity of the ion beam profile for a broad beam Kaufman-type ion source [173], across a 6-inch diameter. The radial reduction in the ion current density and ion directionality contributes to a reduction in the etch rate and etch angle, respectively. The etch rate and etch angle change linearly by 12.3% and 5%, respectively, from the center to the circumference of a 5-inch wafer. The variation in etch rate and etch angle among the four samples on the circumference of a 4-inch wafer was 1.2% and 0.6%, respectively. This RIBE process has an etch rate of (25.9 ± 1.4) nm/min, etch angle of $(27 \pm 0.8)^\circ$, and etch selectivity of $>$ 8:1. To our knowledge, this is the first demonstration of a wafer-scale etch process for fabricating suspended nanophotonic structures in bulk 4H-SiC.

The RIBE etch performs uniformly for a range of neighboring active and passive nanophotonic devices, as shown in Figure 7.3. We measured the emission properties of the nitrogen vacancy centers integrated in the fabricated triangular photonic devices using our 3-in-1 integrated cryogenic system for emission, collection and photon-detection [112]. The photoluminescence spectrum of a triangular cross-section ring resonator at 7 K is shown in Figure 7.4a. The spectrum features zero-phonon lines (ZPLs) corresponding to the naturally occurring divacancy centers (red) with wavelengths 1078 nm, 1108 nm, 1131 nm, 1132 nm [174] and the implanted nitrogen-vacancy centers (green) with wavelengths 1175 nm, 1179 nm, 1222 nm, 1243 nm [166]. This shows that the key challenge in integrating color centers with photonic devices is solved in our process, as many fabrication processes destroy the ZPL emission [92]. To measure an extent of the emission preservation, we take high-resolution photoluminescence spectra at $T = 1.56$ K shown in Figure 7.4b where we compare NV center emission from bulk (unetched pads) and from triangular

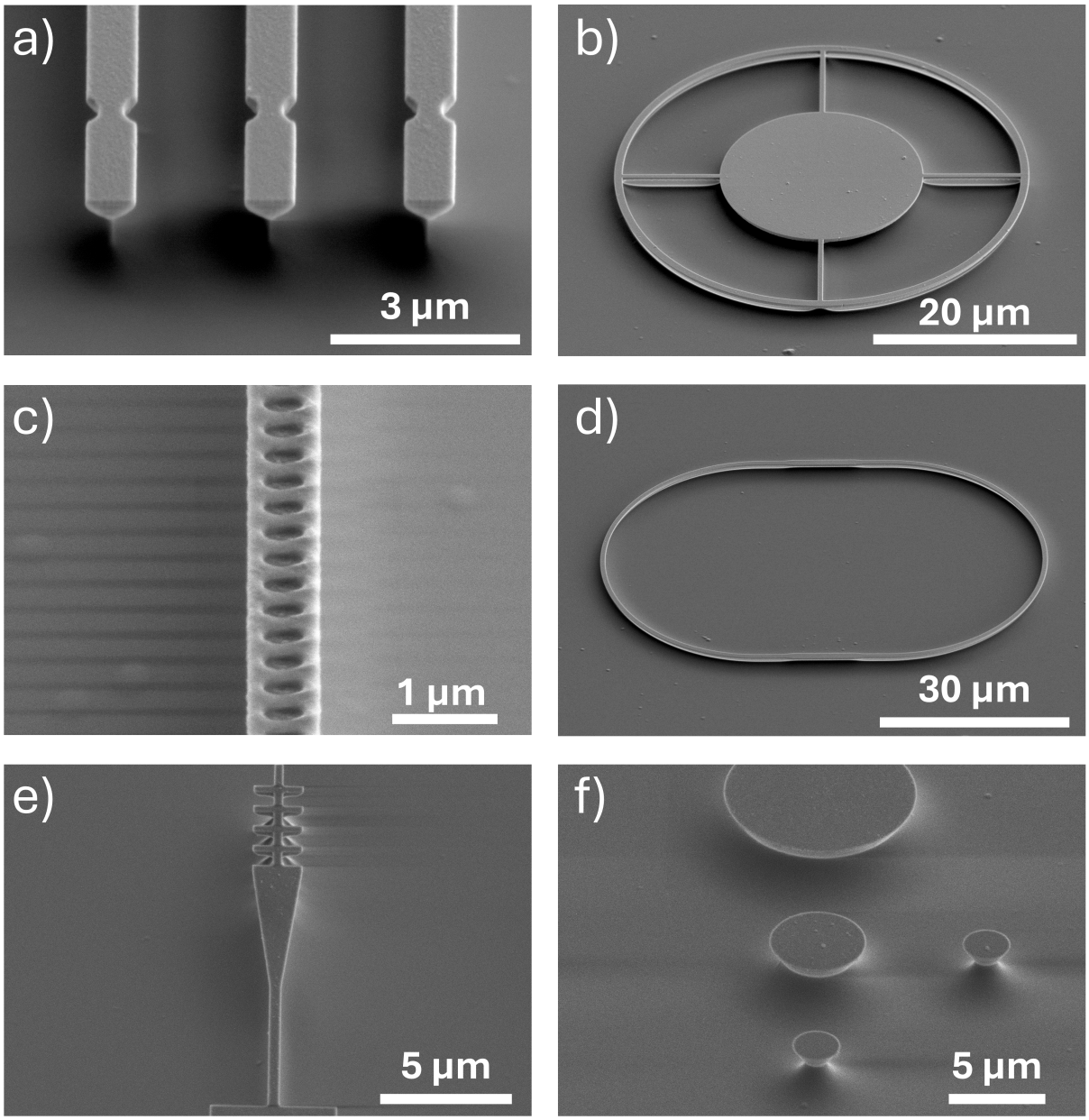

Figure 7.3. SEM images of the nanofabricated SiC photonic devices using the wafer-scale angle-etch RIBE process: a) 0.8 μm waveguides with notch couplers, b) microring resonator with radius 20 μm, c) photonic crystal cavity of width 0.9 μm, with 0.495 μm spacing between adjacent elliptical holes, d) racetrack resonator with a width of 0.8 μm and radius of curvature 24.6 μm, e) fish-bone grating coupler with teeth of width 2 μm and spacing of 0.8 μm, and f) microdisk resonators with radii 1.25 μm, 2.5 μm and 5 μm. SEM images in a-d) are obtained with the nickel metal hard mask on top of the devices, while e-f) have the nickel mask removed.

waveguides. Due to the background noise, the signal-to-noise ratio is modest, however, the inhomogeneous linewidth broadening between the two sets of spectra is quite comparable. This indicates that there is no significant strain or amorphization generated and that color center optical properties are preserved upon integration into triangular cross-section photonic devices fabricated using the developed RIBE process.

7.2 Nanofabrication Methods

Prior to the lithographic process, we generated nitrogen vacancy centers in 4H-SiC through commercial (CuttingEdge Ions, LLC) implantation using $^{14}N^{+}$ ions at an energy of 65 keV and a dose of 1×10^{14} cm^{-2} [105], resulting in a peak nitrogen concentration at a depth of $\sim$ 100 nm, as calculated by stopping and range of ions in matter (SRIM) simulations. This was followed by an annealing step in a 1-inch Lindberg Blue tube furnace at 1050 °C in nitrogen atmosphere for 60 minutes [105], to activate the implants. The process flow used for nanofabrication of triangular photonic devices in bulk 4H-SiC is shown in Figure 7.1a. First the 4H-SiC samples were spin coated with a 350 nm electron beam resist PMMA layer, and photonic patterns were transferred into this layer using a 100 keV electron-beam lithography (ii-iii). Then e-beam evaporation was used to deposit a 5 nm titanium adhesion layer and a 120 nm nickel hard mask layer, and lift-off was used to transfer the photonic patterns to this metal layer (iv-v). Triangular cross-section photonic devices were etched in 4H-SiC using the Intlvac Nanoquest II ion beam etching tool, and finally the metal layers were removed by wet etching the samples in Transene's nickel and titanium etchants (v-vi).

The SiC chips with Ni patterns were etched using RIBE in the Intlvac Nanoquest II, equipped with a 16 cm diameter Kaufman & Robinson RF ion source and a tilting and rotating stage. The optimized RIBE process parameters are: beam voltage = 300 V, accelerating voltage = 120 V, beam current = 110 mA, RF power = 150 W, $Ar/SF_6/O_2$ flow rates = 10/10/2.5 sccm, pressure = 0.24 mTorr, substrate temperature = 20 °C, etch time = 2 etch cycles of 35 minutes each with 2 minutes cooling time between the two etch cycles. Argon gas is added to the ion source along with SF_6 and O_2 to maintain the

stability of beam parameters.

7.3 Results and Discussion

The data in previous sections show results of what we believe is the first wafer-scale angle etch process using ion beam etching to fabricate triangular cross-section photonics in quantum-grade bulk 4H-SiC. Importantly, the etching process does not interfere with the optical properties of the photonic integrated color centers. This approach can be used to fabricate devices with a wide range of etch angles. Over a 5-inch wafer diameter, the variation in the etch rate and the etch angle is 5.4% and 2.9%, respectively, which can be countered by adjustments in the lithographic mask. In comparison, the silicon carbide on insulator (SiCOI) approach quotes a variation of 1 μm in thickness across a 4-inch wafer [20], which could potentially triple the device thickness across the wafer if fabricated in a unified process.

Previous modeling results have shown that variation in etch angles of triangular photonic crystal cavities shifts the resonant wavelength of the cavity without significantly affecting the quality factor and the mode volume [141]. The change in etch angle from the center to 2.5 inches away from the center results in a 1.2% change in the resonant wavelength, and this can be compensated by including a variation of 1.6% in the lattice constant within the mask design to counter this resonant wavelength shift. For triangular waveguides, a variation of 2.9% in the etch angle does not significantly change the coupling efficiencies of the color center emission or the single-mode nature of these waveguides [141, 21]. The variation in the etch rate does not play a significant role in the fabrication of triangular devices because it does not affect the shape of the device, but only the height of the undercut region. The origin of the 15° deviation in the etch angle from the ideal scenario, where the etch angle is equal to the tilt angle, is yet to be fully understood. Some possible explanations for the origins of this issue could be shrinking of the metal mask at the edges during the etch or over-etching of the sidewalls and the apex of the triangular cross-section during the additional etch time required to create an undercut, which would require further investigations.

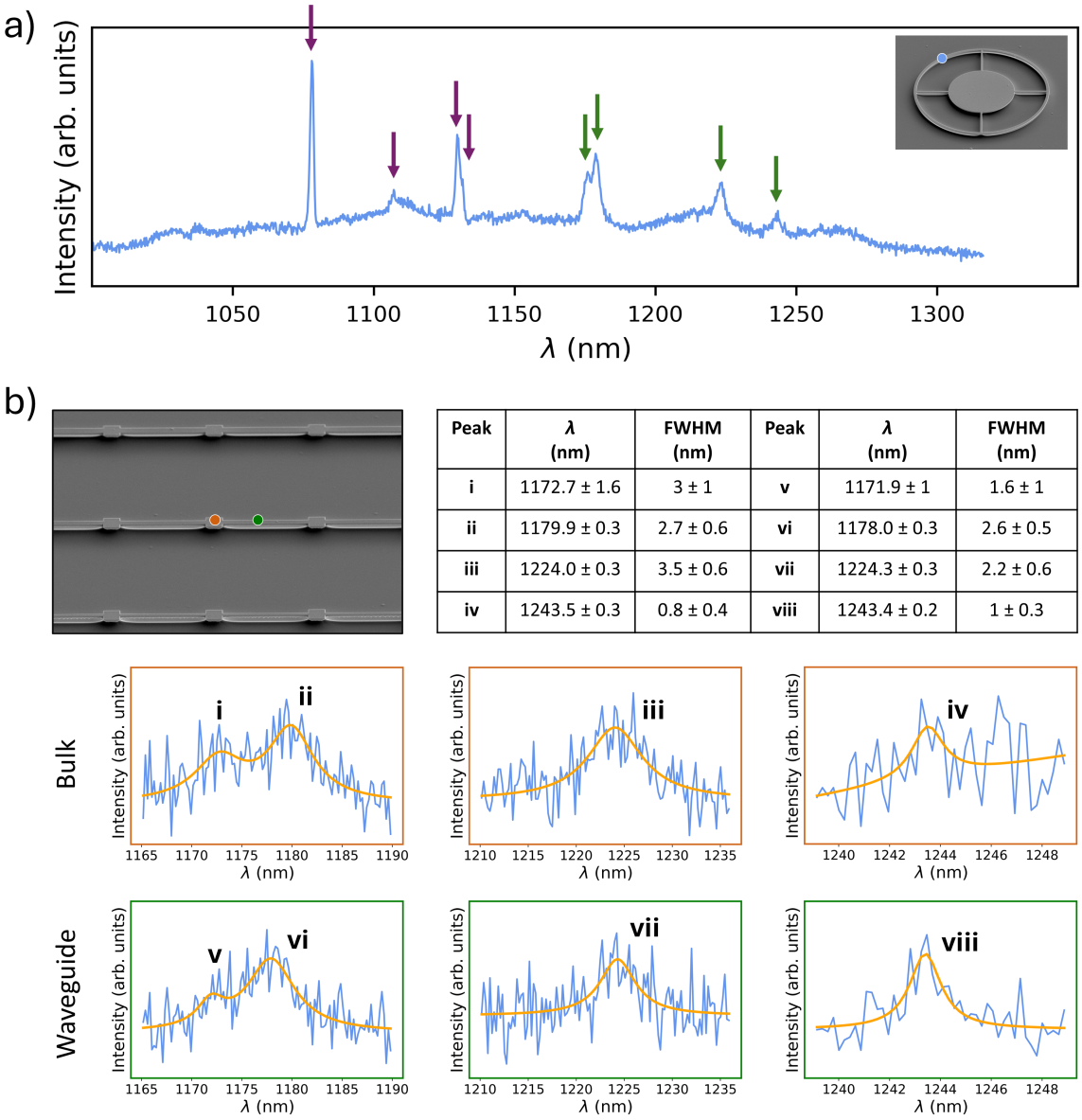

Peak	λ (nm)	FWHM (nm)	Peak	λ (nm)	FWHM (nm)
i	1172.7 ± 1.6	3 ± 1	v	1171.9 ± 1	1.6 ± 1
ii	1179.9 ± 0.3	2.7 ± 0.6	vi	1178.0 ± 0.3	2.6 ± 0.5
iii	1224.0 ± 0.3	3.5 ± 0.6	vii	1224.3 ± 0.3	2.2 ± 0.6
iv	1243.5 ± 0.3	0.8 ± 0.4	viii	1243.4 ± 0.2	1 ± 0.3

Figure 7.4. a) Photoluminescence spectrum of an angle-etched 4H-SiC ring resonator with integrated color centers at $T = 7$ K, showing ZPLs from divacancy (VV^0) centers (1070 - 1130 nm) and NV centers (1170 - 1245 nm), marked with purple and green arrows respectively. (Inset) SEM image of the triangular cross-section ring resonator fabricated using the optimized wafer-scale RIBE process, the blue dot indicates the spot where photoluminescence spectra were obtained from. b) High resolution comparison of NV center ZPL photoluminescence from 4H-SiC bulk (marked by an orange dot in the SEM image) and waveguide (green dot) measured at $T = 1.56$ K with peak and linewidth fits to a Lorentzian curve shown in the table.

This process will have applications in the scalable fabrication of uniformly performing linear, nonlinear, and quantum photonic devices, such as waveguides, microresonators, and photonic crystal cavities, as well as in complex quantum optical circuits such as mesh photonics with color center emitters in silicon carbide. Applications in optomechanics, optofluidics, and biosensing can also be supported in this platform by taking advantage of its acoustic properties and chemical inertness.

Chapter 8

Wafer-Level Testing with Triangular Cross-Section Fishbone Grating Couplers

An on-chip wafer-scale testing mechanism is required for characterizing color center interaction with triangular shaped nanophotonic hardware. Although edge couplers offer highly efficient coupling over a large bandwidth, they do not support wafer-level testing and have complex post-fabrication steps with limited access to the circuits [175, 176]. Vertical grating coupler (GC) is a convenient choice for flexible integration with other photonic elements on the same chip, allowing for wafer-scale testing. Fiber-based GCs exhibit excellent coupling efficiency at the cost of large footprints and precise fiber alignment [176]. As a cryogenic environment is required for color center characterization [112], free-space GCs in combination with a microscope objective have proven to be a very practical solution [177, 178]. Typical microscopy systems have a higher NA compared to optical fibers and provide wider bandwidth [179]. Moreover, due to the absence of mode mismatch issues between the fiber core and the GC, free-space GCs can be optimized for a compact layout.

In this chapter, we design, fabricate, and characterize SiC triangular cross-section grating couplers compatible with quantum-grade color center substrates. We first model periodic and aperiodic GC designs using the FDTD method. We then use e-beam lithog-

raphy, ICP-RIE and RIBE processes to undercut devices with triangular cross-section. We characterize devices in room-temperature transmission and cryogenic photoluminescence setups and obtain waveguide propagation loss and GC efficiencies, indicating that fishbone grating couplers are a suitable device to outcouple light from triangular color center quantum photonics to free-space optics in a scalable process.

8.1 Triangular Cross-Section Fishbone Grating Coupler

In this section, we analyze the design parameters for triangular cross-section suspended GC in SiC. The grating coupler, illustrated in Fig. 8.1(a), consists of (i) a triangular waveguide, (ii) an adiabatically tapered region, and (iii) a fishbone-like grating structure. We choose the fishbone grating design in accordance with the fabrication compatibility of the RIBE process to produce wafer-scale triangular cross-section devices. Fig. 8.1(b) shows the top view schematic of the GC with waveguide width w_1, etch angle (half angle at the apex) α, taper angle θ_{taper}, taper length L_{taper}, maximum taper width w_2, grating period a, and the central bone width w_{bone}. The refractive index of SiC is kept $n_{\text{SiC}} = 2.6$ throughout the analysis. We parameterize the scales w.r.t. wavelength of interest λ_0 to make the design scalable for the variety of color centers SiC hosts. We optimize each component individually to achieve the most efficient design.

8.1.1 Single-Mode Waveguide

Single-mode propagation is an important requirement in the waveguide design for performing on-chip QIP [168, 180]. For each α, there exists an optimal width for single-mode propagation in the triangular cross-section waveguides [21]. In this work, we choose $\alpha = 45°$ as it offers higher confinement [171] and coupling [21, 181] compared to other etch angles that have been fabricated with the RIBE process in SiC [182].

Based on the dipole orientation in the SiC crystal lattice, color center emission can couple to fundamental transverse electric (f-TE), fundamental transverse magnetic (f-TM), and other higher-order modes supported by the triangular waveguide. Therefore, we optimize the triangular waveguide width w_1 for maintaining single-mode propagation

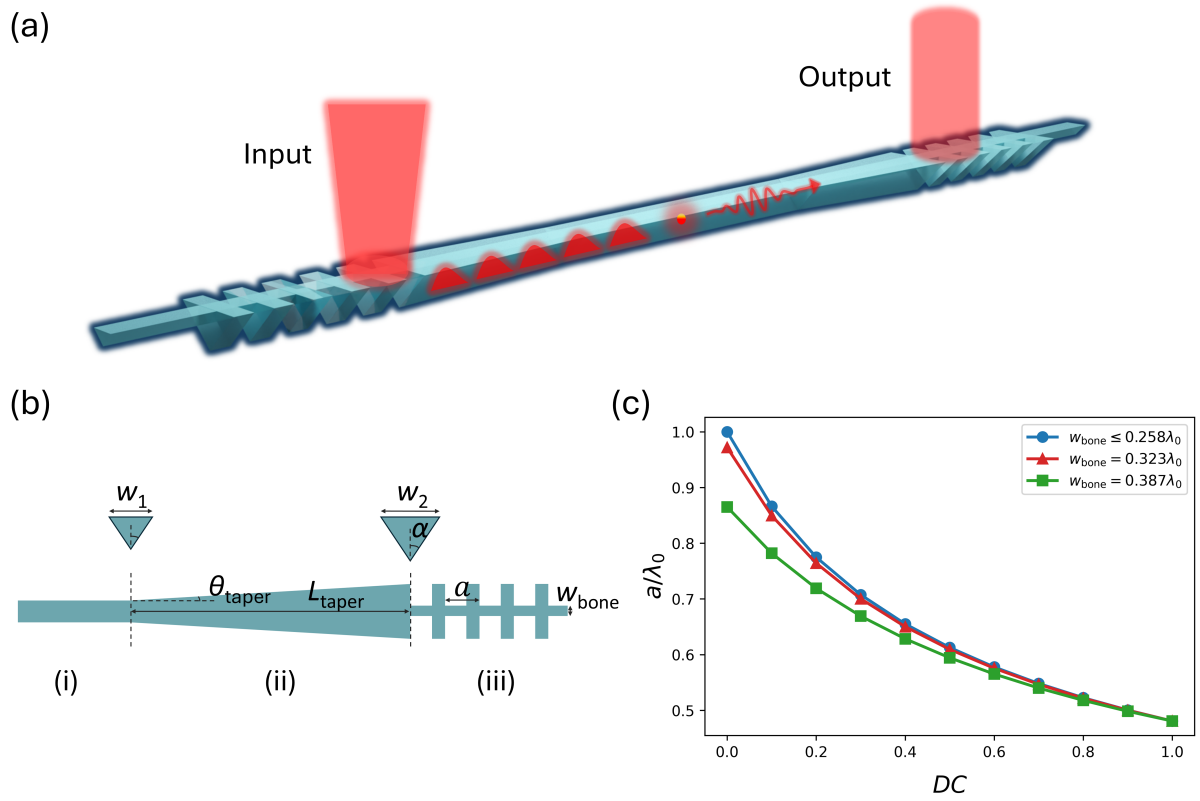

Figure 8.1. (a) A perspective figure of the triangular cross-section grating couplers (GCs) used for the characterization of color center coupling with integrated nanophotonic hardware. The red sphere at the center of the waveguide represents the color center. (b) Top view of triangular cross-section fishbone GC with three regions: (i) waveguide, (ii) adiabatic taper, and (iii) fishbone grating. (c) Grating period a and duty cycle DC which satisfy the 1st order vertical grating phase matching condition for $w_{\text{bone}} = 0.258\lambda_0$, $0.323\lambda_0$, $0.387\lambda_0$.

of both horizontal and vertical electric dipole radiations with high coupling efficiency (C_{EFF}) using Lumerical FDTD package, as shown in Figure 8.2(a). We position the dipole sources with emission wavelength λ_0 at the centroid of the triangle, which is the optimum color center position in triangular geometry for the best coupling to the waveguide modes [141, 21, 152]. We pre-select the w_1 range using Lumerical MODE (Finite-Difference Eigensolver) package so that the horizontal (vertical) dipole couples only to the f-TE (f-TM) mode. Although the proposed design is a 1D-GC structure in which we can optimize only for a single state of polarization [176], we choose $w_1 = 0.548\lambda_0$ to obtain high coupling for both the f-TE and the f-TM modes of the waveguide.

8.1.2 Adiabatic Taper

An adiabatically tapered region is instrumental to coupling light in and out of the chip [183]. It allows for a smooth transition of light from the waveguide mode to the Gaussian mode by gradually changing the size and shape of the optical mode along the taper. The slow transition of the effective refractive index (n_{eff}) of the waveguide cross-section ensures minimal mode conversion to higher-order or radiation modes resulting in high coupling efficiency. Traditional fiber-coupled GCs require very long taper regions to match the mode field diameter of the single-mode optical fibers [175]. On the other hand, light coupling through the microscope objective enables very compact designs for such tapers as the focused Gaussian beam spot size becomes orders of magnitude smaller compared to the optical fiber mode.

In the SOI platform, it has been observed that linear tapers with small taper angle (θ_{taper}) result in higher transmission [184]. We apply a similar strategy in designing the triangular cross-section taper region by linearly increasing the taper width for $\theta_{\text{taper}} = 1^\circ, 2^\circ, 3^\circ$, shown in Figure 8.2(a). To ensure gradual change in n_{eff} of the waveguide mode, we calculate the n_{eff} of the f-TE and f-TM modes (mode #1 and mode #2, respectively) of the triangular waveguide along L_{taper}. Figure 8.2(c) demonstrates that the adiabatic condition for triangular waveguides [185]: $dn/dx < (2\pi/\lambda_0)|n_{\text{eff},1}(x) - n_{\text{eff},2}(x)|^2$, where n is the effective index of the waveguide cross-section with maximum taper width w_2 and $n_{\text{eff},i}$ is the effective index of the ith waveguide mode along L_{taper}, is satisfied for all three θ_{taper}. However, owing to the etch selectivity of the mask in the developed RIBE wafer-scale process[182], we restrict w_2 to be $0.774\lambda_0$, $\sim 40\%$ larger than w_1, for undercutting both w_1 and w_2 cross-section profiles in a single etch. Although all three θ_{taper} designs exhibit unity transmission for the f-TE mode injection from the waveguide, we choose $\theta_{\text{taper}} = 2^\circ$, leading to $L_{\text{taper}} = 3.225\lambda_0$ for $w_2 = 0.774\lambda_0$, for a highly efficient compact adiabatic taper.

8.1.3 Fishbone Grating

Refractive index variation with periodic configuration in the direction of light propagation is the most preferred approach for breaking the device symmetry to achieve out-of-plane

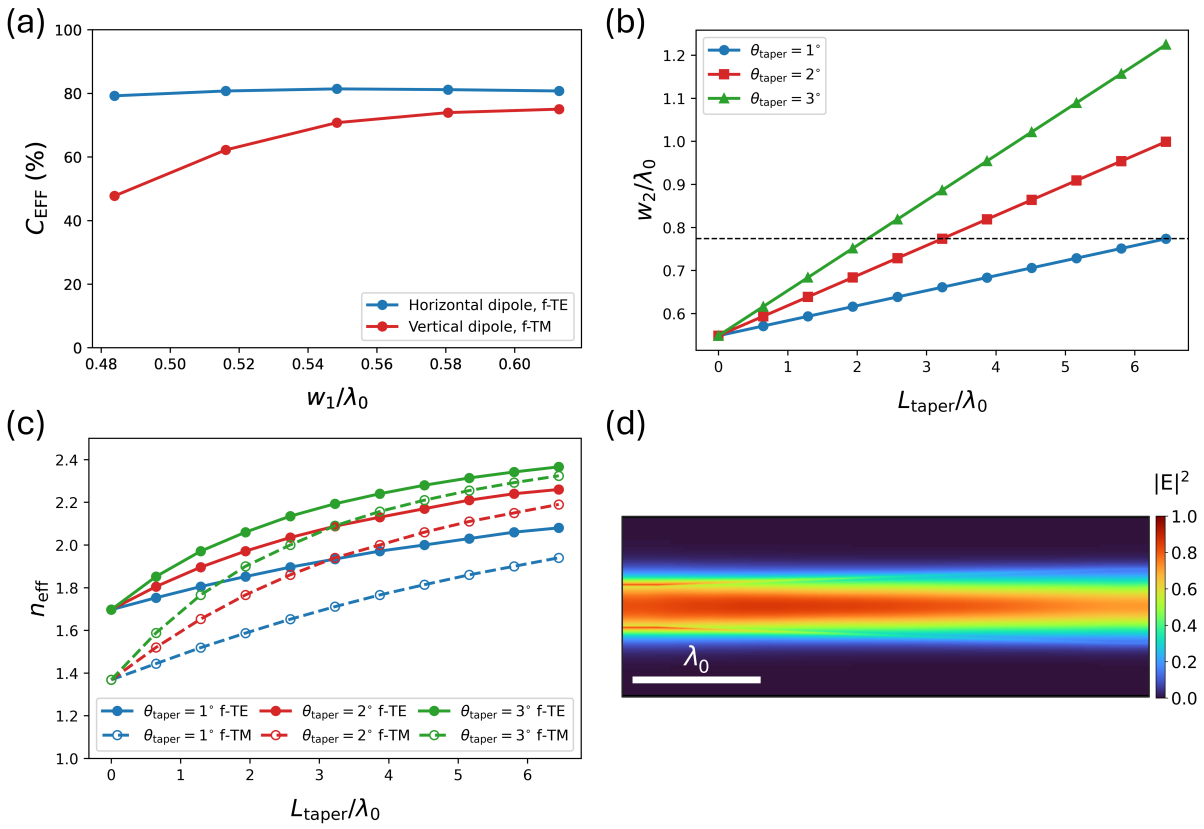

Figure 8.2. (a) Coupling efficiency (C_{EFF}) of horizontal and vertical dipoles into the fundamental transverse electric (f-TE) and the fundamental transverse magnetic (f-TM) modes, respectively, of triangular waveguides with etch angle, $\alpha = 45°$.(b) Taper width w_2 w.r.t taper length L_{taper} for taper angles $\theta_{\mathrm{taper}} = 1°, 2°, 3°$. The dashed (black) line shows the fabrication constraint imposed on w_2. (c) Effective refractive indices n_{eff} of the f-TE and the f-TM modes along L_{taper} for $\theta_{\mathrm{taper}} = 1°, 2°, 3°$. (d) Top view cross-section of the electric field (E-field) intensity ($|\mathrm{E}|^2$) profile for the adiabatic taper design with $\theta_{\mathrm{taper}} = 2°$, $L_{\mathrm{taper}} = 3.225\lambda_0$, and $w_2 = 0.774\lambda_0$ where the f-TE mode of the waveguide with $w_1 = 0.548\lambda_0$ is injected into the taper region. The cross-section is taken at the centroid plane of the maximum taper width $w_{\mathbf{2}}$.

coupling through diffraction[175]. Our fishbone grating is constructed by varying the width of the triangular cross-section periodically to implement refractive index contrast. The central bone ensures the mechanical stability of the suspended structure. The diffraction mechanism for a GC is governed by Bragg phase matching condition: $N_{\text{eff}} - n_{\text{air}}\sin\theta = m\lambda_0/a$, where N_{eff} is the effective index of the guided mode in the grating medium, n_{air} is the refractive index of air, θ is the diffraction angle, m is the grating order, λ_0 is the target wavelength, and a is the grating period. For 1D-GC, the 1st order diffracted mode is vertically emitted from the grating [176]. With $\theta = 0^\circ$ and $m = 1$, we can achieve vertical outcoupling and the phase matching condition reduces to $a = \lambda_0/N_{\text{eff}}$. Due to the 1D periodicity, we can optimize for only one polarization state, in our case the f-TE mode. We estimate the N_{eff} using the analytical expression [186]: $N_{\text{eff}} = \sqrt{(1 - DC)n_1^2 + DCn_2^2}$, where DC is the duty cycle, or the fill factor, of the wider section, and n_1 and n_2 are the effective indices of the triangular cross-section with widths w_{bone} and w_2, respectively. The grating period a and duty cycle DC that satisfy the phase matching condition for different w_{bone} values are presented in Fig. 8.1(c). We observe that there exists no physical mode in the triangular cross-section for $w_{\text{bone}} \leq 0.258\lambda_0$ at λ_0, which means the effective index of the narrow regions is $n_1 = 1$. Therefore, we choose $w_{\text{bone}} = 0.258\lambda_0$ for obtaining maximum index contrast.

8.2 Design Optimization

The GC design optimization is focused on enhancing the collection efficiency from color center integrated nanophotonic devices for characterizing light-matter interaction. Fig. 8.3(a) shows the side view of the 3D FDTD simulation setup for calculating the collection efficiency. We use a mode source to inject the f-TE mode of the waveguide (width w_1) at λ_0 into the grating. A field and power monitor is placed above the triangular cross-section GC at a $\lambda_0/2$ distance for measuring the fraction of power going in the upward direction. As we are interested in maximizing the light collection through a microscope objective, we add another field and power monitor very close to the top surface of the GC to calculate the far field radiation pattern and subsequently the fraction of power

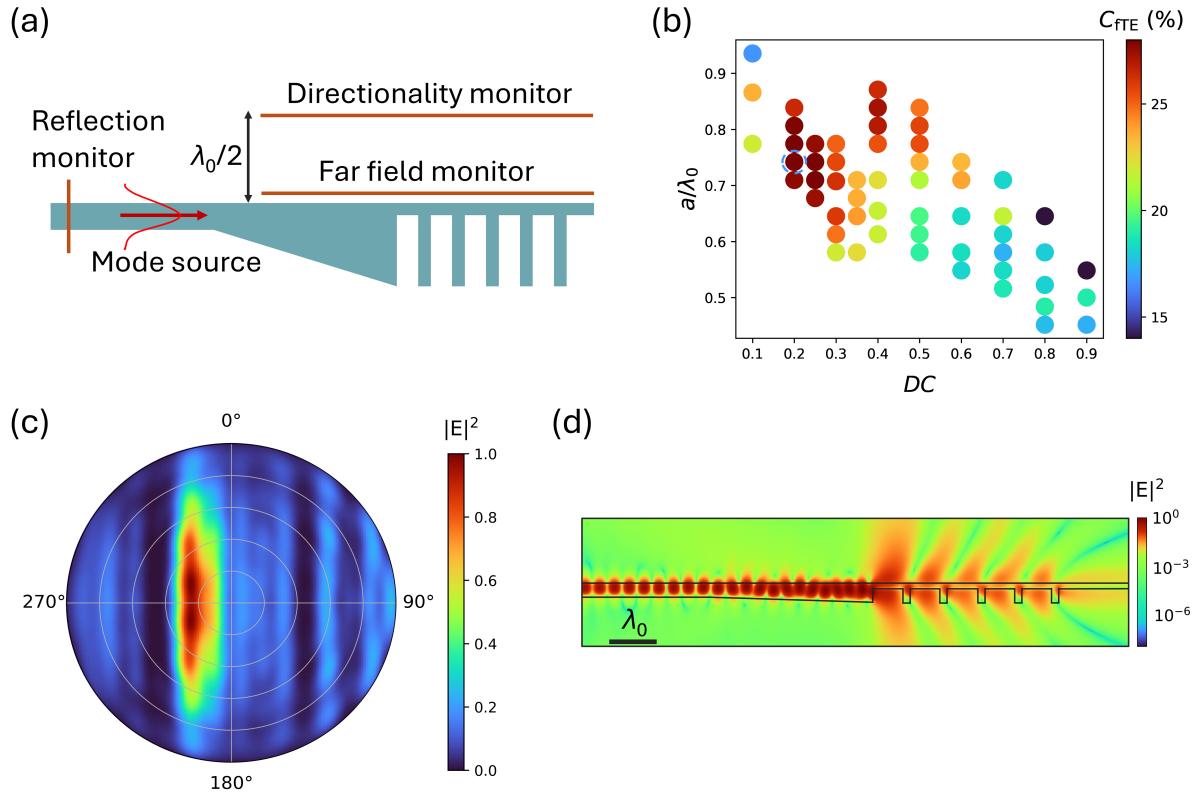

Figure 8.3. (a) Side view of the FDTD simulation setup for calculating collection efficiency. (b) Collection efficiency (C_{fTE}) for the f-TE mode injection from the waveguide with variation in DC and a. The dashed (blue) circle indicates the most optimized design for the maximum C_{fTE}. (c)-(d) The far field radiation pattern and the side view cross-section $|\mathrm{E}|^2$ distribution, respectively, of the triangular GC with $DC = 0.2$ and $a = 0.742\lambda_0$, marked with blue dashed circle in (b).

collected by an objective with a given NA (0.65 in this work). The collection efficiency is obtained by multiplying the power fractions calculated from these two monitors. We use a field and power monitor before the source to check the amount of light reflected back into the waveguide.

For a given design, the collection increases with the number of grating periods and saturates for 5 unit cells. As a result, we use 5 grating periods for all the GCs in our analysis. Fig. 8.3(b) exhibits the collection efficiencies (C_{fTE}) from the injected f-TE waveguide mode with variation in DC and a. We observe that reflection decreases with the increase in C_{fTE}. The maximum C_{fTE} is $\sim 29\%$, acquired from a design with $DC = 0.2$ and $a = 0.742\lambda_0$. The obtained C_{fTE} value is comparable to another compact GC design

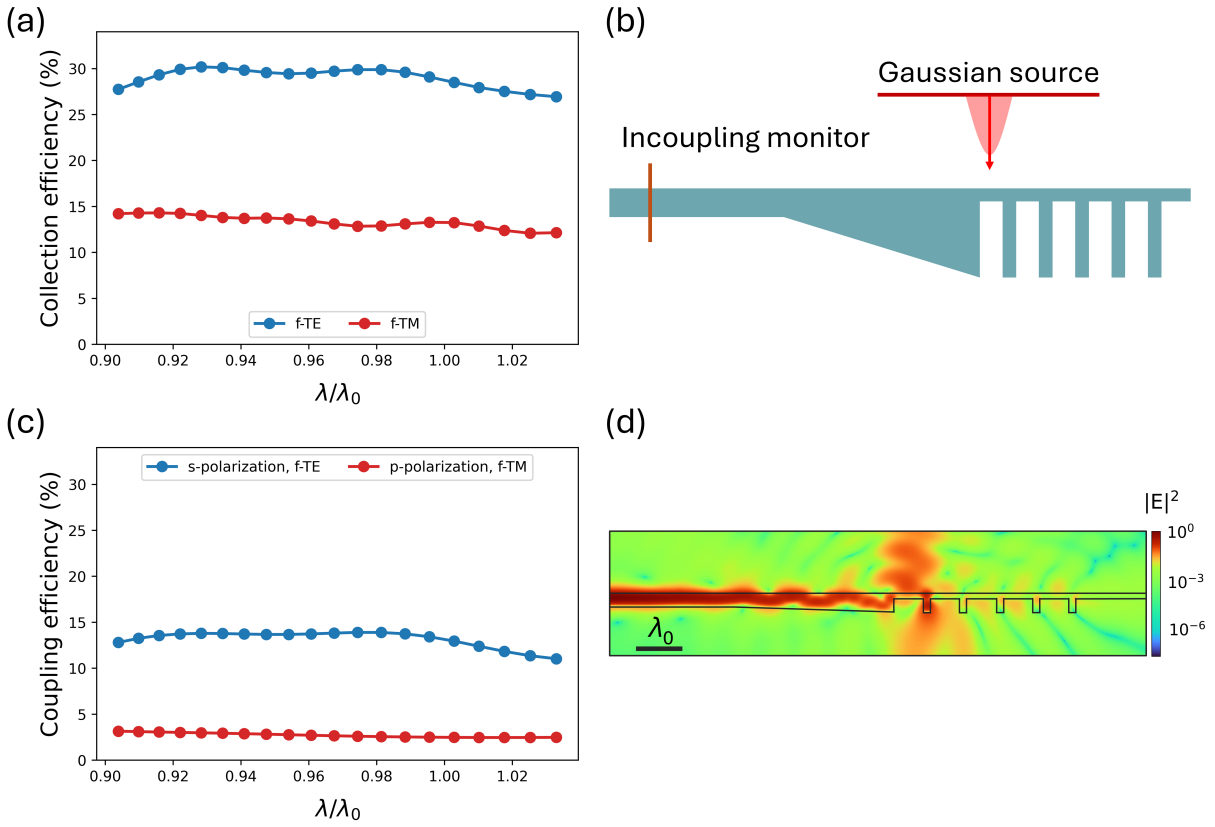

Figure 8.4. (a) Collection efficiency of the optimized design with periodic grating for the f-TE and f-TM modes as a function of normalized wavelength λ/λ_0. (b) Side view of the FDTD simulation setup for calculating the incoupling efficiency. (c) Incoupling efficiency for the s-polarized and p-polarized Gaussian beams as a function of normalized wavelength λ/λ_0. (d) The side view cross-section $|E|^2$ distribution of the triangular GC for an s-polarized Gaussian beam focused from above at λ_0.

realized in silicon nitride for microscope objective collection where the theoretical coupling efficiency reaches up to 40% (60% with a reflective mirror coating on the substrate) [179]. Notably, the most efficient design does not satisfy the phase matching condition which can stem from the broken symmetry of the triangular profile compared to rectangular structures. This phenomenon is observed in another theoretical work with triangular cross-section GCs in gallium nitride [187]. Fig. 8.3(c)-(d) show the far field radiation pattern and side view cross-section of electric field intensity ($|E|^2$) distribution, respectively, at λ_0 for the most efficient design. We also simulate the collection efficiency of the optimized design as a function of normalized wavelength λ/λ_0. The collection efficiency for the f-TM mode at λ_0 is $\sim$ 13%, lower than half of C_{fTE}, which is expected. Con-

ventional 1D grating couplers have to deal with bandwidth issues [188, 189] whereas the triangular cross-section GC response appears flat over a wide bandwidth, meaning the same design can be utilized for studying different zero-phonon line (ZPL) emissions from a color center in SiC. To characterize the incoupling efficiency of the optimized design, we employ a Gaussian source focused from above by an objective with 0.65 NA and a power monitor in the waveguide region as shown in Fig. 8.4(b). For higher incoupling, the source needs to be focused on the first grating period. Focusing on other unit cells results in lower incoupling as a large amount of light readily couples to the guided mode of the adiabatic taper as seen in Fig. 8.4(d). The s-polarized Gaussian beam mostly couples to the f-TE mode while the p-polarized beam couples mostly to the f-TM mode. Although we observe some initial coupling to high-order modes, they diminish as the incoupled light propagates through the waveguide. Fig. 8.4(c) illustrates the broadband response for the incoupling efficiency of the optimized design. The incoupling efficiency is much lower than outcoupling as our optimization technique prioritizes the collection efficiency.

Non-uniform GCs have proven to be very effective in enhancing the overall efficiency [176, 190, 191]. Non-uniformity is generally introduced by linearly apodizing the DC or a along the direction of propagation. In search of the most optimized design, we opt for a similar technique. Keeping $a = 0.742\lambda_0$ constant, we linearly change the DC of each unit cell with the following equation: $DC_i = DC_0 \pm r \times i$, where r is the apodization factor, $DC_0 = 0.2$, and $i = 0, 1, 2, 3, 4$. However, we observe the C_{fTE} slowly decreasing for both cases with variation in r from 0 to 0.02. On the other hand, we linearly change a for each grating section, with constant $DC = 0.2$, by the following equation: $a_i = a_0(1 \pm f \times i)$, where f is the aperiodic factor, $a_0 = 0.742\lambda_0$, and $i = 0, 1, 2, 3, 4$. Fig. 8.5(a) demonstrates that C_{fTE} gradually increases (decreases) with increasing (decreasing) a and starts to decrease (increase) after reaching an inversion point. We notice that even for the most optimized aperiodic design, with $f = 0.07$, C_{fTE} only increases by $\sim 2\%$. However, we observe a significant change in the broadband response, Fig. 8.5(b), and the far field radiation pattern, Fig. 8.5(d), of the aperiodic GC. The far field radiation appears less dispersive compared to the periodic design. While collection and incoupling efficiencies for

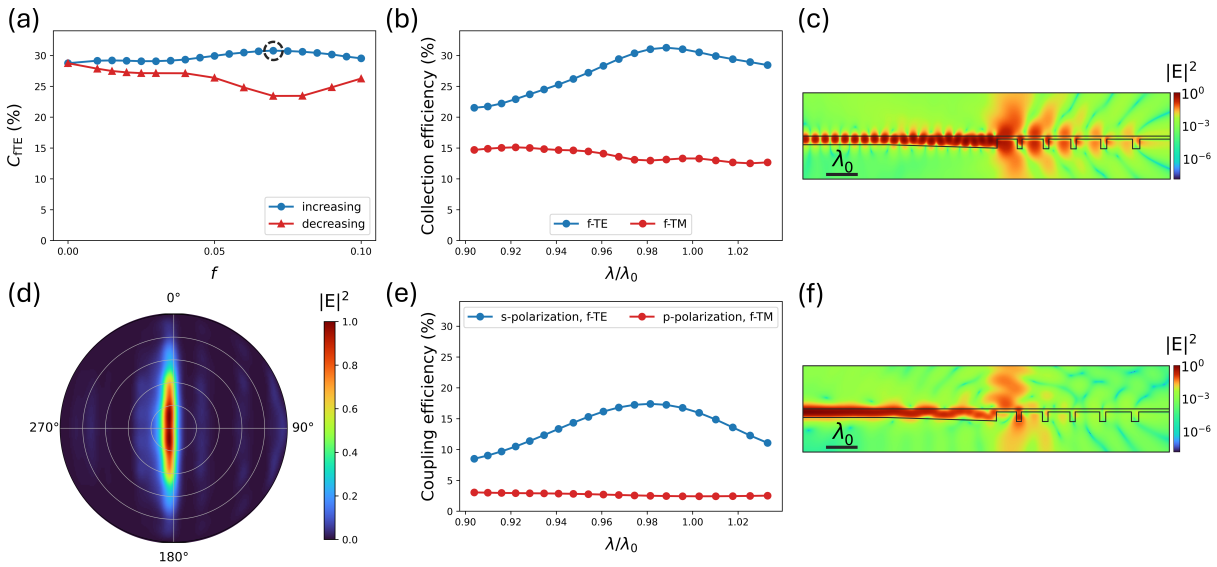

Figure 8.5. (a) C_{fTE} with variation in aperiodic factor f for linear increase and decrease of a. The dashed (black) circle shows the most efficient aperiodic design for the maximum C_{fTE}. (b) Collection efficiency of the optimized design with aperiodic grating, marked with a black circle in (a), as a function of normalized wavelength λ/λ_0. (c)-(d) The side view cross-section $|\mathrm{E}|^2$ distribution and the far field radiation pattern, respectively, of the triangular aperiodic GC with $f = 0.07$ at λ_0. (e) Incoupling efficiency for the s-polarized and p-polarized Gaussian beams as a function of normalized wavelength λ/λ_0 for the optimized aperiodic GC. (f) The side view cross-section $|\mathrm{E}|^2$ distribution of the triangularly shaped aperiodic GC for an s-polarized Gaussian beam focused from above at λ_0.

the f-TM mode remain invariant for the aperiodic optimization, the broadband response for the f-TE mode becomes a normal distribution. Based on the specific application requirement, one can adopt either the periodic or the aperiodic design as both designs exhibit comparable collection efficiencies.

8.3 Experimental Results

Designed grating couplers can readily be implemented with the wafer-scale nanophotonic fabrication processes. As illustrated in Fig. 8.1(a), a suspended triangular waveguide has grating couplers on its both ends. One coupler is used to direct the laser into the waveguide and excite the color center with off-resonant excitation. The other one couples both the excitation light and the color center emission out into free-space optics where the excitation beam is filtered out. With this mechanism, light-matter interaction in

the triangular geometry can be experimentally characterized for all suspended active and passive photonic devices.

8.3.1 Nanofabrication Process

We implement the key step in the fabrication of the studied GC designs in SiC using the RIBE process [182]. We choose $\lambda_0 = 1310$ nm, considering the broadband response, for both the periodic and aperiodic GC fabrication. Fig. 8.6(a) shows the nanofabrication process flow. For generating nitrogen vacancy (NV) centers, before nanofabrication, each 4H-SiC sample is irradiated with $^{14}N^{+}$ ions with a dose energy of 65 keV and a fluence of 1×10^{14} cm^{-2} at room temperature [182, 105]. The implantation is performed commercially through CuttingEdge Ions, LLC. The dose energy results in a peak nitrogen concentration at ∼115 nm depth from the surface, calculated by stopping and range of ions in matter (SRIM) simulations, close to the highest $|E|^2$ point in the simulated triangular cross-section devices for the best coupling to the waveguide modes. The samples are subsequently annealed at 1050°C in a nitrogen atmosphere for one hour to activate the NV centers [182, 105].

We use electron beam lithography for defining the GC patterns on the NV center implanted 4H-SiC samples. Then we deposit 120 nm thick nickel as a hard mask using electron beam evaporation and transfer the GC patterns on to the mask through a lift-off process. To obtain a deeper undercut (∼1.5 μm etch depth), we perform 3 minutes of inductively coupled plasma-reactive ion etching (ICP-RIE) with SF_6 and O_2 chemistry, which has higher etch rate and selectivity than the RIBE process [112]. The triangular cross-section waveguides and GCs are then fabricated by the RIBE process using SF_6, O_2, and Ar gas ions, with the substrate tilt angle set to 60° to achieve $\alpha = 45°$ [182] and overall device undercut >1.6 μm. However, after the nickel hard mask removal, we notice that most of the devices break near the attachment point between the thin (∼300 nm) triangular cross-section bone and the square pads. Previous fabrication efforts in triangular diamond nanobeams faced similar difficulties after mask removal [192]. On a subsequent attempt, we handle the sample with extreme caution during mask removal which results in a higher fabrication yield (∼70%).

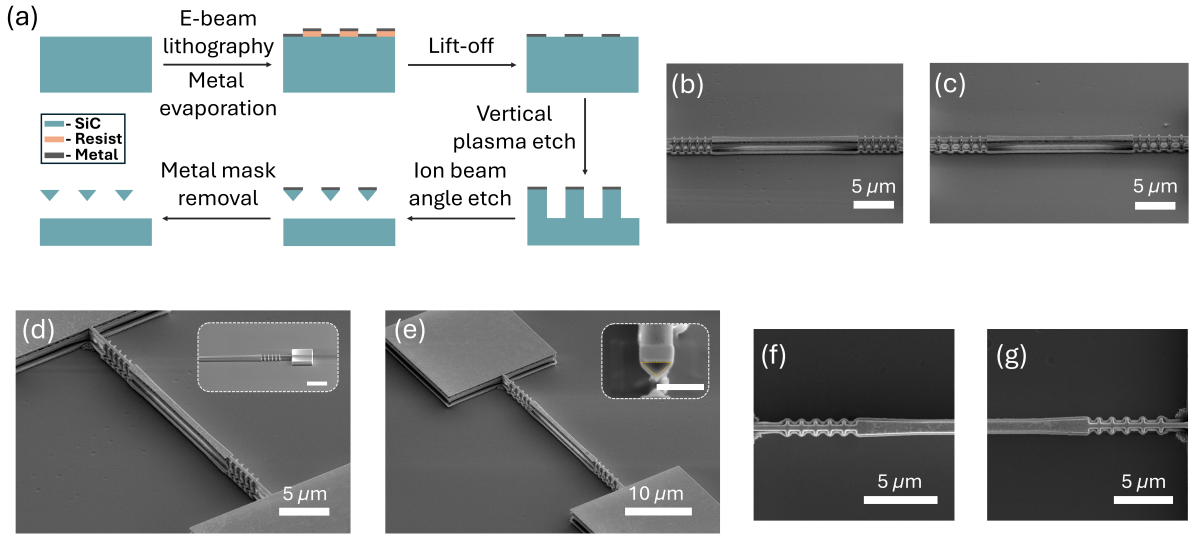

Figure 8.6. (a) Nanofabrication process flow of triangular cross-section fishbone GC in SiC. (b)-(c) Side view and (d)-(e) Perspective view SEM images of the triangular cross-section periodic and aperiodic GCs, respectively, with a 52° tilt. (f)-(g) Top view SEM images of triangular cross-section periodic and aperiodic GCs, respectively. Inset (d) shows the side view (52° tilt) of a periodic GC after vertical etch, scale bar indicates 5 μm. Inset (e) shows the FIB cross-section SEM image (52° tilt) of a triangular waveguide with $\alpha \simeq 42°$, scale bar indicates 1 μm. All the SEM images, except inset (e), are obtained with the nickel hard mask on top of the devices.

8.3.2 Transmission Measurements

To characterize the overall efficiency of the triangular waveguides and fishbone GCs, we use a confocal correlator setup, shown in Fig. 8.7(a), to spatially filter out the reflection of the input beam at the Fourier plane. A linearly polarized tunable laser (Santec TSL-570-A, 1240-1380 nm) is used to perform the transmission measurements at room temperature. The input beam is mostly s-polarized with a 10° tilt (CCW) due to the slow axis position of the polarization-maintaining fiber (PMF) at the fiber coupler (FC) end. The NA of the microscope objective in the setup is 0.65, similar to the simulations. We employ a short-wave infrared (SWIR) camera to monitor the input and the output beams. The collected beam power is measured by an InGaAs photodetector (PD), Thorlabs DET01CFC, which is connected to a benchtop photodiode amplifier (PDA), Thorlabs PDA200C, to ensure stable output.

To account for all potential losses arising from both optical and electronic compo-

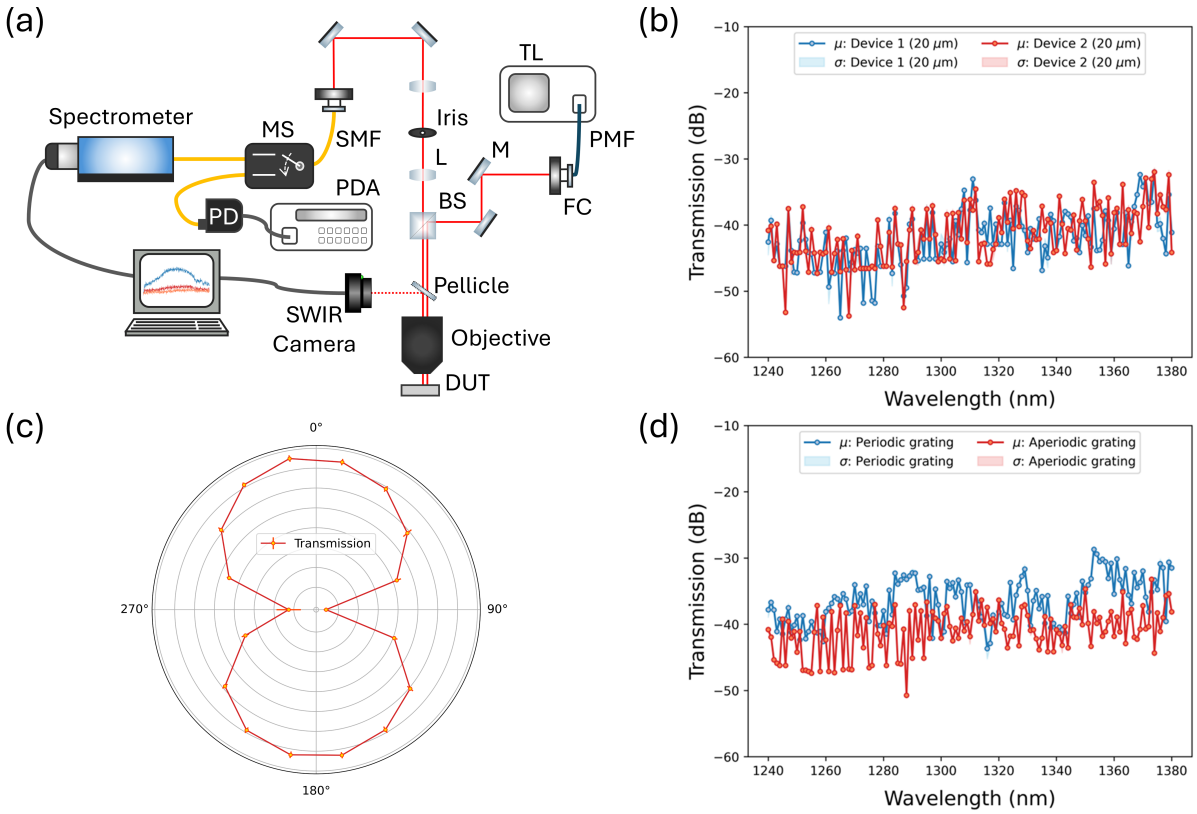

Figure 8.7. (a) A sketch of the experimental setup used to characterize fabricated devices; TL: tunable laser, PMF: polarization-maintaining fiber, FC: fiber coupler, M: mirror, BS: 10:90 (R:T) beamsplitter, L: achromatic doublet lens, SMF: single-mode fiber, MS: manual switch, PD: photo detector, PDA: photodiode amplifier, DUT: device under test, SWIR: short-wave infrared. (b) The spectral profile of transmission efficiency of two identically fabricated devices (periodic GCs connected by a 20 μm waveguide) showing uniform performance. (c) Transmission efficiency as a function of the polarization of the incoupled light, where 0° corresponds to the polarization orthogonal to the waveguide propagation direction. (d) The spectral profile of transmission efficiency of devices with periodic and aperiodic GCs (waveguide length 10 μm).

nents, we determine the reference input power by measuring the reflected signal from a p-type single-side polished 620 μm thick test grade silicon substrate. We calculate the input power by normalizing the reflected signal with known reflectance (R) of the silicon substrate where $R = \frac{(n-1)^2+k^2}{(n+1)^2+k^2}$ and (n, k) values in the 1240-1380 nm range are obtained from literature [193]. To minimize measurement bias, collected power at each wavelength is recorded three times for the silicon reflection and the GC output signals. The mean (μ) and the standard deviation (σ) of the measurements are calculated by the following equations: $\mu = \frac{1}{N}\sum_{i=1}^{N} x_i$, $\sigma = \sqrt{\frac{1}{N-1}\sum_{i=1}^{N}(x_i - \mu)^2}$ where x_i represents individual measurements and $N = 3$. We normalize the GC output power by the input power for obtaining the transmission efficiency with $\mu_{\text{norm}} = \frac{\mu_{\text{GC}}}{\mu_{\text{Si}}}$, however, to accurately propagate the measurement uncertainty, we calculate the normalized σ with $\sigma_{\text{norm}} = \mu_{\text{norm}}\sqrt{\left(\frac{\sigma_{\text{GC}}}{\mu_{\text{GC}}}\right)^2 + \left(\frac{\sigma_{\text{Si}}}{\mu_{\text{Si}}}\right)^2}$. Although conversion to decibels (dB) is straightforward for μ_{norm}, converting propagated uncertainty σ_{norm} to dB requires careful consideration of error propagation in logarithmic scales [194]. The conversion equations used for the measured transmission (dB) presented in Fig. 8.7, 8.8 are $\mu_{\text{dB}} = 10\log_{10}(\mu_{\text{norm}})$ and $\sigma_{\text{dB}} \approx \frac{10\cdot\sigma_{\text{norm}}}{\mu_{\text{norm}}\cdot\ln(10)}$ where we consider $\frac{\sigma_{\text{norm}}}{\mu_{\text{norm}}} \ll 1$.

Transmission efficiency measurements from two identical devices, where each device consists of two identical periodic GCs connected by a 20 μm triangular waveguide, are presented in Fig. 8.7(b). The comparable performance of the identical devices highlights the uniformity and reproducibility of the fabrication process. The spectral response exhibits the broadband nature of the fishbone GCs, in good agreement with the simulation results. To verify the polarization response, we insert a half-wave plate in the input beam path and observe a higher transmission for the s-polarized beam compared to the p-polarized beam, shown in Fig. 8.7(c), consistent with the design optimization for the f-TE mode. In the polar plot, we account for the 10° tilt correction of the PMF slow-axis position. Although the aperiodic GCs are expected to outperform the periodic GCs, we observe a slight decrease in the overall transmission, illustrated in Fig. 8.7(d). On the other hand, the overall transmission efficiencies for both periodic and aperiodic GC devices are orders of magnitude lower compared to the simulation results. Therefore, to evaluate the loss

contributions from individual components of the devices, we measure the transmission efficiency of the periodic GC devices as a function of waveguide length, shown in Fig. 8.8. We choose four wavelengths, covering the operational bandwidth of the devices, and quantify the loss contributions from the individual components, presented in Table 8.1.

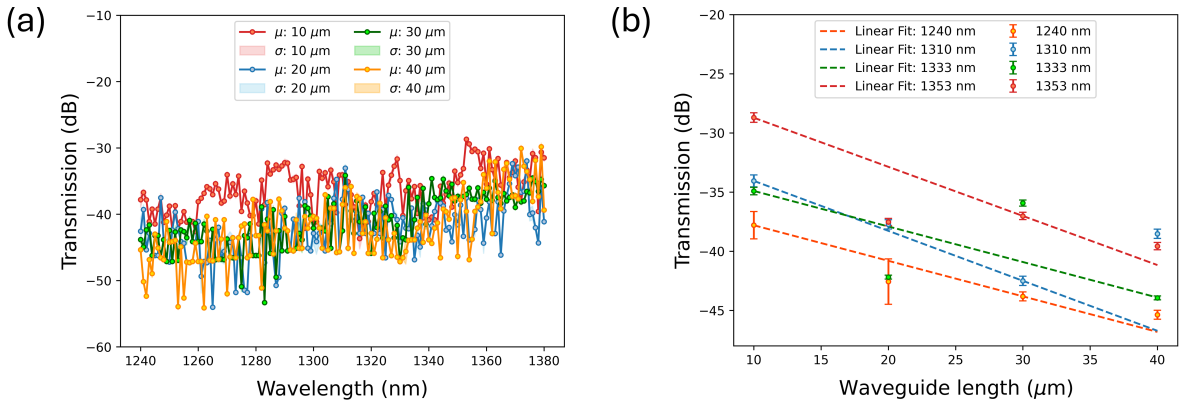

Figure 8.8. (a) The spectral profile of transmission efficiency through a pair of periodic GCs connected by a waveguide with varying length. (b) Transmission efficiency as a function of the waveguide length for a set of wavelengths indicating waveguide loss in the range [0.3, 0.4] dB/μm. Error bars indicate the uncertainty in dB.

Table 8.1. Efficiency of individual components for the four nominal wavelengths

Wavelength (nm)	Waveguide (dB/μm)	Periodic GCs (dB)	Incoupling[a] (simulation) (dB)	Outcoupling[a] (simulation) (dB)	Incoupling[b] (dB)	Outcoupling[b] (dB)
1240	-0.30 ± 0.01	-34.8 ± 0.2	-8.64	-5.29	-21.58	-13.22
1310	-0.42 ± 0.01	-29.8 ± 0.1	-8.88	-5.45	-18.47	-11.35
1333	-0.30 ± 0.02	-31.9 ± 0.6	-9.27	-5.60	-19.88	-12.02
1353	-0.41 ± 0.02	-24.6 ± 0.3	-9.57	-5.70	-15.4	-9.16

[a] Incoupling and outcoupling efficiencies are considered only for the f-TE mode, as Fig. 8.7(c) shows very low coupling for the f-TM mode compared to the f-TE mode.

[b] Incoupling and outcoupling efficiencies are calculated by applying the method of proportionality between the measured and simulated efficiencies. Uncertainties are neglected as they are orders of magnitude lower than the mean values.

We observe substantial losses [0.3,0.4] dB/μm in the waveguides, contrary to both the simulation results and previous reports on fabricated triangular nanobeams in diamond [95, 192]. Although scattering losses may arise from the surface roughness induced by

the lift-off of the metal mask, the losses are too high even for an imperfect waveguide supporting only the fundamental mode(s) [195]. Such high losses are more consistent with the damage introduced during the ion-implantation process [196, 197]. Considering the implantation energy and fluence, we expect a high density of defects spanning most of the f-TE mode region of the triangular waveguide.

The high implantation energy (65 keV) and fluence (1×10^{14} cm^{-2}) result in a high concentration of vacancies (V_{Si}, VV) in the triangular waveguide, as seen in Figure 8.9(a). Despite annealing for an hour at 1050°C, the 4H-SiC lattice exhibits only partial recovery [99], which is reflected in the transmission measurements. Annealing in a nitrogen atmosphere suppresses the diffusion of the implanted N-ions, preserving the depth distribution predicted by the SRIM simulations. However, at 1050°C, the V_{Si} and VV defects diffuse towards the surface [107]. Based on this analysis, the estimated depth regions corresponding to both vacancy-type defects and NV centers are indicated in Figure 8.9(a).

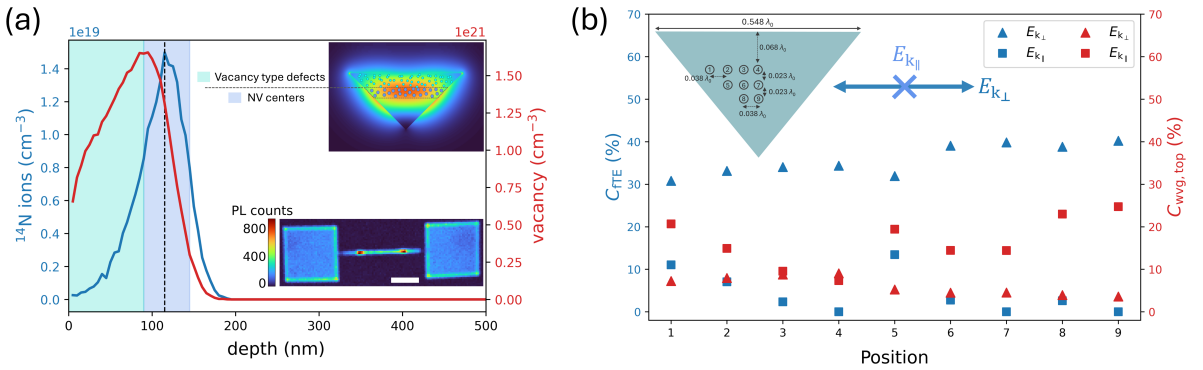

Figure 8.9. (a) Depth profile of implanted $^{14}N^{+}$ ion and induced vacancy concentrations in 4H-SiC, as simulated by stopping and range of ions in matter (SRIM). The top right inset illustrates the spatial overlap between the f-TE mode and regions containing vacancy-type defects and NV ensemble in the triangular waveguide. The bottom right inset shows the 2D Photoluminescence scan of the NV centers, scale bar indicates 10 μm. (b) Simulated coupling fraction into the f-TE mode in one direction (C_{fTE}) and collection efficiency through an objective with 0.85 NA from the top of a triangular waveguide ($C_{\mathrm{wvg,top}}$) as a function of emitter positions spanning the spatial range of NV ensemble marked in (a).

Such dense defects can result in high losses due to either Rayleigh scattering, optical absorption, or coupling to the radiation modes. However, due to the long operational wavelengths, Rayleigh scattering losses are expected to contribute minimally. On the

other hand, ion implantation is known to alter the real and the imaginary parts of the complex refractive index [198], while annealing above 1600°C is not able to fully recover the crystal damage in 4H-SiC introduced by nitrogen ion implantation conditions comparable to this study [199, 99]. Since ion implantation facilitates mode conversion into higher-order modes [200], we attribute the losses primarily to radiation, given that the designed waveguides support only the fundamental modes. Consequently, we speculate the incoupling (outcoupling) efficiencies, presented in Table 8.1, are overestimated (underestimated) as incoupling demands more stringent phase matching conditions to the guided modes compared to outcoupling [201], which can be the potential reason behind the overall inferior performance of the aperiodic GC devices compared to the periodic ones. Therefore, we proceed with cryogenic photoluminescence (PL) measurements for obtaining a more comprehensive insight.

8.3.3 Cryogenic Photoluminescence Spectroscopy Measurements

We employ the ICECAP 3-in-1 system [112] to conduct the PL characterization of the fabricated devices. All the measurements presented in Fig. 8.10 are performed below 1.6 K, using an above-band CW excitation (785 nm) for the NV centers in 4H-SiC. PL is collected through a higher NA (0.85) objective and a 1150 nm long-pass filter, and subsequently measured using either a superconducting nanowire single-photon detector (SNSPD) or a spectrometer. Fig. 8.10(a) shows the 2D and 1D PL scans of the fabricated devices where the excitation beam is fixed at the center of the triangular waveguide and a 1-second integration time per point. In the 2D scans, the central red spot corresponds to PL collected directly from the top of the waveguide, whereas the two peripheral bright spots indicate PL extraction via the GCs. The aperiodic GCs yield tighter collection spots relative to the periodic ones, matching the expected far field angular distribution from the simulations.

Although the GCs connected by the triangular waveguide are symmetric, the 1D PL scans exhibit a slightly asymmetric collection profile. The consistent observation of this phenomenon across both the periodic and aperiodic designs suggests it originates from the sample tilt, likely due to an uneven adhesive application during the cryogenic mounting.

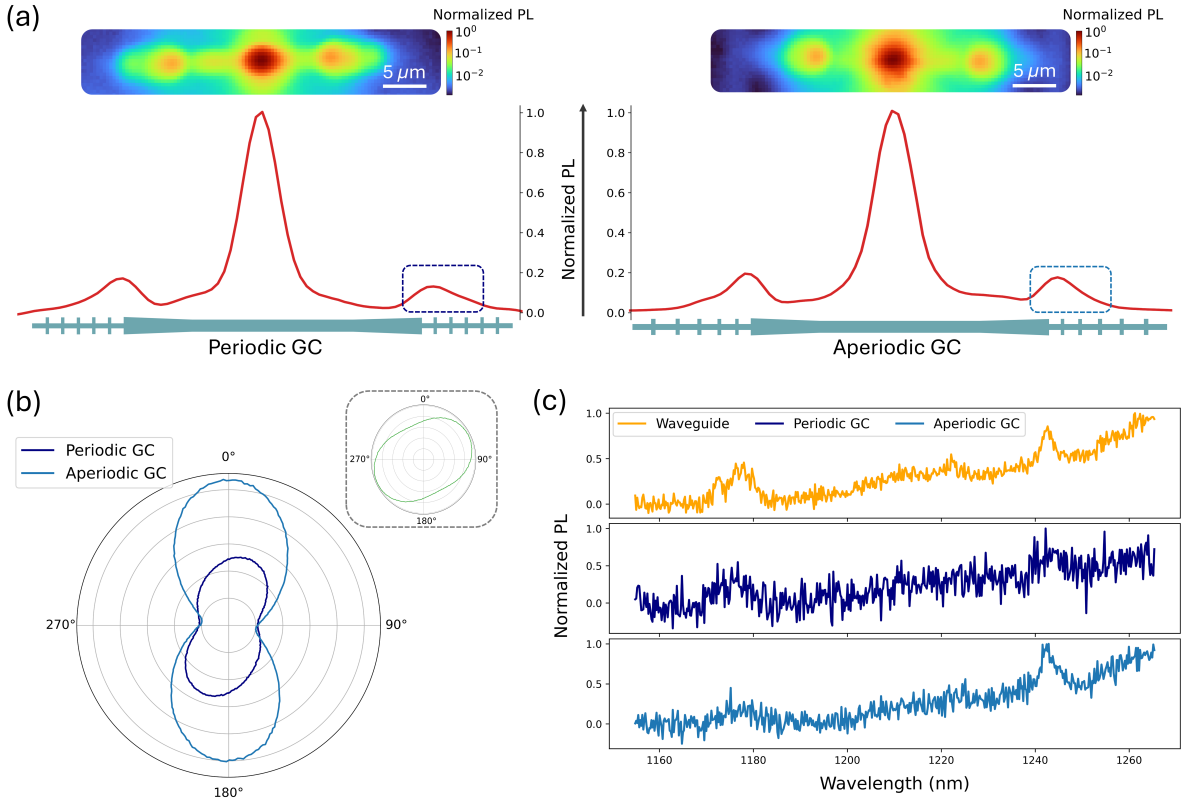

Figure 8.10. (a) The 2D and 1D scans of normalized photoluminescence (PL) from SiC triangular waveguides terminated by periodic and aperiodic GCs, respectively, with the excitation beam fixed at the center of a 10 μm waveguide exciting an ensemble of NV centers. The dashed boxes in the 1D PL plots highlight the regions corresponding to the results presented in (b) and (c). (b) PL counts from periodic and aperiodic GCs collected through an analyzer, 0° corresponding to the polarization orthogonal to the waveguide propagation direction. The inset shows PL counts from the NV centers in bulk 4H-SiC, the elliptical shape originating from the non-uniform polarization mixing in the SMF coil of the excitation beam. (c) Normalized PL spectra collected from the center of the waveguide (where NV centers are excited), periodic GC, and aperiodic GC, respectively.

Assuming the following conditions: (i) PL (dipole) emission couples equally into the parallel and perpendicular directions w.r.t. the waveguide propagation, and (ii) a 1:1 ratio of axial to basal defects in the NV ensemble, we quantify the collection efficiencies of the GCs based on the FDTD simulations and experimental results.

8.3.4 Collection Efficiency Calculation

We perform Lumerical FDTD simulations to estimate the photoluminescence (PL) emission coupling to one side of the fundamental mode waveguide (C_{fTE}), as well as the collection from the waveguide top through a 0.85 NA objective ($C_{\mathrm{wvg,top}}$), under the same conditions as our cryogenic confocal microscopy setup. The dipole moment of axial defects lies in the device plane, while that of basal defects is oriented in a plane tilted by 19° from the c-axis [112]. To emulate the spatial distribution of NV centers in the triangular waveguide, electrical dipoles are configured parallel ($k_{\parallel}$) and perpendicular ($k_{\perp}$) to the waveguide propagation direction (k) at nine different positions, delineated in Figure 8.9(b). In the following calculations, we consider a 1:1 ratio of axial to basal defects in the NV ensemble and dipole emission coupling equally into $k_{\parallel}$ and $k_{\perp}$. From the simulations, we obtain the average values of $C_{\mathrm{wvg,top}}$ and C_{fTE} to be 11.29% and 20.08%, respectively. Due to the dipole moment orientation, the average C_{fTE} for axial defects remains the same; however, for the basal defects, it reduces to $\cos(71°) \cdot C_{\mathrm{fTE}} = 6.55\%$. Assuming a 1:1 ratio for axial and basal, the overall C_{fTE} value becomes 13.32%.

From the 1D PL scans, we obtain the normalized PL intensity from the top of a 10 μm long triangular waveguide (where the NV centers are excited) and the periodic and aperiodic GCs. As the NV center emission spectrum is close to 1240 nm, for the efficiency calculations, we utilize the waveguide loss of 0.3 dB/μm at 1240 nm, as presented in Table 8.1. As we excite the center of the waveguide, the PL emission travels 5 μm before reaching the GC. Hence, the total propagation loss amounts to 1.5 dB, corresponding to a transmission efficiency of 70.8%.

Considering the calculated average 13.32% coupling of NV ensemble emission to the f-TE mode of the waveguide and the waveguide transmission efficiency of 70.8%, the accumulated system efficiency reduces to 9.4%. In both periodic and aperiodic configurations,

the normalized maximum PL (1 a.u.) is collected from the top surface at the waveguide center. Considering the $C_{\text{wvg,top}}$ value to be 11.29%, the actual normalized PL emission in the waveguide becomes 8.857 a.u., and multiplying the value by the system efficiency of 9.4%, we obtain the normalized PL emission of 0.8326 a.u. reaching the GC end. As we observe a slightly asymmetric collection profile from the two GC ends, we report both values for periodic and aperiodic designs in the following table.

Table 8.2. Grating coupler efficiency

GC	**Position**	**Norm. PL before GC (a.u.)**	**Norm. PL after GC (a.u.)**	**Collection efficiency (%)**
Periodic	Right	0.8326	0.15	18
Periodic	Left	0.8326	0.19	23
Aperiodic	Right	0.8326	0.175	21
Aperiodic	Left	0.8326	0.20	24

We achieve a maximum collection efficiency of 24% (23%) for the aperiodic (periodic) design from the 1D PL scans. The aperiodic design demonstrates 1-3% higher efficiency than the periodic, aligning well with the simulated predictions. The polarization characteristics of the collected PL from the periodic and aperiodic GCs, shown in Fig. 8.10(b), reveal similar f-TM outcoupling for both but a higher f-TE outcoupling for the aperiodic design, as expected from the simulations. Enhanced performance of the aperiodic design is evident from the PL spectra, illustrated in Fig. 8.10(c). Although all the devices are optimized for $\lambda_0 = 1310$ nm, the PL spectra reflect the inherent broadband nature of this approach.

8.4 Outlook

In this work, we have expanded the utility of the wafer-scale angle-etching fabrication process to integrate efficient grating couplers with triangular cross-section color center photonics. The process preserves color center optical properties, enabling the implementation of on-chip QIP with integrated quantum photonic mesh architecture. With the addition of the proposed GCs on the same chip, wafer-level testing can be executed on the fabricated devices. Our presented results show that the triangular cross-section fishbone grating design can yield broadband high collection efficiency (theoretical: $\sim 31\%$,

experimental: 24%) for studying the color center coupling with the integrated nanophotonic devices. The uniformity in device performance, along with the consistency with the FDTD simulations, underscores the reliability and reproducibility of the optimized designs using the RIBE process. However, integrating NV centers into SiC triangular photonic devices without compromising the crystal quality remains a nontrivial challenge. Strategies such as hot ion implantation [202], specialized thermal annealing protocol [203], and the use of implantation masks [204] offer promising pathways for minimizing lattice damage and enhancing the emitter performance. In summary, the demonstrated grating couplers can be integrated with mesh photonics, cavity QED systems, and any other process where free-space modes are coupled to quantum photonic devices.

Chapter 9

Systematic Analysis of Nanofabrication Processes and Parameter Optimization

Expanding on the process baselines and tool configurations established in Chapter 3, this chapter presents a systematic analysis of nanofabrication process engineering and parameter optimization to bridge theoretical plasma physics with empirical device fabrication. In this chapter, we begin with a comparative analysis of the ICP-RIE recipes employed in the Oxford and PlasmaTherm tools, detailing how fundamental differences in chamber geometry and radical generation efficiency necessitate tailored gas flows and operational parameters for each tool. Later, we investigate the physical mechanics governing the IBE process, tracing the operational cascade from plasma discharge and sheath formation to grid-level perveance dynamics. This study establishes a predictive framework for process control and signifies the importance of parameter optimization for obtaining minimal angular mismatch with expected results.

9.1 Comparative Analysis of ICP-RIE Processes

To achieve reproducible nanoscale features, the process transferability across different platforms must account for tool-specific physical configurations and plasma dynamics. Sidewall anisotropy and mask integrity become top priorities as the patterned substrates undergo the subsequent RIBE process. Although both the Oxford PlasmaLab and PlasmaTherm systems rely on ICP sources, key structural differences alter radical generation, plasma density, and dissociation efficiencies. The baseline ICP-RIE recipe established in the Oxford tool (at the Molecular Foundry) operates at an ICP power of 1000 W, an RF bias power of 230-270 W (generating a DC bias of $\sim$ 300 V), a chamber pressure of 4-5 mTorr, a stage temperature of 20°C, and an SF_6/O_2 gas mixture of 40/10 sccm. The

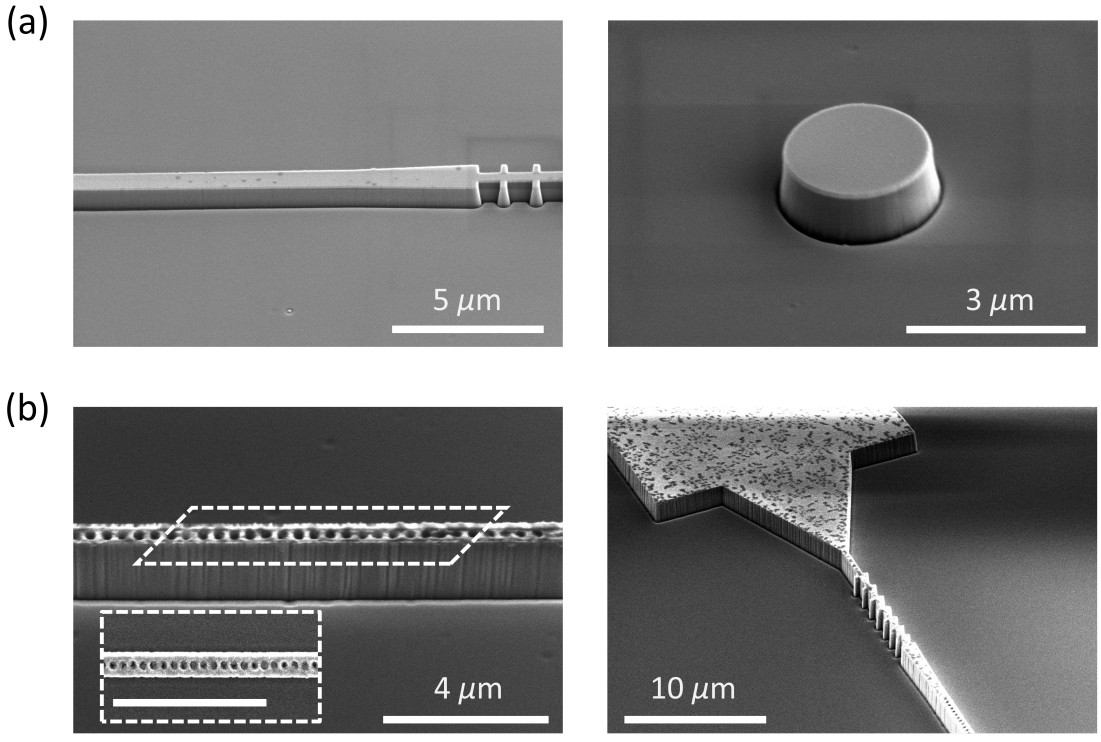

Figure 9.1. SEM images (52° tilt) of fabricated nanostructures (Ni mask on top) after vertical etching with ICP power = 1000 W, RF bias power = 260 W, pressure = 5 mTorr, temperature = 20°C, SF_6:O_2 = 40:10 sccm using (a) Oxford PlasmaLab 150 and (b) PlasmaTherm Apex SLR ICP/RIE tools, respectively. Inset scale bar indicates 5 μm

elevated ICP power compensates for the lower relative power-coupling efficiency of the tool [205], while the automated throttle valve remains fully open for maximizing the effective pumping speed to stabilize the low-pressure discharge [206]. Moreover, the high DC bias facilitates physical surface activation of the SiC substrate and promotes the sputter-assisted removal of non-volatile byproducts from mask material. Fabricated devices using this recipe are presented in Figure 9.1a.

When we implement the same recipe in the PlasmaTherm Apex SLR ICP/RIE tool at CNM2, we obtain a very low DC bias of ~ 41.5 V. Figure 9.1b shows the SEM images of the etched 4H-SiC structures fabricated using the PlasmaTherm tool. From visual inspection and resultant DC bias, we anticipate the two interconnected physical mechanisms behind the discrepancies in etched sidewall and mask quality. Firstly, owing to PlasmaTherm's relatively smaller chamber volume and superior power-coupling efficiency, the 1000 W ICP power generates a substantially higher plasma density (n_i). This elevated ion density compresses the sheath thickness $s \propto n_i^{-1/2}$. Thereby, the sheath capacitance increases $C_s \propto 1/s$ and lowers the overall sheath impedance $Z_s = 1/\omega C_s$. At a constant RF bias power, this reduced sheath impedance diminishes the RF voltage across the plasma boundary, resulting in a suppressed DC bias. Secondly, the dominance of reactive chemical radicals over physical sputtering (low DC bias) leads to severe oxidation and structural deformation of the mask, owing to NiO_x formation. Consequently, vertical anisotropy becomes heavily reliant on chemical sidewall passivation with SiO_xF_y rather than directional ion bombardment.

To increase the DC bias, the natural idea is to reduce the plasma density, increasing the sheath thickness, and use the highest permissible RF bias power (300 W). Operating at an elevated pressure of 7 mTorr with a brief 500 W ICP power at the ignition step, we evaluate the following three ICP power and RF bias power combinations: (i) ICP = 300 W, RF bias = 280 W, resultant DC bias = 85 V; (ii) ICP = 280 W, RF bias = 300 W, resultant DC bias = 90 V; and (iii) ICP = 200 W, RF bias = 300 W, resultant DC bias = 103 V. We use 2-4 times larger structure patterns, compared to simulated waveguide widths, for conducting these tests. Although increasing the DC bias gradually reduces

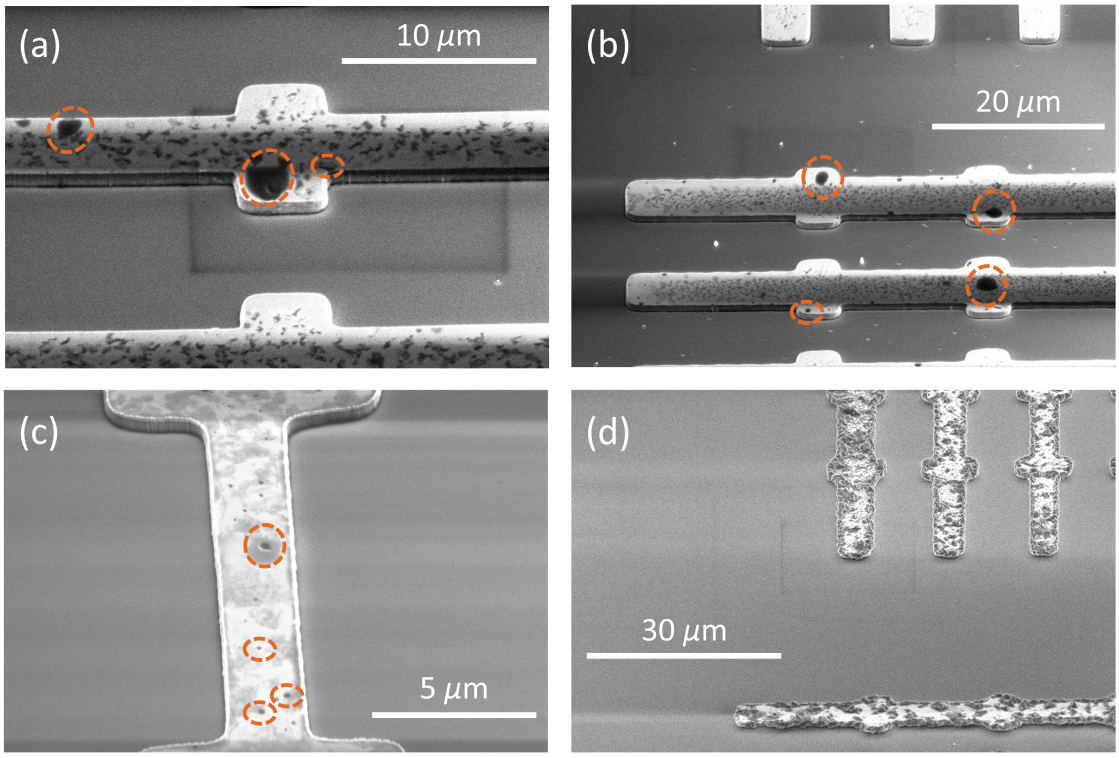

Figure 9.2. SEM images (45° tilt) of fabricated test structures (Ni mask on top) after vertical etching with (a) ICP power = 300 W, RF bias power = 280 W; (b) ICP power = 280 W, RF bias power = 300 W; and (c) ICP power = 200 W, RF bias power = 300 W. The orange dashed circles indicate the pinholes and microcracks on the Ni mask. (d) SEM image (52° tilt) of the test structures from (c) after subsequent angle-etching.

mask degradation, oxidation of the Ni mask remains dominant over physical sputtering. This reaction produces localized defects in the brittle NiO_x layer, leading to random pinholes and microcracks [207, 208], as shown in Figure 9.2a-c. Figure 9.2d reflects the degraded mask condition after the subsequent RIBE process, where we observe little to no angle-etching.

In our subsequent attempts, we completely replace O_2 with argon (Ar) to eliminate mask oxidation. The addition of Ar enhances physical ion sputtering, promotes directional etch rate, and assists in removing the byproduct CF_x polymer. Flow rates of Ar are systematically evaluated in the 8-10 sccm range. Figure 9.3b-d display the resulting structures achieved with the optimized recipe: ICP power = 450 W, RF bias power = 100

W (resultant DC bias $\sim$ 41 V), pressure = 5 mTorr, temperature = 20°C, SF_6:Ar = 40:10 sccm. This recipe yields an anisotropic etch rate of 206 nm/min and a substantial SiC to Ni selectivity of 48:1. In conclusion, process transferability between distinct reactor architectures for Ni hard mask based 4H-SiC substrates requires tailored chemical choices based on tool geometry and plasma coupling efficiency.

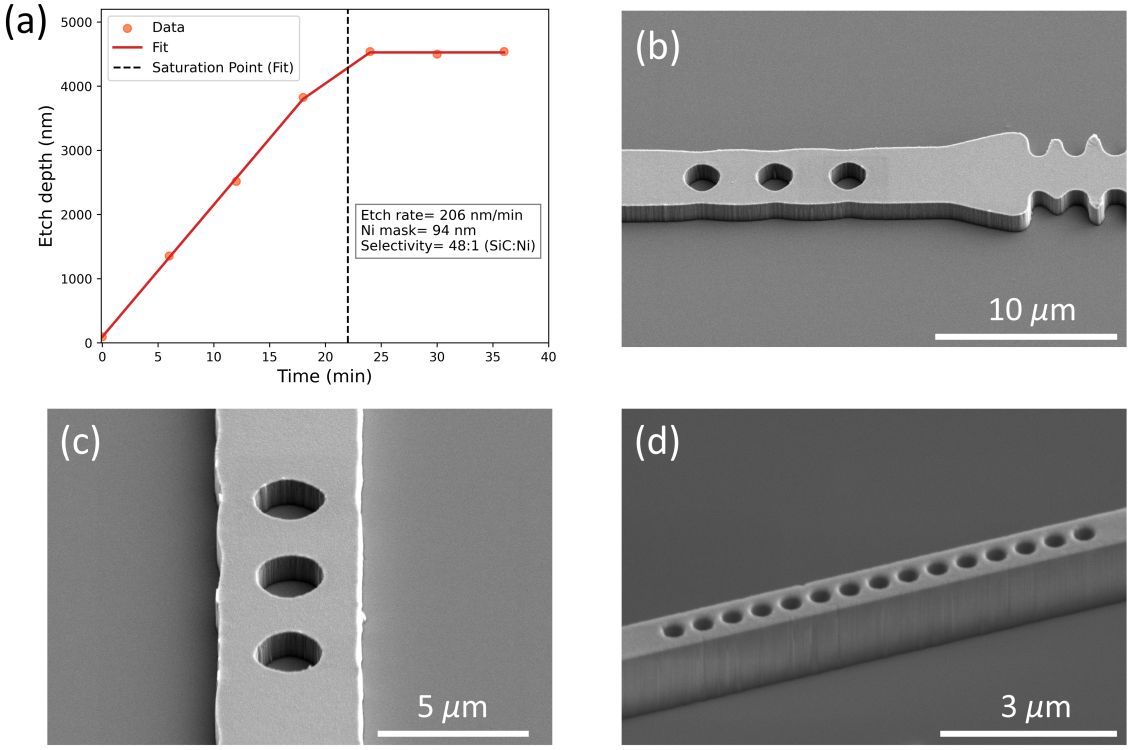

Figure 9.3. (a) 4H-SiC etch depth as a function of time; the saturation point indicates the time when the 94 nm Ni mask layer is completely consumed. SEM images (52° tilt) of fabricated (b)-(c) test structures and (d) photonic crystal pattern after vertical etching with the optimized SF_6/Ar recipe. All the images are taken with the Ni hard mask on top.

9.2 Beam Extraction Physics and Etch Angle Optimization in RIBE

In our previous work in Chapter 7, we observed an appreciable (15°) angular mismatch between the substrate tilt angle and the resultant etched sidewall slope. For a considerable time, researchers frequently attributed such angular mismatches during angled RIBE to mask material erosion, redeposition, or secondary fabrication processes [209, 210, 182], rather than evaluating them as a core electro-physical transport problem. In this section,

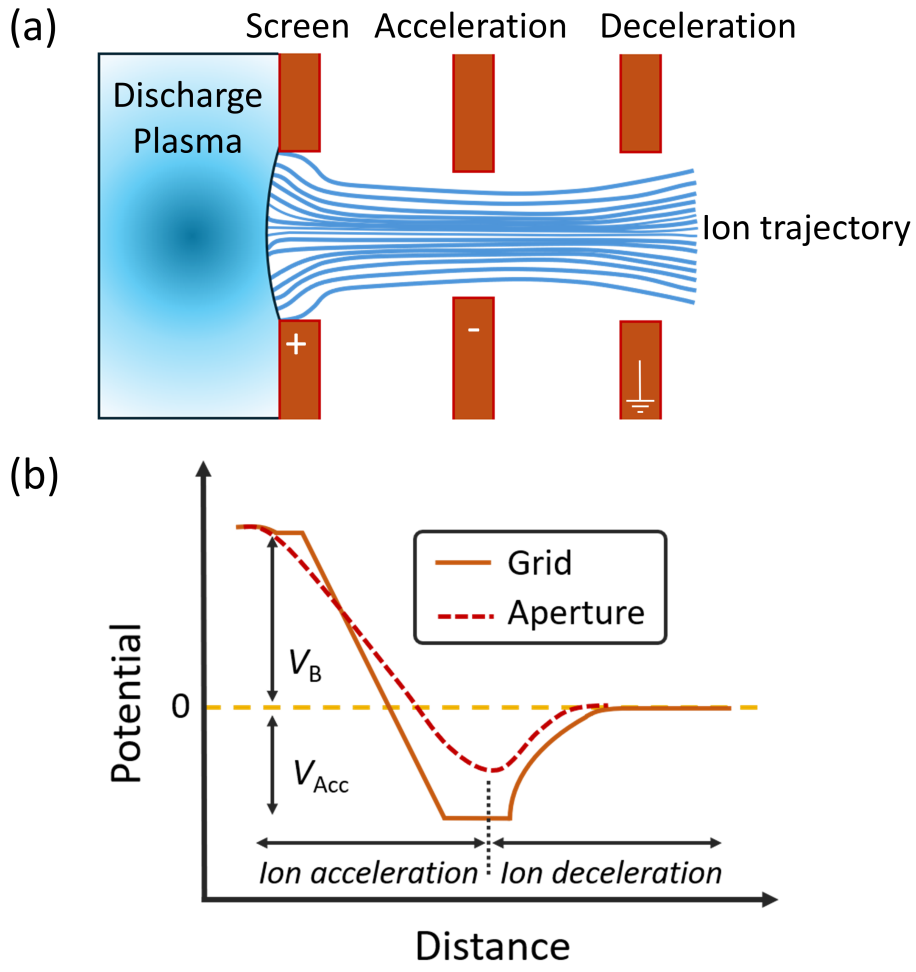

Figure 9.4. (a) Schematic representation of ion trajectories from a plasma sheath in a beamlet (through aperture) inside a three-grid accelerator. (b) Corresponding potential variation through the grids and apertures, where V_B is beam voltage and V_{Acc} is acceleration voltage.

we systematically investigate the system to demonstrate that beam collimation and angular fidelity are fundamentally governed by the spatial electrostatic potential distribution maintained across the tool's perforated grid optics. As the bulk plasma, extraction grids, and downstream drift region operate at distinct electrical potentials, this axial potential landscape dictates every phase of ion transport, from initial sheath formation and meniscus curvature to beamlet focusing and space-charge expansion. Figure 9.4 illustrates the characteristic electrostatic potential profile along the central axis of the tool, where V_{B} is beam voltage, V_{Acc} is acceleration voltage, and $V_{\mathrm{min}} < 0$ to prevent electron backstreaming. Accordingly, the complete IBE architecture introduced in Chapter 3 is partitioned into distinct subsystems governing the ion beam optics.

9.2.1 Discharge Chamber and Screen Grid: Sheath Formation and Meniscus Physics

To accurately model ion extraction optics in RIBE, the ICP discharge chamber and the screen grid can be treated as a single electrostatically coupled subsystem. The bulk discharge plasma floats relative to ground and is pinned directly to the positive high beam voltage (V_{B}) applied to the screen grid. The screen grid does not actively pull ions out of the discharge (ICP) chamber, but it establishes the positive potential baseline of the plasma source and forms the physical boundary layer from which ions are extracted. The formation of this boundary layer is governed by fundamental sheath dynamics. In the discharge chamber, the plasma is at a slightly higher potential than the screen grid. Upon discharge ignition, electrons possess a significantly higher thermal velocity than heavy ions due to a higher mobility. The fast-moving electrons rapidly stream toward the screen grid surface and are neutralized (initially) or repelled (after sheath formation), leaving behind a positive ion-rich space-charge region adjacent to the grid apertures, which forms the plasma sheath. As the plasma is at a higher potential, the resulting electric field within the sheath points toward the screen grid. Therefore, the sheath acts as an electrostatic barrier that repels bulk electrons back into the plasma core.

To maintain steady-state charge transport across the sheath, the electric field leaks slightly into the bulk plasma, creating an extended transition region known as the pre-

sheath. The pre-sheath develops an internal potential drop approximately equal to half the electron temperature:

$$\Delta V_{\text{pre}} \approx \frac{k_B T_e}{2q}$$

This potential drop accelerates positive ions from random thermal motion up to the Bohm velocity (v_B) [211], establishing the sonic speed requirement for stable sheath formation:

$$v_i \geq v_B = \sqrt{\frac{k_B T_e}{M_i}}$$

where v_i is the ion velocity, k_B is the Boltzmann constant, T_e is the electron temperature, q is the elementary charge, and M_i is the ion mass.

Once ions enter the sheath at Bohm velocity, they reach the screen grid aperture. The boundary interface between the bulk and the sheath across each aperture sags under the influence of the downstream external extraction field, forming a curved equipotential surface termed the plasma meniscus. The curvature of this meniscus acts as the primary electrostatic lens in the ion optics assembly. Depending on plasma density and grid bias, the meniscus can form a concave, flat, or convex profile. The meniscus profile establishes the initial emission angle and the laminar trajectory of the extracted beamlets (through grid apertures) before they enter the acceleration gap. Therefore, process control within this subsystem is governed by two primary independent process variables:

Ion beam current (I_{B}): Although RF power regulates the electron impact ionization rate and bulk plasma density, a closed-loop feedback control adjusts the RF power dynamically to deliver and stabilize the targeted I_{B} in the Intlvac Nanoquest II tool. Hence, I_{B} is the primary input parameter for ion current density control.

Beam voltage (V_{B}): V_{B} biases the screen grid to a positive potential, which elevates the plasma potential and sets the final kinetic energy ($E_k \approx qV_{\text{B}}$) of the directional ions that etch the target substrate.

9.2.2 Acceleration Grid: *R* Parameter and Perveance Mechanics

The acceleration grid is immediately downstream of the screen grid and is biased to a negative voltage ($-V_{\mathrm{Acc}}$). This creates a strong electrostatic extraction field across the inter-grid gap. The total effective extraction voltage (historically termed total accelerating voltage [212]) V_{T} across the screen-acceleration boundary is given by:

$$V_{\mathrm{T}} = V_{\mathrm{B}} + |V_{\mathrm{Acc}}|$$

This large potential gradient penetrates through the screen grid apertures, draws positive ions out of the plasma meniscus, and accelerates them into discrete beamlets. The spatial voltage step between V_{B} and $-V_{\mathrm{Acc}}$ bends the equipotential field lines inside the aperture, forming an electrostatic lens at the plasma sheath. The focal length of this lens and consequently the initial collimation of the beamlet is determined by the voltage ratio R (historically termed net-to-total accelerating voltage ratio [212]):

$$R = \frac{V_{\mathrm{B}}}{V_{\mathrm{B}} + |V_{\mathrm{Acc}}|} = \frac{V_{\mathrm{B}}}{V_{\mathrm{T}}}$$

The R-parameter sets the initial angular bending of ion trajectories. However, the net collimation remains strictly constrained by space-charge limitations within the acceleration gap, as described by the Child-Langmuir Law [213]. In a space-charge-limited extraction gap, the maximum ion current density (J) that can be transported across an effective gap distance (l) is governed by the Child-Langmuir equation:

$$J = \frac{4\epsilon_0}{9}\sqrt{\frac{2q}{M_i}}\frac{{V_{\mathrm{T}}}^{3/2}}{l^2}$$

From this equation, we obtain the ion beam current per hole (J_{B}) [212]:

$$J_{\mathrm{B}} = {V_{\mathrm{T}}}^{3/2}\frac{\pi\epsilon_0}{9}\sqrt{\frac{2q}{M_i}}\left(\frac{d_s}{l_e}\right)^2$$

where

$$l_e = [{l_g}^2 + \left({d_s}^2/4\right)]^{1/2}$$

In the above equations, ϵ_0 is the vacuum permittivity, d_s is the screen hole diameter, l_e is the effective acceleration length, l_g is the grid separation distance, and the area of ion

emission through the aperture is assumed to be $\pi {d_s}^2/4$. Consequently, we obtain the normalized perveance per hole (P_{norm}) to characterize the variations in beam extraction efficiency [214]:

$$P_{norm} = \frac{I_{\mathrm{B}}}{N_a {V_{\mathrm{T}}}^{3/2}} \left(\frac{l_e}{d_s}\right)^2$$

Here, N_a is the number of apertures in each grid. P_{norm} is a geometric and physical figure of merit that represents the extraction capability of the grid optics for a given applied voltage. The combination of R and P_{norm} is the primary factor that controls the ion beam divergence angle. Historically, in two-grid accelerator Ar propellant systems,

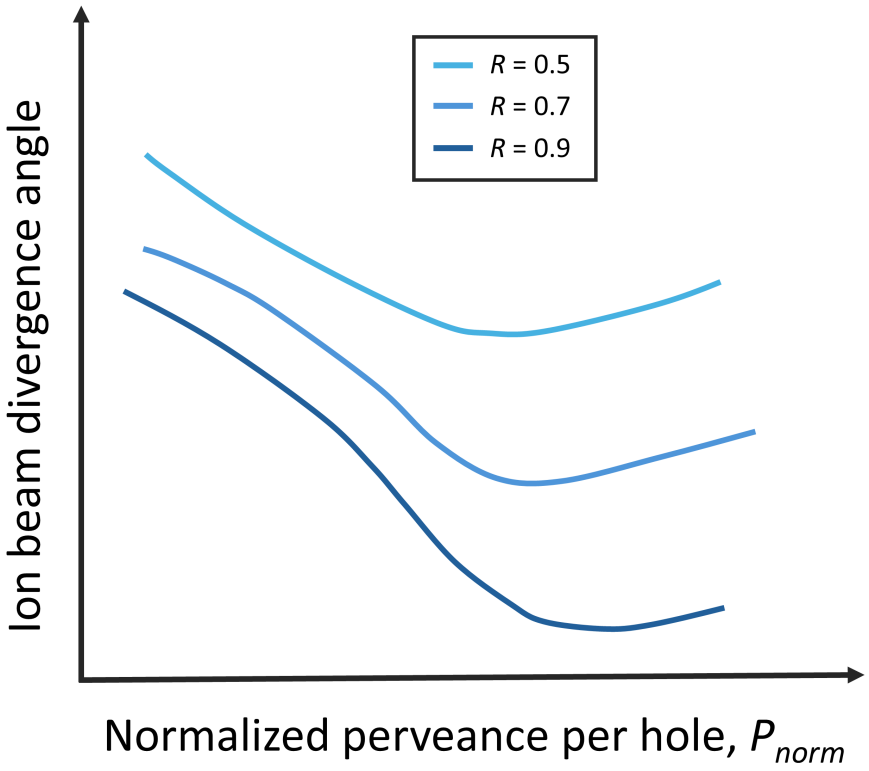

Figure 9.5. Effect of R on ion beam divergence for dual-grid Ar ion thrusters with a large grid separation ratio, $l_g/d_s = 1.00$. The characteristic plots are adapted from *Aston et al.* (1978) [212].

the ion beam divergence angle traces a characteristic U-curve with P_{norm} variation for a fixed R value [212]. Concurrently, ion beam divergence decreases with increasing R value. Figure 9.5 presents the characteristic ion beam divergence curves for two-grid accelerator systems. Although early works suggested keeping the R value between 0.7

and 0.8 [215] to avoid electron backstreaming and reduce beam divergence, modern tools (with a downstream deceleration grid) can achieve stable operation with higher R values. In this work, we optimize the overall system perveance P by tuning the ion beam current (I_B):

$$P = \frac{I_B}{{V_T}^{3/2}}$$

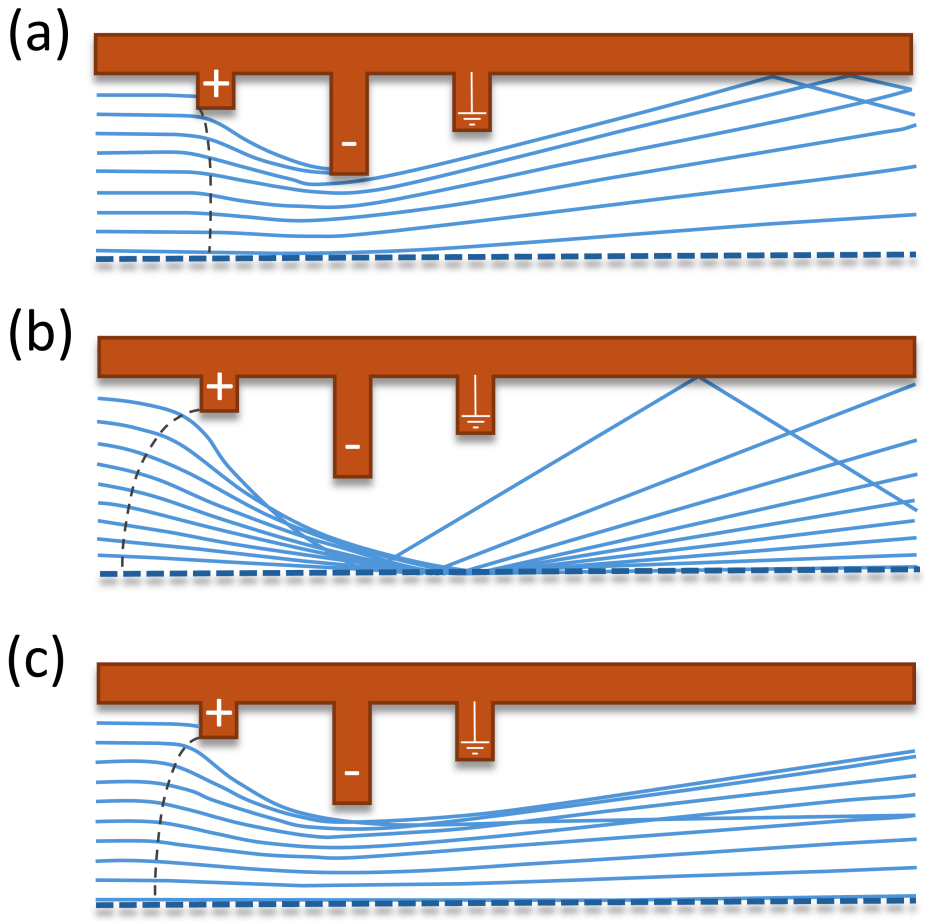

Figure 9.6. Representative ion trajectories in a half-beamlet for three perveance conditions: (a) over-perveance with direct acceleration grid interception, (b) under-perveance producing crossover interception, and (c) optimal perveance. The schematic diagrams are adapted from 2D charge-exchange (CEX) mechanism calculations in an ion thruster textbook [216].

For a fixed grid geometry and R value, the characteristic ion beam divergence angle vs P_{norm} curve defines three distinct beam optics regimes, as illustrated in Figure 9.6:

Over-Perveance occurs when I_B is too high for a given V_T or V_T is insufficient to extract the generated ion flux. High space-charge density pushes the sheath boundary downstream, causing the plasma meniscus to bow convexly out of the screen grid aperture [217]. The resulting electrostatic lens under-focuses the ions and produces divergent beamlets that strike the upstream face of the acceleration grid. This regime leads to high acceleration grid current (I_{Acc}) and severe grid degradation.

Under-Perveance occurs when V_T is much higher relative to I_B i.e., generated plasma density. In this regime, the strong extraction field penetrates deep through the screen grid aperture and forms a strongly concave meniscus bowing upstream. The resulting electrostatic lens over-focuses the incoming ions, causing the beamlet trajectories to cross over within the inter-grid gap. Beyond the crossover point, the expanding beamlet diverges and intercepts the downstream boundaries of the accelerator and decelerator grids.

Optimal Perveance represents the exact space-charge matching condition. The electrostatic forces and space-charge repulsion balance to produce a slightly concave meniscus. Ions enter the acceleration gap along parallel laminar trajectories, which minimizes the beamlet divergence angle and maximizes target directionality.

9.2.3 Deceleration Grid and Space-Charge Neutralization

The deceleration grid forms the final stage of the three-grid assembly and is maintained at system ground. By establishing a grounded equipotential plane, it terminates the strong acceleration field and allows the collimated beamlets to transition smoothly into the field-free process chamber without residual acceleration. The deceleration grid fulfills two critical functions: (i) it creates a potential barrier that prevents thermal electrons emitted by downstream neutralizers from being drawn upstream into the positive bias of the discharge chamber; and (ii) it physically shields the downstream face of the acceleration grid from re-deposited etch products and back-sputtered target material.

Immediately downstream of the deceleration grid, a low-frequency neutralizer (termed LFN) ion source injects low-energy thermal electrons directly into the ion beam drift space. Without electron neutralization, mutual electrostatic repulsion among positive ions (I_B) would cause rapid space-charge beam divergence, though the effect is not as substantial as

setting the R value. Moreover, when etching insulating or semi-insulating substrates such as 4H-SiC, unneutralized positive ion impact creates severe surface charge accumulation. This positive surface potential repels incoming ions, causing beam deflection and trench profile distortion. The effect is observed as a bowed sidewall, rather than a sharp slope in the etched devices. For stable operations, neutralizer electron supply should be kept at least 8-20% higher than the beam current I_{B}.

9.2.4 Experimental Results: Angle-Etch Fidelity and Benchmark Comparison

In this work, we focus on optimizing the device etch angle offset compared to substrate stage tilt by tuning the system perveance P for a fixed voltage ratio R. In the beginning, we prepare the test patterned pristine 4H-SiC samples with 6 minutes of anisotropic vertical etching, which yields a depth of ~ 1.2 μm. For RIBE, we utilize a nominal 300 V beam voltage (V_{B}) and 50 V acceleration voltage (V_{Acc}), resulting in $R = 0.857$. We tune P by sweeping the beam current (I_{B}) from 80 mA to 140 mA. The upper limit of this range is chosen based on observed etch angles. Additionally, we update the warmup RF ICP power for each recipe starting from 120 W, though the final RF power during the process is feedback-controlled to maintain a stable I_{B}. We use three different total gas flow rates of SF_6, Ar, and O_2 mixture for different I_{B} range: (i) 22.5 sccm for $I_{\mathrm{B}} = 80$, 100, 110 mA; (ii) 27 sccm for $I_{\mathrm{B}} = 120$, 130 mA; and (iii) 31.5 sccm for $I_{\mathrm{B}} = 140$ mA, while keeping a constant ratio of $SF_6 : Ar : O_2 = 4 : 4 : 1$. The chamber pressure, stage temperature, and stage tilt are kept at 5×10^{-5} Torr, 20°C, and 60°, respectively, for all processes. At the fixed R value, increasing I_{B} and consequently P causes the offset angle mismatch between substrate stage tilt and etched device sidewall slope to initially decrease to a minimum before increasing beyond the optimal extraction point. Figure 9.7 illustrates the etch angle mismatch trajectory as the ion beam extraction optics transition sequentially from under-perveance, through optimal perveance, to over-perveance. Under these optimized perveance conditions, a steepest inner sidewall angle of $\sim 33°$ is achieved for the 4H-SiC RIBE process, corresponding to an angular offset of only $\sim 3°$ relative to the substrate stage tilt.

Table 9.1. Comparison of angular offsets between this work and reported values in literature

Reference	Substrate	Mask	Chemistry	V_B (V)	V_{Acc} (V)	V_T (V)	R	I_B (mA)	P (mA/V$^{3/2}$)	Offset
Zubrzycki et al. (1999) [218]	AlGaAs	Ni	Cl_2	400	50	450	0.889	50	0.005	12.5°
Chia et al. (2022) [209]	Diamond	HSQ-Nb	O_2	200	26	226	0.885	100	0.029	8°
		HSQ-alumina	O_2	150	22	172	0.872	80	0.035	13°
Majety et al. (2025) [182]	4H-SiC	Ni	SF_6,O_2,Ar	300	120	420	0.714	110	0.013	15°
This work	4H-SiC	Ni	SF_6,O_2,Ar	300	50	350	0.857	80	0.012	15.3° ± 0.3°
								100	0.015	14°
								110	0.017	6.03° ± 0.06°
								120	0.018	3.43° ± 0.35°
								130	0.02	14.7° ± 1.01°
								140	0.021	18.27° ± 0.3°

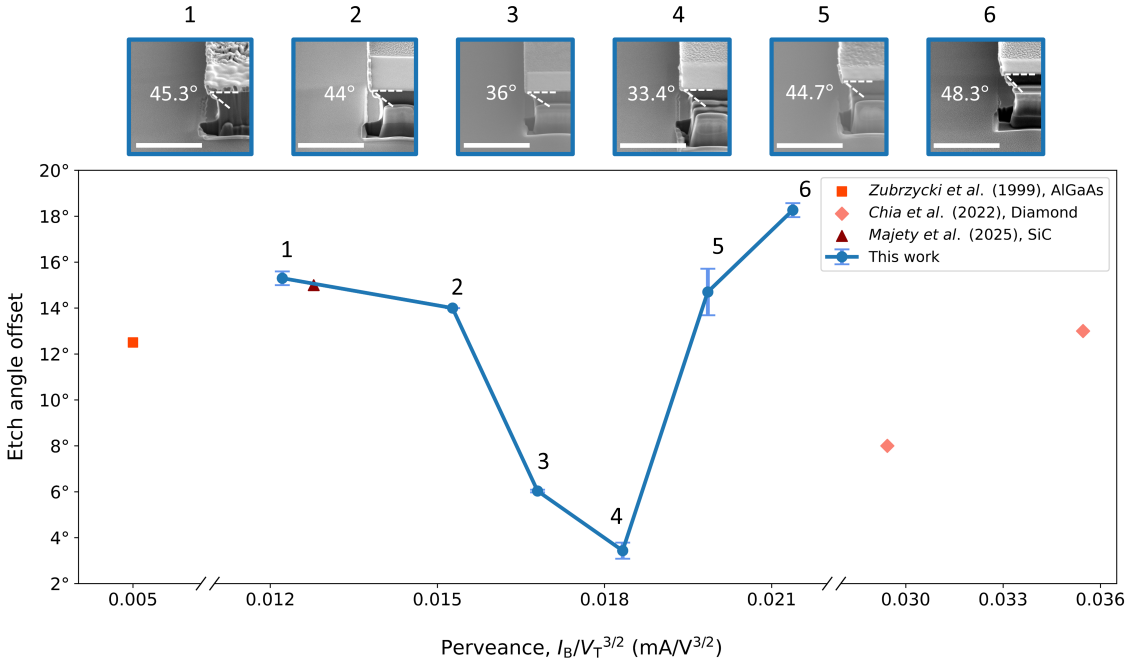

Figure 9.7. Etch angle offset as a function of system perveance $P = I_B/V_T^{3/2}$, tuned by adjusting the ion beam current I_B at a fixed total voltage V_T. Experimental data points represent mean values with standard deviation error bars from FIB cross-section measurements of 3 μm, 3.5 μm, and 4 μm wide stripes. Top SEM images (52° tilt) show the FIB cross-sections of 3.5 μm wide stripes with inner sidewall angle for each data point, and the scale bars indicate 4 μm. Literature data from *Zubrzycki et al.* (1999) [218], *Chia et al.* (2022) [209], and *Majety et al.* (2025) [182] for comparison across different material systems.

To our knowledge, this is the steepest device etch angle achieved with the RIBE process in bulk 4H-SiC. Notably, this angular mismatch is lower than reported values in existing literature for both diamond and 4H-SiC RIBE processes employing hard masks. A detailed comparative benchmark against prior studies is provided in Table 9.1. Although lateral mask erosion contributes substantially to angular mismatch, particularly in photoresist-based soft masks [219], this work demonstrates that precise control of ion beam perveance parameters is the primary mechanism governing sidewall angular mismatch.

9.2.5 Practical Tool Non-Idealities: Nanoquest II Analysis

While theoretical models assume rigid and clean metallic grid geometries, real-world operation introduces physical non-idealities that degrade beam collimation over time. Unlike modern three-grid architectures such as Oxford Instruments, Veeco, and NT GmbH that incorporate a grounded deceleration grid to shield the optics, the Intlvac Nanoquest II tool utilizes a traditional two-grid extraction assembly consisting of a screen grid and an acceleration grid. In fluorine-rich SF_6 based RIBE processes, this dual-grid configuration severely compromises grid operational lifetime. Without a downstream deceleration grid to act as a sacrificial physical barrier, the negative accelerator grid is directly exposed to back-sputtered target material, reactive neutral radicals, and unshielded space-charge forces. Although the ion beam physics and corresponding calculations remain the same for a dual-grid system, such an environment accelerates both chemical corrosion and physical erosion, drastically shortening grid longevity and requiring frequent maintenance during extended SF_6 and O_2 runs.

On the other hand, molybdenum is used as the primary material for the Nanoquest II grid system, a material highly susceptible to chemical etching by SF_6 plasma species. Therefore, the UC Davis CNM2 facility implements a protective aluminum coating that requires replenishment every three to six months, depending on the system usage. In reactive plasmas containing SF_6 and O_2, fluorine and oxygen radicals react with the exposed grid surfaces and form insulating thin films, such as aluminum fluorides (AlF_x) and aluminum oxides (Al_xO_y). Localized electrostatic charging on these insulating patches distorts local electric field lines across the apertures of both grids, altering the effective

focal length and collimation of individual beamlets.

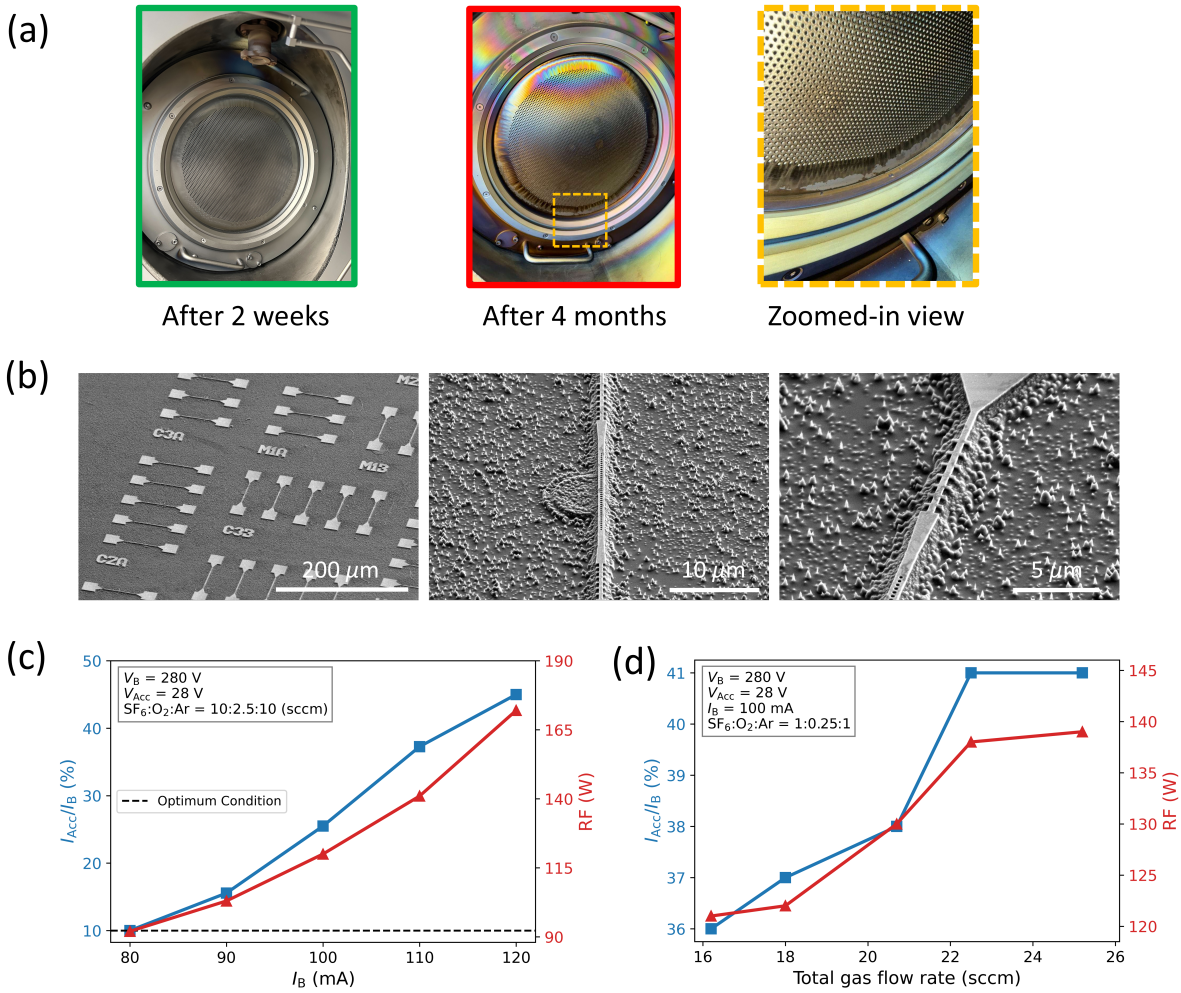

Figure 9.8. (a) Images of the accelerator grid back plane after 2 weeks and 4 months of usage. (b) SEM images (52° tilt) of nanophotonic patterns after grid coating degradation, exhibiting severe micromasking. Fraction of I_{Acc} as a function of (c) ion beam current I_{B}, where the fraction overshoots beyond the 10% optimal threshold due to direct ion impingement caused by grid degradation, and (d) total gas flow rates, where the fraction deviates from a linear increase, following the onset of micromasking presented in (b).

Early foundational studies on dual-grid accelerator assemblies primarily evaluated only inert gases such as Ar or Xe. Hence, the baseline ion current per hole from Child-Langmuir formulation assumes a monochromatic ion flux of single atomic mass (M_i). In RIBE with gas mixtures, the extracted beam consists of multi-component ion spectrum with distinct mass-to-charge ratios. As the ion beam current per hole scales inversely with the square

root of ion mass, multi-species extraction fundamentally modifies the system's effective space-charge limit.

Together with the charge-exchange (CEX) mechanism, i.e., momentum transfer between fast ions and slow neutral atoms, these non-idealities cause the accelerator grid interception current I_{Acc} to increase monotonically with ion beam current I_{B}, irrespective of the operating perveance regime. To prevent acceleration grid erosion and ensure discharge stability, I_{Acc} must be maintained within 5-10% of I_{B}. Consequently, for grid longevity, the recipe which consistently yields I_{Acc} within this limit needs to be employed, even at the expense of beamlet divergence, as minor angular divergence can be easily compensated by adjusting the substrate stage tilt to yield the targeted sidewall profile. Furthermore, the operational lifespan of the grid's protective coating can be monitored either visually (Figure 9.8a) or empirically via substrate morphology. As the protective layer degrades, back-sputtered grid material induces severe micromasking on etched features, as shown in Figure 9.8b. Subsequently, in Figure 9.8c-d, we evaluate I_{Acc} as a function of I_{B} and gas flow rates (in random order) following the onset of micromasking, which provides an empirical diagnostic framework to determine grid degradation timelines and schedule coating replenishment.

Chapter 10

Nanophotonic Manipulation of Color Center Emission

Color centers fundamentally exhibit an optical dipole-like radiation pattern and emit photons over a broad spatial angular distribution. In bulk materials, these emission characteristics limit photon extraction and collection efficiencies. To effectively route, direct, and extract a higher fraction of emitted photons, engineered nanophotonic structures are required. To this end, photonic crystal mirrors can be implemented to reflect and redirect emission toward on-chip collection optical components. On the other hand, photonic crystal cavities facilitate both spatial and spectral confinement, and leverage the Purcell effect to enhance the spontaneous emission rate directly into well-defined optical modes. In this chapter, we examine and design both geometric structures to control and enhance the optical emission of color centers.

10.1 Photonic Crystal Mirror

Our photonic crystal mirror design is based on the studies presented in Chapter 5. We optimize our designs for the fundamental TE (f-TE) mode of the waveguide with etch angle $\alpha = 45°$, as hole-based 1D photonic crystal structures typically favor the formation of TE band gaps. We investigate two photonic crystal designs to enhance color center emission collection: (i) $w = 1.36a$, $r = 0.349a$; and (ii) $w = 1.41a$, $r = 0.349a$, where w is the waveguide width, a is the lattice constant, and r is the hole radius. Band structure

analyses (Figure 10.1) from Plane Wave Expansion (PWE) simulations show that both designs yield gap sizes (gap-to-midgap ratio) of $\sim$ 19% and $\sim$ 20%, respectively. As we optimize for single-mode operation in our designs, we select a based on the waveguide width. Considering $w = 720$ nm, the crystal parameters for Design (i) are $\{a_1, r_1\} = \{530, 185\}$ nm and for Design (ii) are $\{a_2, r_2\} = \{511, 178.4\}$ nm. We employ FDTD simulations to calculate the broadband reflectivity of the photonic crystal mirror designs with 20 holes, though the peak reflectivity saturates at 15 holes. The reflectivity simulation results, illustrated in Figure 10.1, show that both designs are compatible with NV center ZPLs and PSB in 4H-SiC.

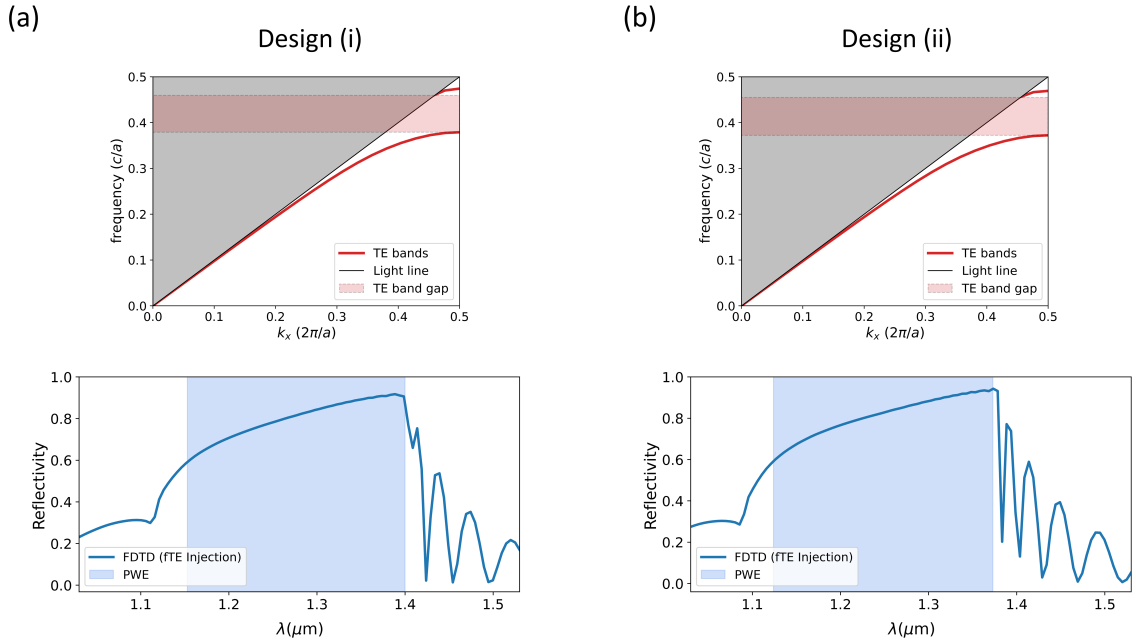

Figure 10.1. Band structure analyses from PWE simulations and corresponding FDTD reflectivity simulation results for (a) Design (i): $\{w, a_1, r_1\} = \{720, 530, 185\}$ nm with $\alpha = 45°$ and (b) Design (ii): $\{w, a_2, r_2\}$=$\{720, 511, 178.4\}$ nm with $\alpha = 45°$.

The asymmetric tilt in the reflectivity spectrum across the photonic bandgap is primarily governed by wavelength-dependent out-of-plane radiative scattering. As demonstrated by PWE band structure calculations, the short-wavelength (λ) regime of the bandgap, corresponding to the higher normalized frequency air band, resides deeply inside the light line ($k_x < \omega/c$) which overlaps with the free-space radiation continuum. At these shorter wavelengths near the air band edge (minimum), the E-field concentrates predominantly

within the etched air holes and outer boundaries. In a triangular cross-section waveguide, the broken vertical symmetry enhances out-of-plane coupling and results in substantial top and bottom scattering losses, as shown in Figure 10.2a, thereby reducing the effective guided reflection. Conversely, as λ increases toward the dielectric band edge, the mode approaches the guided regime below the light line, where the field intensity concentrates within the high-index core. This transition steadily suppresses out-of-plane radiation leakage, allowing the reflection to rise up to 94% for Design (ii). The continuous power conservation between the rising reflection and declining top/bottom scattering losses confirms that the asymmetric profile is a direct consequence of this radiative continuum transition across the light line. To visualize this behavior, side-view field intensity ($|E|^2$) profiles are evaluated at three representative wavelengths across the bandgap: the short-wavelength edge (1131 nm), mid-gap (1282 nm), and the long-wavelength edge (1368 nm), presented in Figure 10.2b.

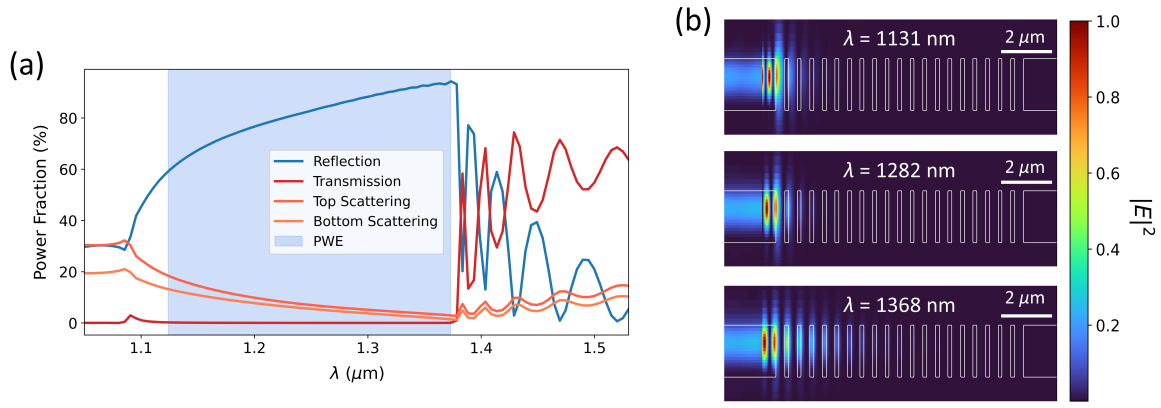

Figure 10.2. (a) Broadband power fraction results from fundamental TE mode injection in Design (ii). (b) Side view normalized E-field intensity ($|E|^2$) profiles of Design (ii) at $\lambda = 1131$ nm, 1282 nm, and 1368 nm, respectively.

During angle etching, ion beam divergence can deform the hole features into a teardrop profile with slanted sidewalls. To account for the etched inner walls, we simulate the reflectivity with a tilted inner wall angle (θ) in a realistic range of $0° \leq \theta \leq 22°$ for Design (ii), as shown in Figure 10.3a. We observe that as θ increases, the photonic bandgap narrows while the center wavelength progressively blueshifts. Finally, we fabricate the photonic

crystal mirrors with the developed ICP-RIE and RIBE processes, as demonstrated in Figure 10.3b-c.

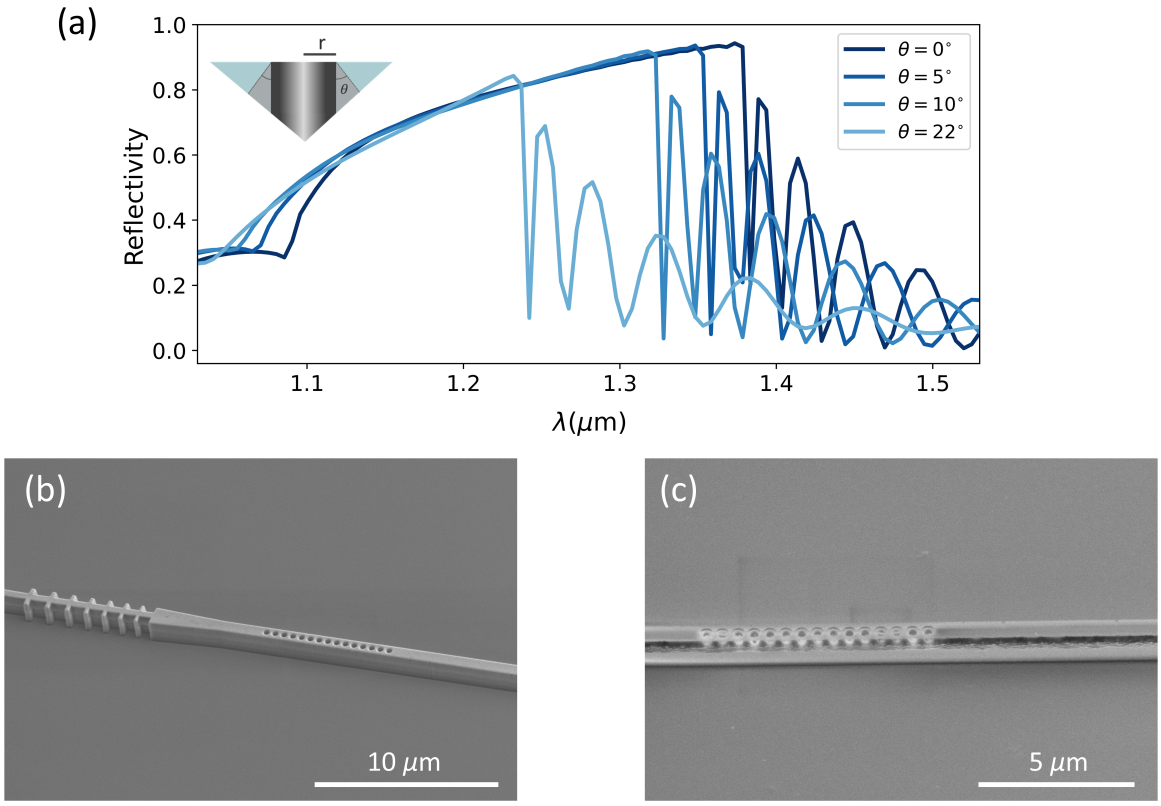

Figure 10.3. (a) Reflectivity variation of Design (ii) with inner wall angle $0° \leq \theta \leq 22°$. SEM (52° tilt) images of fabricated photonic crystal mirror (b) after vertical etching (with Ni mask on top) and (c) after angle-etching and subsequent post-etching processes.

10.2 Photonic Crystal Cavity

Our photonic crystal cavity design is based on a zero-cavity length [125] photonic crystal structure proposed in Ref. [141]. The design (Figure 10.4a) consists of symmetric elliptical air holes in a triangular cross-section waveguide with etch angle $\alpha = 45°$, where the major axis radius is quadratically tapered along the device over 30 holes on each side. The elliptical holes have uniform spacing of lattice constant a. We propose two designs that target the 1223 nm and the 1242 nm ZPLs of the NV center in 4H-SiC. The two proposed design parameters and their corresponding quality factor Q and mode volume

Table 10.1. Zero-cavity length photonic crystal cavity design parameters and respective results

Design	**Lattice constant a (nm)**	**Width w**	**Major axis radius max r_1**	**Major axis radius min r_{30}**	**Minor axis radius r_{minor}**	**Cavity resonance (f-TE mode) (nm)**	**Q factor**	**Mode volume V $(\lambda/n)^3$**
(i)	379	$1.94a$	$0.486a$	$0.292a$	$0.292a$	1219.5	7.82×10^6	0.82
(ii)	380	$1.98a$	$0.486a$	$0.292a$	$0.292a$	1236	8.34×10^6	1.26

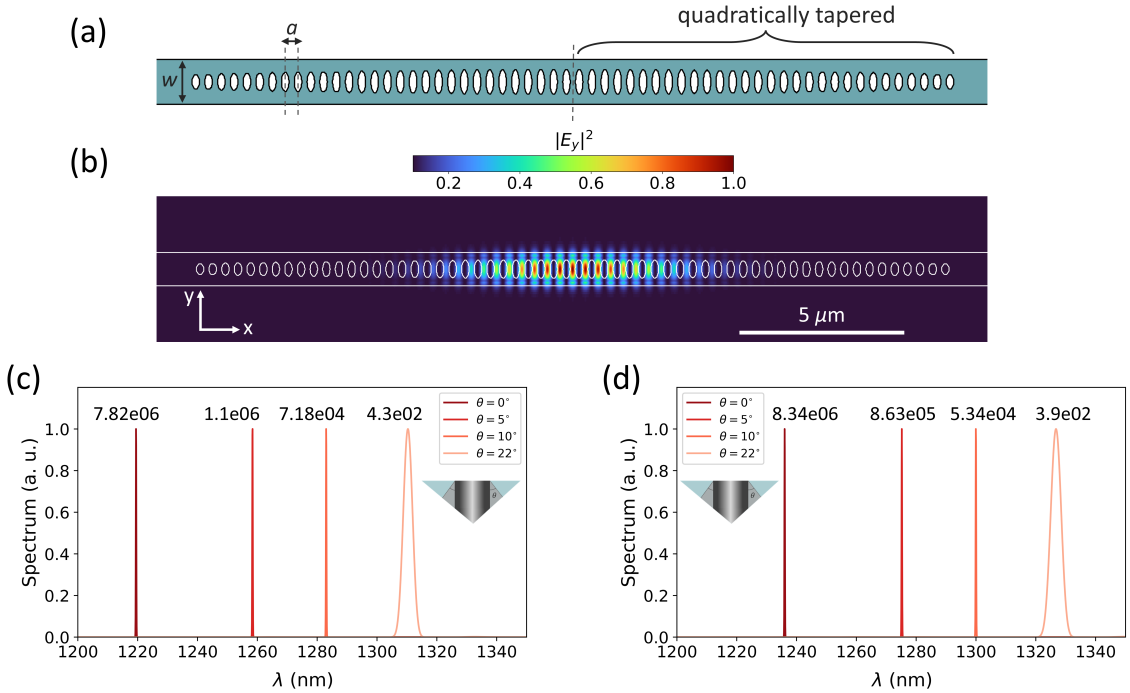

Figure 10.4. (a) Schematic diagram of zero-cavity length photonic crystal cavity design with quadratic tapering of the major axis radii over 30 elliptical holes on each end, where w is the waveguide width and a is the lattice constant. (b) E_y-field intensity profile (at the centroid plane) of the fundamental cavity mode at a resonant wavelength of 1219.5 nm. (c)-(d) Fundamental cavity resonances and corresponding Q-factors with the variation in inner sidewall angle θ for Design (i) and (ii), respectively, as mentioned in Table 10.1.

V for the fundamental TE mode are presented in Table 10.1. Figure 10.4b illustrates the E_y-field intensity profile (at the centroid plane) of the fundamental TE mode at a resonant wavelength of 1219.5 nm. We intentionally detune the cavity resonances from the targeted ZPLs to account for minor fabrication deviations. Additionally, we simulate the cavity resonance and corresponding Q factors, taking into account the inner sidewall angle of the holes, shown in Figure 10.4c-d. We observe that as the inner angle increases,

the cavity resonance redshifts while the respective Q factor decreases. Fabricated devices with developed processes are presented in Figure 10.5.

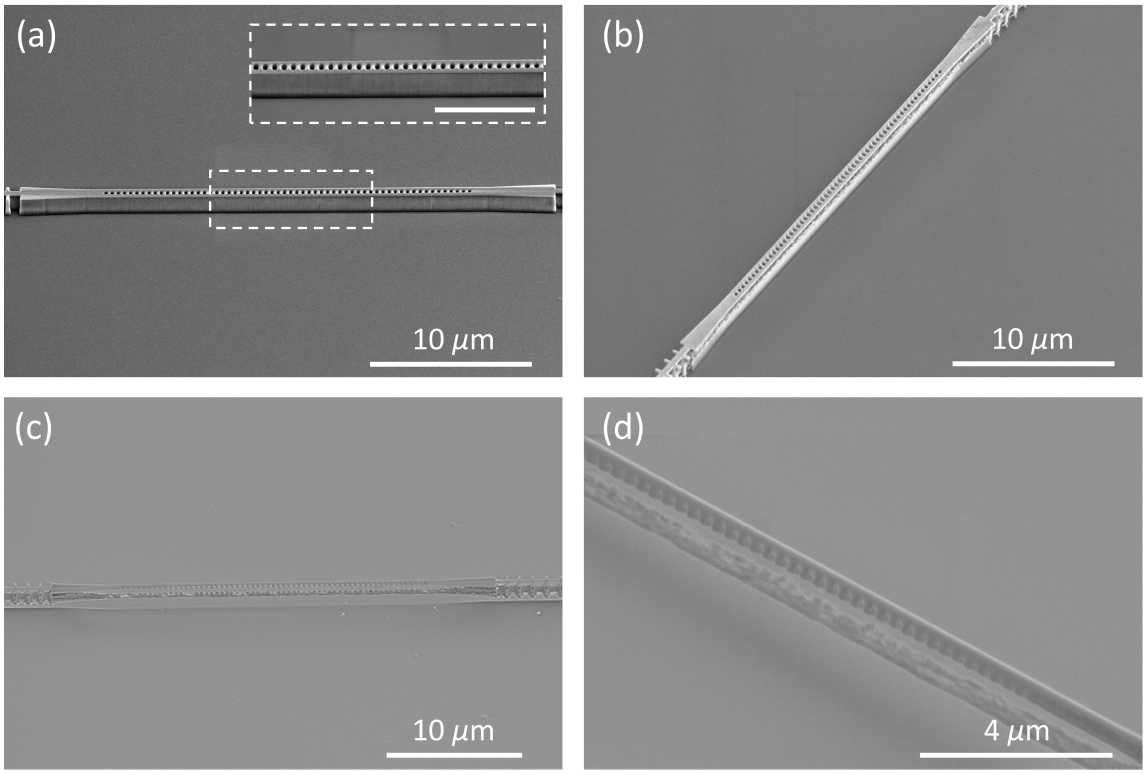

Figure 10.5. (a) Side view SEM image of the photonic crystal cavity (PCC) pattern after vertical etching. The inset scale bar indicates 4 μm. (b) Perspective view SEM image of the PCC after angle-etching. (c) Side view SEM image of the PCC after post-etching processes. (d) SEM image of the PCC sidewall profile taken from a broken device. All the SEM images are obtained at a 52° tilt angle, where (a) and (b) are taken with the Ni mask on top.

The cavity resonance of the zero-cavity length design is predominantly governed by the lattice constant a, which constrains the central spacing region available to spatially isolate single color centers. Our photoluminescence excitation (PLE) measurements on nanopillars indicate that a 300 nm diameter footprint hosts approximately 1-3 NV centers. Therefore, we propose a new photonic crystal cavity design consisting of tapered elliptical holes in the defect region and terminal Bragg mirrors on both ends, shown in Figure 10.6, targeting a central spacing of 150 nm.

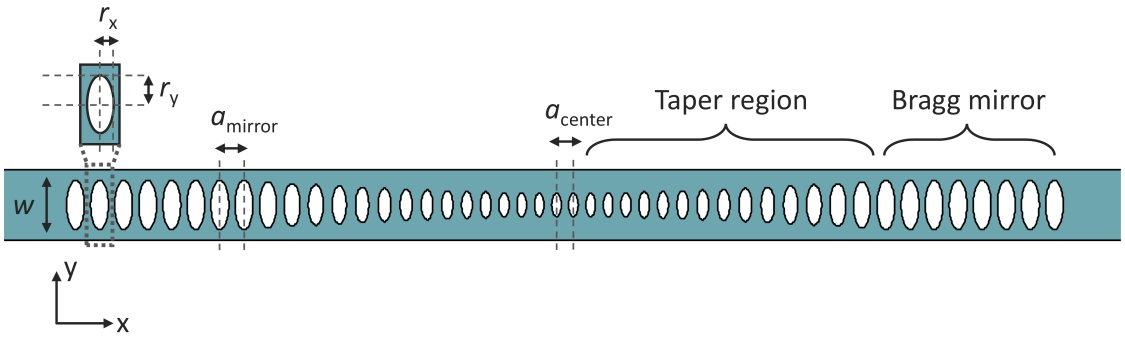

Figure 10.6. (a) Schematic diagram of the inversely tapered photonic crystal cavity design with terminal Bragg mirrors, where w is the waveguide width, a_{mirror} is the lattice constant of the Bragg mirror, a_{center} is the lattice constant at the center, and r_{x} and r_{y} are the minor and major axis radii of the elliptical holes, respectively.

To realize the proposed photonic crystal cavity, we first design the Bragg mirror within a 45° angle-etched triangular cross-section waveguide. Starting with a nominal waveguide width of $w = 1.98a$, where a is the lattice period, we perform a coarse design-of-experiment parameter sweep using the PWE simulations to maximize the f-TE bandgap size, $\Delta f/f_{\mathrm{m}}$ (Δf: photonic bandgap, f_{m}: gap center). The major axis radius is swept across $r_{\mathrm{y}} = 0.15a - 0.8a$ and the minor axis radius across $r_{\mathrm{x}} = 0.1a - 0.4a$, as shown in Figure 10.7a. The lower and upper limits of the sweep are chosen based on fabrication feasibility. Based on the coarse optimization, a refined design-of-experiment sweep is conducted over the high bandgap region of $r_{\mathrm{y}} = 0.45a{-}0.7a$ and $r_{\mathrm{x}} = 0.3a{-}0.4a$, shown in Figure 10.7b. From these simulations, we identify three $\{r_{\mathrm{x}}, r_{\mathrm{y}}\}$ combinations, $\{0.37, 0.575\}a$, $\{0.38, 0.55\}a$, and $\{0.4, 0.65\}a$, which yield gap sizes $\geq 25\%$. Subsequently, we sweep the waveguide width w from $1.6a$ to $2a$, as shown in Figure 10.7c, exclusively for these three selected configurations to further optimize the f-TE bandgap size. We choose $w = 800$ nm for single-mode operation and the $\{w, r_{\mathrm{x}}, r_{\mathrm{y}}\} = \{1.7, 0.37, 0.575\}a$ configuration that provides a wide bandgap, resulting in $a = 471$ nm. Later, we perform FDTD simulations to evaluate the reflectivity as a function of mirror period count for 5, 8, 10, and 12 holes, where the reflection saturates at 8 holes, as shown in Figure 10.7e. Consequently, an 8-hole Bragg mirror configuration with finalized physical dimensions of $\{a_{\mathrm{mirror}}, w, r_{\mathrm{x,mirror}}, r_{\mathrm{y,mirror}}\} = \{471, 800, 174, 271\}$ nm is chosen as the terminal reflector for the cavity.

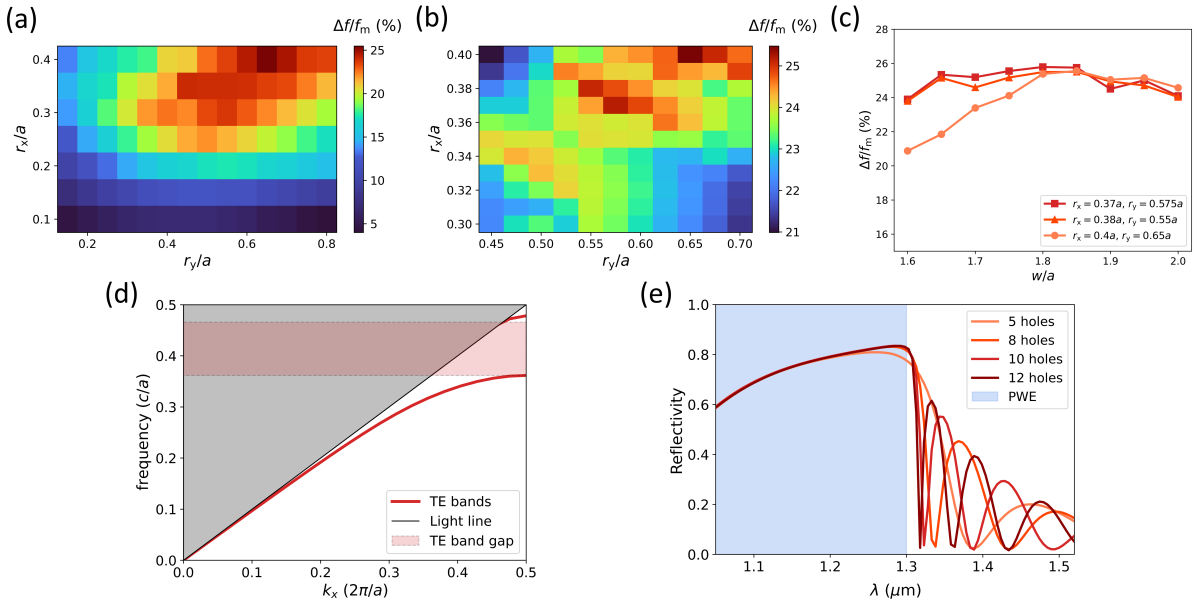

Figure 10.7. (a)-(b) PWE simulation results of the TE photonic bandgap size $\Delta f/f_{\mathrm{m}}$ (Δf: bandgap, f_{m}: gap center) as a function of the normalized minor axis radius r_{x}/a and major axis radius r_{y}/a of the elliptical holes, where the triangular waveguide width $w = 1.98a$ and etch angle $\alpha = 45°$. (c) Gap size as a function of the normalized waveguide width w/a for three $\{r_{\mathrm{x}}, r_{\mathrm{y}}\}$ combinations of $\{0.37, 0.575\}a$, $\{0.38, 0.55\}a$, and $\{0.4, 0.65\}a$. (d) Band structure of the optimized configuration $\{w, r_{\mathrm{x}}, r_{\mathrm{y}}\} = \{1.7, 0.37, 0.575\}a$. (e) Broadband reflectivity variation with no. of holes for the Bragg mirror configuration of $\{a_{\mathrm{mirror}}, w, r_{\mathrm{x,mirror}}, r_{\mathrm{y,mirror}}\} = \{471, 800, 174, 271\}$ nm.

Within the defect region enclosed by the terminal Bragg mirrors, we initially apply a quadratic tapering profile to a, r_{x}, and r_{y} from the mirror boundaries toward the cavity center. To maintain the targeted central spacing of 150 nm, we set $a_{\mathrm{center}} = 350$ nm, with corresponding central hole radii of $r_{\mathrm{x,center}} = 100$ nm and $r_{\mathrm{y,center}} = 130$ nm. Although the Q-factor steadily increases with an increased number of taper periods, we fix the taper hole counts to 15 holes per segment to simultaneously optimize the effective mode volume and simplify nanofabrication. The initial optimized design, shown in Figure 10.8, exhibits an f-TE cavity resonance at $\lambda = 1256$ nm with a high Q-factor of 1.2×10^6 and a small mode volume (V) of 0.438 $(\lambda/n)^3$.

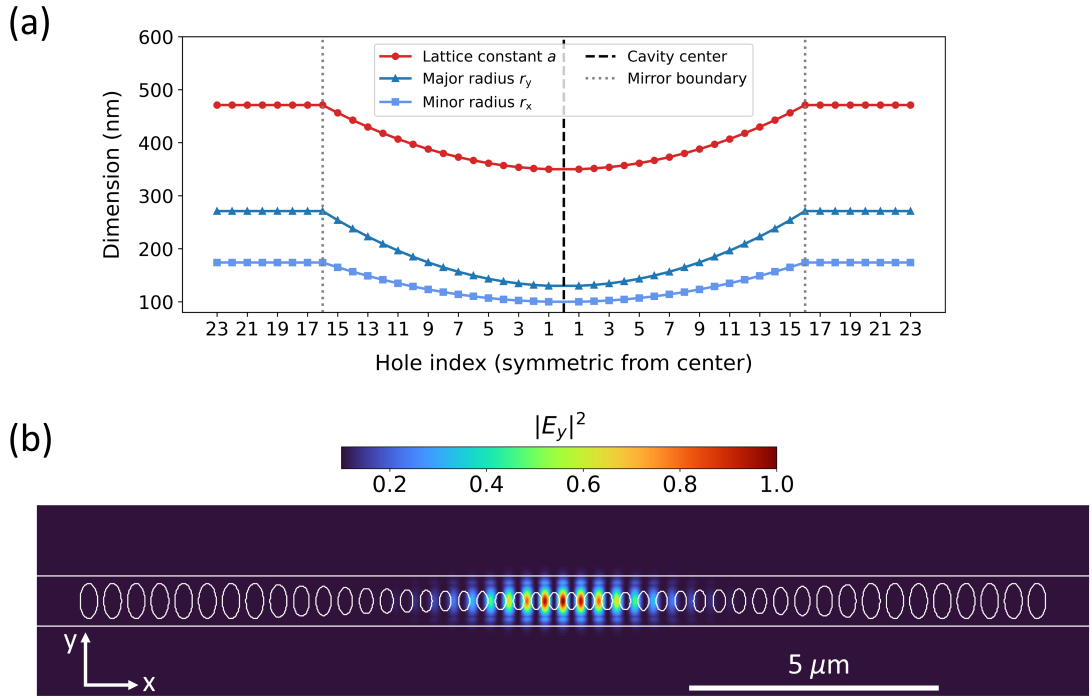

Figure 10.8. (a) Geometric parameter profile of the quadratically tapered photonic crystal nanobeam cavity showing the symmetric variation of the lattice constant a, major axis radius r_y, and minor axis radius r_x from the cavity center through the taper and into the terminal Bragg mirror. (b) Corresponding E_y-field intensity profile (at the centroid plane) of the f-TE cavity mode at $\lambda = 1256$ nm with a Q-factor of 1.2×10^6.

Aiming to enhance the Q-factor without drastically expanding the physical footprint, we implement a hybrid tapering scheme where r_x and r_y are tapered quadratically while a is modulated sinusoidally with the following equation: $a(i) = a_{\text{center}} + (a_{\text{mirror}} - a_{\text{center}}) \cdot \sin^2[\frac{\pi}{2}(\frac{i-1}{N-1})]$, where $1 \leq i \leq N$. In this case, we use a modified parameter set of $\{a_{\text{center}}, r_{x,\text{center}}, r_{y,\text{center}}\} = \{335, 92.5, 128\}$ nm, as shown in Figure 10.9. This sinusoidal period modulation provides a smoother spatial impedance matching near the Bragg walls and yields a $\sim 7\times$ enhanced Q-factor of 8.26×10^6 while retaining a tightly confined V of 0.638 $(\lambda/n)^3$ at a resonant wavelength of $\lambda = 1240$ nm, close to the hk ZPL of the NV center in 4H-SiC. Coupling color centers to such high-Q/V photonic crystal cavities enables substantial Purcell enhancement of the spontaneous ZPL emission rate, which is critical for efficient spin-photon interfaces in quantum networking hardware.

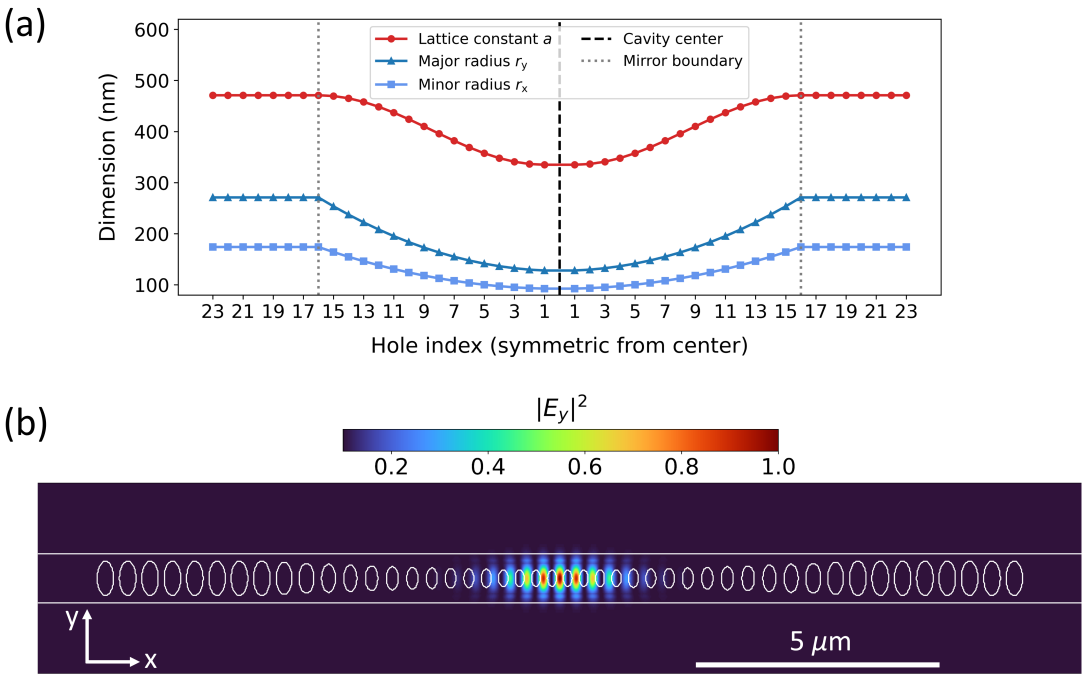

Figure 10.9. (a) Geometric parameter profile of the hybrid-tapered photonic crystal nanobeam cavity where the lattice constant a is modulated following a sinusoidal profile, while the major axis radius r_y and minor axis radius r_x are modulated quadratically from the cavity center to the terminal Bragg mirror. (b) Corresponding E_y-field intensity profile (at the centroid plane) of the f-TE cavity mode at $\lambda = 1240$ nm with a Q-factor of 8.26×10^6.

Chapter 11

Outlook

While the preceding chapters of this dissertation established the design, numerical modeling, wafer-scale angle-etching, and optical characterization of bulk 4H-SiC triangular quantum nanophotonics, several technological and physical frontiers remain to be addressed. In this chapter, we outline the immediate roadmap toward achieving full monolithic integration and active quantum control, followed by contextualizing our findings alongside recent experimental advances in SiC color center technology, charting the path toward fault-tolerant quantum repeater networks on a scalable hardware platform.

11.1 Monolithic Heterogeneous Integration

Realizing a fully monolithic quantum photonic integrated circuit requires the seamless on-chip integration of single-photon detectors alongside stable quantum emitters and passive routing elements. Towards this goal, process development for integrating superconducting nanowire single-photon detectors (SNSPDs) via niobium titanium nitride (NbTiN) thin films onto 4H-SiC waveguides is currently underway. Through collaborative efforts, NbTiN thin films are sputtered directly onto bulk 4H-SiC substrates for the first time, and their corresponding optical and electrical transport properties are comprehensively characterized. Importantly, the measured properties of NbTiN on 4H-SiC demonstrated performance metrics comparable to NbTiN thin films on standard SiO_2 substrates [152]. Initial fabrication runs have validated the chemical and dry-etch compatibility of patterning NbTiN on suspended 4H-SiC triangular waveguides, as shown in Figure 11.1,

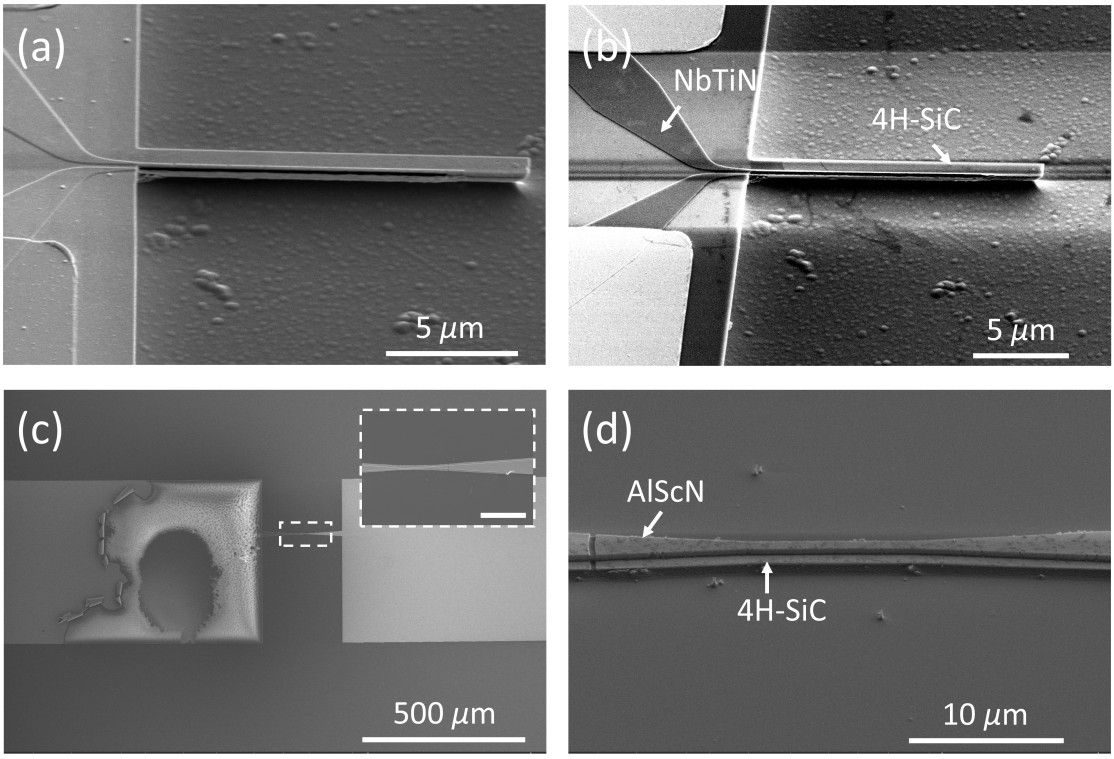

Figure 11.1. (a)-(b) SEM images (52° tilt) of NbTiN thin film overlaid onto 4H-SiC triangular waveguides after angle etching and post-etching processes, respectively. SEM images of AlScN integrated 4H-SiC triangular waveguides (c) after lift-off (top view) and (d) after angle etching (52° tilted image). The inset in (c) shows a successful device after lift-off, and the scale bar indicates 20 μm.

providing the structural basis for integrated readout. In parallel, active emitter tuning via spin-phonon coupling can be realized by incorporating piezoelectric aluminum scandium nitride (AlScN) thin films onto the 4H-SiC triangular waveguide architecture [220]. In another collaborative effort, initial fabrication attempts to integrate AlScN thin films onto 4H-SiC waveguides have faced yield limitations, specifically an unsuccessful lift-off process caused by pinhole defect structures forming on the grown AlScN following the vertical dry-etching step, as shown in Figure 11.1. Refining the film deposition and the vertical etch process for AlScN will provide a clear route to robust electro-acoustic control.

11.2 The Broader Quantum Landscape in SiC

Ultimately, the research presented in this dissertation establishes the foundational design, modeling, and nanofabrication toolkit for scalable quantum photonic integrated architectures in SiC. With the demonstrations of high-efficiency routing, directional beam splitters, broadband grating interfaces, resonant cavity filtering, and wafer-scale angle-etching in bulk 4H-SiC, this body of work provides the complete suite of structural building blocks for an all-triangular quantum photonics platform. Looking ahead, the immediate frontier lies in utilizing the integrated piezoelectric and metallic gate layers for localized acoustic and electrical control, enabling dynamic Stark-shift tuning, spectral stabilization, and active strain modulation of color centers.

While we were making progress towards our vision of implementing monolithic quantum networking hardware natively in SiC, the broader field of SiC quantum photonics has advanced at an extraordinary pace, establishing exceptional experimental benchmarks across charge control, multi-qubit memory registers, optical networking, and native telecom emitters. Crucial breakthroughs in electrostatic engineering have enhanced emitter stability with the integration of Schottky junctions to control the local charge environment and protect spin coherence [221]. Moreover, utilization of p-i-n diode architectures in isotopically engineered SiC has unlocked record-breaking nuclear spin coherence exceeding 100 seconds [222], while coherent control of registers comprising up to 25 individual nuclear spins has been achieved [77], establishing multi-qubit stationary nodes for quantum error correction. On the networking frontier, the landmark first demonstration of spin-photon entanglement in SiC [223] has firmly confirmed the material's viability as a bona fide light-matter interface for quantum repeaters. Furthermore, the discovery and characterization of chlorine vacancy centers provide native telecom-band emission spanning the O- through L-bands [224], effectively bypassing the substantial conversion loss penalties associated with optical frequency down-conversion. With these rapidly maturing optical and spin coherence milestones within a foundry-compatible platform, SiC now sits in a sweet spot to become the clear market leader for commercial solid-state quantum technologies. Merging our wafer-scale triangular nanophotonic architecture with these

concurrent breakthroughs in electrical stabilization, dense nuclear-spin registers, spin-photon entanglement, and native telecom defects establishes a definitive roadmap toward a global quantum internet.

References

[1] F. Arute, K. Arya, R. Babbush, D. Bacon, J. C. Bardin, R. Barends, R. Biswas, S. Boixo, F. G. Brandao, D. A. Buell, *et al.*, "Quantum supremacy using a programmable superconducting processor," *nature*, vol. 574, no. 7779, pp. 505–510, 2019.

[2] H.-S. Zhong, H. Wang, Y.-H. Deng, M.-C. Chen, L.-C. Peng, Y.-H. Luo, J. Qin, D. Wu, X. Ding, Y. Hu, *et al.*, "Quantum computational advantage using photons," *Science*, vol. 370, no. 6523, pp. 1460–1463, 2020.

[3] D. Bluvstein, S. J. Evered, A. A. Geim, S. H. Li, H. Zhou, T. Manovitz, S. Ebadi, M. Cain, M. Kalinowski, D. Hangleiter, *et al.*, "Logical quantum processor based on reconfigurable atom arrays," *Nature*, vol. 626, no. 7997, pp. 58–65, 2024.

[4] J.-S. Chen, E. Nielsen, M. Ebert, V. Inlek, K. Wright, V. Chaplin, A. Maksymov, E. Páez, A. Poudel, P. Maunz, *et al.*, "Benchmarking a trapped-ion quantum computer with 30 qubits," *Quantum*, vol. 8, p. 1516, 2024.

[5] D. Reilly, "Challenges in scaling-up the control interface of a quantum computer," in *2019 IEEE International Electron Devices Meeting (IEDM)*, pp. 31–7, IEEE, 2019.

[6] C. H. Bennett and G. Brassard, "Quantum cryptography: Public key distribution and coin tossing," *arXiv preprint arXiv:2003.06557*, 2020.

[7] B. C. Nichol, R. Srinivas, D. P. Nadlinger, P. Drmota, D. Main, G. Araneda, C. J. Ballance, and D. M. Lucas, "A quantum network of entangled optical atomic clocks," *arXiv preprint arXiv:2111.10336*, 2021.

[8] Y.-C. Wei, P.-J. Stas, A. Suleymanzade, G. Baranes, F. Machado, Y. Q. Huan, C. M. Knaut, S. W. Ding, M. Merz, E. N. Knall, *et al.*, "Universal distributed blind quantum computing with solid-state qubits," *Science*, vol. 388, no. 6746, pp. 509–513, 2025.

[9] N. Sangouard, C. Simon, H. De Riedmatten, and N. Gisin, "Quantum repeaters based on atomic ensembles and linear optics," *Reviews of Modern Physics*, vol. 83, no. 1, pp. 33–80, 2011.

[10] K. Gaur, A. Barua, S. Tripathi, L. J. Roche, S. Wilksen, A. Steinhoff, S. Baraz, N. Nitin, C. C. Palekar, A. Koulas-Simos, *et al.*, "Scalable quantum photonic platform based on site-controlled quantum dots coupled to circular bragg grating resonators," *Light: Science & Applications*, vol. 15, no. 1, p. 260, 2026.

[11] S. I. Azzam, K. Parto, and G. Moody, "Prospects and challenges of quantum emitters in 2d materials," *Applied Physics Letters*, vol. 118, no. 24, 2021.

[12] C. Nguyen, D. Sukachev, M. Bhaskar, B. Machielse, D. Levonian, E. Knall, P. Stroganov, C. Chia, M. Burek, R. Riedinger, *et al.*, "An integrated nanophotonic quantum register based on silicon-vacancy spins in diamond," *Physical Review B*, vol. 100, no. 16, p. 165428, 2019.

[13] Y. Xiong, J. Zheng, S. McBride, X. Zhang, S. M. Griffin, and G. Hautier, "Computationally driven discovery of t center-like quantum defects in silicon," *Journal of the American Chemical Society*, vol. 146, no. 44, pp. 30046–30056, 2024.

[14] C. P. Anderson, E. O. Glen, C. Zeledon, A. Bourassa, Y. Jin, Y. Zhu, C. Vorwerk, A. L. Crook, H. Abe, J. Ul-Hassan, *et al.*, "Five-second coherence of a single spin with single-shot readout in silicon carbide," *Science advances*, vol. 8, no. 5, p. eabm5912, 2022.

[15] S. Majety, P. Saha, V. A. Norman, and M. Radulaski, "Quantum information processing with integrated silicon carbide photonics," *Journal of Applied Physics*, vol. 131, no. 13, p. 130901, 2022.

[16] R. Anzalone, A. Severino, G. D'arrigo, C. Bongiorno, G. Abbondanza, G. Foti, S. Saddow, and F. La Via, "Heteroepitaxy of 3c-sic on different on-axis oriented silicon substrates," *Journal of Applied Physics*, vol. 105, no. 8, 2009.

[17] F. La Via, G. D'Arrigo, A. Severino, N. Piluso, M. Mauceri, C. Locke, and S. E. Saddow, "Patterned substrate with inverted silicon pyramids for 3c–sic epitaxial growth: A comparison with conventional (001) si substrate," *Journal of Materials Research*, vol. 28, no. 1, pp. 94–103, 2013.

[18] R. Anzalone, G. D'arrigo, M. Camarda, C. Locke, S. Saddow, and F. La Via, "Advanced residual stress analysis and fem simulation on heteroepitaxial 3c–sic for mems application," *Journal of Microelectromechanical Systems*, vol. 20, no. 3, pp. 745–752, 2011.

[19] A. L. Crook, C. P. Anderson, K. C. Miao, A. Bourassa, H. Lee, S. L. Bayliss, D. O. Bracher, X. Zhang, H. Abe, T. Ohshima, *et al.*, "Purcell enhancement of a single silicon carbide color center with coherent spin control," *Nano Letters*, vol. 20, no. 5, pp. 3427–3434, 2020.

[20] D. M. Lukin, C. Dory, M. A. Guidry, K. Y. Yang, S. D. Mishra, R. Trivedi, M. Radulaski, S. Sun, D. Vercruysse, G. H. Ahn, *et al.*, "4h-silicon-carbide-on-insulator for integrated quantum and nonlinear photonics," *Nature photonics*, vol. 14, no. 5, pp. 330–334, 2020.

[21] C. Babin, R. Stöhr, N. Morioka, T. Linkewitz, T. Steidl, R. Wörnle, D. Liu, E. Hesselmeier, V. Vorobyov, A. Denisenko, *et al.*, "Fabrication and nanophotonic waveguide integration of silicon carbide colour centres with preserved spin-optical coherence," *Nature Materials*, vol. 21, no. 1, pp. 67–73, 2022.

[22] H. A. Atikian, P. Latawiec, M. J. Burek, Y.-I. Sohn, S. Meesala, N. Gravel, A. B. Kouki, and M. Lončar, "Freestanding nanostructures via reactive ion beam angled etching," *APL Photonics*, vol. 2, no. 5, 2017.

[23] B. Bai, J. Laukkanen, M. Kuittinen, and S. Siitonen, "Optimization of nonbinary slanted surface-relief gratings as high-efficiency broadband couplers for light guides," *Applied optics*, vol. 49, no. 28, pp. 5454–5464, 2010.

[24] W. Zhang, W. Li, T. Zhang, Z. Zheng, Z. Chi, Y. Jiang, and N. Wu, "A large-size and polarization-independent two dimensional grating fabricated by scanned reactive-ion-beam etching," *Nanophotonics*, vol. 11, no. 21, pp. 4649–4657, 2022.

[25] D. Cheng, Q. Wang, Y. Liu, H. Chen, D. Ni, X. Wang, C. Yao, Q. Hou, W. Hou, G. Luo, *et al.*, "Design and manufacture ar head-mounted displays: A review and outlook," *Light: Advanced Manufacturing*, vol. 2, no. 3, pp. 350–369, 2021.

[26] K. Yee, "Numerical solution of initial boundary value problems involving maxwell's equations in isotropic media," *IEEE Transactions on antennas and propagation*, vol. 14, no. 3, pp. 302–307, 1966.

[27] M. Stern, "Semivectorial polarised finite difference method for optical waveguides with arbitrary index profiles," *IEE Proceedings J (Optoelectronics)*, vol. 135, no. 1, pp. 56–63, 1988.

[28] K. Ho, C. T. Chan, and C. M. Soukoulis, "Existence of a photonic gap in periodic dielectric structures," *Physical review letters*, vol. 65, no. 25, p. 3152, 1990.

[29] I. Aharonovich, D. Englund, and M. Toth, "Solid-state single-photon emitters," *Nature photonics*, vol. 10, no. 10, pp. 631–641, 2016.

[30] M. Atatüre, D. Englund, N. Vamivakas, S.-Y. Lee, and J. Wrachtrup, "Material platforms for spin-based photonic quantum technologies," *Nature Reviews Materials*, vol. 3, no. 5, pp. 38–51, 2018.

[31] M. S. Islam, K. Singh, Y. Zhao, N. Singh, and W. Qarony, "Spin-photon qubits for scalable quantum network," *arXiv preprint arXiv:2512.06285*, 2025.

[32] N. Somaschi, V. Giesz, L. De Santis, J. Loredo, M. P. Almeida, G. Hornecker, S. L. Portalupi, T. Grange, C. Anton, J. Demory, *et al.*, "Near-optimal single-photon sources in the solid state," *Nature Photonics*, vol. 10, no. 5, pp. 340–345, 2016.

[33] L. Zhai, G. N. Nguyen, C. Spinnler, J. Ritzmann, M. C. Löbl, A. D. Wieck, A. Ludwig, A. Javadi, and R. J. Warburton, "Quantum interference of identical photons from remote gaas quantum dots," *Nature nanotechnology*, vol. 17, no. 8, pp. 829–833, 2022.

[34] E. Schöll, L. Hanschke, L. Schweickert, K. D. Zeuner, M. Reindl, S. F. Covre da Silva, T. Lettner, R. Trotta, J. J. Finley, K. Müller, *et al.*, "Resonance fluorescence of gaas quantum dots with near-unity photon indistinguishability," *Nano letters*, vol. 19, no. 4, pp. 2404–2410, 2019.

[35] N. Spitzer, E. Kersting, M. Grell, D. Kohminaei, M. Schmidt, N. Bart, A. D. Wieck, and A. Ludwig, "Telecom o-band quantum dots fabricated by droplet etching," *Crystals*, vol. 14, no. 12, p. 1014, 2024.

[36] H. Liu, "Epitaxial growth of semiconductor quantum dots: An overview," *Journal of Molecular and Engineering Materials*, vol. 11, no. 03n04, p. 2330004, 2023.

[37] S. Yu, X. Zhang, X. Lei, and L. Zhai, "A concise primer on solid-state quantum emitters," *IEEE Journal of Selected Topics in Quantum Electronics*, 2025.

[38] C. Bradac, "High-resolution optical imaging and sensing using quantum emitters in hexagonal boron-nitride," *Frontiers in Physics*, vol. 9, p. 641341, 2021.

[39] H. Zhao, M. T. Pettes, Y. Zheng, and H. Htoon, "Site-controlled telecom-wavelength single-photon emitters in atomically-thin mote2," *Nature communications*, vol. 12, no. 1, p. 6753, 2021.

[40] A. B. Kaul, Y. Wang, A.-P. Li, X. Li, and X. Ma, "Single photon emitters in van der waals solids for quantum photonics: materials, theory and molecular-scale characterization probes," *Journal of Physics D: Applied Physics*, vol. 58, no. 12, p. 123001, 2025.

[41] H. Ge, J. Liu, M. Sebek, Z. Li, W. Fu, Z. Wang, and Z. Wang, "Ai-assisted wafer-scale exfoliation and transfer of 2d materials: Status, challenges and perspectives," *AI for Science*, vol. 1, no. 1, p. 013002, 2025.

[42] T. Vogl, V. Ivády, I. J. Luxmoore, and H. L. Stern, "Defects in hexagonal boron nitride for quantum technologies: a perspective," *2D Materials*, vol. 13, no. 2, p. 023001, 2026.

[43] F. J. Heremans, C. G. Yale, and D. D. Awschalom, "Control of spin defects in wide-bandgap semiconductors for quantum technologies," *Proceedings of the IEEE*, vol. 104, no. 10, pp. 2009–2023, 2016.

[44] J. A. Smith, C. Clear, K. C. Balram, D. P. McCutcheon, and J. G. Rarity, "Nitrogen-vacancy center coupled to an ultrasmall-mode-volume cavity: A high-efficiency source of indistinguishable photons at 200 k," *Physical Review Applied*, vol. 15, no. 3, p. 034029, 2021.

[45] S. E. Economou and P. Dev, "Spin-photon entanglement interfaces in silicon carbide defect centers," *Nanotechnology*, vol. 27, no. 50, p. 504001, 2016.

[46] B. Hensen, H. Bernien, A. E. Dréau, A. Reiserer, N. Kalb, M. S. Blok, J. Ruitenberg, R. F. Vermeulen, R. N. Schouten, C. Abellán, *et al.*, "Loophole-free bell inequality violation using electron spins separated by 1.3 kilometres," *Nature*, vol. 526, no. 7575, pp. 682–686, 2015.

[47] T. Yamamoto, H. B. van Ommen, K.-N. Schymik, B. de Zoeten, S. Onoda, S. Saiki, T. Ohshima, H. Arjmandi-Tash, R. Vollmer, and T. H. Taminiau, "Ten-second electron-spin coherence in isotopically engineered diamond," *arXiv preprint arXiv:2604.07439*, 2026.

[48] M. Gulka, D. Wirtitsch, V. Ivády, J. Vodnik, J. Hruby, G. Magchiels, E. Bourgeois, A. Gali, M. Trupke, and M. Nesladek, "Room-temperature control and electrical readout of individual nitrogen-vacancy nuclear spins," *Nature Communications*, vol. 12, no. 1, p. 4421, 2021.

[49] T. H. Taminiau, J. Cramer, T. van der Sar, V. V. Dobrovitski, and R. Hanson, "Universal control and error correction in multi-qubit spin registers in diamond," *Nature nanotechnology*, vol. 9, no. 3, pp. 171–176, 2014.

[50] H. Choi, M. Pant, S. Guha, and D. Englund, "Percolation-based architecture for cluster state creation using photon-mediated entanglement between atomic memories," *npj Quantum Information*, vol. 5, no. 1, p. 104, 2019.

[51] A. Russo, E. Barnes, and S. E. Economou, "Generation of arbitrary all-photonic graph states from quantum emitters," *New Journal of Physics*, vol. 21, no. 5, p. 055002, 2019.

[52] M. Pompili, S. L. Hermans, S. Baier, H. K. Beukers, P. C. Humphreys, R. N. Schouten, R. F. Vermeulen, M. J. Tiggelman, L. dos Santos Martins, B. Dirkse, *et al.*, "Realization of a multinode quantum network of remote solid-state qubits," *Science*, vol. 372, no. 6539, pp. 259–264, 2021.

[53] S. Hermans, M. Pompili, H. Beukers, S. Baier, J. Borregaard, and R. Hanson, "Qubit teleportation between non-neighbouring nodes in a quantum network," *Nature*, vol. 605, no. 7911, pp. 663–668, 2022.

[54] A. J. Stolk, K. L. van der Enden, M.-C. Slater, I. te Raa-Derckx, P. Botma, J. Van Rantwijk, J. B. Biemond, R. A. Hagen, R. W. Herfst, W. D. Koek, *et al.*, "Metropolitan-scale heralded entanglement of solid-state qubits," *Science advances*, vol. 10, no. 44, p. eadp6442, 2024.

[55] S. Johansson, D. Lönard, I. Cardoso Barbosa, J. Gutsche, J. Witzenrath, and A. Widera, "Miniaturized magnetic-field sensor based on nitrogen-vacancy centers," *Physical Review Applied*, vol. 24, no. 5, p. 054078, 2025.

[56] Y. Beerden, B. Carmans, R. Vandebosch, D. Hendrikx, S. Bammens, M. Aydogan, S. Achten, J. Gorissen, S. Vanspauwen, S. Vandervoort, *et al.*, "Diamond-based

magnetometer aboard the international space station," *Physical Review Applied*, vol. 25, no. 5, p. 054017, 2026.

[57] B. McCullian, H. Cheung, H. Chen, and G. Fuchs, "Quantifying the spectral diffusion of n-v centers by symmetry," *Physical Review Applied*, vol. 18, no. 6, p. 064011, 2022.

[58] J. A. Zuber, M. Li, M. l. Grimau Puigibert, J. Happacher, P. Reiser, B. J. Shields, and P. Maletinsky, "Shallow silicon vacancy centers with lifetime-limited optical linewidths in diamond nanostructures," *Nano Letters*, vol. 23, no. 23, pp. 10901–10907, 2023.

[59] M. E. Trusheim, B. Pingault, N. H. Wan, M. Gündoğan, L. De Santis, R. Debroux, D. Gangloff, C. Purser, K. C. Chen, M. Walsh, *et al.*, "Transform-limited photons from a coherent tin-vacancy spin in diamond," *Physical review letters*, vol. 124, no. 2, p. 023602, 2020.

[60] B. Pingault, D.-D. Jarausch, C. Hepp, L. Klintberg, J. N. Becker, M. Markham, C. Becher, and M. Atatüre, "Coherent control of the silicon-vacancy spin in diamond," *Nature communications*, vol. 8, no. 1, p. 15579, 2017.

[61] R. Debroux, C. P. Michaels, C. M. Purser, N. Wan, M. E. Trusheim, J. Arjona Martínez, R. A. Parker, A. M. Stramma, K. C. Chen, L. De Santis, *et al.*, "Quantum control of the tin-vacancy spin qubit in diamond," *Physical Review X*, vol. 11, no. 4, p. 041041, 2021.

[62] D. D. Sukachev, A. Sipahigil, C. T. Nguyen, M. K. Bhaskar, R. E. Evans, F. Jelezko, and M. D. Lukin, "Silicon-vacancy spin qubit in diamond: a quantum memory exceeding 10 ms with single-shot state readout," *Physical review letters*, vol. 119, no. 22, p. 223602, 2017.

[63] E. I. Rosenthal, S. Biswas, G. Scuri, H. Lee, A. J. Stein, H. C. Kleidermacher, J. Grzesik, A. E. Rugar, S. Aghaeimeibodi, D. Riedel, *et al.*, "Single-shot readout and weak measurement of a tin-vacancy qubit in diamond," *Physical Review X*, vol. 14, no. 4, p. 041008, 2024.

[64] P.-J. Stas, Y. Q. Huan, B. Machielse, E. N. Knall, A. Suleymanzade, B. Pingault, M. Sutula, S. W. Ding, C. M. Knaut, D. R. Assumpcao, *et al.*, "Robust multi-qubit quantum network node with integrated error detection," *Science*, vol. 378, no. 6619, pp. 557–560, 2022.

[65] D. Dhaliah, Y. Xiong, A. Sipahigil, S. M. Griffin, and G. Hautier, "First-principles study of the t center in silicon," *Physical Review Materials*, vol. 6, no. 5, p. L053201, 2022.

[66] S. Li, A. Gali, and B. Huang, "Computation-aided design of color centers for quantum information processing," *Newton*, vol. 2, no. 5, 2026.

[67] T. Zhong, J. M. Kindem, J. G. Bartholomew, J. Rochman, I. Craiciu, V. Verma, S. W. Nam, F. Marsili, M. D. Shaw, A. D. Beyer, *et al.*, "Optically addressing single rare-earth ions in a nanophotonic cavity," *Physical review letters*, vol. 121, no. 18, p. 183603, 2018.

[68] E. Sörman, N. T. Son, W. M. Chen, O. Kordina, C. Hallin, and E. Janzén, "Silicon vacancy related defect in 4h and 6h sic," *Physical Review B*, vol. 61, no. 4, p. 2613, 2000.

[69] N. Son, P. Carlsson, J. Ul Hassan, E. Janzén, T. Umeda, J. Isoya, A. Gali, M. Bockstedte, N. Morishita, T. Ohshima, *et al.*, "Divacancy in 4h-sic," *Physical review letters*, vol. 96, no. 5, p. 055501, 2006.

[70] S. Zargaleh, B. Eble, S. Hameau, J.-L. Cantin, L. Legrand, M. Bernard, F. Margaillan, J.-S. Lauret, J.-F. Roch, H. Von Bardeleben, *et al.*, "Evidence for near-infrared photoluminescence of nitrogen vacancy centers in 4 h-sic," *Physical Review B*, vol. 94, no. 6, p. 060102, 2016.

[71] W. F. Koehl, B. Diler, S. J. Whiteley, A. Bourassa, N. T. Son, E. Janzén, and D. D. Awschalom, "Resonant optical spectroscopy and coherent control of c r 4+ spin ensembles in sic and gan," *Physical Review B*, vol. 95, no. 3, p. 035207, 2017.

[72] T. Bosma, G. J. Lof, C. M. Gilardoni, O. V. Zwier, F. Hendriks, B. Magnusson, A. Ellison, A. Gällström, I. G. Ivanov, N. Son, *et al.*, "Identification and tunable optical coherent control of transition-metal spins in silicon carbide," *npj Quantum Information*, vol. 4, no. 1, p. 48, 2018.

[73] G. Wolfowicz, C. P. Anderson, B. Diler, O. G. Poluektov, F. J. Heremans, and D. D. Awschalom, "Vanadium spin qubits as telecom quantum emitters in silicon carbide," *Science advances*, vol. 6, no. 18, p. eaaz1192, 2020.

[74] J. Bader, S. Q. Lim, F. A. Inam, A. Lyasota, B. C. Johnson, A. Peruzzo, J. C. McCallum, Q. Li, S. Rogge, and S. Castelletto, "Photoluminescence properties of ion-implanted er3+ defects in 4h-sicoi for integrated quantum photonics," *ACS Applied Nano Materials*, vol. 8, no. 16, pp. 7920–7927, 2025.

[75] Q. Li, J.-F. Wang, F.-F. Yan, J.-Y. Zhou, H.-F. Wang, H. Liu, L.-P. Guo, X. Zhou, A. Gali, Z.-H. Liu, *et al.*, "Room-temperature coherent manipulation of single-spin qubits in silicon carbide with a high readout contrast," *National Science Review*, vol. 9, no. 5, p. nwab122, 2022.

[76] E. Hesselmeier, P. Kuna, W. Knolle, F. Kaiser, N. T. Son, M. Ghezellou, J. Ul-Hassan, V. Vorobyov, and J. Wrachtrup, "High-fidelity optical readout of a nuclear-spin qubit in silicon carbide," *Physical Review Letters*, vol. 132, no. 18, p. 180804, 2024.

[77] P. Kuna, E. Hesselmeier-Hüttmann, P. Schillinger, F. Gloistein, I. Takács, V. Ivády, W. Knolle, J. Ul-Hassan, J. Wrachtrup, and V. Vorobyov, "Localization and coherent control of 25 nuclear spins in silicon carbide," *arXiv preprint arXiv:2512.20281*, 2025.

[78] O. Bulancea-Lindvall, M. T. Eiles, N. T. Son, I. A. Abrikosov, and V. Ivády, "Isotope-purification-induced reduction of spin-relaxation and spin-coherence times in semiconductors," *Physical Review Applied*, vol. 19, no. 6, p. 064046, 2023.

[79] A. Bourassa, C. P. Anderson, K. C. Miao, M. Onizhuk, H. Ma, A. L. Crook, H. Abe, J. Ul-Hassan, T. Ohshima, N. T. Son, *et al.*, "Entanglement and control of single nuclear spins in isotopically engineered silicon carbide," *Nature Materials*, vol. 19, no. 12, pp. 1319–1325, 2020.

[80] R. Nagy, M. Niethammer, M. Widmann, Y.-C. Chen, P. Udvarhelyi, C. Bonato, J. U. Hassan, R. Karhu, I. G. Ivanov, N. T. Son, *et al.*, "High-fidelity spin and optical control of single silicon-vacancy centres in silicon carbide," *Nature communications*, vol. 10, no. 1, p. 1954, 2019.

[81] P. Cilibrizzi, M. J. Arshad, B. Tissot, N. T. Son, I. G. Ivanov, T. Astner, P. Koller, M. Ghezellou, J. Ul-Hassan, D. White, *et al.*, "Ultra-narrow inhomogeneous spectral distribution of telecom-wavelength vanadium centres in isotopically-enriched silicon carbide," *Nature Communications*, vol. 14, no. 1, p. 8448, 2023.

[82] L. M. Pham, N. Bar-Gill, D. Le Sage, C. Belthangady, A. Stacey, M. Markham, D. Twitchen, M. D. Lukin, and R. L. Walsworth, "Enhanced metrology using preferential orientation of nitrogen-vacancy centers in diamond," *Physical Review B—Condensed Matter and Materials Physics*, vol. 86, no. 12, p. 121202, 2012.

[83] A. H. Rubin, V. Žalandauskas, P. Saha, R. Poudel, A. Teien, L. Hofmann, N. R. Gonzalez, S. Dhuey, M. E. Bathen, and M. Radulaski, "Seeing the forbidden: overcoming optical selection rules through nanophotonic integration," *arXiv preprint arXiv:2605.04277*, 2026.

[84] H. Jurgen von Bardeleben, J.-L. Cantin, U. Gerstmann, W. G. Schmidt, and T. Biktagirov, "Spin polarization, electron–phonon coupling, and zero-phonon line of the nv center in 3 c-sic," *Nano Letters*, vol. 21, no. 19, pp. 8119–8125, 2021.

[85] M. Radulaski, M. Widmann, M. Niethammer, J. L. Zhang, S.-Y. Lee, T. Rendler, K. G. Lagoudakis, N. T. Son, E. Janzen, T. Ohshima, *et al.*, "Scalable quantum photonics with single color centers in silicon carbide," *Nano Letters*, vol. 17, no. 3, pp. 1782–1786, 2017.

[86] M. A. Guidry, K. Y. Yang, D. M. Lukin, A. Markosyan, J. Yang, M. M. Fejer, and J. Vučković, "Optical parametric oscillation in silicon carbide nanophotonics," *Optica*, vol. 7, no. 9, pp. 1139–1142, 2020.

[87] B.-S. Song, S. Jeon, H. Kim, D. D. Kang, T. Asano, and S. Noda, "High-Q-factor nanobeam photonic crystal cavities in bulk silicon carbide," *Applied Physics Letters*, vol. 113, no. 23, p. 231106, 2018.

[88] M. Widmann, S.-Y. Lee, T. Rendler, N. T. Son, H. Fedder, S. Paik, L.-P. Yang, N. Zhao, S. Yang, I. Booker, *et al.*, "Coherent control of single spins in silicon carbide at room temperature," *Nature Materials*, vol. 14, no. 2, pp. 164–168, 2015.

[89] F. Sardi, T. Kornher, M. Widmann, R. Kolesov, F. Schiller, T. Reindl, M. Hagel, and J. Wrachtrup, "Scalable production of solid-immersion lenses for quantum emitters in silicon carbide," *Applied Physics Letters*, vol. 117, no. 2, p. 022105, 2020.

[90] A. Reiserer and G. Rempe, "Cavity-based quantum networks with single atoms and optical photons," *Reviews of modern physics*, vol. 87, no. 4, pp. 1379–1418, 2015.

[91] J. Borregaard, A. S. Sørensen, and P. Lodahl, "Quantum networks with deterministic spin–photon interfaces," *Advanced Quantum Technologies*, vol. 2, no. 5-6, p. 1800091, 2019.

[92] G. Calusine, A. Politi, and D. D. Awschalom, "Silicon carbide photonic crystal cavities with integrated color centers," *Applied Physics Letters*, vol. 105, no. 1, 2014.

[93] F. L. Via, M. Zimbone, C. Bongiorno, A. La Magna, G. Fisicaro, I. Deretzis, V. Scuderi, C. Calabretta, F. Giannazzo, M. Zielinski, *et al.*, "New approaches and understandings in the growth of cubic silicon carbide," *Materials*, vol. 14, no. 18, p. 5348, 2021.

[94] J. Lipton, B. Yurash, A. Sorensen, J. Vajo, S. Whiteley, T. Wang, B. Huang, X. Bai, A. Portales, S. Rubin, *et al.*, "Low-loss nanophotonic devices with chip-level uniformity and integrated color centers in sic-on-insulator," *Acs Photonics*, vol. 12, no. 5, pp. 2397–2405, 2025.

[95] M. J. Burek, Y. Chu, M. S. Liddy, P. Patel, J. Rochman, S. Meesala, W. Hong, Q. Quan, M. D. Lukin, and M. Lončar, "High quality-factor optical nanocavities in bulk single-crystal diamond," *Nature communications*, vol. 5, no. 1, p. 5718, 2014.

[96] M. K. Bhaskar, R. Riedinger, B. Machielse, D. S. Levonian, C. T. Nguyen, E. N. Knall, H. Park, D. Englund, M. Lončar, D. D. Sukachev, *et al.*, "Experimental demonstration of memory-enhanced quantum communication," *Nature*, vol. 580, no. 7801, pp. 60–64, 2020.

[97] B. Zeng, C. De-Eknamkul, D. Assumpcao, D. Renaud, Z. Wang, D. Riedel, J. Ha, C. Robens, D. Levonian, M. Lukin, *et al.*, "Cryogenic packaging of nanophotonic devices with a low coupling loss< 1 db," *Applied physics letters*, vol. 123, no. 16, 2023.

[98] M. Gurfinkel, S. Potbhare, H. Xiong, J. Suehle, Y. Shapira, A. Lelis, D. Habersat, and N. Goldsman, "Ion implantation and sic transistor performance," *Journal of Applied Physics*, vol. 105, no. 8, 2009.

[99] K. Piskorski, M. Guziewicz, M. Wzorek, and L. Dobrzański, "Investigation of al-and n-implanted 4h–sic applying visible and deep uv raman scattering spectroscopy," *AIP Advances*, vol. 10, no. 5, 2020.

[100] J. Wang, X. Zhang, Y. Zhou, K. Li, Z. Wang, P. Peddibhotla, F. Liu, S. Bauerdick, A. Rudzinski, Z. Liu, *et al.*, "Scalable fabrication of single silicon vacancy defect arrays in silicon carbide using focused ion beam," *Acs Photonics*, vol. 4, no. 5, pp. 1054–1059, 2017.

[101] A. F. M. Almutairi, J. Partridge, C. Xu, I. Cole, and A. Holland, "Direct writing of divacancy centers in silicon carbide by femtosecond laser irradiation and subsequent thermal annealing," *Applied Physics Letters*, vol. 120, no. 1, 2022.

[102] A. M. Day, J. R. Dietz, M. Sutula, M. Yeh, and E. L. Hu, "Laser writing of spin defects in nanophotonic cavities," *Nature Materials*, vol. 22, no. 6, pp. 696–702, 2023.

[103] H. Kraus, D. Simin, C. Kasper, Y. Suda, S. Kawabata, W. Kada, T. Honda, Y. Hijikata, T. Ohshima, V. Dyakonov, *et al.*, "Three-dimensional proton beam writing of optically active coherent vacancy spins in silicon carbide," *Nano letters*, vol. 17, no. 5, pp. 2865–2870, 2017.

[104] J. Wang, Y. Zhou, X. Zhang, F. Liu, Y. Li, K. Li, Z. Liu, G. Wang, and W. Gao, "Efficient generation of an array of single silicon-vacancy defects in silicon carbide," *Physical Review Applied*, vol. 7, no. 6, p. 064021, 2017.

[105] J.-F. Wang, F.-F. Yan, Q. Li, Z.-H. Liu, H. Liu, G.-P. Guo, L.-P. Guo, X. Zhou, J.-M. Cui, J. Wang, *et al.*, "Coherent control of nitrogen-vacancy center spins in silicon carbide at room temperature," *Physical review letters*, vol. 124, no. 22, p. 223601, 2020.

[106] I. Zhigulin, K. Shimazaki, S. M. Stephens, A. Gale, K. Yamamura, H. H. Tan, I. Aharonovich, and M. Kianinia, "Coupling nitrogen vacancy centers in silicon carbide to nanophotonic resonators," *arXiv preprint arXiv:2602.21505*, 2026.

[107] T. Mitani, R. Hattori, and M. Yoshikawa, "Diffusion of point defects from ion implanted 4h-sic: Cathodoluminescence observation," in *Materials Science Forum*, vol. 615, pp. 481–484, Trans Tech Publ, 2009.

[108] F. Khan and I. Adesida, "High rate etching of sic using inductively coupled plasma reactive ion etching in sf 6-based gas mixtures," *Applied physics letters*, vol. 75, no. 15, pp. 2268–2270, 1999.

[109] J. Choi, L. Latu-Romain, E. Bano, F. Dhalluin, T. Chevolleau, and T. Baron, "Fabrication of sic nanopillars by inductively coupled sf6/o2 plasma etching," *Journal of Physics D: Applied Physics*, vol. 45, no. 23, p. 235204, 2012.

[110] R. J. Shul and S. J. Pearton, *Handbook of advanced plasma processing techniques*. Springer Science & Business Media, 2011.

[111] H. R. Kaufman, *Applications of Broad-Beam Ion Sources: An Introduction*. Kaufman & Robinson, 2011.

[112] V. A. Norman, S. Majety, A. H. Rubin, P. Saha, N. R. Gonzalez, J. Simo, B. Palomarez, L. Li, P. B. Curro, S. Dhuey, *et al.*, "Sub-2 kelvin characterization of nitrogen-vacancy centers in silicon carbide nanopillars," *ACS photonics*, vol. 12, no. 5, pp. 2604–2611, 2025.

[113] E. Yablonovitch, "Inhibited spontaneous emission in solid-state physics and electronics," *Physical Review Letters*, vol. 58, no. 20, p. 2059, 1987.

[114] S. John, "Strong localization of photons in certain disordered dielectric superlattices," *Physical Review Letters*, vol. 58, no. 23, p. 2486, 1987.

[115] M. Born, "Wave propagation in periodic structures," *Nature*, vol. 158, no. 4026, pp. 926–926, 1946.

[116] A. Shakoor, K. Nozaki, E. Kuramochi, K. Nishiguchi, A. Shinya, and M. Notomi, "Compact 1D-silicon photonic crystal electro-optic modulator operating with ultralow switching voltage and energy," *Optics Express*, vol. 22, no. 23, pp. 28623–28634, 2014.

[117] T. Zhou, M. Tang, H. Li, Z. Zhang, Y. Cui, J.-S. Park, M. Martin, T. Baron, S. Chen, H. Liu, *et al.*, "Single-mode photonic crystal nanobeam lasers monolithically grown on Si for dense integration," *IEEE Journal of Selected Topics in Quantum Electronics*, vol. 28, no. 3, pp. 1–6, 2021.

[118] P. R. Villeneuve and M. Piché, "Photonic band gaps in two-dimensional square lattices: Square and circular rods," *Physical Review B*, vol. 46, no. 8, p. 4973, 1992.

[119] R. Wang, X.-H. Wang, B.-Y. Gu, and G.-Z. Yang, "Effects of shapes and orientations of scatterers and lattice symmetries on the photonic band gap in two-dimensional photonic crystals," *Journal of Applied Physics*, vol. 90, no. 9, pp. 4307–4313, 2001.

[120] S. G. Johnson, M. L. Povinelli, and J. D. Joannopoulos, "New photonic crystal system for integrated optics," in *Active and Passive Optical Components for WDM Communication*, vol. 4532, pp. 167–179, SPIE, 2001.

[121] M. Notomi, E. Kuramochi, and H. Taniyama, "Ultrahigh-Q nanocavity with 1D photonic gap," *Optics Express*, vol. 16, no. 15, pp. 11095–11102, 2008.

[122] Y. Kalra and R. Sinha, "Modelling and design of complete photonic band gaps in two-dimensional photonic crystals," *Pramana*, vol. 70, no. 1, pp. 153–161, 2008.

[123] J. Zhou, H. Li, L. Ye, J. Liu, J. Wang, T. Zhao, L. Jiang, and Y. Song, "Facile fabrication of tough SiC inverse opal photonic crystals," *The Journal of Physical Chemistry C*, vol. 114, no. 50, pp. 22303–22308, 2010.

[124] B.-S. Song, S. Yamada, T. Asano, and S. Noda, "Demonstration of two-dimensional photonic crystals based on silicon carbide," *Optics Express*, vol. 19, no. 12, pp. 11084–11089, 2011.

[125] Q. Quan and M. Loncar, "Deterministic design of wavelength scale, ultra-high Q photonic crystal nanobeam cavities," *Optics Express*, vol. 19, no. 19, pp. 18529–18542, 2011.

[126] M. Eguchi and Y. Tsuji, "Single-polarization elliptical-hole lattice core photonic-bandgap fiber," *Journal of Lightwave Technology*, vol. 31, no. 1, pp. 177–182, 2012.

[127] M. Radulaski, T. M. Babinec, S. Buckley, A. Rundquist, J. Provine, K. Alassaad, G. Ferro, and J. Vučković, "Photonic crystal cavities in cubic (3C) polytype silicon carbide films," *Optics Express*, vol. 21, no. 26, pp. 32623–32629, 2013.

[128] J. Shi, M. E. Pollard, C. A. Angeles, R. Chen, J. C. Gates, and M. D. Charlton, "Photonic crystal and quasi-crystals providing simultaneous light coupling and beam splitting within a low refractive-index slab waveguide," *Scientific Reports*, vol. 7, no. 1, pp. 1–10, 2017.

[129] J. Hou, L. Wang, C. Yang, B. Wang, and S. Chen, "Compact high extinction ratio asymmetric polarization beam splitter of periodic rods waveguide," *Applied Optics*, vol. 54, no. 34, pp. 10277–10282, 2015.

[130] M. Butt and N. Kazanskiy, "Two-dimensional photonic crystal heterostructure for light steering and TM-polarization maintaining applications," *Laser Physics*, vol. 31, no. 3, p. 036201, 2021.

[131] E. Anagha and R. Jeyachitra, "An investigation on the cascaded operation of photonic crystal based all optical logic gates and verification of de morgan's law," *Optical and Quantum Electronics*, vol. 52, no. 6, pp. 1–26, 2020.

[132] S. Swarnakar, S. Rathi, and S. Kumar, "Design of all optical xor gate based on photonic crystal ring resonator," *Journal of Optical Communications*, vol. 41, no. 1, pp. 51–56, 2020.

[133] D. Zhao, H. Yang, Z. Ma, and W. Zhou, "Polarization independent broadband reflectors based on cross-stacked gratings," *Optics Express*, vol. 19, no. 10, pp. 9050–9055, 2011.

[134] Y. K. Zhong, S. M. Fu, S. L. Yan, P. Y. Chen, and A. Lin, "Arbitrarily-wide-band dielectric mirrors and their applications to SiGe solar cells," *IEEE Photonics Journal*, vol. 7, no. 4, pp. 1–12, 2015.

[135] M. Scullion, A. Di Falco, and T. Krauss, "Slotted photonic crystal cavities with integrated microfluidics for biosensing applications," *Biosensors and Bioelectronics*, vol. 27, no. 1, pp. 101–105, 2011.

[136] Y. Zhuo, H. Hu, W. Chen, M. Lu, L. Tian, H. Yu, K. D. Long, E. Chow, W. P. King, S. Singamaneni, *et al.*, "Single nanoparticle detection using photonic crystal enhanced microscopy," *Analyst*, vol. 139, no. 5, pp. 1007–1015, 2014.

[137] O. Painter, R. Lee, A. Scherer, A. Yariv, J. O'brien, P. Dapkus, and I. Kim, "Two-dimensional photonic band-gap defect mode laser," *Science*, vol. 284, no. 5421, pp. 1819–1821, 1999.

[138] H.-Y. Lu, S.-C. Tian, C.-Z. Tong, L.-J. Wang, J.-M. Rong, C.-Y. Liu, H. Wang, S.-L. Shu, and L.-J. Wang, "Extracting more light for vertical emission: high power continuous wave operation of 1.3-μm quantum-dot photonic-crystal surface-emitting laser based on a flat band," *Light: Science & Applications*, vol. 8, no. 1, pp. 1–6, 2019.

[139] P. Bermel, C. Luo, L. Zeng, L. C. Kimerling, and J. D. Joannopoulos, "Improving thin-film crystalline silicon solar cell efficiencies with photonic crystals," *Optics Express*, vol. 15, no. 25, pp. 16986–17000, 2007.

[140] D.-K. Hwang, B. Lee, and D.-H. Kim, "Efficiency enhancement in solid dye-sensitized solar cell by three-dimensional photonic crystal," *RSC advances*, vol. 3, no. 9, pp. 3017–3023, 2013.

[141] S. Majety, V. A. Norman, L. Li, M. Bell, P. Saha, and M. Radulaski, "Quantum photonics in triangular-cross-section nanodevices in silicon carbide," *Journal of Physics: Photonics*, vol. 3, no. 3, p. 034008, 2021.

[142] S. Fan, J. N. Winn, A. Devenyi, J. Chen, R. D. Meade, and J. Joannopoulos, "Guided and defect modes in periodic dielectric waveguides," *JOSA B*, vol. 12, no. 7, pp. 1267–1272, 1995.

[143] O. Cranwell Schaeper, J. E. Fröch, S. Kim, Z. Mu, M. Toth, W. Gao, and I. Aharonovich, "Fabrication of photonic resonators in bulk 4H-SiC," *Advanced Materials Technologies*, vol. 6, no. 11, p. 2100589, 2021.

[144] G. Chen, T. Wang, K. Ooi, A. Chee, L. Ang, and D. Tan, "Wavelength selective mode division multiplexing on a silicon chip," *Optics Express*, vol. 23, no. 6, pp. 8095–8103, 2015.

[145] S. Shi, C. Chen, and D. W. Prather, "Plane-wave expansion method for calculating band structure of photonic crystal slabs with perfectly matched layers," *JOSA A*, vol. 21, no. 9, pp. 1769–1775, 2004.

[146] A. Panda and P. D. Pukhrambam, "Analysis of GaN-based 2D photonic crystal sensor for real-time detection of alcohols," *Brazilian Journal of Physics*, vol. 51, no. 3, pp. 481–492, 2021.

[147] J. D. Joannopoulos, S. G. Johnson, J. N. Winn, and R. D. Meade, *Photonic Crystals: Molding the Flow of Light (Second Edition)*. Princeton University Press, 2 ed., 2008.

[148] S. G. Johnson and J. D. Joannopoulos, "Block-iterative frequency-domain methods for maxwell's equations in a planewave basis," *Optics Express*, vol. 8, no. 3, pp. 173–190, 2001.

[149] J. D. Joannopoulos, P. R. Villeneuve, and S. Fan, "Photonic crystals: putting a new twist on light," *Nature*, vol. 386, no. 6621, pp. 143–149, 1997.

[150] M. Butt, S. Khonina, and N. Kazanskiy, "Recent advances in photonic crystal optical devices: A review," *Optics & Laser Technology*, vol. 142, p. 107265, 2021.

[151] P. D. Anderson and G. Subramania, "Unidirectional edge states in topological honeycomb-lattice membrane photonic crystals," *Optics Express*, vol. 25, no. 19, pp. 23293–23301, 2017.

[152] S. Majety, S. Strohauer, P. Saha, F. Wietschorke, J. J. Finley, K. Müller, and M. Radulaski, "Triangular quantum photonic devices with integrated detectors in silicon carbide," *Materials for Quantum Technology*, vol. 3, no. 1, p. 015004, 2023.

[153] R. Yusof, N. Ali, P. Kolenderski, K. Slowik, and N. A. Hambali, "Comparative studies of rib waveguide material for quantum communication application," *IOP Conference Series: Materials Science and Engineering*, vol. 551, no. 1, p. 012018, 2019.

[154] M. Westig, H. Thierschmann, A. Katan, M. Finkel, and T. M. Klapwijk, "Analysis of a single-mode waveguide at sub-terahertz frequencies as a communication channel," *AIP Advances*, vol. 10, no. 1, p. 015008, 2020.

[155] L. Spindlberger, A. Csóré, G. Thiering, S. Putz, R. Karhu, J. U. Hassan, N. Son, T. Fromherz, A. Gali, and M. Trupke, "Optical properties of vanadium in 4h silicon carbide for quantum technology," *Physical Review Applied*, vol. 12, no. 1, p. 014015, 2019.

[156] J.-F. Wang, Z.-H. Liu, F.-F. Yan, Q. Li, X.-G. Yang, L. Guo, X. Zhou, W. Huang, J.-S. Xu, C.-F. Li, *et al.*, "Experimental optical properties of single nitrogen vacancy centers in silicon carbide at room temperature," *ACS Photonics*, vol. 7, no. 7, pp. 1611–1616, 2020.

[157] S. Castelletto, A. Peruzzo, C. Bonato, B. C. Johnson, M. Radulaski, H. Ou, F. Kaiser, and J. Wrachtrup, "Silicon carbide photonics bridging quantum technology," *ACS Photonics*, vol. 9, no. 5, pp. 1434–1457, 2022.

[158] R. Hamerly, S. Bandyopadhyay, and D. Englund, "Asymptotically fault-tolerant programmable photonics," *Nature Communications*, vol. 13, no. 1, p. 6831, 2022.

[159] M. Dong, M. Zimmermann, D. Heim, H. Choi, G. Clark, A. J. Leenheer, K. J. Palm, A. Witte, D. Dominguez, G. Gilbert, *et al.*, "Programmable photonic integrated meshes for modular generation of optical entanglement links," *npj Quantum Information*, vol. 9, no. 1, p. 42, 2023.

[160] W. Bogaerts, D. Pérez, J. Capmany, D. A. Miller, J. Poon, D. Englund, F. Morichetti, and A. Melloni, "Programmable photonic circuits," *Nature*, vol. 586, no. 7828, pp. 207–216, 2020.

[161] S. Gyger, J. Zichi, L. Schweickert, A. W. Elshaari, S. Steinhauer, S. F. Covre da Silva, A. Rastelli, V. Zwiller, K. D. Jöns, and C. Errando-Herranz, "Reconfigurable photonics with on-chip single-photon detectors," *Nature Communications*, vol. 12, no. 1, p. 1408, 2021.

[162] F. Martini, A. Gaggero, F. Mattioli, and R. Leoni, "Single photon detection with superconducting nanowires on crystalline silicon carbide," *Optics Express*, vol. 27, no. 21, pp. 29669–29675, 2019.

[163] M. Reck, A. Zeilinger, H. J. Bernstein, and P. Bertani, "Experimental realization of any discrete unitary operator," *Physical Review Letters*, vol. 73, no. 1, p. 58, 1994.

[164] E. Knill, R. Laflamme, and G. J. Milburn, "A scheme for efficient quantum computation with linear optics," *Nature*, vol. 409, no. 6816, pp. 46–52, 2001.

[165] Y. Xu, Z. Tian, X. Meng, and Z. Chai, "Methods and applications of on-chip beam splitting: A review," *Frontiers in Physics*, vol. 10, p. 985208, 2022.

[166] Z. Mu, S. A. Zargaleh, H. J. von Bardeleben, J. E. Fröch, M. Nonahal, H. Cai, X. Yang, J. Yang, X. Li, I. Aharonovich, *et al.*, "Coherent manipulation with resonant excitation and single emitter creation of nitrogen vacancy centers in 4H silicon carbide," *Nano Letters*, vol. 20, no. 8, pp. 6142–6147, 2020.

[167] S.-i. Sato, T. Narahara, Y. Abe, Y. Hijikata, T. Umeda, and T. Ohshima, "Formation of nitrogen-vacancy centers in 4H-SiC and their near infrared photoluminescence properties," *Journal of Applied Physics*, vol. 126, no. 8, 2019.

[168] C. M. Caves and P. D. Drummond, "Quantum limits on bosonic communication rates," *Reviews of Modern Physics*, vol. 66, no. 2, p. 481, 1994.

[169] W. Yuan, G. E. Town, and O. Bang, "Refractive index sensing in an all-solid twin-core photonic bandgap fiber," *IEEE Sensors Journal*, vol. 10, no. 7, pp. 1192–1199, 2010.

[170] L. Zhang, L. Jie, M. Zhang, Y. Wang, Y. Xie, Y. Shi, and D. Dai, "Ultrahigh-Q silicon racetrack resonators," *Photonics Research*, vol. 8, no. 5, pp. 684–689, 2020.

[171] P. Saha, S. Majety, and M. Radulaski, "Utilizing photonic band gap in triangular silicon carbide structures for efficient quantum nanophotonic hardware," *Scientific Reports*, vol. 13, no. 1, p. 4112, 2023.

[172] M. J. Burek, N. P. De Leon, B. J. Shields, B. J. Hausmann, Y. Chu, Q. Quan, A. S. Zibrov, H. Park, M. D. Lukin, and M. Lončar, "Free-standing mechanical and photonic nanostructures in single-crystal diamond," *Nano Letters*, vol. 12, no. 12, pp. 6084–6089, 2012.

[173] G. Dornberg, E. Rohkamm, P. Birtel, F. Scholze, and F. Frost, "Characterization of a broad beam kaufman-type ion source operated with chf3 and o2," *Journal of Vacuum Science & Technology A*, vol. 41, no. 5, 2023.

[174] A. L. Falk, B. B. Buckley, G. Calusine, W. F. Koehl, V. V. Dobrovitski, A. Politi, C. A. Zorman, P. X.-L. Feng, and D. D. Awschalom, "Polytype control of spin qubits in silicon carbide," *Nature Communications*, vol. 4, no. 1, p. 1819, 2013.

[175] L. Cheng, S. Mao, Z. Li, Y. Han, and H. Fu, "Grating couplers on silicon photonics: Design principles, emerging trends and practical issues," *Micromachines*, vol. 11, no. 7, p. 666, 2020.

[176] R. Marchetti, C. Lacava, L. Carroll, K. Gradkowski, and P. Minzioni, "Coupling strategies for silicon photonics integrated chips," *Photonics Research*, vol. 7, no. 2, pp. 201–239, 2019.

[177] A. Faraon, I. Fushman, D. Englund, N. Stoltz, P. Petroff, and J. Vučković, "Dipole induced transparency in waveguide coupled photonic crystal cavities," *Optics express*, vol. 16, no. 16, pp. 12154–12162, 2008.

[178] X. Zhou, I. Kulkova, T. Lund-Hansen, S. L. Hansen, P. Lodahl, and L. Midolo, "High-efficiency shallow-etched grating on gaas membranes for quantum photonic applications," *Applied Physics Letters*, vol. 113, no. 25, 2018.

[179] Y. Zhu, J. Wang, W. Xie, B. Tian, Y. Li, E. Brainis, Y. Jiao, and D. Van Thourhout, "Ultra-compact silicon nitride grating coupler for microscopy systems," *Optics express*, vol. 25, no. 26, pp. 33297–33304, 2017.

[180] P. C. Humphreys, B. J. Metcalf, J. B. Spring, M. Moore, X.-M. Jin, M. Barbieri, W. S. Kolthammer, and I. A. Walmsley, "Linear optical quantum computing in a single spatial mode," *Physical review letters*, vol. 111, no. 15, p. 150501, 2013.

[181] S. Majety, P. Saha, Z. Kekula, S. Dhuey, and M. Radulaski, "Triangular cross-section beam splitters in silicon carbide for quantum information processing," *MRS communications*, vol. 14, no. 6, pp. 1262–1268, 2024.

[182] S. Majety, V. A. Norman, P. Saha, A. H. Rubin, S. Dhuey, and M. Radulaski, "Wafer-scale integration of freestanding photonic devices with color centers in silicon carbide," *npj Nanophotonics*, vol. 2, no. 1, p. 3, 2025.

[183] G. Son, S. Han, J. Park, K. Kwon, and K. Yu, "High-efficiency broadband light coupling between optical fibers and photonic integrated circuits," *Nanophotonics*, vol. 7, no. 12, pp. 1845–1864, 2018.

[184] Y. Fu, T. Ye, W. Tang, and T. Chu, "Efficient adiabatic silicon-on-insulator waveguide taper," *Photonics Research*, vol. 2, no. 3, pp. A41–A44, 2014.

[185] M. J. Burek, C. Meuwly, R. E. Evans, M. K. Bhaskar, A. Sipahigil, S. Meesala, B. Machielse, D. D. Sukachev, C. T. Nguyen, J. L. Pacheco, *et al.*, "Fiber-coupled diamond quantum nanophotonic interface," *Physical Review Applied*, vol. 8, no. 2, p. 024026, 2017.

[186] J. Zhang, J. Yang, H. Lu, W. Wu, J. Huang, and S. Chang, "Subwavelength te/tm grating coupler based on silicon-on-insulator," *Infrared Physics & Technology*, vol. 71, pp. 542–546, 2015.

[187] J. Hadden, C. Maynard, D. M. Beggs, R. A. Taylor, and A. J. Bennett, "Design of free-space couplers for suspended triangular nano-beam waveguides," *Journal of Physics D: Applied Physics*, vol. 55, no. 47, p. 474002, 2022.

[188] L. C. Andreani, D. Gerace, M. Passoni, A. Bozzola, and L. Carroll, "Optimizing grating couplers for silicon photonics," in *2016 18th International Conference on Transparent Optical Networks (ICTON)*, pp. 1–4, IEEE, 2016.

[189] V. Vitali, T. Domínguez Bucio, C. Lacava, R. Marchetti, L. Mastronardi, T. Rutirawut, G. Churchill, J. Faneca, J. C. Gates, F. Gardes, *et al.*, "High-efficiency reflector-less dual-level silicon photonic grating coupler," *Photonics Research*, vol. 11, no. 7, pp. 1275–1283, 2023.

[190] Y. Ding, H. Ou, and C. Peucheret, "Ultrahigh-efficiency apodized grating coupler using fully etched photonic crystals," *Optics letters*, vol. 38, no. 15, pp. 2732–2734, 2013.

[191] M. H. Lee, J. Y. Jo, D. W. Kim, Y. Kim, and K. H. Kim, "Comparative study of uniform and nonuniform grating couplers for optimized fiber coupling to silicon waveguides," *Journal of the Optical Society of Korea*, vol. 20, no. 2, pp. 291–299, 2016.

[192] I. Bayn, S. Mouradian, L. Li, J. Goldstein, T. Schröder, J. Zheng, E. Chen, O. Gaathon, M. Lu, A. Stein, *et al.*, "Fabrication of triangular nanobeam waveguide networks in bulk diamond using single-crystal silicon hard masks," *Applied Physics Letters*, vol. 105, no. 21, 2014.

[193] C. Schinke, P. Christian Peest, J. Schmidt, R. Brendel, K. Bothe, M. R. Vogt, I. Kröger, S. Winter, A. Schirmacher, S. Lim, *et al.*, "Uncertainty analysis for the coefficient of band-to-band absorption of crystalline silicon," *Aip Advances*, vol. 5, no. 6, 2015.

[194] G. Taraldsen, T. Berge, F. Haukland, B. H. Lindqvist, and H. Jonasson, "Uncertainty of decibel levels," *The Journal of the Acoustical Society of America*, vol. 138, no. 3, pp. EL264–EL269, 2015.

[195] D. Melati, A. Melloni, and F. Morichetti, "Real photonic waveguides: guiding light through imperfections," *Advances in Optics and Photonics*, vol. 6, no. 2, pp. 156–224, 2014.

[196] P. Foster, J. Doylend, P. Mascher, A. Knights, and P. Coleman, "Optical attenuation in defect-engineered silicon rib waveguides," *Journal of applied physics*, vol. 99, no. 7, 2006.

[197] C. Shakespeare, T. Loippo, H. Lyyra, and J. T. Muhonen, "The effects of ion implantation damage to photonic crystal optomechanical resonators in silicon," *Materials for Quantum Technology*, vol. 1, no. 4, p. 045003, 2021.

[198] A. Baydin, H. Krzyzanowska, M. Dhanunjaya, S. Nageswara Rao, J. L. Davidson, L. C. Feldman, and N. H. Tolk, "Depth dependent modification of optical constants arising from h+ implantation in n-type 4h-sic measured using coherent acoustic phonons," *APL Photonics*, vol. 1, no. 3, 2016.

[199] J. Gimbert, T. Billon, T. Ouisse, J. Grisolia, G. Ben-Assayag, and C. Jaussaud, "Nitrogen implantation in 4h and 6h–sic," *Materials Science and Engineering: B*, vol. 61, pp. 368–372, 1999.

[200] R. Xu, S. Taheriniya, A. Varri, M. Ulanov, I. Konyshev, L. Krämer, L. McRae, F. L. Ebert, J. R. Bankwitz, X. Ma, *et al.*, "Mode conversion trimming in asymmetric directional couplers enabled by silicon ion implantation," *Nano Letters*, vol. 24, no. 35, pp. 10813–10819, 2024.

[201] T. Spuesens, S. Pathak, M. Vanslembrouck, P. Dumon, and W. Bogaerts, "Grating couplers with an integrated power splitter for high-intensity optical power distribution," *IEEE photonics technology letters*, vol. 28, no. 11, pp. 1173–1176, 2016.

[202] M. W. Ngandeu Ngambou, P. Perrin, I. Balasa, A. Tiranov, O. Brinza, F. Bénédic, J. Renaud, M. Reveillard, J. Silvent, P. Goldner, *et al.*, "Hot ion implantation to create dense nv center ensembles in diamond," *Applied Physics Letters*, vol. 124, no. 13, 2024.

[203] B. L. Green, A. T. Collins, and C. M. Breeding, "Diamond spectroscopy, defect centers, color, and treatments," *Reviews in Mineralogy and Geochemistry*, vol. 88, no. 1, pp. 637–688, 2022.

[204] P. Spinicelli, A. Dréau, L. Rondin, F. Silva, J. Achard, S. Xavier, S. Bansropun, T. Debuisschert, S. Pezzagna, J. Meijer, *et al.*, "Engineered arrays of nitrogen-vacancy color centers in diamond based on implantation of cn- molecules through nanoapertures," *New Journal of Physics*, vol. 13, no. 2, p. 025014, 2011.

[205] M. A. Lieberman and A. J. Lichtenberg, *Principles of Plasma Discharges and Materials Processing*. Hoboken, NJ: John Wiley & Sons, 2nd ed., 2005.

[206] K. Suzuki, K. Nakamura, H. Ohkubo, and H. Sugai, "Power transfer efficiency and mode jump in an inductive rf discharge," *Plasma Sources Science and Technology*, vol. 7, no. 1, pp. 13–20, 1998.

[207] R. Haugsrud, "On the high-temperature oxidation of nickel," *Corrosion Science*, vol. 45, no. 1, pp. 211–235, 2003.

[208] P. Hou and R. Cannon, "Spallation behavior of thermally grown nickel oxide on nickel," *Oxidation of metals*, vol. 71, no. 5, pp. 237–256, 2009.

[209] C. Chia, B. Machielse, A. Shams-Ansari, and M. Lončar, "Development of hard masks for reactive ion beam angled etching of diamond," *Optics Express*, vol. 30, no. 9, pp. 14189–14201, 2022.

[210] Y. Wang, A. Pan, X. Zhu, and B. Cui, "Fabrication of blazed gratings by tilted reactive ion beam etching with the side mask for augmented reality applications," *Journal of Vacuum Science & Technology B*, vol. 42, no. 1, 2024.

[211] D. Bohm, "Minimum ionic kinetic energy for a stable sheath," *in The characteristics of electrical discharges in magnetic fields (eds. A. Guthrie and RK Wakerling)*, p. 77, 1949.

[212] G. Aston, H. Kaufman, and P. Wilbur, "Ion beam divergence characteristics of two-grid accelerator systems," *AiAA Journal*, vol. 16, no. 5, pp. 516–524, 1978.

[213] C. Child, "Discharge from hot cao," *Physical Review (Series I)*, vol. 32, no. 5, p. 492, 1911.

[214] L. T. Williams and M. L. Walker, "Initial performance evaluation of a gridded radio frequency ion thruster," *Journal of Propulsion and Power*, vol. 30, no. 3, pp. 645–655, 2014.

[215] H. Kaufman, J. Cuomo, and J. Harper, "Technology and applications of broad-beam ion sources used in sputtering. part i. ion source technology," *Journal of Vacuum Science and Technology*, vol. 21, no. 3, pp. 725–736, 1982.

[216] D. M. Goebel, I. Katz, and I. G. Mikellides, *Fundamentals of electric propulsion*. John Wiley & Sons, 2023.

[217] H. Li, J. Yang, L. Zhang, S. Zhang, and A. Sun, "Structural characteristics of the upstream sheath of the ion optics and its application in evaluating the beam performance of an ion thruster," *Journal of Applied Physics*, vol. 131, no. 2, 2022.

[218] W. Zubrzycki, G. Vawter, and J. Wendt, "High-aspect-ratio nanophotonic components fabricated by cl 2 reactive ion beam etching," *Journal of Vacuum Science & Technology B: Microelectronics and Nanometer Structures Processing, Measurement, and Phenomena*, vol. 17, no. 6, pp. 2740–2744, 1999.

[219] A. Finzel, F. Koch, G. Dornberg, D. Lehr, F. Frost, and T. Glaser, "Reactive ion beam etching of highly dispersive, high-efficiency transmission gratings for the vis range," *Optical Engineering*, vol. 58, no. 9, pp. 092614–092614, 2019.

[220] Y. Deng, D. Anderson, X. Du, W. Roberts, M. Miller, B. Smith, L. Hackett, R. H. Olsson, and M. Eichenfield, "Monolithic alscn/sic phononic waveguides for scalable acoustoelectric and quantum devices," *APL Materials*, vol. 13, no. 10, 2025.

[221] T. Steidl, P. Kuna, E. Hesselmeier-Hüttmann, D. Liu, R. Stöhr, W. Knolle, M. Ghezellou, J. Ul-Hassan, M. Schober, M. Bockstedte, *et al.*, "Single v2 defect in 4h silicon carbide schottky diode at low temperature," *Nature communications*, vol. 16, no. 1, p. 4669, 2025.

[222] C. Zeledon, B. Pingault, J. C. Marcks, M. Onizhuk, Y. Tsaturyan, Y.-x. Wang, B. S. Soloway, H. Abe, M. Ghezellou, J. Ul-Hassan, *et al.*, "Minute-long quantum coherence enabled by electrical depletion of magnetic noise," *arXiv preprint arXiv:2504.13164*, 2026.

[223] R.-Z. Fang, X.-Y. Lai, T. Li, R.-Z. Su, B.-W. Lu, C.-W. Yang, R.-Z. Liu, Y.-K. Qiao, C. Li, Z.-G. He, *et al.*, "Experimental generation of spin-photon entanglement in silicon carbide," *Physical Review Letters*, vol. 132, no. 16, p. 160801, 2024.

[224] A. N. Anisimov, A. V. Mathews, K. Mavridou, U. Kentsch, M. Helm, and G. V. Astakhov, "Engineering chlorine-based emitters in silicon carbide for telecom-band quantum technologies," *Optics Express*, vol. 33, no. 26, pp. 54285–54294, 2025.